On Asymptotical & Numerical Analyses of Liquid Jets

by

Muhammad Mohsin

A thesis submitted to
The University of Birmingham
for the degree of
Doctor of Philosophy

School of Mathematics
College of Engineering
& Physical Sciences
The University of Birmingham
July 2012

Acknowledgements

I would like to express my sincere and heartfelt thankfulness and appreciation to my supervisors Dr. Jamal Uddin and Professor Stephen Decent for helping me with every difficulty that I had during my research. Their guidance, commitment and co-operation were really blessings for me throughout this research. In particular, I am really grateful to Jamal for all of his help, support, encouragement and very useful advices throughout my whole research life.

My sincere thanks also go to Dr. Emilian Părău, from the University of East Anglia, for providing me with his excellent numerical codes for the liquid jet breakup, which are used in the seventh chapter of this thesis.

I wish to express my special thanks to EPSRC for giving me the funding for this research. I also want to convey my gratitude to Dr. Chris Gurney, for all of his fruitful discussions with me. Finally, I thank all of my family members, especially my mother and my wife, for all of their support during this research.

Mohsin.

Dedication

I am dedicating this thesis to the person that I love the most in the world; my mother, whose prayers, love, affection, support, encouragement and kindness enable me to achieve success in every step of my life. She always took great care of me throughout my life. Even today when I go to my home, my mother asks me "Son, have you eaten food?" Indeed, you are a great blessing mother. Thank you mother!

Abstract

Liquid jet breakup is a commonly occurring phenomenon in the world and controlling the breakup process is very important and useful in many industrial, engineering and medical fields. In this thesis, we investigate the behaviour of liquid jets and, in particular, how to control the breakup of liquid jets. For that purpose, we examine the behaviour of linear and nonlinear waves travelling along a liquid jet using two different methods, the classical method and then the Needham-Leach method.

The outline and the advantages of the classical method are as follows. We use a long wavelength asymptotic expansion to reduce the governing equations of a given problem in to a set of one-dimensional model equations. We first obtain the steady-state solutions of these model equations and then we perform a linear temporal instability analysis of steady-state solutions. This process yields a temporal dispersion relation, which we solve numerically to investigate the behaviour of maximum growth rates and maximum wavenumbers of the most unstable wave disturbance, by changing key physical parameters of the problem. In addition, we estimate the breakup length of compound liquid jets falling under gravity, using the linear temporal stability analysis and we compare our results with numerical simulations. Furthermore, using classical method, we obtain the nonlinear temporal equations, which we solve to get useful information about the breakup length, main and satellite drop sizes, by changing key physical parameters of the problem.

The outline and the advantages of the Needham-Leach method are as follows. We consider the model equations of a given problem, along with initial and boundary conditions, and we divide the whole domain in different space and time asymptotic regions. We next find the solution to the model equations in each region, which consists of some unknown constants and then we do asymptotic matching between each neighbouring region to find out the values of the unknown constants. This process is repeated in each asymptotic region until the whole asymptotic domain is fully covered. The Needham-Leach method gives useful information about the liquid jet breakup, the region of breakup and, most importantly, the means of controlling the liquid jet breakup. We also obtain an asymptotic solution to the liquid jet equations for large space and time limits. We also find the onset of nonlinear wave instability, where the nonlinear wave starts to dominate. Hence, we find the mode competition of the imposed wave from linearity into nonlinearity. In order to get the onset of nonlinear wave instability, we must do this kind of the Needham-Leach method analysis, as we cannot get the onset of nonlinear wave instability through numerical analysis.

Contents

Chapter 1

Introduction

The breakup of a liquid jet into small drops is a commonly occurring phenomenon in the world. In many industrial and engineering problems, it is highly desirable to control the breakup of liquid jets and to obtain drops of a desired size. Liquid jet breakup is used in many fields like in pharmaceutics (see Mitragotri (2006)), prilling process (see Wallwork (2002)), sprays (see Lefebvre (1989)) and agricultural irrigation (see Eggers & Villermaux (2008)). Normally, a disturbance, in the form of a sinusoidal wave, is applied at the orifice of the liquid jet to control the size of the resulting drops. This disturbance can be a high frequency sound wave (see Partridge (2006)) or in the form of a vibrating needle (see Chauhan (2003)). As a result of this imposed disturbance, two kinds of drops are produced; drops of equal sizes, known as uniform or main drops, and drops of much smaller sizes, known as satellite droplets. In industrial and engineering applications, such as in the process of agricultural irrigation, the satellite droplets lead to waste (see Eggers & Villermaux (2008)). The primary aim, in such studies, is therefore to obtain uniform drops and no satellite droplets.

Our main objective in this thesis is to use the classical method and then the Needham-Leach method to control the liquid jet breakup. We first use the classi-

cal method to obtain the steady-state solutions of the model equations of a given problem and then we perform a temporal instability analysis to obtain a dispersion relation, which gives us useful information about the maximum growth rate and the maximum wavenumber of the imposed wave-like disturbance. Next, we use the Needham-Leach method to describe the different regions of the breakup of liquid jets. This asymptotic method tells us the onset of the nonlinearity or the mode competition of the wave from linearity into nonlinearity. We use matched asymptotic expansions to calculate the large time and space asymptotic structure of the long wavelength evolution equations. We determine some useful quantities, like the amplitude, frequency, wavenumber (and hence the wavelength) and the growth rate of the disturbance, which are associated with the travelling of nonlinear waves. These will give useful information about the liquid jet breakup, the region of breakup and, most importantly, how we can control the breakup of liquid jets. In addition, we will also compare the results of our asymptotic method with a numerical method. Our aim will be to ultimately obtain a parameter space in which uniform drops with no or very few satellite droplets can be achieved.

This thesis is divided into two parts. In the first part, we present the classical method and in the second part, we present the Needham-Leach method. We arrange this thesis in the following manner. The second chapter of this thesis contains a short summary about liquid jets and the importance of controlling them. We also describe the different types of breakup regimes and the different types of instability analyses. In addition, we describe compound liquid jets and important experimental and theoretical works on them.

In the third chapter, we perform a theoretical analysis to examine the instability of an axisymmetric inviscid compound liquid jet which falls vertically under the influence of gravity. This problem is a generalization of the problem, which was considered by Sanz & Meseguer (1985). We use a long-wavelength, slender-

jet asymptotic expansion to reduce the governing equations of the problem into a set of one dimensional partial differential equations, which describe the evolution of the leading-order axial velocities of the jet as well as the radii of both the inner and the outer interfaces. We first determine the steady-state solutions of the one dimensional model equations and then we perform a linear temporal instability analysis to obtain a dispersion relation, which gives us useful information about the maximum growth rate and the maximum wavenumber of the imposed wave-like disturbance. We use our results to estimate the location and qualitative nature of breakup and then compare our results with numerical simulations.

In the fourth chapter, we perform a theoretical analysis to examine the instability of an axisymmetric shear thinning compound liquid jet which falls vertically under the influence of gravity. This problem is a generalization of the problem solved in Mohsin $et\ al.$ (2012). We use a long-wavelength, slender-jet asymptotic expansion to reduce the governing equations of the problem into a set of one dimensional partial differential equations, which describe the evolution of the leading-order axial velocities of the jet as well as the radii of both the inner and the outer interfaces. We first determine the steady-state solutions of the one dimensional model equations and then we perform a linear temporal instability analysis to obtain a dispersion relation, which gives us useful information about the maximum growth rate and the maximum wavenumber of the imposed wave-like disturbance. We next use the Lax-Wendroff method to determine the non-linear temporal solution.

In the fifth chapter, we give a description of the Needham-Leach method. After that, we give a review of Decent (2009), which is an application of the Needham-Leach method to the breakup of liquid jets. Decent (2009) applied the Needham-Leach method for the very first time to the breakup of liquid jets and, consequently, obtained very useful information regarding the regions of jet

breakup.

In the sixth chapter, we consider a straight uniform vertically falling Newtonian liquid jet under the influence of gravity. We obtain a leading-order solution of this problem. We next apply the Needham-Leach method to this problem and we find an equation that describes an uncontrollable and unstable nonlinear wave. Moreover, we obtain an asymptotical solution of that equation and we also find asymptotically the onset of that uncontrollable and unstable nonlinear wave. In addition, we solve the nonlinear wave equation computationally and we also obtain the onset of the uncontrollable and unstable nonlinear wave computationally. In order to have uniform drops with no or few satellite droplets, we postulate that we must break the liquid jet before the onset of the uncontrollable and unstable nonlinear wave. At the end, we carry out a linear wave regime analysis and using this analysis and asymptotic matching, we derive a dispersion relation, that gives a relationship between the frequency and the wavenumber.

In the seventh chapter, we consider a rotating Newtonian liquid jet. We obtain a leading-order solution of this problem. We next apply the Needham-Leach method to this problem and, similar to the previous chapter, we find an equation that describes an uncontrollable and unstable nonlinear wave. Moreover, we obtain an asymptotical solution of that equation and we also find asymptotically the onset of that uncontrollable and unstable nonlinear wave. In addition, we solve the nonlinear wave equation computationally and we also obtain the onset of the uncontrollable and unstable nonlinear wave computationally. We also describe different types of modes of the breakup of liquid jets. We use a numerical model to support our analysis. Using the numerical model, we find the mode of breakup and the point of breakup on the computational solution of the unstable nonlinear wave. We examine the impact of varying the physical parameters of this problem on the breakup modes of liquid jets. This chapter mainly examines regions in

which we can get uniform drops with no or very few satellite droplets.

In the eight chapter, we include gravity in the problem described in previous chapter seven and we consider a rotating Newtonian jet which is falling under the influence of gravity. We first obtain a leading-order solution of this problem. We next apply the Needham-Leach method to this problem and, similar to the previous chapter, we find an equation that describes an uncontrollable and unstable nonlinear wave. Moreover, we obtain an asymptotical solution of that equation and we also find asymptotically the onset of that uncontrollable and unstable nonlinear wave. In addition, we solve the nonlinear wave equation computationally and we also obtain the onset of the uncontrollable and unstable nonlinear wave computationally.

The penultimate chapter of this thesis contains a brief summary of all the results we have obtained in the previous chapters. In the last chapter, we look towards the future directions and the possible extensions of our work in this thesis.

In Appendix A, we describe a generalization of Decent (2009), by examining a straight uniform non-Newtonian liquid jet. We apply the Needham-Leach method to this problem and we also calculate the non-Newtonian viscosity in each region. Finally, in Appendix B, we mention the numerical model, which we use in fourth and seventh chapters of this thesis.

Chapter 2

Literature Review on Liquid Jets

2.1 Introduction

The breakup of liquid jets is a commonly occurring phenomenon and it can be observed in many places in our daily life. For example, if we open a water tap very slowly, we can observe the water dripping from it, resulting in the drop formulation of liquid jets. The breakup and the drop formulation of liquid jets is an important phenomenon in many scenarios; for example, in the production of fertilizer pellets, which are used in the industrial prilling process, where liquid jets are used to make tiny pellets (see Figure 2.1).

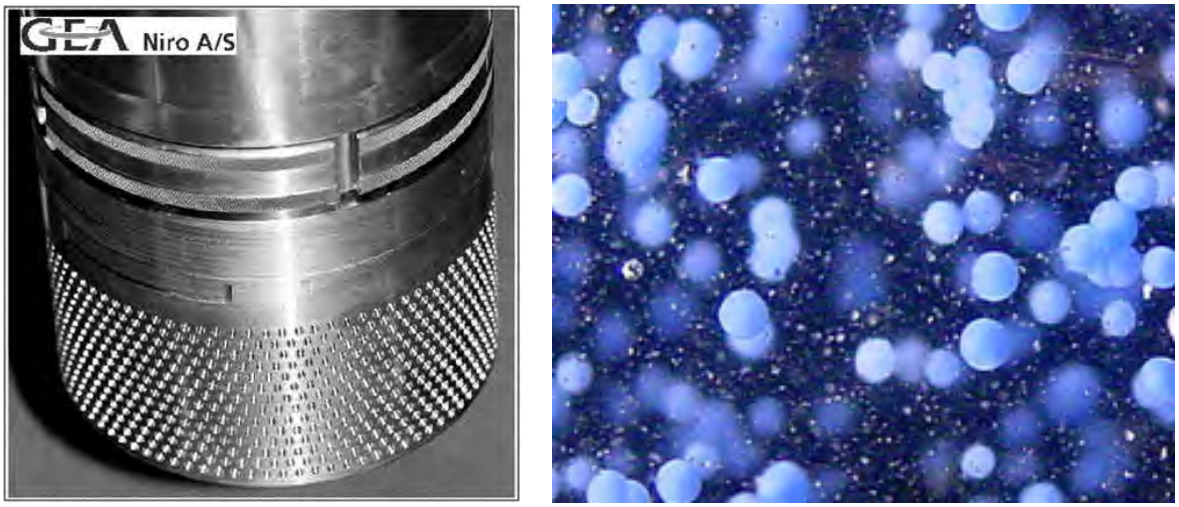

Figure 2.1: Left is a prilling drum used to manufacture pellets in the industry and right is a large number of pellets or beads. Figures are respectively taken from GEA Process Engineering Inc. and Aveka group.

Liquid jets are also widely used in the process of agricultural irrigation (see Eggers and Villermaux (2008) for details), where liquid jets are used to form sprays (see Figure 2.2) as well as cutting various materials, including meat and metal plates (see Figure 2.3).

The flow of liquid jets is of two types; $laminar\ flow$ (also known as the smooth flow) and $turbulent\ flow$ (also known as the rough flow). A laminar flow is a flow in which the fluid particles move in layers or laminas and these layers move along the well-defined paths. In such a flow, one layer of fluid smoothly slides over an adjacent layer and there is no mixing of adjacent fluid layers. Consequently, there is no movement of fluid particles from one layer to another (see Massoud (2005) and Sawhney (2011)). In a turbulent flow, on the other hand, there is mixing of adjacent fluid layers and this type of flow is characterized by chaotic and disordered property changes of the fluid. Flows with very high Reynolds numbers, greater than 4,000 (see Holman (2002)), usually become turbulent, while those with low Reynolds numbers usually remain laminar. The region in between

Figure 2.2: Liquid jets are used as sprays in agricultural irrigation. Reproduced from Eggers and Villermaux (2008).

Figure 2.3: A figure showing the cutting of metal plates by high speed water jets. Reproduced from Eggers and Villermaux (2008).

is called *the transition region*. In this thesis, we consider the liquid jet flow which is laminar.

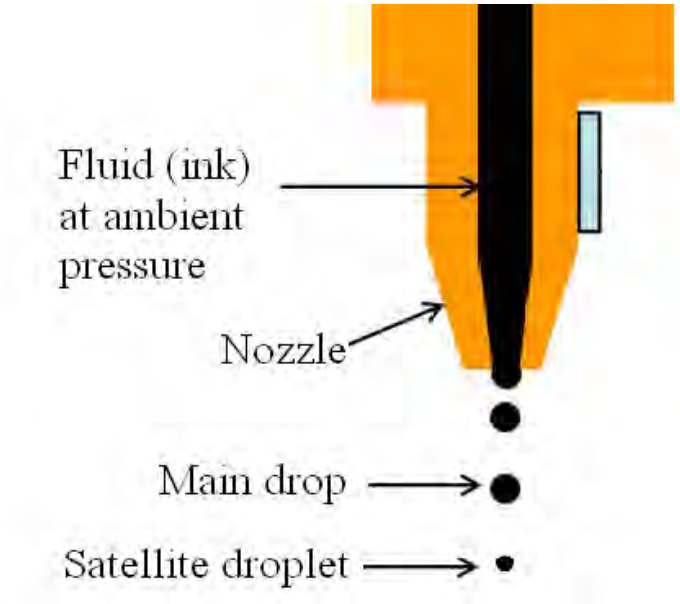

Figure 2.4: A figure showing the main drop and the satellite droplet emission from an ink-jet printer. Reproduced from Aveka Printer Groups Ltd.

As mentioned earlier, when a liquid jet breaks, small drops of different sizes are produced. We ideally want the size of the drops to be equal and the elimination of very small droplets; the satellite droplets. For example, in the process of ink-jet printing, the tiny nozzle, inside the printer, normally produces drops of equal size (the uniform or main drops) along with some satellite droplets (see Figure 2.4) and these satellite droplets always reduce the quality of the image produced by the ink-jet printer. We, therefore, want a total eradication of these unwanted satellite droplets.

2.2 Important Contributions to the Field

The study of liquid jets goes back to the 15th century when da Vinci (1508) studied the behaviour and the breakup of liquid jets. He correctly noted that the force of

gravity is responsible for the detachment of a water drop from a water orifice (see Eggers and Villermaux (2008) for details).

After da Vinci's work, there was a large gap until the 19th century when Savart (1833) firstly noted that when a liquid jet is perturbed with a periodic disturbance, the jet becomes unstable and breaks into a series of equally spaced drops and he also noted the appearance of a satellite droplet. He also noted that the frequency of this periodic disturbance could be controlled by changing the frequency of the periodic disturbance at the nozzle of the liquid jet.

After that, Plateau (1849) found that if a liquid jet is given any small disturbance, then the disturbance will reduce the surface area of the jet, and so it will be the surface tension which will eventually break the jet. Hence Plateau was the first to found that surface tension is important for the breakup of liquid jets.

Then it was Rayleigh (1879) who studied inviscid jets and he introduced $linear\ temporal\ stability\ analysis$. Rayleigh also obtained a dispersion relation linking the wavenumber k of the imposed disturbance to the frequency ω of the disturbance. Rayleigh found that waves with wavelength larger than the undisturbed jet circumference are unstable and thus they grow and break the jet. Rayleigh's most important finding was that $ka = 0.697$ for $most\ unstable\ wavenumber$, where a is the undisturbed radius of the orifice, and hence ω has the greatest value only when $ka = 0.697$, which consequently gives $most\ unstable\ wavelength\ \lambda = 2\pi/k = 2\pi a/0.697 = 9a$.

After that, Weber (1931) extended Rayleigh's analysis by including the viscosity and his result $ka = 0.7 \approx 0.697$ showed good agreement with that of Rayleigh. His most important result was that the viscosity reduces the growth rate of disturbances in liquid jets.

After Weber, it was Keller $et\ al.$ (1973) who examined the impact of the disturbance at the orifice and considered spatially propagating disturbances. Keller was

the first to present the $spatial\ instability\ analysis$, which deals with instabilities propagating with respect to the space.

Then Peregrine $et\ al.$ (1990) found that the breakup behaviour of a liquid jet depends highly on three internal properties of the jet, namely, the density, the surface tension and the viscosity. Hence, for inviscid fluids, jet breakup will depend highly on two internal properties of the liquid jet; the density and the surface tension. Note that at pinch-off (or at the breakup point), the radius of the jet goes to zero while the velocity of the jet goes to infinity, which results in a singularity in the solution of the liquid jet equations. In order to avoid this singularity, it is a usual trend to stop the numerical simulations of the liquid jet equations when the radius of the jet becomes 5 $\%$ of the initial non-dimensional undisturbed jet radius (See Părău (2006) and Uddin & Decent (2010) for more details).

2.3 Types of Breakup Regimes

If the exit velocity of a fluid is not too low, then there exists four different types of breakup regimes, which are given below:

$$1 : the\ Rayleigh\ regime,\ 2 : the\ first\ wind{-}induced\ regime,$$

$$3 : the\ second\ wind{-}induced\ regime \text{ and } 4 : the\ atomization\ regime.$$

$The\ Rayleigh\ regime$ and $the\ first\ wind\text{-}induced\ regime$ fall into one category, having the following three identical properties:

1: They both occur at lower speeds,

2: They both have breakup taking place far away from the orifice and

3: They both have the size of the resulting drops equal to the size of the orifice.

The rest of the two regimes, $the\ second\ wind\text{-}induced\ regime$ and $the\ atomization\ regime$, are totally opposite to the first two, but they can also be

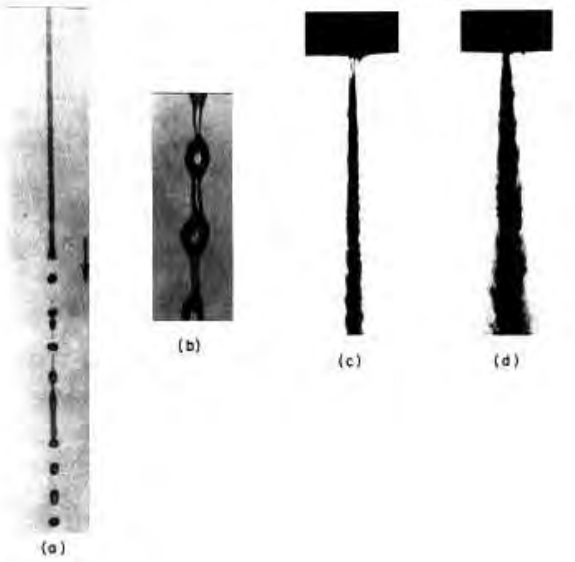

Figure 2.5: Four breakup regimes, (a) Rayleigh regime, (b) first wind-induced regime, (c) second wind-induced regime and (d) atomization regime. Reproduced from Lin and Reitz (1998).

classified into one group having following three similar properties:

1: They both occur at higher speeds,

2: They both have breakup taking place very near to the orifice and

3: They both have the size of the resulting drops much less than the size of the orifice.

Reitz and Bracco (1986) did the experimental observation to view the four different breakup regimes, which are shown in Figure 2.5. In this thesis, we consider the liquid jet breakup at the Rayleigh regime.

2.4 Instability Analyses and Types of Instabilities

There are two types of analyses for instabilities; $the\ temporal\ instability\ analysis$ and $the\ spatial\ instability\ analysis$. We consider imposed wavelike disturbances of the form $exp(\omega t - ikz)$, where k is the wavenumber and ω is the frequency of the imposed disturbance.

In the temporal instability analysis, we force ω to be complex and k to be purely real, that is,

$$\omega = \omega_r + i\omega_i \text{ and } k = k_r,$$

where for the positive temporal growth rate ω_r, the disturbance grows with time t. In this case, ω_i is the frequency of oscillation, k is the real wavenumber and ω_i/k (i.e., frequency/wavenumber) is the phase-speed of the wave (or simply the wavespeed). We note that the wavenumber k of the imposed wave disturbance is related to the wavelength λ of the wave, as $\lambda = 2\pi/k$, and hence it is related to the size of the resulting drops. That is, the larger the wavenumber is, the smaller the wavelength is and so the smaller the resulting drop sizes will be. In addition, the growth rate of the imposed wave disturbance is related to the breakup length of the jet. That is, the larger the growth rate is, the smaller the breakup length of the jet will be.

In the spatial instability analysis, on the other hand, we force k to be complex and ω to be purely imaginary, that is,

$$k = k_r + ik_i \text{ and } \omega = i\omega_i.$$

In this case, k_i is the spatial growth rate, k_r is the real wavenumber and ω_i is the frequency.

We now describe the types of instabilities. There are two types of instabilities; *the convective instability* and *the absolute instability*. The convective instability do not grow at the disturbance base and it only grows away from it. The absolute instability, on the other hand, grows everywhere including at the disturbance base and also it grows away from it (as shown in Figure 2.6). In other words, we can say that the convective instability grows only in one direction while the absolute instability grows in all directions (see Schmid & Henningson (2001)

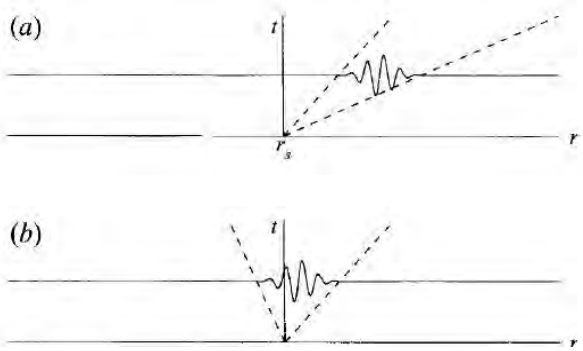

Figure 2.6: Sketch of convective and absolute instabilities. (a) (r, t) plane diagram of a convectively unstable disturbance; (b) (r, t) plane diagram of an absolutely unstable disturbance. Reproduced from Schmid and Henningson (2001).

and Bassi (2011) for more details).

We can use both temporal and spatial instability analyses to investigate convective or absolute instability. In our thesis, we shall only consider the convective instability and we shall use the temporal instability analysis to investigate it. In addition, Ruyer-Quil $et\ al.$ (2008) has shown that for a similar problem, involving a liquid film falling down a vertical cylinder, a temporal-spatial stability analysis is needed to fully capture the dynamics of instability and a similar analysis would provide an interesting extension of the current work.

2.5 Compound Liquid Jets

A compound liquid jet, which consists of an inner fluid that is completely surrounded by an outer immiscible fluid, is unstable to imposed axisymmetric interfacial disturbances (see Sanz & Meseguer (1985)). It is desirable to study and understand the mechanism of instability in compound liquid jets as they are used in capsule production in pharmaceutics (see Berkland $et\ al.$ (2007) and Chen $et\ al.$ (2009)) and in various technological devices such as in ink-jet printing (see Hertz (1980) and Hertz & Hermanrud (1983)).

The first experimental work on compound liquid jets was performed by Hertz

& Hermanrud (1983), who generated a compound jet by forcing a core fluid to emerge from a nozzle below a stationary immiscible shell fluid. Later, Sanz & Meseguer (1985) performed a theoretical analysis on the instability of inviscid compound jets. They used a long wavelength asymptotic expansion, with the assumption that the leading-order axial velocity is independent of the radial coordinate, to derive a one-dimensional model for inviscid compound jets. They performed a linear temporal instability analysis of the one-dimensional inviscid compound jet equations for axisymmetric disturbances and found two growing modes; $the\ stretching\ mode$ and $the\ squeezing\ mode$. Sanz & Meseguer (1985) found that the stretching mode has much larger growth rate than that of the squeezing mode (see Figure 2.7), for all parameters of the problem. The effects of viscosity and radial flows in compound liquid jets were considered by Radev & Tchavdarov (1988) and Shkadov & Sisoev (1996) who found that the structure and properties of wave modes remain the same. Chauhan et al. (2000) further extended the work of Radev & Tchavdarov (1988) by considering temporal disturbances along a viscous compound jet and performed a systematic analysis of the effects of viscosity, surface tension and density ratios on the maximum growth rate and maximum wavenumber. The theoretical works of all these authors have results which agree qualitatively with the experimental work of Hertz & Hermanrud (1983). The spatial instability analysis of compound liquid jets was performed by Chauhan $et\ al.$ (1996) while the effects of gravity on the breakup dynamics of inviscid compound liquid jets have been investigated by Uddin & Decent (2010). Recently, Mohsin $et\ al.$ (2012) considered non-Newtonian (shear thinning) compound liquid jets and obtained very useful information about the breakup and the droplet formation.

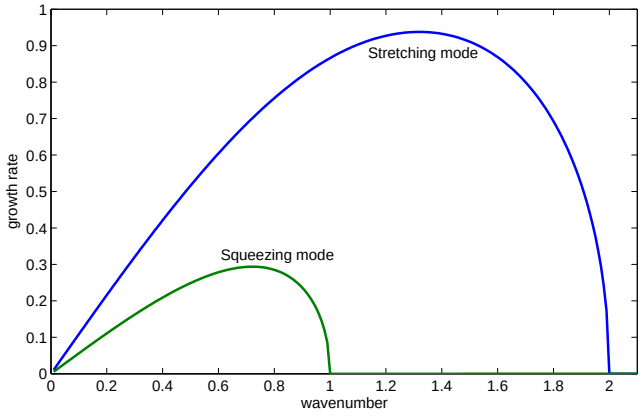

Figure 2.7: The stretching and the squeezing modes.

2.6 Summary

In this chapter, we described an introduction to liquid jets and some of the major contributions to the field of liquid jets. We next presented four different types of breakup regimes. We mentioned that we consider the liquid jet breakup at only the Rayleigh regime in this thesis.

In addition, we also described the temporal and the spatial instability analyses. We next mentioned two types of instabilities, and mentioned that we shall only consider the convective instability, using the temporal instability analysis in this thesis. At the end, we also gave a description about compound liquid jets and significant experimental and theoretical works on them.

Chapter 3

Temporal Instability Analysis of Inviscid Compound Jets Falling Under Gravity

3.1 Introduction

Compound liquid jets can be used in a variety of industrial applications ranging from capsule production in pharmaceutics to enhance printing methods in ink-jet printing. An appreciation of how instability along compound jets can lead to breakup and droplet formation is thus critical in many fields in science and engineering.

The main objective of the present chapter is to include the effects of gravity into the dynamics of a compound inviscid liquid jet and to investigate the effects of changing key physical parameters on its temporal stability to small disturbances. This extends the work of Sanz & Meseguer (1985) by introducing a spatially non-uniform steady state and results in growth rates and most unstable wavenumbers which differ along the jet. We use a long wavelength asymptotic expansion to

reduce the governing equations of the problem. We first obtain the steady-state solutions of the one dimensional model equations and then we perform a linear temporal instability analysis of steady-state solutions. This process yields a temporal dispersion relation, which we solve numerically to investigate the behaviour of maximum growth rates and maximum wavenumbers of the most unstable disturbance. In addition, we estimate the breakup length of an inviscid compound jet, falling under gravity, using the linear temporal stability analysis and we compare our results with numerical simulations found in Uddin & Decent (2010).

3.2 Problem Formulation

In order to formulate this problem, we make the following physical assumptions:

1: The compound liquid jet is inviscid and it comes out of a concentric cylindrical tube having an outer radius a and inner radius χa, where $0 < \chi < 1$.

2: Both the inner and the outer fluids have constant densities and constant interfacial surface tensions, and that both the fluids are not mixable.

3: The jet falls vertically downwards under the influence of gravity and, at the orifice of the nozzle, the jet has already formed as a uniform jet, but the effects of gravity are not present.

4: We choose the cylindrical polar coordinates (x, r, θ) to describe the dynamics of the jet, where x is the length along the centreline of the jet, r is the radial coordinate and θ is the azimuthal coordinate, and we further assume that the flow is axis-symmetric (so that the problem is independent of the azimuthal coordinate).

5: We take U as the initial uniform velocity of the jet on exit and we neglect the effects of the surrounding air.

6: We take $\mathbf{u}^{[j]} = (u^{[j]}, v^{[j]}, 0)$ as the velocity vector which describes the flow. Here the superscript $j = i$ is for the inner fluid and $j = o$ is for the outer fluid. We

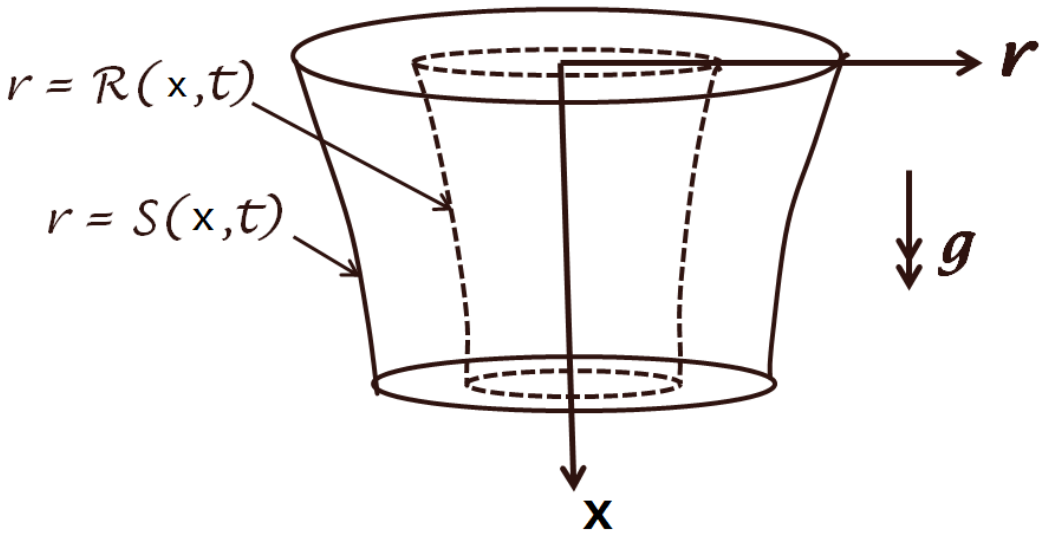

Figure 3.1: A sketch of an inviscid compound jet falling under gravity. The axis of symmetry of the jet is represented by the x-axis while the inner interface (denoted by dashed lines) and outer interface (denoted by solid lines) are given by $r = R(x,t)$ and $r = S(x,t)$ respectively.

denote $u^{[j]}$ as the axial velocity, $v^{[j]}$ as the radial velocity, $R(x,t)$ as the interface of the inner fluid with the outer one, $S(x,t)$ as the interface of the outer fluid with the air (or simply as the free surface), $p^{[j]}$ as the pressure, t as the time $\rho^{[j]}$ as the density, $\sigma^{[j]}$ as the surface tension and $\boldsymbol{g} = (g, 0)$ as the gravity (see Figure 3.1 for a sketch of this set-up).

The continuity equation and the Euler's equations, which describe the flow in the inner and the outer jets, are respectively given by

$$\frac{\partial u^{[j]}}{\partial x} + \frac{\partial v^{[j]}}{\partial r} + \frac{v^{[j]}}{r} = 0, \tag{3.1}$$

$$\frac{\partial u^{[j]}}{\partial t} + u^{[j]}\frac{\partial u^{[j]}}{\partial x} + v^{[j]}\frac{\partial u^{[j]}}{\partial r} = -\frac{1}{\rho^{[j]}}\frac{\partial p^{[j]}}{\partial x} + g \tag{3.2}$$

and

$$\frac{\partial v^{[j]}}{\partial t} + u^{[j]}\frac{\partial v^{[j]}}{\partial x} + v^{[j]}\frac{\partial v^{[j]}}{\partial r} = -\frac{1}{\rho^{[j]}}\frac{\partial p^{[j]}}{\partial r}. \tag{3.3}$$

The kinematic boundary conditions, at the interface of two jets $r = R(x,t)$, and at the free surface of the outer jet $r = S(x,t)$, are respectively given by

$$v^{[j]} = \frac{\partial R}{\partial t} + u^{[j]}\frac{\partial R}{\partial x} \tag{3.4}$$

and

$$v^{[o]} = \frac{\partial S}{\partial t} + u^{[o]}\frac{\partial S}{\partial x}. \tag{3.5}$$

For inviscid fluids, we have the classical free surface condition of constant pressure and hence zero tangential stress boundary condition. The normal stress boundary conditions, at the interface of two jets $r = R(x,t)$, and at the free surface of the outer jet $r = S(x,t)$, are respectively given by

$$p^{[i]} - p^{[o]} = \sigma^{[i]}\kappa^{[i]} \tag{3.6}$$

and

$$p^{[o]} = \sigma^{[o]}\kappa^{[o]}, \tag{3.7}$$

where $\kappa^{[i]}$ and $\kappa^{[o]}$ are respectively the curvatures of the inner free surface and the outer free surface. These are given by

$$\kappa^{[i]} = \frac{\left(1 + \left(\frac{\partial R}{\partial x}\right)^2\right)^{-\frac{1}{2}}}{R} - \frac{\frac{\partial^2 R}{\partial x^2}}{\left(1 + \left(\frac{\partial R}{\partial x}\right)^2\right)^{\frac{3}{2}}} \tag{3.8}$$

and

$$\kappa^{[o]} = \frac{\left(1 + \left(\frac{\partial S}{\partial x}\right)^2\right)^{-\frac{1}{2}}}{S} - \frac{\frac{\partial^2 S}{\partial x^2}}{\left(1 + \left(\frac{\partial S}{\partial x}\right)^2\right)^{\frac{3}{2}}}. \tag{3.9}$$

3.3 Non-Dimensionalization

We non-dimensionalize our variables as

$$\bar{u}^{[j]} = \frac{u^{[j]}}{U}, \quad \bar{v}^{[j]} = \frac{v^{[j]}}{U}, \quad \bar{x} = \frac{x}{L}, \quad \bar{r} = \frac{r}{a},$$

$$\bar{t} = \frac{tU}{L}, \quad \bar{p}^{[j]} = \frac{p^{[j]}}{\rho^{[o]}U^2},$$

where L is a characteristic wavelength in the axial direction (see Papageorgiou (1995)), which can be chosen as $L = U^2/g$. Here the quantities with the overbars are dimensionless quantities. We next assume that the jet is slender and so we define a small parameter ϵ as $\epsilon = a/L << 1$ (see Sanz & Meseguer (1985) and Radev & Tchavdarov (1988)). Hence, in the following analysis, we are assuming that $a << L$ in our long wavelength slender jet theory. Note that $S(0,t) = 1$, as a is the outer tube radius.

3.4 Asymptotic Expansions

We next drop overbars form the variables and then, similar to Eggers (1997), we expand the variables using an asymptotic slender jet expansion of the form

$$\{u^{[j]}, v^{[j]}, p^{[j]}\} = \{u_0^{[j]}(x,t), v_0^{[j]}(x,t), p_0^{[j]}(x,t)\} + (\epsilon r)\{u_1^{[j]}(x,t), v_1^{[j]}(x,t), p_1^{[j]}(x,t)\} + O((\epsilon r)^2), \tag{3.10}$$

$$\{R, S\} = \{R_0(x,t), S_0(x,t)\} + \epsilon\{R_1(x,t), S_1(x,t)\} + O(\epsilon^2). \tag{3.11}$$

We substitute the above asymptotic expansions in to the continuity equation (3.1), which at leading order $O(1/\epsilon)$ gives $v_0^{[j]} = 0$, while at next order $O(1)$ gives

$$v_1^{[j]} = -\frac{1}{2}\frac{\partial u_0^{[j]}}{\partial x}. \tag{3.12}$$

Using equation (3.12), the kinematic boundary conditions (3.4) (at $r = R(x,t)$) and (3.5) (at $r = S(x,t)$), at leading orders, respectively give

$$(R_0^2)_t + (R_0^2 u_0^{[i]})_x = 0, \tag{3.13}$$

and

$$(S_0^2 - R_0^2)_t + ((S_0^2 - R_0^2)u_0^{[o]})_x = 0. \tag{3.14}$$

Similarly, the normal stress boundary conditions, at $r = S(x,t)$ and $r = R(x,t)$, at leading order, respectively give

$$p_0^{[o]} = \frac{1}{S_0 We} \quad \text{and} \quad p_0^{[i]} = \frac{1}{We}\left(\frac{\sigma}{R_0} + \frac{1}{S_0}\right), \tag{3.15}$$

where $\sigma = \sigma^{[i]}/\sigma^{[o]}$ is the ratio of surface tension between inner and outer fluid interfaces and $We = \rho^{[o]}U^2 a/\sigma^{[o]}$ is the Weber number.

We use equation (3.15) in the axial momentum equation (3.2) and obtain equations for the inner and outer fluids, at leading order,

$$\frac{\partial u_0^{[i]}}{\partial t} + u_0^{[i]}\frac{\partial u_0^{[i]}}{\partial x} = -\frac{1}{\rho We}\frac{\partial}{\partial x}\left(\frac{\sigma}{R_0} + \frac{1}{S_0}\right) + \frac{1}{F^2} \tag{3.16}$$

and

$$\frac{\partial u_0^{[o]}}{\partial t} + u_0^{[o]} \frac{\partial u_0^{[o]}}{\partial x} = -\frac{1}{We} \frac{\partial}{\partial x} \left(\frac{1}{S_0} \right) + \frac{1}{F^2}, \tag{3.17}$$

where $\rho = \rho^{[i]}/\rho^{[o]}$ is the density ratio of the inner fluid to the outer fluid and $F = U/\sqrt{Lg}$ is the Froude number. Since an appropriate choice for the length scale L, in the vertical direction, is given by $L = U^2/g$, so F has the value of unity. Since this choice of L is a natural length scale in this problem, we henceforth use $F = 1$ throughout this chapter (apart from the steady-state solutions, where we vary all the parameters of the problem). Moreover, the radial momentum equation (3.3), after using equations (3.12) and (3.15), gives $\partial p_0^{[j]}/\partial r = 0$.

Equations (3.13), (3.14), (3.16) and (3.17) are the model equations, for four unknowns $R_0, S_0, u_0^{[i]}$ and $u_0^{[o]}$. In addition, we have the boundary conditions, at the nozzle $x = 0$, as

$$u_0^{[i]}(0,t) = u_0^{[o]}(0,t) = S(0,t) = 1 \quad \text{and} \quad R(0,t) = \chi, \ \text{ where } \ 0 < \chi < 1.$$

If we set $We = 1$ and ignore the term with F (i.e., have $F \to \infty$) in equations (3.16) and (3.17), then our model equations are the same as those found in Sanz & Meseguer (1985).

3.5 Steady-State Solution

The system of equations (3.13), (3.14), (3.16) and (3.17) with the time derivative terms removed can be solved for the four variables $u_0^{[i]}$, $u_0^{[o]}$, R_0 and S_0 with the resulting solution, which will be spatially non-uniform, as the steady state solution. Similar to Uddin & Decent (2010), we make use of the boundary conditions

at $x = 0$, so that we can write equations (3.13) and (3.14) as

$$R_0 = \frac{\chi}{\sqrt{u_0^{[i]}}} \quad \text{and} \quad S_0 = \sqrt{\frac{u_0^{[i]}(1-\chi^2) + u_0^{[o]}\chi^2}{u_0^{[i]}u_0^{[o]}}}. \tag{3.18}$$

Therefore, after substituting the values for R_0 and S_0, from equation (3.18) into equations (3.16) and (3.17), we end up with two equations in two unknowns $u_0^{[i]}$ and $u_0^{[o]}$.

We solve the above nonlinear system of steady-state equations (3.16)-(3.18) using Newton's method (as in Uddin & Decent (2010)) and present the solutions in following figures. In Figure 3.2, we plot the steady-state solution for the inner and the outer jet velocities, for various Froude numbers. We observe, from this figure, that a decrease in the Froude number (or increase in gravity) causes in turn the jet velocities to increase. In Figure 3.3, we plot the steady-state solution for the inner and the outer jet radii, for various Froude numbers. We observe, from this figure, that an increase in the Froude number (which corresponds to a decrease in the gravity) causes in turn the jet radii to increase. In Figure 3.4, we plot the steady-state solution for the inner and the outer jet radii, for various Weber numbers. We observe that an increase in the Weber number (which could correspond to a decrease in the surface tension of the outer interface) leads to a more rapid decay of the jet radii along the jet. In Figure 3.5, we plot the steady-state solution for the inner and the outer jet radii, for various interfacial surface tension ratios. We observe, from this figure, that as we increase the surface tension ratio σ (or as the surface tension of the inner interface is increased with respect to the outer intrface), the jet radii increases slightly. In Figure 3.6, we plot the steady-state solution for the inner and the outer jet radii, for various density ratios. We observe, from this figure, that as we increase the density ratio ρ (or as the density of the inner fluid is increased with respect to the outer fluid), the jet radii decreases

very slightly. Consequently, we deduce that ρ has very little impact on steady-state solutions. Finally, in Figure 3.7, we plot the steady-state solution for the inner and the outer jet radii, for various values of initial inner jet radius χ. We observe, from this figure, that as we decrease the initial inner jet radius χ, the jet inner radius decreases clearly, whereas, the jet outer radius remains unaffected.

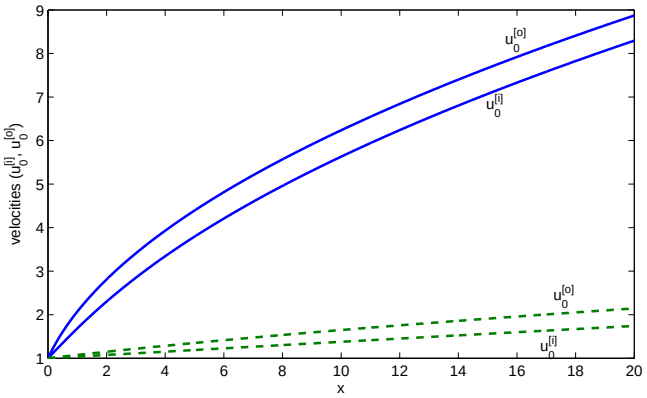

Figure 3.2: The steady-state solution for the inner and the outer jet velocities, for various Froude numbers. The solid line represents $F = 0.5$ while the dashed line represents $F = 1$. It can be seen that a decrease in the Froude number (or increase in gravity) causes in turn the jet velocities to increase. The other parameters are $We = 10$, $\rho = 2$, $\sigma = 3$ and $\chi = 0.5$.

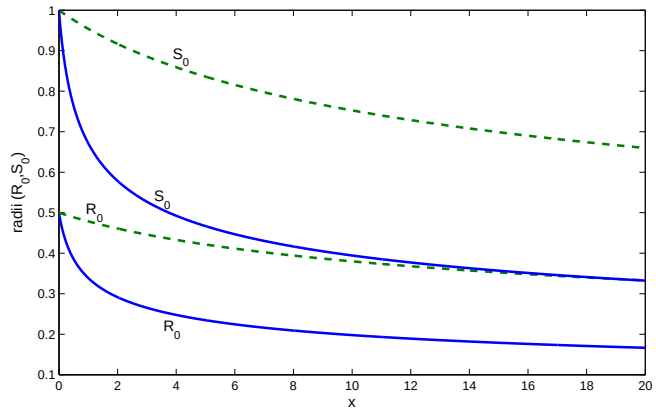

Figure 3.3: The steady-state solution for the inner and the outer jet radii, for various Froude numbers. The solid line represents $F = 0.5$ while the dashed line represents $F = 1$. It can be seen that an increase in the Froude number (or decrease in gravity) causes in turn the jet radii to increase. The other parameters are $We = 10$, $\rho = 2$, $\sigma = 3$ and $\chi = 0.5$.

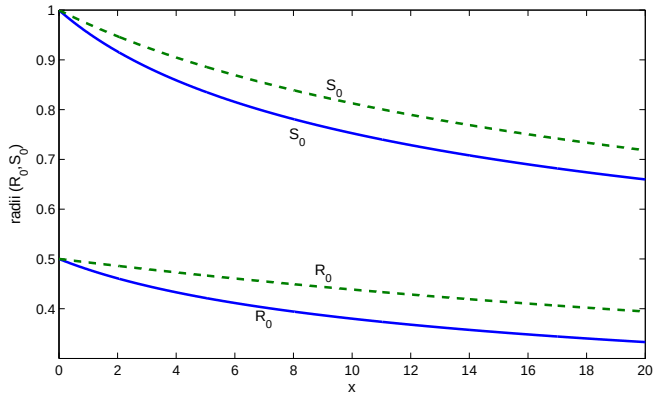

Figure 3.4: The steady-state solution for the inner and the outer jet radii, for various Weber numbers. The solid line represents $We = 10$ while the dashed line represents $We = 0.7$. It can be seen that a decrease in the Weber number causes the jet radii to increase. The other parameters are $F = 1$, $\rho = 2$, $\sigma = 3$ and $\chi = 0.5$.

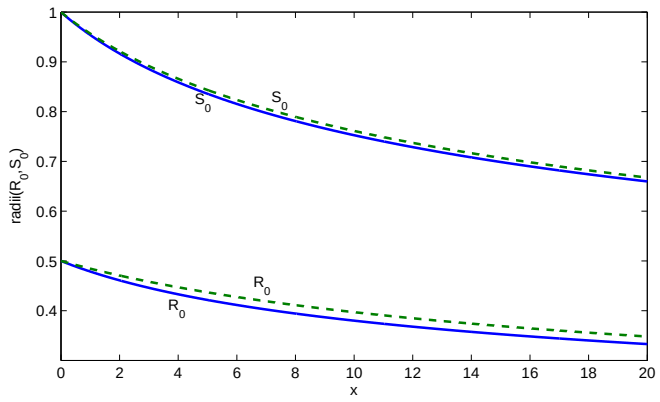

Figure 3.5: The steady-state solution for the inner and the outer jet radii, for various surface tension ratios. The solid line represents $\sigma = 3$ while the dashed line represents $\sigma = 13$. It can be seen that as we increase the interfacial surface tension ratio σ (or as the surface tension of the inner interface is increased with respect to the outer intrface), the jet radii increases slightly. The other parameters are $F = 1$, $We = 10$, $\rho = 2$ and $\chi = 0.5$.

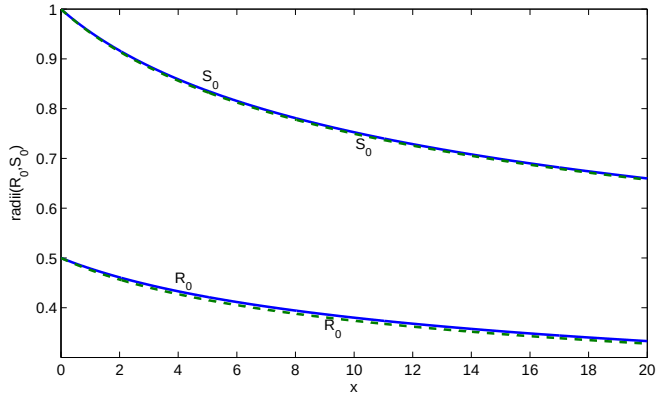

Figure 3.6: The steady-state solution for the inner and the outer jet radii, for various density ratios. The solid line represents $\rho = 2$ while the dashed line represents $\rho = 12$. It can be seen that as we increase the density ratio ρ (or as the density of the inner fluid is increased with respect to the outer fluid), the jet radii decreases very slightly. The other parameters are $F = 1$, $We = 10$, $\sigma = 3$ and $\chi = 0.5$.

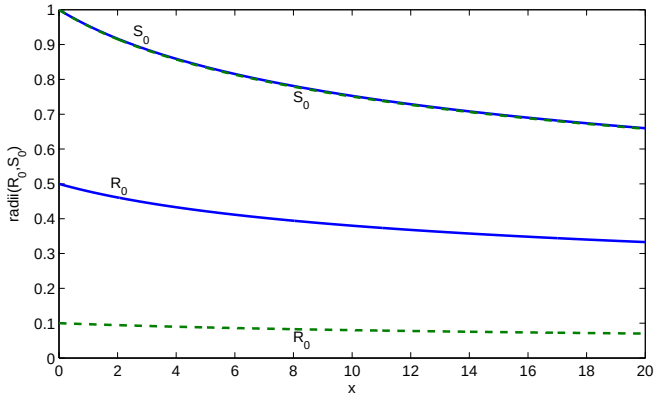

Figure 3.7: The steady-state solution for the inner and the outer jet radii, for various values of initial inner jet radius χ. The solid line represents $\chi = 0.5$ while the dashed line represents $\chi = 0.1$. It can be seen that as we decrease the initial inner jet radius χ, the jet inner radius decreases clearly, whereas, the jet outer radius remains unaffected. The other parameters are $F = 1$, $We = 10$, $\sigma = 3$ and $\rho = 2$.

3.6 Linear Temporal Instability Analysis

We now investigate the instability of an inviscid compound jet by performing a linear temporal instability analysis. The length scale over which the jet evolves is $x = O(1)$. However, disturbances along the jet are much smaller, typically of the order of the jet radius a (which is comparable to ϵ when $x = O(1)$). Similar to Wallwork *et al.* (2002) and Uddin *et al.* (2006), we consider travelling short-wavelength modes (or short waves) of the form $\exp(\omega\bar{t} + ik\bar{x})$, where $\bar{t} = t/\epsilon$ and $\bar{x} = x/\epsilon$ are small length and time scales. In addition, $\omega = \omega(x) = O(1)$ and $k = k(x) = O(1)$ are the frequency and the wavenumber of the imposed wave-like temporal disturbance. Therefore, we have small $O(\epsilon)$ wavelength perturbations along the jet. We next perturb the steady-state solution by a small time-dependent,

short-wave disturbance and assume

$$u^{[j]} = u_0^{[j]}(x) + \delta \exp(\omega \bar{t} + ik\bar{x})\hat{u}_1^{[j]}(x), \tag{3.19}$$

$$R = R_0(x) + \delta \exp(\omega \bar{t} + ik\bar{x})\hat{R}_1(x), \tag{3.20}$$

$$S = S_0(x) + \delta \exp(\omega \bar{t} + ik\bar{x})\hat{S}_1(x), \tag{3.21}$$

where $\delta << \epsilon$. We substitute equations (3.19) – (3.21) into equations (3.13), (3.14), (3.16) and (3.17) and we use the full curvature terms in order to prevent instability of waves with zero wavenumber (see Brenner $et\ al.$ (1997) for more details). Consequently, we obtain the following set of four equations at the next order $O(\delta/\epsilon)$ [1]

$$\left(ikR_0^2\right)\hat{u}_1^{[i]} + \left(2\omega R_0 + 2ikR_0u_0^{[i]}\right)\hat{R}_1 = 0, \tag{3.22}$$

$$\left(ik(S_0^2 - R_0^2)\right)\hat{u}_1^{[o]} - \left(2\omega R_0 + 2ikR_0u_0^{[o]}\right)\hat{R}_1$$

$$+ \left(2\omega S_0 + 2ikS_0u_0^{[o]}\right)\hat{S}_1 = 0, \tag{3.23}$$

$$\left(\omega + iku_0^{[i]}\right)\hat{u}_1^{[i]} + \frac{\sigma}{\rho We}\left(\frac{-ik}{R_0^2} + ik^3\right)\hat{R}_1 + \frac{1}{\rho We}\left(\frac{-ik}{S_0^2} + ik^3\right)\hat{S}_1 = 0 \tag{3.24}$$

and

$$\left(\omega + iku_0^{[o]}\right)\hat{u}_1^{[o]} + \frac{1}{We}\left(\frac{-ik}{S_0^2} + ik^3\right)\hat{S}_1 = 0. \tag{3.25}$$

[1] Note that at the leading order, we obtain the steady-state equations.

Equations (3.22)-(3.25) can be written in terms of matrix form as

$$\begin{pmatrix} ikR_0^2 & 0 & a_{13} & 0 \\ 0 & a_{22} & a_{23} & a_{24} \\ \omega + iku_0^{[i]} & 0 & \frac{\sigma}{\rho We}\left(\frac{-ik}{R_0^2} + ik^3\right) & \frac{a_{34}}{\rho We} \\ 0 & \omega + iku_0^{[o]} & 0 & \frac{a_{44}}{We} \end{pmatrix} \cdot \begin{pmatrix} \hat{u}_1^{[i]} \\ \hat{u}_1^{[o]} \\ \hat{R}_1 \\ \hat{S}_1 \end{pmatrix} = \begin{pmatrix} 0 \\ 0 \\ 0 \\ 0 \end{pmatrix},$$

where

$$a_{13} = 2\omega R_0 + 2ikR_0u_0^{[i]}, \quad a_{22} = ik(S_0^2 - R_0^2),$$

$$a_{23} = -2\left(\omega R_0 + ikR_0u_0^{[o]}\right), \quad a_{24} = 2\omega S_0 + 2ikS_0u_0^{[o]}$$

and

$$a_{34} = a_{44} = \left(\frac{-ik}{S_0^2} + ik^3\right).$$

For the above system to have a non-trivial solution, we require that

$$\det \begin{pmatrix} ikR_0^2 & 0 & a_{13} & 0 \\ 0 & a_{22} & a_{23} & a_{24} \\ \omega + iku_0^{[i]} & 0 & \frac{\sigma}{\rho We}\left(\frac{-ik}{R_0^2} + ik^3\right) & a_{34}/\rho We \\ 0 & \omega + iku_0^{[o]} & 0 & a_{44}/We \end{pmatrix} = 0,$$

and, therefore, we obtain

$$(\omega + iku_0^{[o]})\left[ikR_0^2\left\{\frac{2a_{23}a_{44}}{\rho We} + \frac{\sigma a_{24}}{\rho We}\left(\frac{ik}{R_0^2} - ik^3\right)\right\} + \left\{a_{13}a_{24}(\omega + iku_0^{[i]})\right\}\right]$$

$$-\frac{a_{44}}{We}\left[\left\{\left(\frac{ik\sigma}{\rho We R_0^2}-\frac{ik^3\sigma}{\rho We}\right)(2R_0R_{0,x}+ikR_0^2)a_{22}\right\}+\left\{(\omega+iku_0^{[i]})a_{13}a_{22}\right\}\right]=0. \tag{3.26}$$

We define $\omega' = \omega + iku_0^{[o]}$, which in effect moves us into a frame of reference which moves with the outer jet velocity $u_0^{[o]}$. We can, hence, write

$$\omega + iku_0^{[i]} = \omega' - ik(u_0^{[o]} - u_0^{[i]}),\ \text{as}\ \omega = \omega' - iku_0^{[o]}.$$

Therefore, equation (3.26) can be written as

$$\begin{aligned}&[4R_0S_0](\omega')^4 + [8R_0S_0\alpha_3](\omega')^3\\ &+\left[\frac{2ikR_0^2}{\rho We}(R_0\alpha_2+\sigma S_0\alpha_1)+(4R_0S_0\alpha_3^2)+\frac{2ikR_0\alpha_2}{We}\left(S_0^2-R_0^2\right)\right](\omega')^2\\ &+\left[\frac{4ikR_0\alpha_2\alpha_3}{We}(S_0^2-R_0^2)\right](\omega')+\frac{R_0\alpha_2}{We}\left(2ik\alpha_3^2-\frac{\sigma k^2R_0\alpha_1}{\rho We}\right)\left(S_0^2-R_0^2\right)=0,\end{aligned} \tag{3.27}$$

which is our required dispersion relation. Here

$$\alpha_1 = \frac{ik}{R_0^2} - ik^3,\ \alpha_2 = \frac{ik}{S_0^2} - ik^3\ \text{ and }\ \alpha_3 = -ik(u_0^{[o]} - u_0^{[i]}).$$

Note that in the limiting case of no gravity, i.e., for $u_0^{[i]} = u_0^{[o]} = S_0 = 1$ and $R_0 = \chi$, in our dispersion relation (3.27), we obtain the same dispersion relation as found in Sanz & Meseguer (1985).

3.7 Results and discussion

The dispersion relation (3.27) relates ω' to the wavenumber k. For a given value of k, the equation is seen to be a quartic equation in ω', with coefficients depending on x, the axial distance along the jet. Subsequently, by choosing a value of x and evaluating these coefficients at this particular value, our equation becomes

a quartic equation in ω', with constant coefficients, which may be solved using Ferrari's method (see Bali & Iyengar (2005)). An example of solving (3.27), for a value of x and for different k, is shown in Figure 3.8, where the four solutions of (3.27) are shown, of which two are growing modes (i.e., where $Re(\omega') > 0$ and are unstable), which is similar to what is seen for a straight uniform inviscid compound jet, as found by Sanz & Meseguer (1985). Of the two unstable modes, it is typically assumed that breakup of the jet is caused by the mode with the largest growth rate and, throughout this work, we will focus our attention on this mode and we refer to it as $the\ most\ unstable\ mode$. In such a case, it can be seen that there is a value of the wavenumber k, at which the growth rate is maximal - we refer to this value as $the\ most\ unstable\ wavenumber$ and denote it by k_{max}. The significance of this value of k_{max} is that breakup of the jet is caused by a wave having this wavenumber and so the resulting droplets will scale with this value of k and, in particular, we would expect droplets to become smaller for larger k_{max}. A plot of such most unstable modes for different ratios of surface tension σ, for different density ratios ρ, for different Weber numbers We and for different inner jet radius χ is shown in following figures. As the surface tension ratio is reduced (i.e., as the surface tension of the inner interface is made smaller than the outer interface), the most unstable mode has lower growth rates, which will correspond to larger jets (as the smaller growth rate implies larger jets). Moreover, as the density ratio is reduced (i.e., as the density of the inner jet is made smaller than the outer jet), the most unstable mode has higher growth rates, which will correspond to longer jets. We observe that the qualitative behaviour of increasing σ and ρ, demonstrated in Figures 3.9 and 3.13, is the same as illustrated in Sanz & Meseguer (1985). Since the steady-state values of radii and velocities of the jet vary along x, we see that we have different k_{max} for different axial distances x along the jet. This change is demonstrated in Figures 3.9 and 3.13, for different

σ and ρ respectively. In particular, we see that the most unstable wavenumber k_{max} grows with axial distance x for both cases. The corresponding maximal growth rate $[Re(\omega')]_{max}$ for the above cases are shown in Figures 3.11 and 3.14 respectively, where again we notice that the maximal growth rate increases along the jet.

As explained in the preceding paragraph, k_{max} represents the value of k at which the growth rate $Re(\omega')$ is maximum. For certain parameter ranges, the value of k_{max} is unique, however, as demonstrated in Figure 3.10, for certain parameter values, there exists a non-uniqueness in the value of k_{max}. This behaviour is a result of the two competing wavemodes along the jet and can result in large differences in k_{max}, as certain parameters are changed. In particular, for the case shown in Figure 3.10, for $\sigma = 0.22$, we have $k_{max} = 0.81$, while for $\sigma = 0.23$, we have $k_{max} = 1.35$. Therefore, there exists a value of σ, which we refer to as $threshold\ surface\ tension\ ratio\ \sigma^*$, at which we have two competing wavemodes having different wavenumbers. This is investigated in Figure 3.11, where we demonstrate how k_{max} changes, as σ is increased, for different locations x along the jet. From this figure, it is clear that σ^* is the same, for all values of x, while k_{max} is larger as x increases. Also note from this figure that, for $\sigma < \sigma^*$, an increase in σ causes k_{max} to increase, while for $\sigma > \sigma^*$, an increase in σ causes k_{max} to decrease slightly, for $x = 0$, $x = 2$ and $x = 4$. A plot of how σ^* changes with change in ρ can be seen, for different axial distances x, from Figure 3.12. As the density ratio ρ is increased, we can see that σ^* increases. Additionally, as in Figure 3.14 , we see that k_{max} increases as ρ is increased and is larger for all values of ρ, as one moves down the jet.

From Figure 3.15, it can be seen that a decrease in the Weber number causes the maximum wavenumber to decrease for $x > 0$, while causes the maximum growth rate of the disturbance to increase. Moreover, for a given We, both k_{max}

and $[Re(\omega')]_{max}$ increase as x increases. From Figures 3.15 and 3.16, it can be seen that at $x = 0$ (i.e., at the nozzle, where the effects of gravity are not present), changing the Weber number does not make any difference to the maximum wavenumber $k_{max} = 1.33$. Note that this value of $k_{max} = 1.33$, at $x = 0$, corresponds exactly to the corresponding value for the no-gravity case of Sanz & Meseguer (1985), where $k_{max} = (m^{-1})^{-1} = (0.75)^{-1} = 1.33$, as shown in Figure 3.17. Also note that, for $We = 1$ and at $x = 0$, $[Re(\omega')]_{max} = 0.94$ corresponds exactly to the corresponding value for the no-gravity case of Sanz & Meseguer (1985), where $\tau_m = [Re(\omega')]_{max} = 0.94$, as shown in Figure 3.17. In Figure 3.16, we note that, at $x = 0$, as We is increased, the maximum growth rate of the disturbance does not remain constant and decreases. This is due to the fact that increasing We implies a decrease in the surface tension and hence a decrease in the maximum growth rate of the disturbance (since the growth rate of the disturbance is proportional to the surface tension, as shown in Figure 3.11). We note that this result is easily understood as it is the surface tension that causes the instability in liquid jets. In addition, a decrease in We causes the maximum wavenumber to decrease for $x > 0$, while causes the maximum growth rate of the disturbance to increase, for different values of x. In Figure 3.18, we plot maximum wavenumber k_{max} and maximum growth rate $[Re(\omega')]_{max}$ versus x, for different values of χ. It can be seen that a decrease in χ causes both the maximum wavenumber and the maximum growth rate of the disturbance to increase. Moreover, for a given χ, both k_{max} and $[Re(\omega')]_{max}$ decrease as x decreases.

In Figure 3.19, we plot a diagram to show how changing the surface tension ratio σ and the parameter χ affect the wavenumber of the most unstable mode together with the associated maximal growth rate of this mode. Figure 3.19 consists of a set of points which represent the values of inverse maximum wavenumber $(k_{max})^{-1}$ and associated maximum growth rate $[Re(\omega')]_{max}$, obtained when all

parameters are kept fixed, except either σ or χ (we consider the parameter space $0.1 < \chi < 0.9$ and $0.1 < \sigma < 4$). Together, this constitutes a map of different maximum wavenumbers and associated maximum growth rates, as σ and χ are varied. We have chosen to plot the inverse wavenumber with growth rate as this is consistent with the work of Sanz & Meseguer (1985) but we note that here, unlike in Sanz & Meseguer (1985), we plot only the largest or most unstable wavemode with the reasoning that this mode is responsible for breakup. There are two sets of curves shown in Figure 3.19 which are drawn firstly by fixing χ and varying σ – this usually leads to curves which appear almost vertical in nature and can be seen to be almost straight for smaller values of χ but which take on a more arc shape as χ is increased. With reference to all such figures (Figures 3.19 – 3.24) of this nature, these curves represent fixed χ for different σ with χ increasing as one moves from left to right with the value of χ being represented by the symbols used in the figure. Curves obtained by fixing σ but varying χ are shown as dashed lines in Figure 3.19 and for larger values of σ such curves are continuous in nature. It is important to note that there are some discontinuities in the graph of Figure 3.19. In particular, note that when we fix $\sigma = 0.1$ and vary χ, we find that there are no modes which lie between $0.63 < (k_{max})^{-1} < 1.27$, for $x = 0$, $0.41 < (k_{max})^{-1} < 0.85$, for $x = 2$ and $0.38 < (k_{max})^{-1} < 0.73$, for $x = 4$. This is caused by competing wavemodes which propagate along the jet and which, under different parameters, can alter the value of the most unstable wavenumber significantly (see Figure 3.19). Examination of this figure also reveals that the most unstable wavenumber together with its growth rate decrease as χ is increased for any fixed σ and this trend is apparent for distances along the jet and for different values of ρ (see Figure 3.21 - 3.23). We also notice that growth rates always decrease as σ is decreased but that there is a non-monotonic behaviour for the most unstable wavenumber for fixed χ and varying σ such that,

for larger values of χ, there is a trend for the most unstable wavenumber to decrease as σ is decreased, whilst for smaller χ, there is a tendency for the most unstable wavenumber to increase as σ is made smaller.

Since the jet is accelerating downwards in the vertical direction, the steady-state solution is a function of the vertical distance x from the nozzle. This, in turn, affects the coefficients of our dispersion relation and we, therefore, see differences in the relationship between the most unstable wavenumber and its associated growth rate, as we move down the jet. Figure 3.19 shows three such cases which correspond to $x = 0$, $x = 2$ and $x = 4$. A careful examination of the curves presented in Figure 3.19 (for example one may compare extreme values of the maximal growth rate and most unstable or maximum wavenumber for a fixed value of χ, for three different axial distances) reveals that, for the parameter ranges considered here, the maximum wavenumber increases for any given χ and for all σ, as x increases. Moreover, the associated growth rates are also larger for a given χ and σ, as x increases. This indicates that breakup lengths and droplet sizes are likely to be smaller for a compound liquid jet falling under gravity than those predicted using the analysis of Sanz & Meseguer (1985). We note that due to the presence of a thinning jet in the case with gravity this would be anticipated but our results here show that the thinning nature of the jet affects the maximal growth rates and most unstable wavenumbers.

In Figure 3.20, we show that, for small χ, if χ is kept fixed and σ is allowed to vary, then one observes a similar discontinuity in the value of the most unstable wavenumber and its associated growth rate. It is clear from this figure that, for $\chi = 0.3$ and $\chi = 0.4$, there are no modes which lie between $0.41 < (k_{max})^{-1} < 1.4$ and $0.57 < (k_{max})^{-1} < 1.32$ respectively. We, therefore, conclude that varying both σ and χ have transitional behaviour in the values of $(k_{max})^{-1}$. We reproduce the diagram, found in Figure 3.19, in Figures 3.21 and 3.22 for the cases where

$\rho = 1$ and $\rho = 2$ respectively. We note that the effect of increasing ρ (which corresponds to increasing the relative density of the inner fluid to the outer fluid) is to accentuate (or to emphasize) the effect of increasing k_{max}, for any σ and χ. We find in all of these figures that for $\sigma \geq 0.5$ and for varying χ, we do not have any transitional behaviour in the values of $(k_{max})^{-1}$. However, as we go down to $\sigma = 0.23 = \sigma^*$ and then for $\sigma < 0.23$, we start to get a transitional behaviour in the values of $(k_{max})^{-1}$, for varying χ. In Figure 3.23, we plot a similar graph, but, in this case, we keep σ fixed and choose to vary ρ and χ. We found that k_{max} increases, for any given ρ and χ, as x increases, while as ρ is decreased, $[Re(\omega')]_{max}$ is increased. We observe that the qualitative behaviour of the inverse maximum wavenumber $(k_{max})^{-1}$ and its associated maximum growth rate $[Re(\omega')]_{max}$, for varying σ and χ, demonstrated in Figures 3.19 – 3.22, for $x = 0$, is the same as illustrated in Sanz & Meseguer (1985).

In Figures 3.21 and 3.24, we vary the Weber number and we found that, at $x = 0$, for $We = 40$, all $(k_{max})^{-1}$ values for χ are exactly the same, as for $We = 10$. This behaviour can be estimated from Figure 3.16(a), for $\chi = 0.5$. That is, varying the Weber number does not make any difference to the maximum wave number, at $x = 0$. Moreover, as we increase x, $(k_{max})^{-1}$ decreases, i.e., k_{max} increases (for a fixed χ and varying σ), which is observed before in Figure 3.16(a). Furthermore, as we increase x, $[Re(\omega')]_{max}$ increases, which is shown before in Figure 3.16(b), while as we increase We, $[Re(\omega')]_{max}$ decreases, for a given χ, which is also shown before in Figure 3.16(b).

We show values of threshold surface tension ratio σ^* plotted against χ, for different ρ, in Figures 3.25 and 3.26. We see that σ^* increases with an increase in χ, and that, σ^* is larger, for larger ρ. Furthermore, Figure 3.25 demonstrates that no values of σ^* exist after $\chi = 0.475$ (and in particular, at $\chi = 0.5$), for $\rho = 0.5$, at $x = 0$ (as found in Figure 3.20 and in Sanz & Meseguer (1985)), while Figure

3.26 demonstrates that no values of σ^* exist after $\chi = 0.46$, for $\rho = 0.5$, at $x = 4$.

Figure 3.27 shows all four imaginary solutions of equation (3.27), which represents all four frequencies of the disturbance against wavenumber, at $x = 0$. We only consider the greatest frequency of the disturbance (the blue curve in Figure 3.27). In Figure 3.28, we plot the frequency of the disturbance against wavenumber, for varying the surface tension ratio, at $x = 0$. It can be seen that a decrease in the surface tension ratio causes the frequency of the disturbance to decrease, for large wavenumber. In Figure 3.29, we plot the frequency of the disturbance against wavenumber, for varying the density ratio, at $x = 0$. It can be seen that an increase in the density ratio causes the frequency of the disturbance to decrease, for large wavenumber. In Figure 3.30, we plot the frequency of the disturbance against wavenumber, for varying the Weber number, at $x = 0$. It can be seen that an increase in the Weber number causes the frequency of the disturbance to decrease, for large wavenumber. In Figure 3.31, we plot the frequency of the disturbance against wavenumber, for varying the inner jet radius, at $x = 0$. It can be seen that an increase in the inner jet radius causes the frequency of the disturbance to increase, for large wavenumber.

Recall that we assumed in our Mathematical model that the jet has already formed and is uniform, at the nozzle (i.e., at $x = 0$, where the effects of gravity are not present). This uniform jet (having uniform radius and uniform velocity) at the nozzle, corresponds to the no-gravity case of Sanz & Meseguer (1985). Thus, waves on the jet at $x = 0$, correspond to the behaviour of a uniform jet and we can, therefore, calculate the wavespeed of the wave disturbance on the uniform jet, at $x = 0$. Figure 3.32 shows, a graph obtained from equation (3.27), which represents all four transformed wavespeeds of the disturbance versus the wavenumber, at $x = 0$. We only consider the greatest transformed wavespeed of the disturbance (the blue curve in Figure 3.32). In Figure 3.33, we plot the

transformed wavespeed of the disturbance against wavenumber, for varying the surface tension ratio, at $x = 0$. It can be seen that a decrease in the surface tension ratio causes the transformed wavespeed of the disturbance to decrease, for large wavenumber. In Figure 3.34, we plot the transformed wavespeed of the disturbance against wavenumber, for varying the density ratio, at $x = 0$. It can be seen that a decrease in the density ratio causes the transformed wavespeed of the disturbance to increase, for large wavenumber. In Figure 3.35, we plot the transformed wavespeed of the disturbance against wavenumber, for varying the Weber number, at $x = 0$. It can be seen that a decrease in the Weber number causes the transformed wavespeed of the disturbance to increase, for large wavenumber. In Figure 3.36, we plot the transformed wavespeed of the disturbance against wavenumber, for varying the inner jet radius, at $x = 0$. It can be seen that a decrease in χ causes the transformed wavespeed of the disturbance to decrease, for large wavenumber. We note, from these figures, that the transformed wavespeed moves with the outer jet velocity, for wavenumber $k \leq 1$, while it moves faster than the outer jet velocity, for $k > 1$. This description is anticipated as we are transformed into a frame of reference which moves with the outer jet. Hence transformed wavespeed of the disturbance, at $x = 0$, depends upon the outer jet radius $S(x = 0) = 1$. For $k \leq 1$, we have $\lambda \geq 2\pi$ (as $k = 2\pi/\lambda$). In this case, we have longer waves which travel with the outer jet (or they are stationary with respect to the outer jet velocity). For $k > 1$, $\lambda < 2\pi$. In this case, we have shorter waves which travel faster than the outer jet.

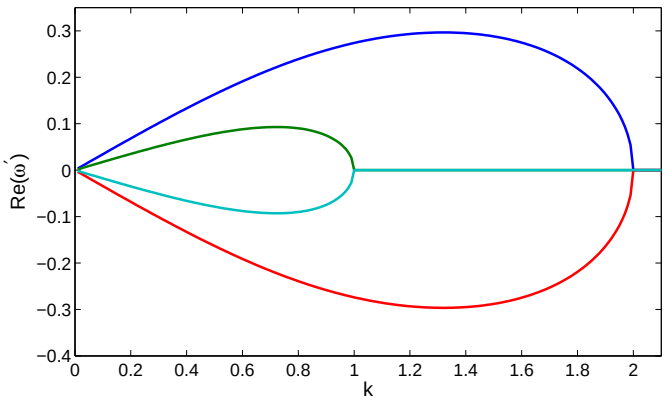

Figure 3.8: All four solutions of dispersion relation (3.27), with only the real part plotted, which represents all four growth rates of the disturbance versus wavenumber, at $x = 0$. The parameters, used here, are $We = 10$, $\rho = 1$, $\sigma = 1$ and $\chi = 0.5$.

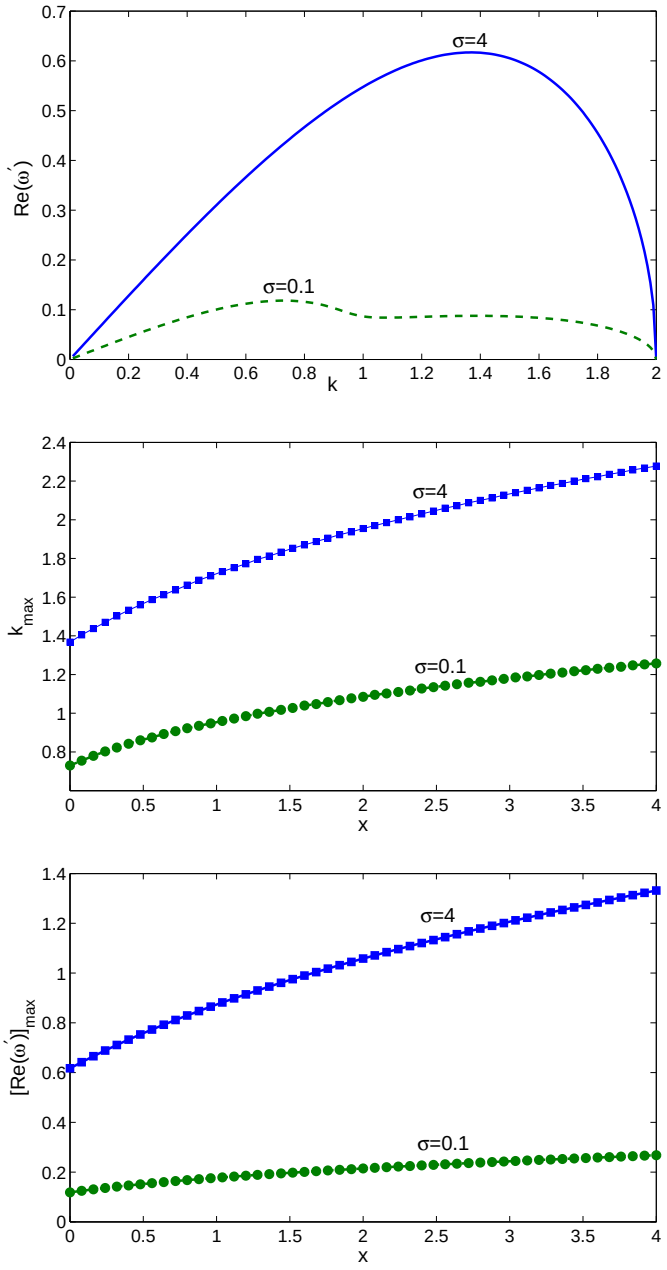

Figure 3.9: Top: Growth rate $Re(\omega')$ versus wavenumber k of the disturbance, for different σ, at $x = 0$. Middle: Maximum wavenumber k_{max} versus axial distance x, for different σ. Bottom: Maximum growth rate $[Re(\omega')]_{max}$ versus axial distance x, for different σ. It can be seen that a decrease in σ causes both k_{max} and $[Re(\omega')]_{max}$ to decrease. The other parameters are $We = 10$, $\rho = 1$ and $\chi = 0.5$.

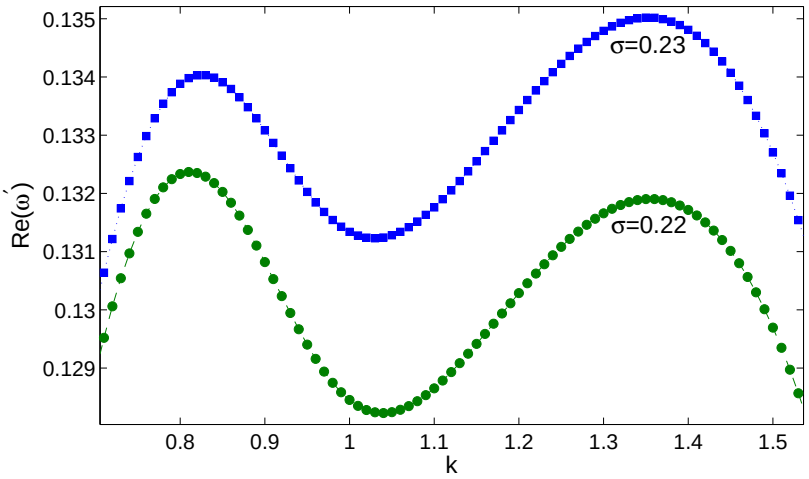

Figure 3.10: Growth rate $Re(\omega')$ versus wavenumber k of the disturbance, which shows that there exists a transition of maximum wavenumber k_{max}, for small σ, at $x = 0$. For $\sigma = 0.22$, we have $k_{max} = 0.81$, while for $\sigma = 0.23$, we have $k_{max} = 1.35$. This interesting behaviour is thoroughly further investigated in the following graph. The other parameters are $We = 10$, $\rho = 1$ and $\chi = 0.5$.

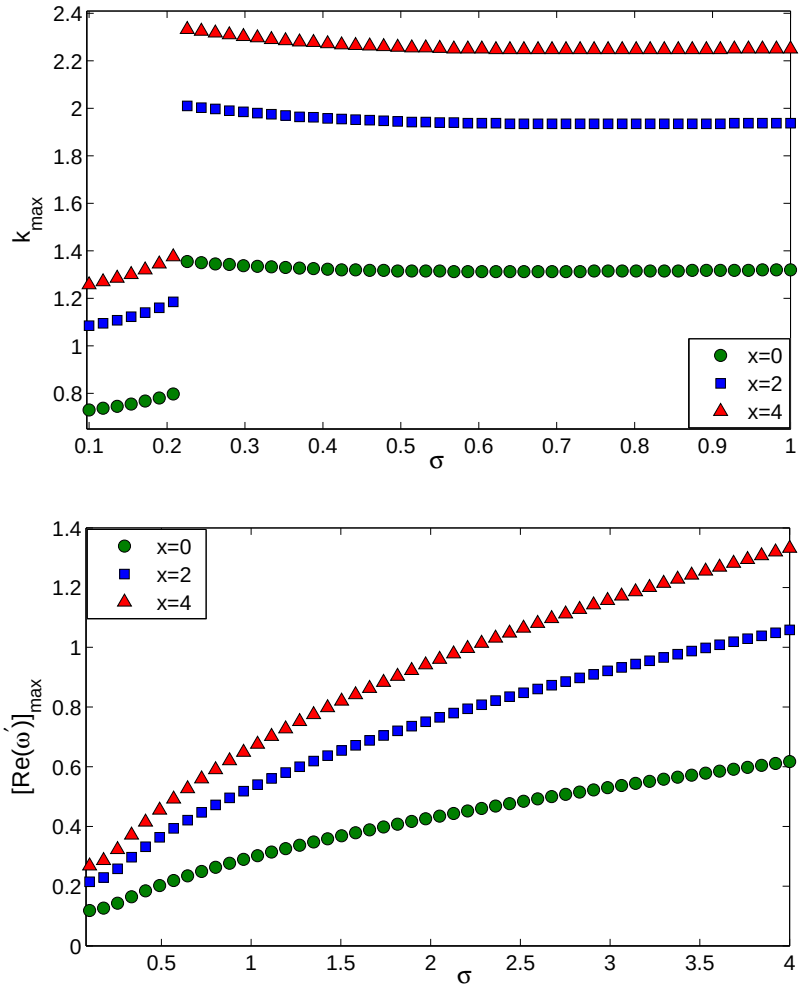

Figure 3.11: Top: Maximum wavenumber k_{max} against surface tension ratio σ, for different values of x. We note that there is a transition in the graphs for $x = 0$, $x = 2$ and $x = 4$, for one value of σ, which we refer to as threshold surface tension ratio σ^*, which occurs at $\sigma^* = 0.224$. Bottom: Maximum growth rate $[Re(\omega')]_{max}$ against σ, for different values of x. It can be seen that a decrease in σ causes $[Re(\omega')]_{max}$ to decrease, for different values of x. The other parameters are $We = 10$, $\rho = 1$ and $\chi = 0.5$.

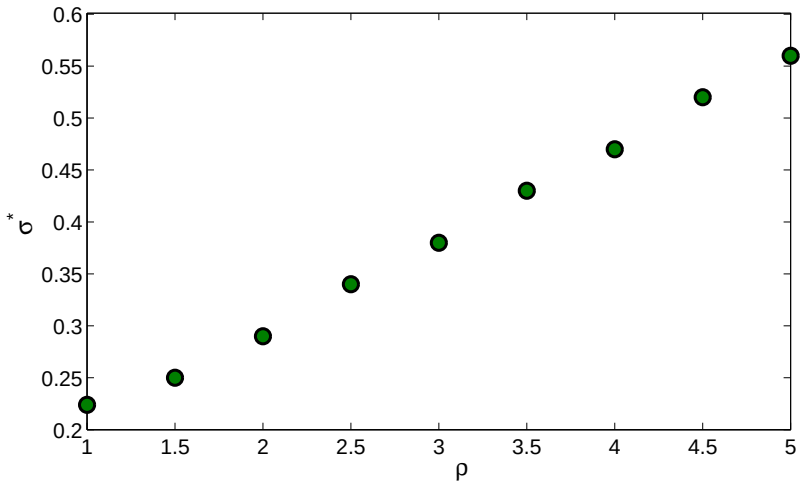

Figure 3.12: Threshold surface tension ratio σ^* against density ratio ρ, at $x = 0$, $x = 2$ and $x = 4$. We note that σ^* increases as we increase ρ. Also note that σ^* does not exist for small ρ (i.e., for $\rho < 1$), at $\chi = 0.5$ (see Figures 3.20 and 3.25, for more details). The other parameters are $We = 10$ and $\chi = 0.5$.

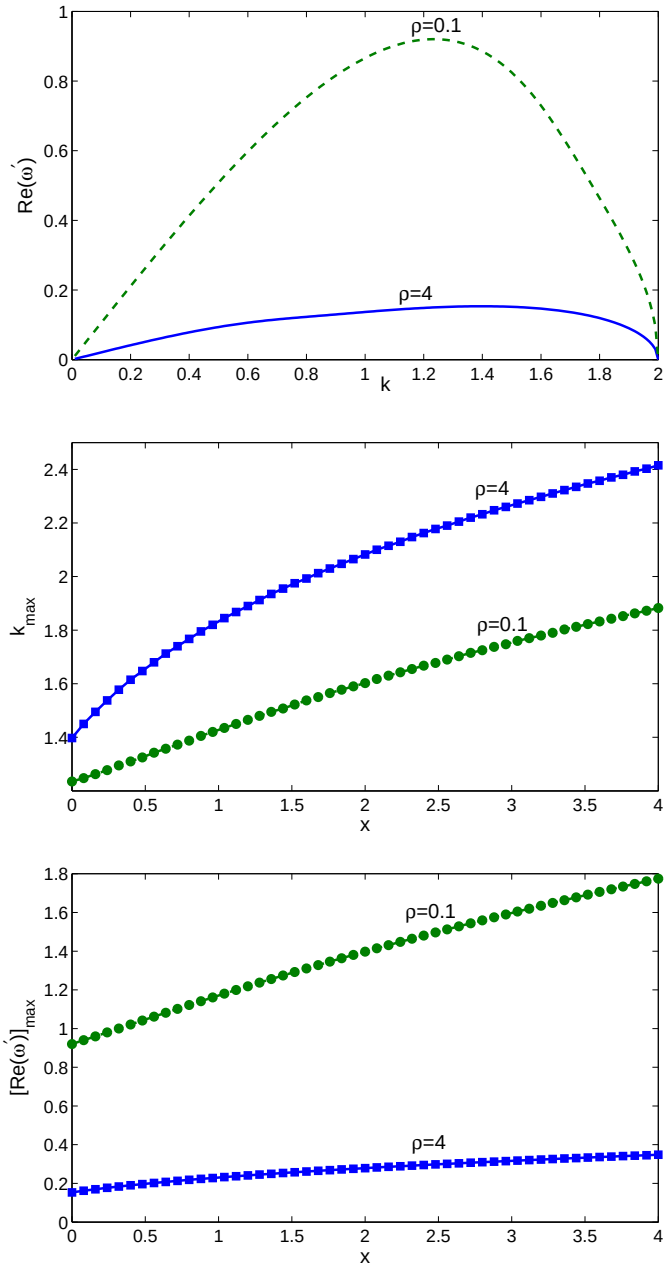

Figure 3.13: Top: Growth rate $Re(\omega')$ versus wavenumber k of the disturbance, for different ρ, at $x = 0$. Middle: k_{max} versus axial distance x, for different ρ. Bottom: $[Re(\omega')]_{max}$ versus axial distance x, for different ρ. It can be seen that a decrease in ρ causes k_{max} to decrease while causes $[Re(\omega')]_{max}$ to increase. Note that there does not exists a transition in the graphs of k_{max}, for varying ρ. The other parameters are $We = 10$, $\sigma = 1$ and $\chi = 0.5$.

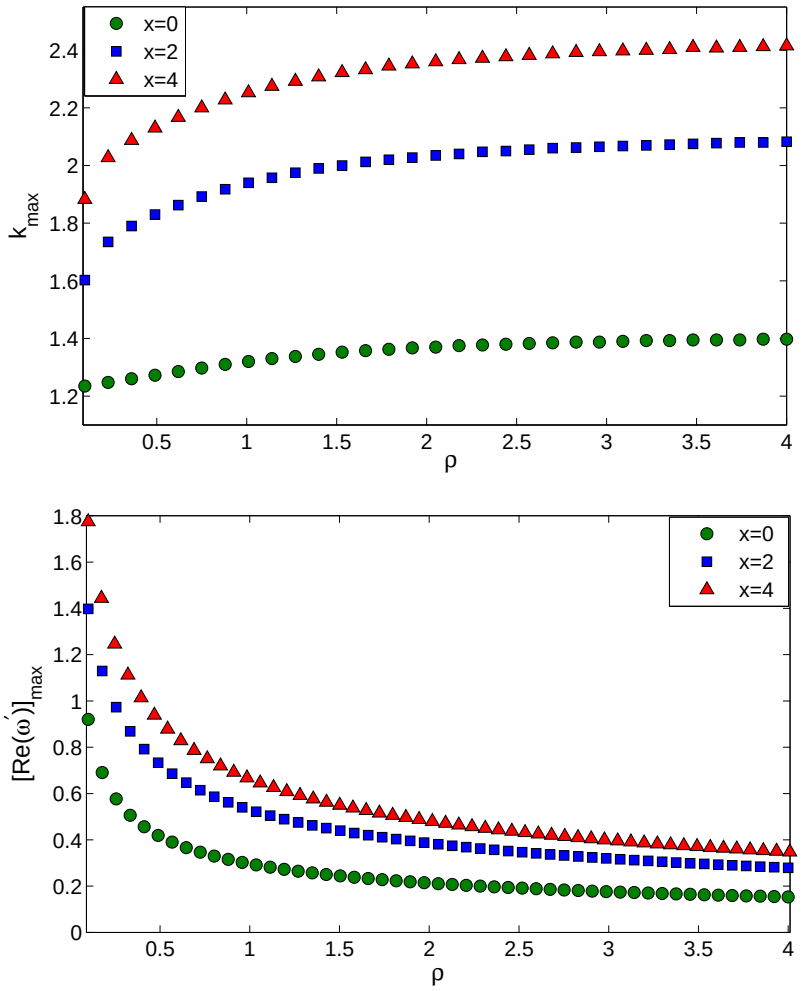

Figure 3.14: Maximum wavenumber k_{max} in the top, while maximum growth rate $[Re(\omega')]_{max}$ in the bottom, against density ratio ρ, for different values of x. It can be seen that a decrease in the density ratio causes the maximum wavenumber k_{max} to decrease for $x = 0$ and $x = 2$, as found in the previous graph, while causes the maximum growth rate $[Re(\omega')]_{max}$ to increase. Moreover, for a given ρ, k_{max} decreases while $[Re(\omega')]_{max}$ increases as x decreases. The other parameters are $We = 10$, $\sigma = 1$ and $\chi = 0.5$.

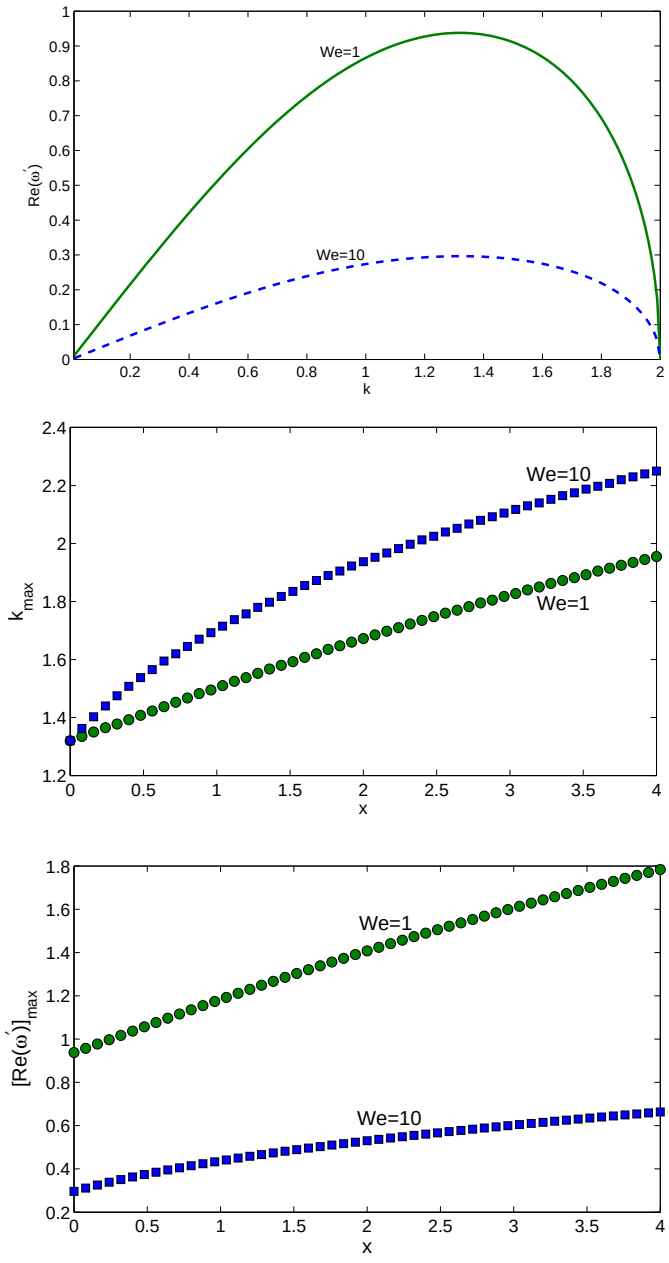

Figure 3.15: Top: Growth rate $Re(\omega')$ versus wavenumber k of the disturbance, for different values of We, at $x = 0$. Middle: k_{max} versus axial distance x, for different We. Bottom: $[Re(\omega')]_{max}$ versus x, for different We. It can be seen that a decrease in the Weber number causes k_{max} to decrease for $x > 0$, while causes $[Re(\omega')]_{max}$ to increase. The other parameters are $\sigma = 1$, $\rho = 1$ and $\chi = 0.5$.

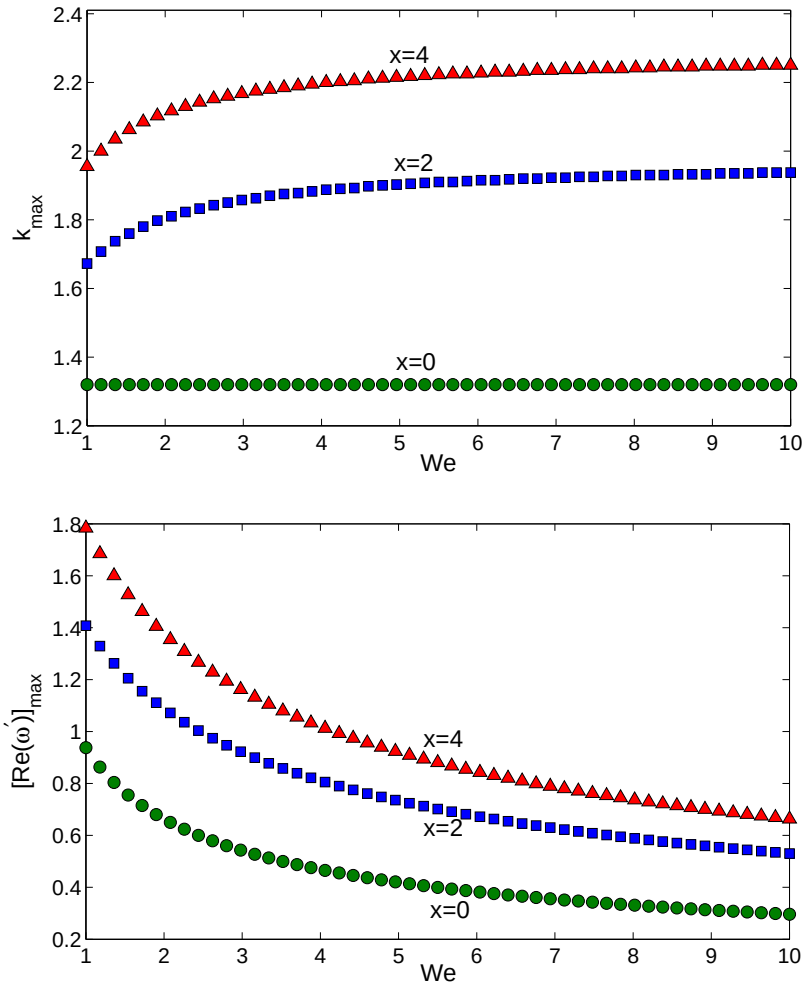

Figure 3.16: Top: Maximum wavenumber k_{max} against the Weber number We, for different values of x. Bottom: Maximum growth rate $[Re(\omega')]_{max}$ versus the Weber number, for different values of x. It can be seen that at $x = 0$, changing the Weber number does not make any difference to the maximum wavenumber $k_{max} = 1.33$. Note that this value of $k_{max} = 1.33$, at $x = 0$, corresponds exactly to the corresponding value for no-gravity case of Sanz & Meseguer (1985), where $k_{max} = (m^{-1})^{-1} = (0.75)^{-1} = 1.33$, as shown in the next figure. Also note that, for $We = 1$ and at $x = 0$, $[Re(\omega')]_{max} = 0.94$ corresponds exactly to the corresponding value for no-gravity case of Sanz & Meseguer (1985), where $\tau_m = [Re(\omega')]_{max} = 0.94$, as shown in the next figure. The other parameters are $\sigma = 1$, $\rho = 1$ and $\chi = 0.5$.

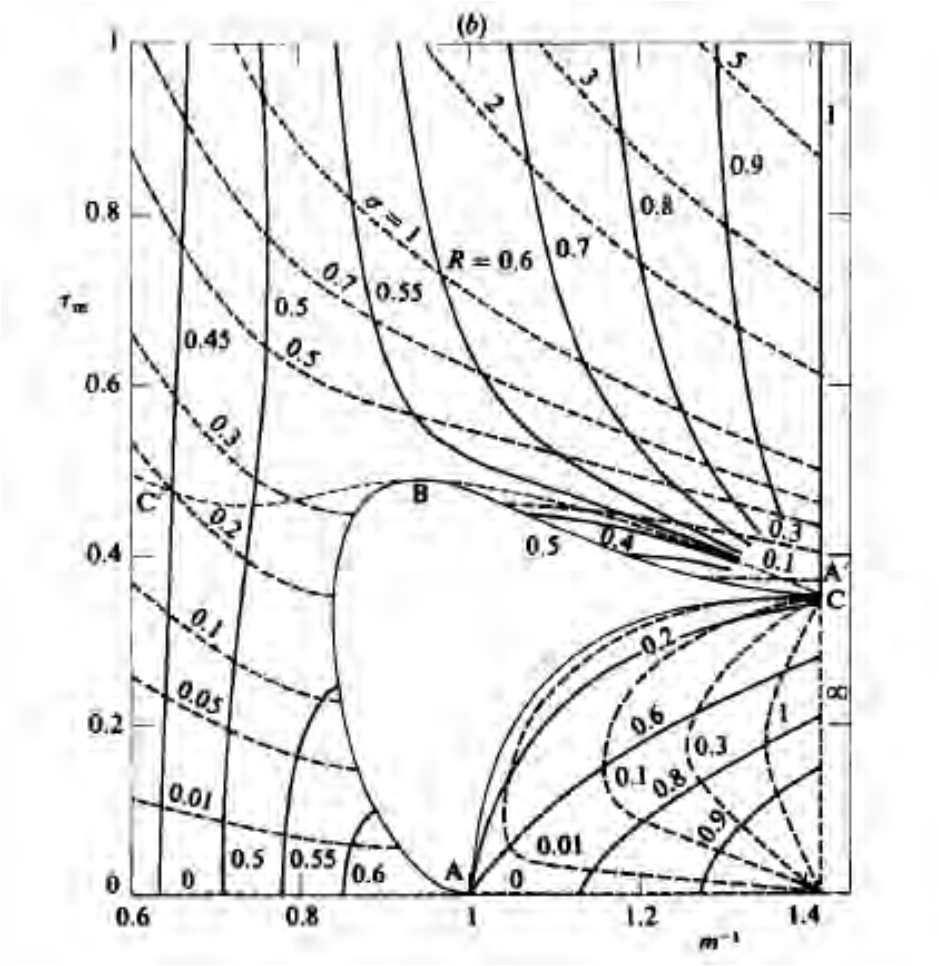

Figure 3.17: A figure taken from Sanz & Meseguer (1985), which shows that our results, at $x = 0$, are in perfect agreement with those of Sanz & Meseguer (1985). This figure shows that for $\sigma = 1$ and $\chi = R = 0.5$, the inverse wavenumber is $m^{-1} = 0.75$ and the maximum growth rate is $\tau_m = 0.94$. In some of our next graphs, we go parallel to this figure, so that we can know how the maximum growth rate and the inverse maximum wavenumber behave with the influence of the gravity. The other parameters are $We = 1$ and $\rho = 1$.

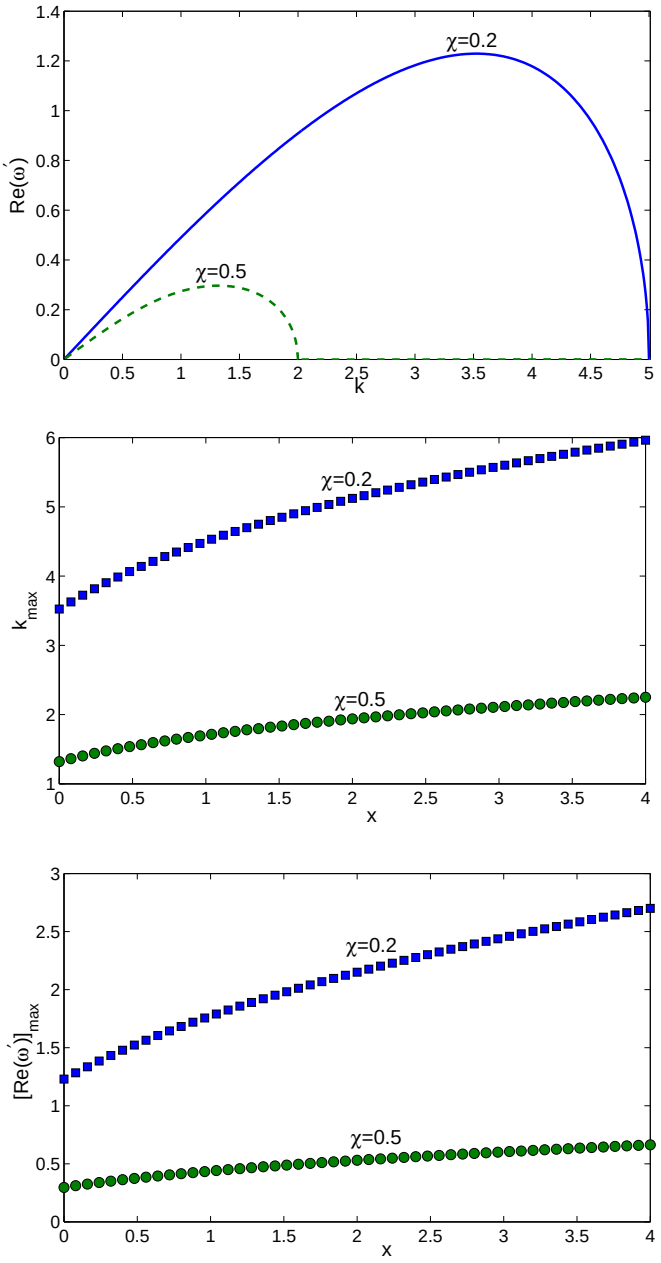

Figure 3.18: Top: Growth rate $Re(\omega')$ versus wavenumber k of the disturbance, for different χ, at $x = 0$. Middle: Maximum wavenumber k_{max} versus axial distance x, for different values of χ. Bottom: Maximum growth rate $[Re(\omega')]_{max}$ versus x, for different values of χ. It can be seen that a decrease in χ causes both k_{max} and $[Re(\omega')]_{max}$ to increase. The other parameters are $\sigma = 1$, $\rho = 1$ and $We = 10$.

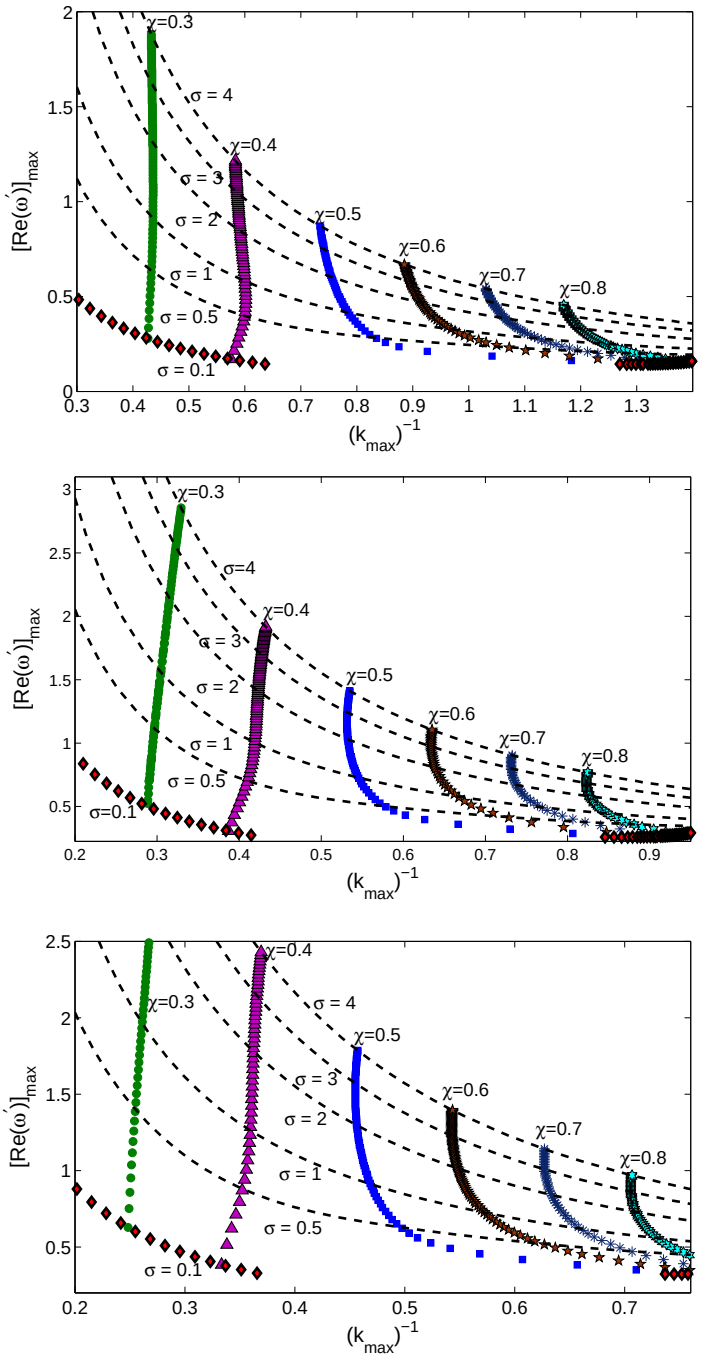

Figure 3.19: Maximum growth rate $[Re(\omega')]_{max}$ against inverse maximum wavenumber $(k_{max})^{-1}$, for various values of σ and χ. The graphs from top to bottom represent $x = 0$, $x = 2$ and $x = 4$ respectively. The other parameters are $We = 10$ and $\rho = 0.5$. The symbols are for $\sigma = 0.1 - 4$, while the dashed lines are for $\chi = 0.1 - 0.9$. The diamonds represent $\sigma = 0.1$, where $\chi = 0.1 - 0.9$, and there is a discontinuity in the diamonds, caused by competing wavemodes.

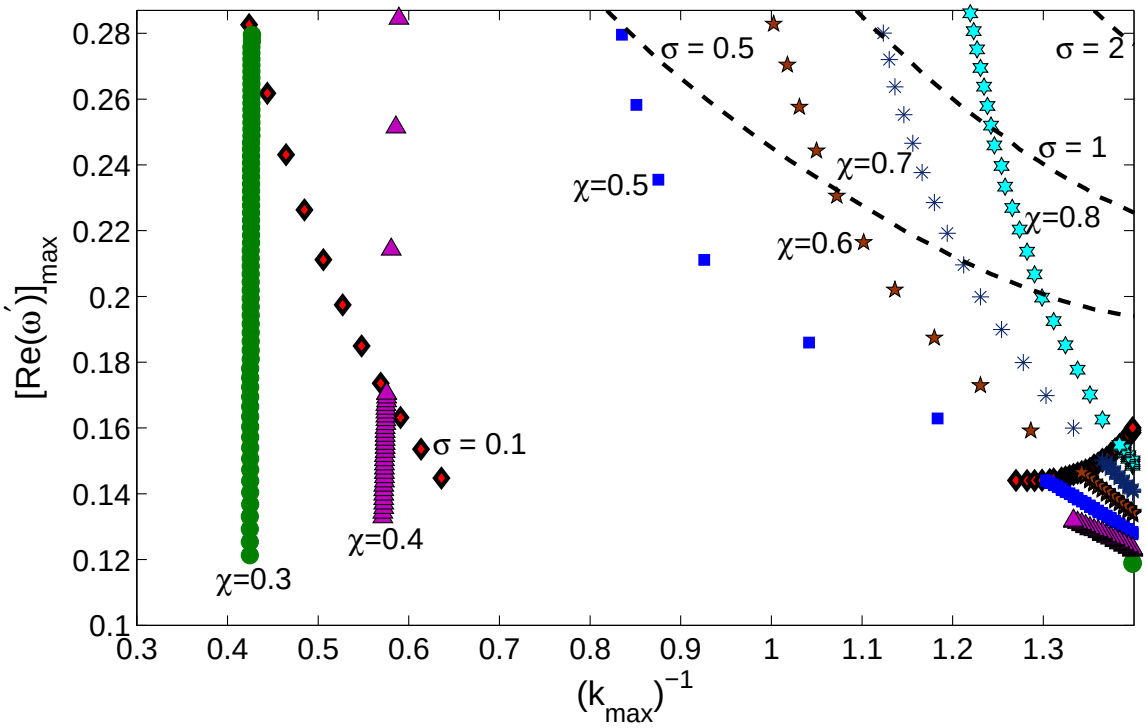

Figure 3.20: Maximum growth rate $[Re(\omega')]_{max}$ against inverse maximum wavenumber $(k_{max})^{-1}$, for various values of σ and χ. This figure is an enlarged version of the previous figure, for $x = 0$, $We = 10$ and $\rho = 0.5$. The symbols are for $\sigma = 0.01 - 0.1$, which are below the dashed line $\sigma = 0.1$, and $\sigma = 0.1 - 4$, which are above the dashed line $\sigma = 0.1$, while the dashed lines are for $\chi = 0.1 - 0.9$. The diamonds represent $\sigma = 0.1$, where $\chi = 0.1 - 0.9$, and there is a discontinuity in the diamonds, caused by competing wavemodes.

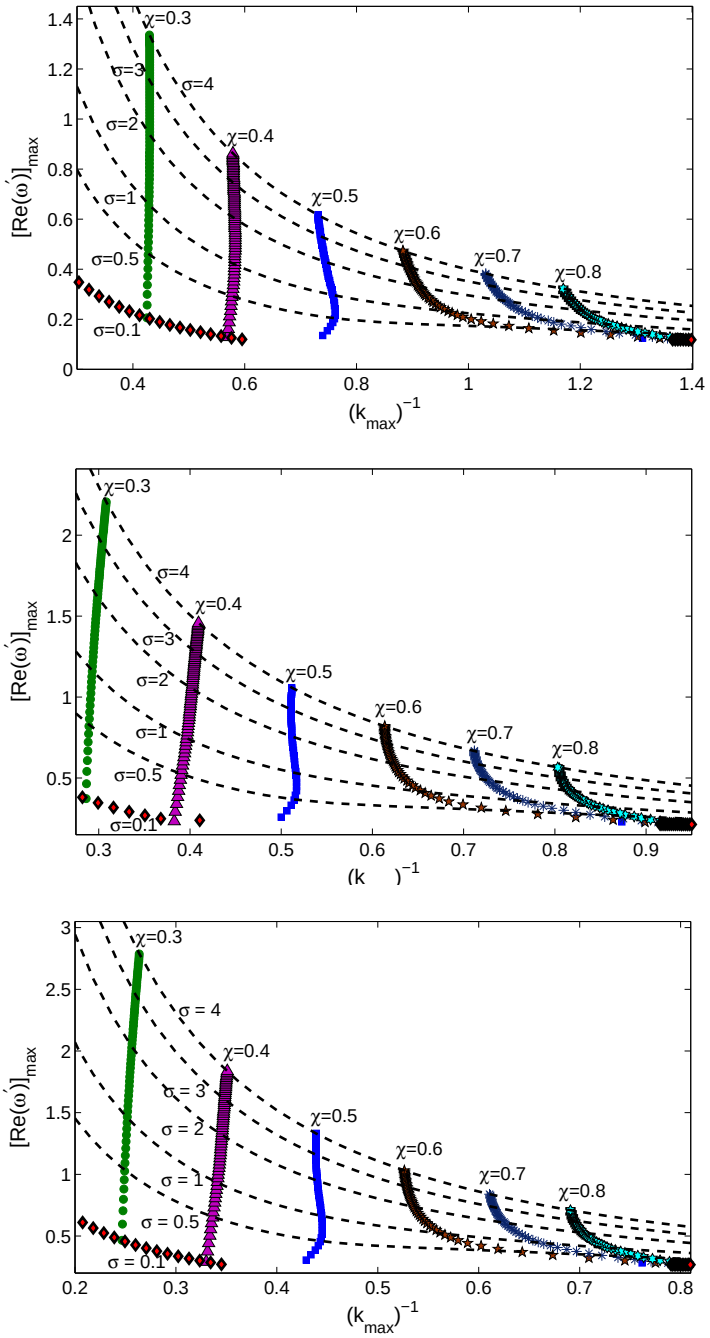

Figure 3.21: Maximum growth rate $[Re(\omega')]_{max}$ against inverse maximum wavenumber $(k_{max})^{-1}$, for various values of σ and χ. The graphs from top to bottom represent $x = 0$, $x = 2$ and $x = 4$ respectively. The other parameters are $We = 10$ and $\rho = 1$. The symbols are for $\sigma = 0.1 - 4$, while the dashed lines are for $\chi = 0.1 - 0.9$. The diamonds represent $\sigma = 0.1$, where $\chi = 0.1 - 0.9$, and there is a discontinuity in the diamonds, caused by competing wavemodes.

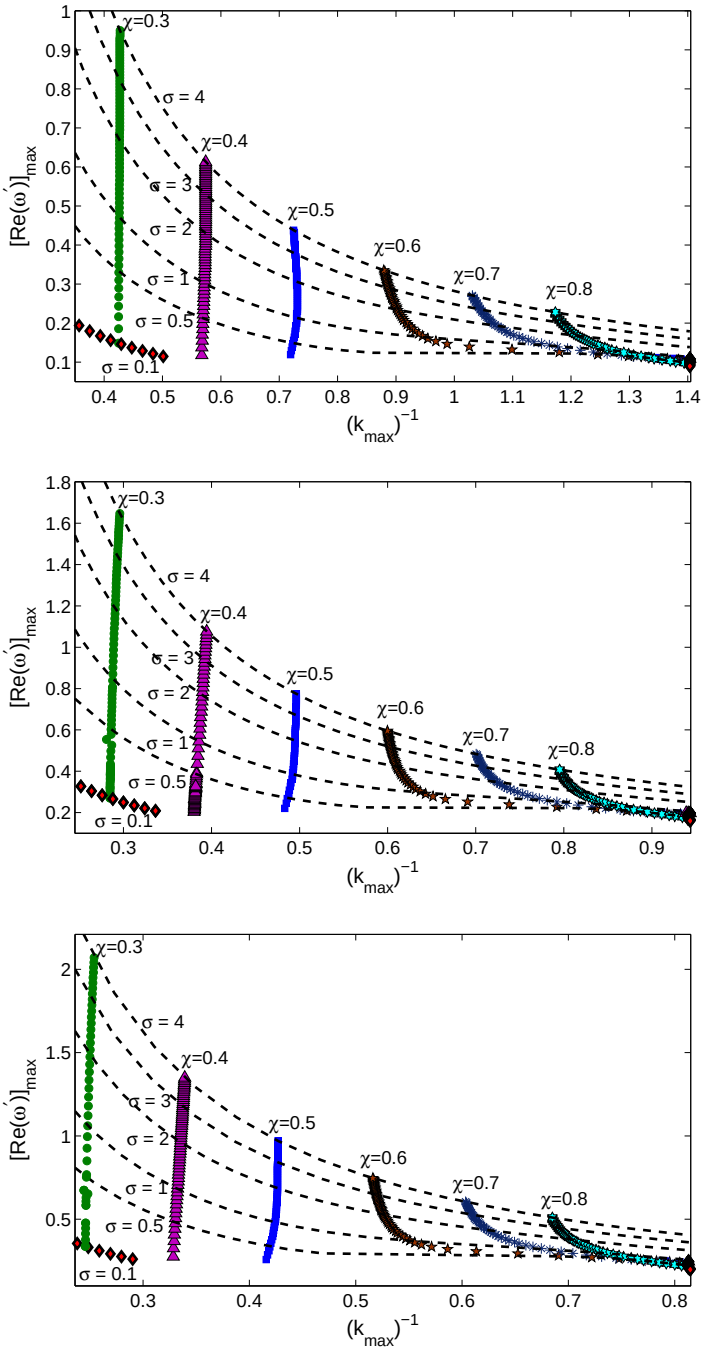

Figure 3.22: Maximum growth rate $[Re(\omega')]_{max}$ against inverse maximum wavenumber $(k_{max})^{-1}$, for various values of σ and χ. The graphs from top to bottom represent $x = 0$, $x = 2$ and $x = 4$ respectively. The other parameters are $We = 10$ and $\rho = 2$. The symbols are for $\sigma = 0.1 - 4$, while the dashed lines are for $\chi = 0.1 - 0.9$. The diamonds represent $\sigma = 0.1$, where $\chi = 0.1 - 0.9$, and there is a discontinuity in the diamonds, caused by competing wavemodes.

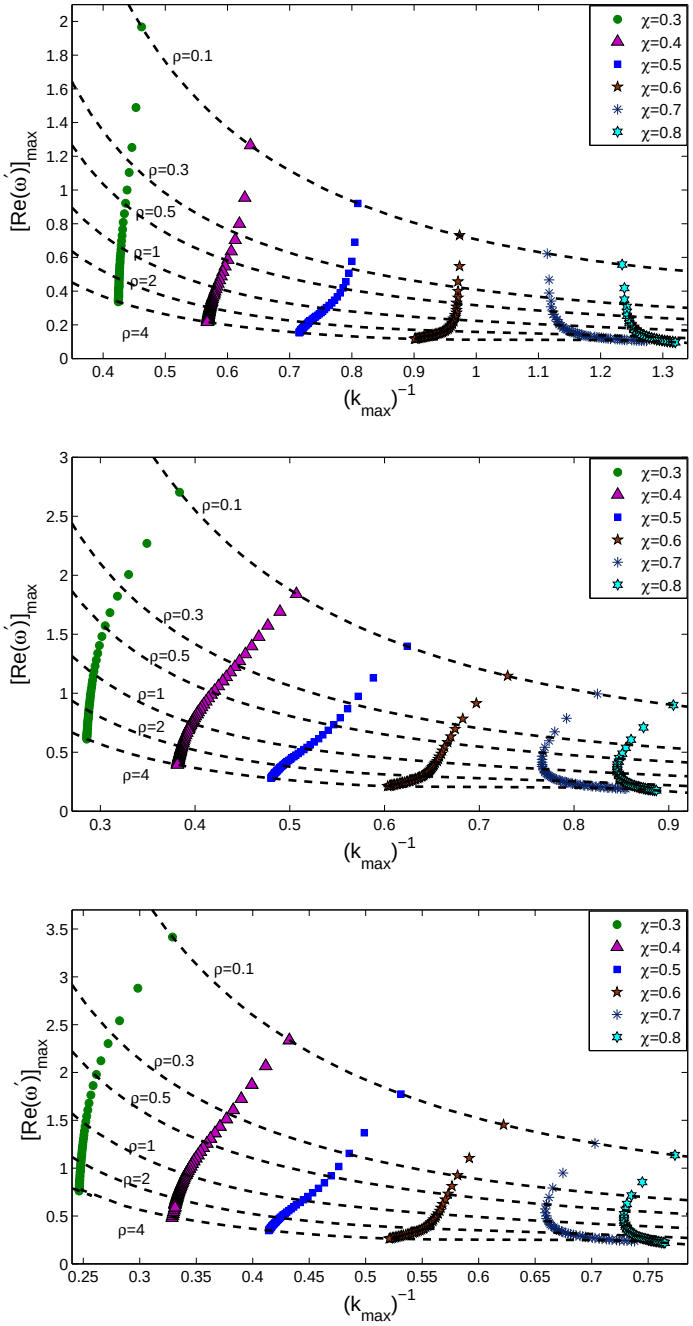

Figure 3.23: Maximum growth rate $[Re(\omega')]_{max}$ against inverse maximum wavenumber $(k_{max})^{-1}$, for various values of σ and χ. The graphs from top to bottom represent $x = 0$, $x = 2$ and $x = 4$ respectively. The other parameters are $We = 10$ and $\sigma = 1$. The symbols are for $\rho = 0.1 - 4$, while the dashed lines are for $\chi = 0.1 - 0.9$.

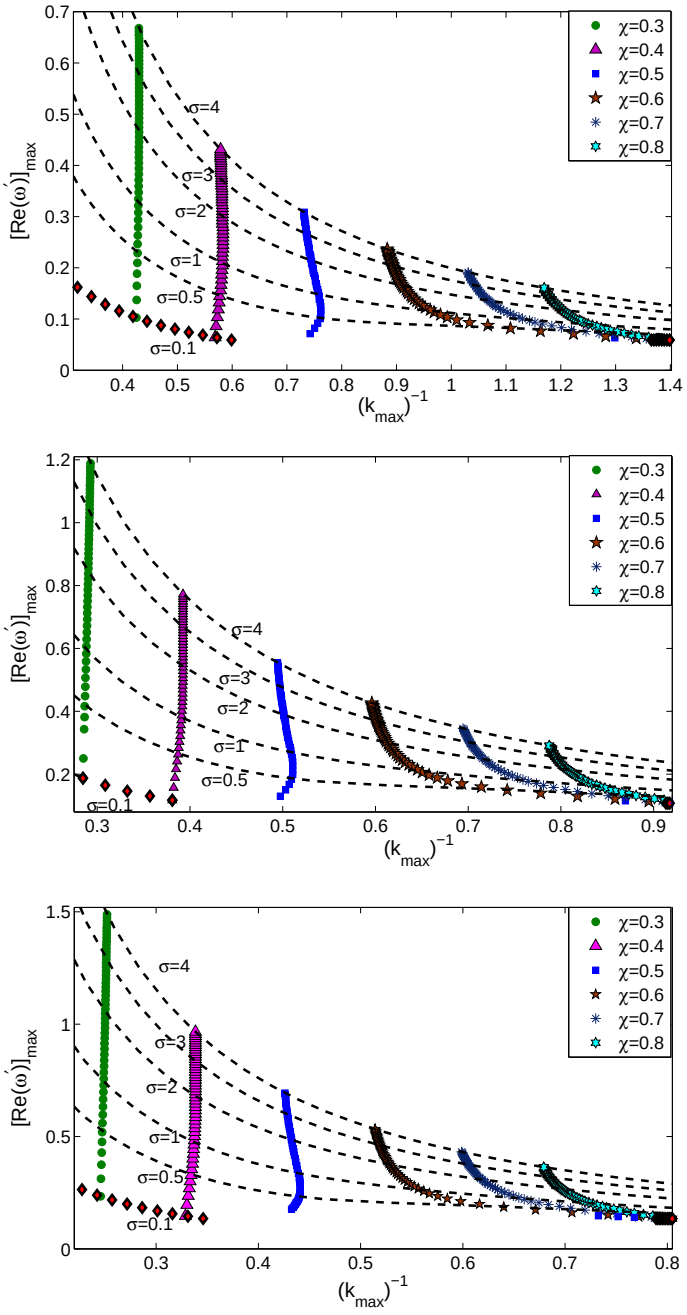

Figure 3.24: Maximum growth rate $[Re(\omega')]_{max}$ against inverse maximum wavenumber $(k_{max})^{-1}$, for various values of σ and χ. The graphs from top to bottom represent $x = 0$, $x = 2$ and $x = 4$ respectively. Here $We = 40$ and $\rho = 1$. The symbols are for $\sigma = 0.1 - 4$, while the dashed lines are for $\chi = 0.1 - 0.9$. The diamonds represent $\sigma = 0.1$, where $\chi = 0.1 - 0.9$, and there is a discontinuity in the diamonds, caused by competing wavemodes.

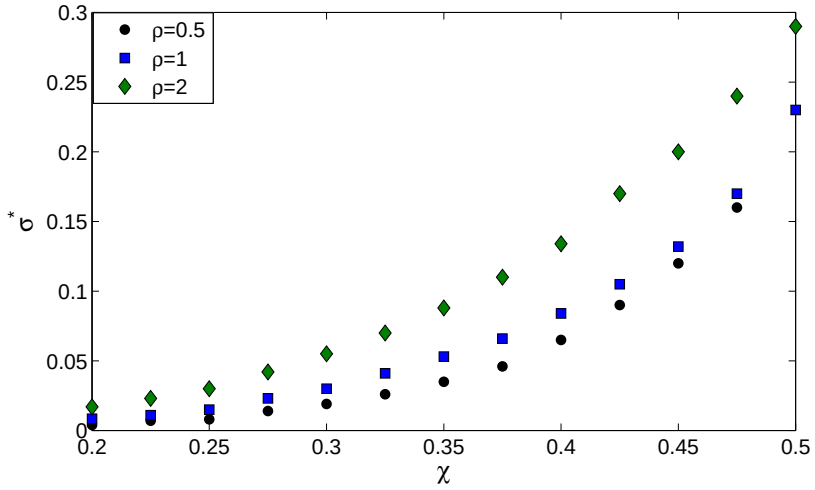

Figure 3.25: Threshold surface tension ratio σ^* against inner jet radius χ, for various density ratio ρ, at $x = 0$. Note that for $\rho = 0.5$, there does not exist σ^* at $\chi = 0.5$, as found in Figure 3.20 and in Sanz & Meseguer (1985). The other parameter is $We = 10$.

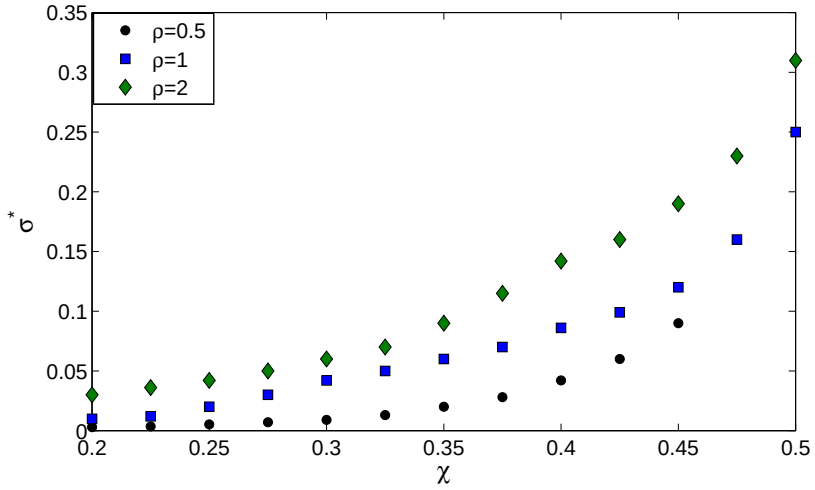

Figure 3.26: Threshold surface tension ratio σ^* against inner jet radius χ, for various density ratio ρ, at $x = 4$. Note that for $\rho = 0.5$, there does not exist σ^* for $\chi > 0.45$. The other parameter is $We = 10$.

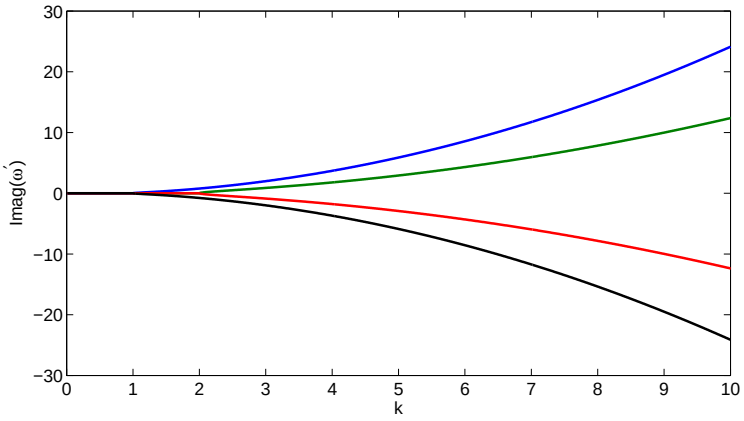

Figure 3.27: A graph showing all four imaginary solutions of equation (3.27), which represents all four frequencies of the disturbance versus wavenumber, at $x = 0$. The parameters, used here, are $We = 10$, $\sigma = 1$, $\rho = 1$ and $\chi = 0.5$.

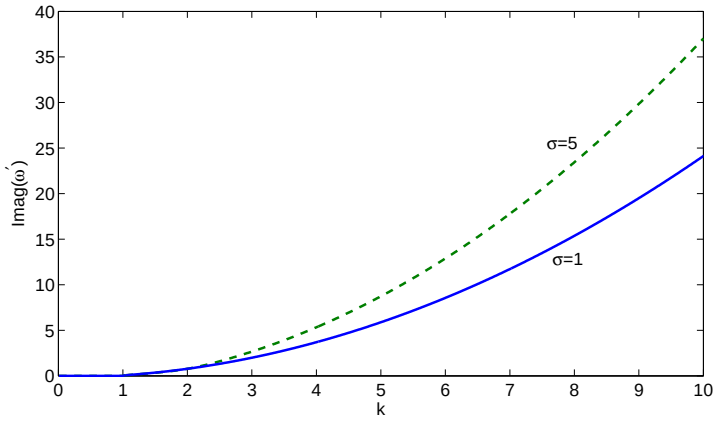

Figure 3.28: Frequency of the disturbance versus wavenumber, for varying the surface tension ratio, at $x = 0$. It can be seen that a decrease in the surface tension ratio causes the frequency of the disturbance to decrease, for large wavenumber. The other parameters are $We = 10$, $\rho = 1$ and $\chi = 0.5$.

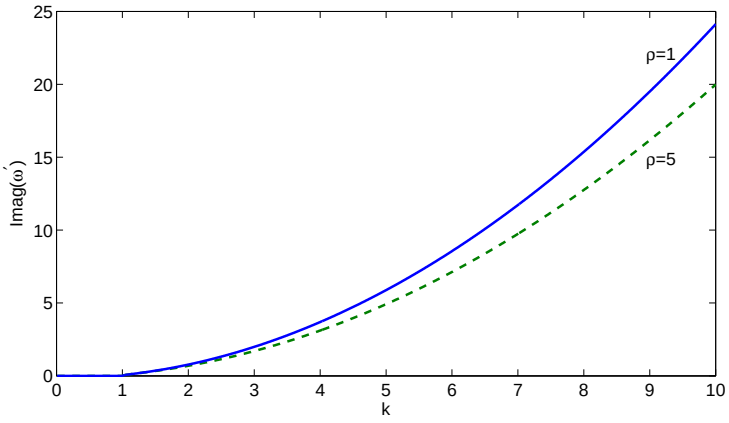

Figure 3.29: Frequency of the disturbance versus wavenumber, for varying the density ratio, at $x = 0$. It can be seen that an increase in the density ratio causes the frequency of the disturbance to decrease, for large wavenumber. The other parameters are $We = 10$, $\sigma = 1$ and $\chi = 0.5$.

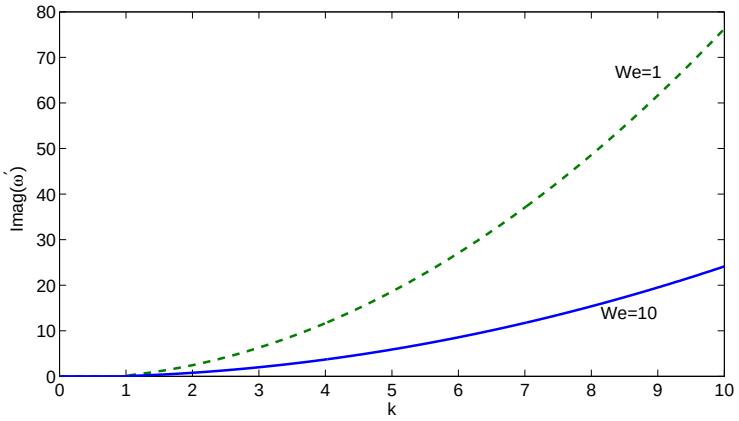

Figure 3.30: Frequency of the disturbance versus wavenumber, for varying the Weber number, at $x = 0$. It can be seen that an increase in the Weber number causes the frequency of the disturbance to decrease, for large wavenumber. The other parameters are $\rho = 1$, $\sigma = 1$ and $\chi = 0.5$.

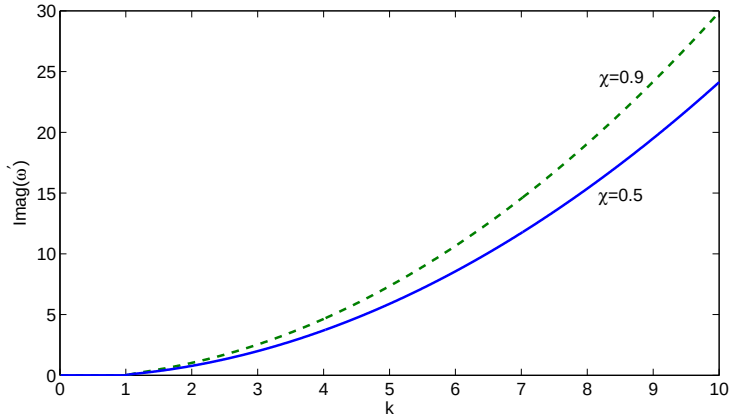

Figure 3.31: Frequency of the disturbance versus wavenumber, for varying the inner jet radius, at $x = 0$. It can be seen that an increase in the inner jet radius causes the frequency of the disturbance to increase, for large wavenumber. The other parameters are $We = 10$, $\rho = 1$ and $\sigma = 1$.

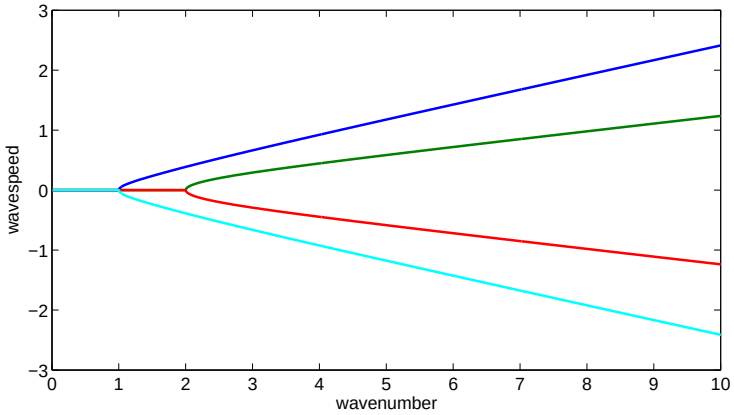

Figure 3.32: A graph obtained from equation (3.27), which represents all four transformed wavespeeds of the disturbance versus the wavenumber, at $x = 0$. The parameters, used here, are $We = 10$, $\rho = 1$, $\sigma = 1$ and $\chi = 0.5$.

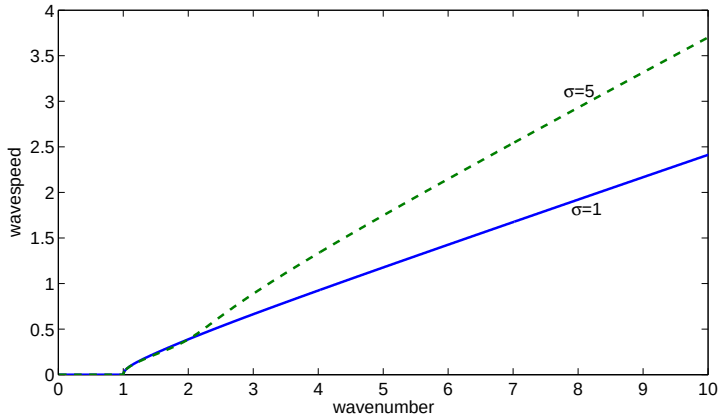

Figure 3.33: Transformed wavespeed of the disturbance versus the wavenumber, for varying the surface tension ratio, at $x = 0$. It can be seen that a decrease in the surface tension ratio causes the transformed wavespeed of the disturbance to decrease, for large wavenumber. The other parameters are $We = 10$, $\rho = 1$ and $\chi = 0.5$.

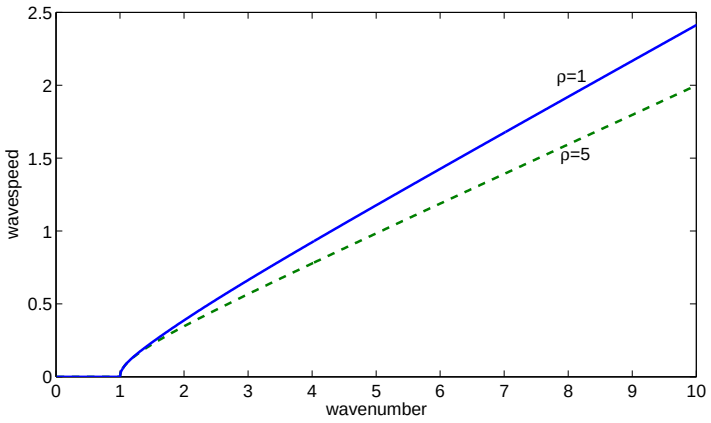

Figure 3.34: Transformed wavespeed of the disturbance versus the wavenumber, for varying the density ratio, at $x = 0$. It can be seen that a decrease in the density ratio causes the transformed wavespeed of the disturbance to increase, for large wavenumber. The other parameters are $We = 10$, $\sigma = 1$ and $\chi = 0.5$.

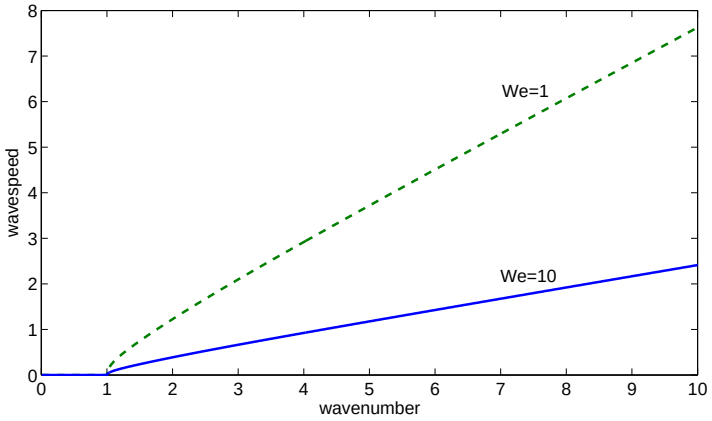

Figure 3.35: Transformed wavespeed of the disturbance versus the wavenumber, for varying the Weber number, at $x = 0$. It can be seen that a decrease in the Weber number causes the transformed wavespeed of the disturbance to increase, for large wavenumber. The other parameters are $\sigma = 1$, $\rho = 1$ and $\chi = 0.5$.

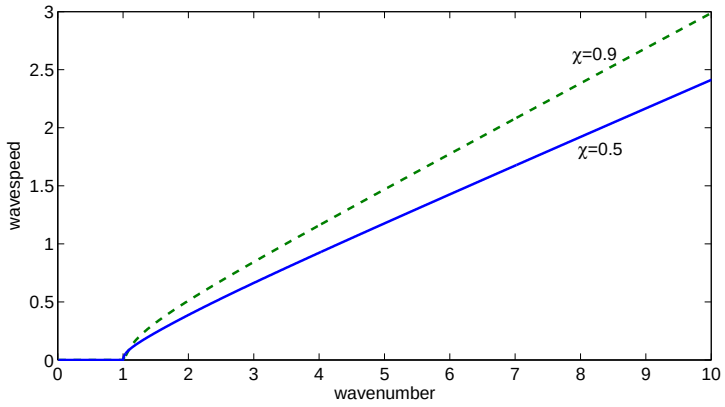

Figure 3.36: Transformed wavespeed of the disturbance versus the wavenumber, for varying χ, at $x = 0$. It can be seen that a decrease in χ causes the transformed wavespeed of the disturbance to decrease, for large wavenumber. The other parameters are $We = 10$, $\sigma = 1$ and $\rho = 1$

3.8 Breakup Lengths

Using the results from our temporal instability analysis, we may determine the profile of waves travelling along both the inner and outer interfaces. In order to do this, we first need to evaluate an expression for time $\bar{t}$ (in equations (3.19) – (3.21)). The variable $\bar{t}$ (= t/ϵ) does not appear explicitly in our analysis but may be approximated using the expression $t(x) = \int_0^x (1/u(s))ds$ (see Uddin & Decent (2009), for more details), so as to specify a value of t for each axial distance x along the jet. Thereafter, we may choose a value of δ and ϵ, and use the results obtained in the previous section to plot R and S (i.e., equations (3.20) and (3.21)). This allows us to determine the axial distance (or breakup length l_b) at which either R reaches zero or both the inner and outer interfaces touch. Compound jet profiles for certain parameter values are shown in Figure 3.37. In this figure, we show two examples of cases where the breakup is a result of the inner interface breaking first and one where the outer interface touches the inner interface first. We can then determine breakup length l_b, when χ is varied, as shown in Figure 3.38. Here we see that the breakup length increases as χ is increased and that there are values of χ at which the jet breakup changes qualitatively, that is, instead of the inner jet rupturing, we have that the outer and inner interfaces touch. The jump in the inner jet breakup length, for $We = 100$ and $\chi = 0.71$, is due to the formation of a neck, as the inner jet breaks later at $l_b = 82.95$ (see Figure 3.37). In addition, a decrease in the outer jet breakup length, for $We = 100$ and $\chi = 0.91$, is again due to the formation of a neck, as the inner jet does not break and the two interfaces touch at $l_b = 94.05$ (see Figure 3.37).

We next want to compare our results to numerical simulations of an inviscid compound jet falling under gravity, as considered by Uddin & Decent (2010). In order to do this, we note that we must take $\delta = \epsilon = 0.01$, as in Uddin & Decent

(2010). Compound jet profiles for certain parameter values (where $\delta = \epsilon = 0.01$) are shown in Figure 3.39. In this figure, we show two examples of cases where the breakup is a result of the inner interface breaking first and one where the outer interface touches the inner interface first. We can then determine breakup length l_b, when χ is varied, as shown in Figure 3.40. Here we see that the breakup length increases as χ is increased and that there are values of χ at which jet breakup changes qualitatively - that is, instead of the inner jet rupturing, we have that the outer and inner interfaces touch. Therefore, we have a transition in the behaviour of breakup lengths of inner and outer fluids, for different We and by varying χ. We note that the transition point, from the inner jet rupturing first to the outer jet rupturing first, increases with an increase in We. The jump in the inner jet breakup length, for $We = 100$ and $\chi = 0.57$, is due to the formation of a neck, as the inner jet does not break near $l_b = 44.51$ but breaks later at $l_b = 57.57$. This phenomenon is illustrated in Figure 3.41. In addition, an increase in the outer jet breakup length, for $We = 20$ and $\chi = 0.82$, is again due to the formation of a neck, as the inner jet does not break and the outer jet breaks at $l_b = 37.42$ (see Figure 3.39). We also investigate the impact of the disturbance amplitude δ on the breakup length l_b, for different Weber numbers, in Figure 3.42. We, consequently, find that increasing the disturbance amplitude implies a decrease in the breakup length, for different Weber numbers. Furthermore, we find from Figures 3.40 and 3.42 that for small Weber number, we have small breakup length. We now compare our results to numerical simulations of an inviscid compound jet falling under gravity, as considered by Uddin & Decent (2010). In particular, we have for $We = 20$ and $\chi = 0.72$, the breakup length, as predicted by Uddin & Decent (2010), is around $l_b \approx 34$, which is in good agreement with a value of $l_b = 29$ (as shown in Figure 3.40), predicted using the present linear theory. It is important to note that the final stages of the breakup, where both the inner and outer jet radii

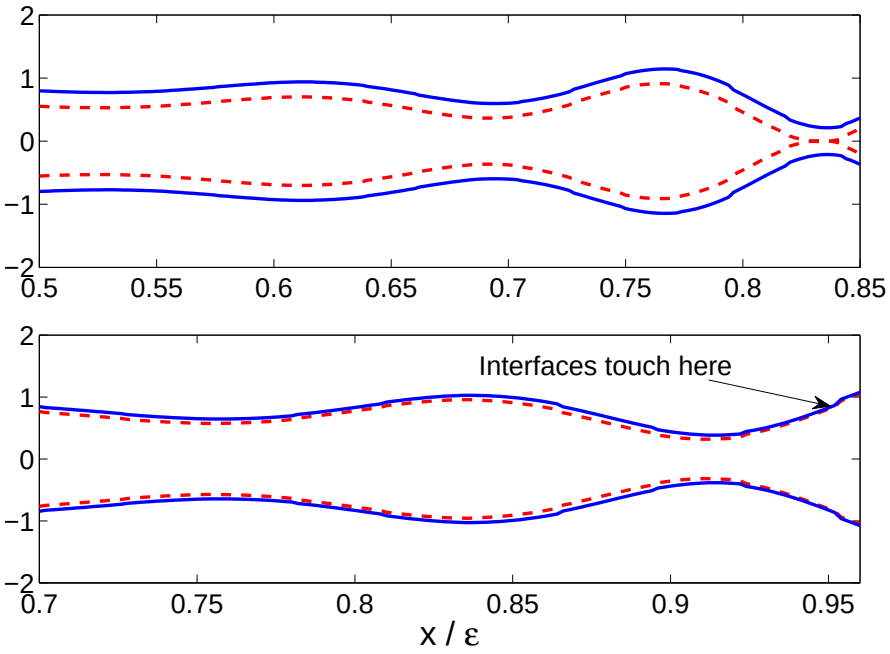

Figure 3.37: Compound jet profiles showing breakup caused by the inner jet rupture (top) and when the inner and outer jet interfaces touch (bottom). In the top figure, we have $We = 100$ and $\chi = 0.71$ (with breakup at $l_b = 82.95$), while for the bottom figure, we have $We = 100$ and $\chi = 0.91$ (with breakup at $l_b = 94.05$). The other parameters are $\delta = 2 \times 10^{-3}$, $\epsilon = 0.01$, $\sigma = 1$ and $\rho = 1$. The inner interface is represented here by a dashed line with the outer interface as a solid line.

approach zero, is inherently nonlinear and, therefore, our linear theory, which is based upon a one-dimensional approximation of the governing equations, will not provide an accurate picture of the latter stages of the breakup process. However, since disturbances grow exponentially, the final stages of the breakup occur over relatively short length and time scales and, therefore, linear theory may be used to provide good predictions of breakup lengths and breakup times (see also Eggers (1997)).

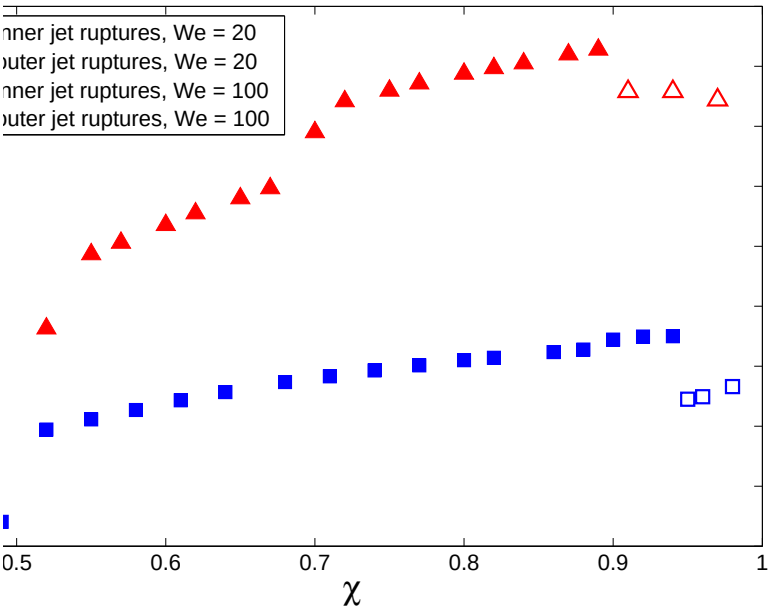

Figure 3.38: A graph of breakup length against χ, for different Weber numbers. Note that, for $We = 20$, the inner jet breaks first when $\chi < 0.94$, while for $We = 100$, the inner jet breaks first when $\chi < 0.9$. The other parameters are $\delta = 2 \times 10^{-3}$, $\epsilon = 0.01$, $\sigma = 1$ and $\rho = 1$.

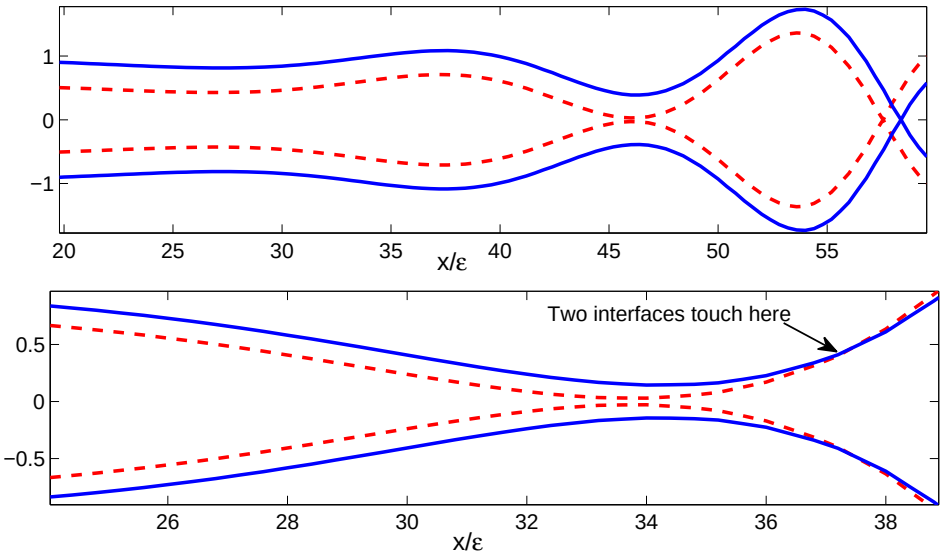

Figure 3.39: Compound jet profiles showing breakup caused by the inner jet rupture (top figure) and when the inner and outer jet interfaces touch (bottom figure). In the top figure, we have $We = 100$ and $\chi = 0.57$ (with breakup at $l_b = 57.57$), whilst for the bottom figure, we have $We = 20$ and $\chi = 0.82$ (with breakup at $l_b = 37.42$). The other parameters are $\delta = 0.01$, $\epsilon = 0.01$, $\sigma = 1$ and $\rho = 1$. The inner interface is represented here by a dashed line with the outer interface as a solid line.

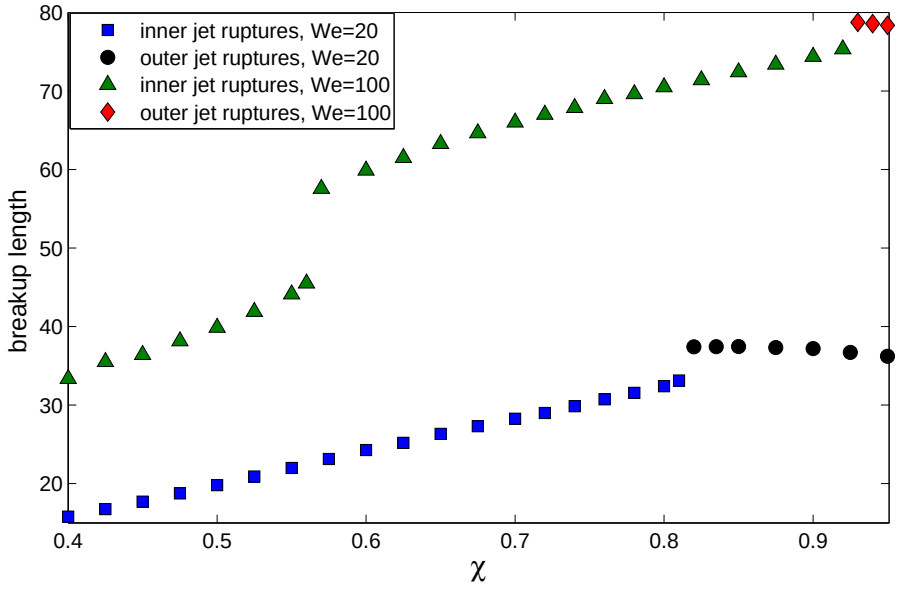

Figure 3.40: A graph of breakup length against χ, for different Weber numbers. This graph clearly shows a transition in the behaviour of breakup lengths. Note that, for $We = 20$, the inner jet breaks first when $\chi < 0.82$, while for $We = 100$, the inner jet breaks first when $\chi < 0.93$. That is, the transition point increases with an increase in We. The jump in the inner jet breakup length, for $We = 100$, is due to the formation of a neck, as the inner jet does not break near $l_b = 44.51$ (see Figure 3.41). The other parameters are $\delta = 0.01$, $\epsilon = 0.01$, $\sigma = 1$ and $\rho = 1$.

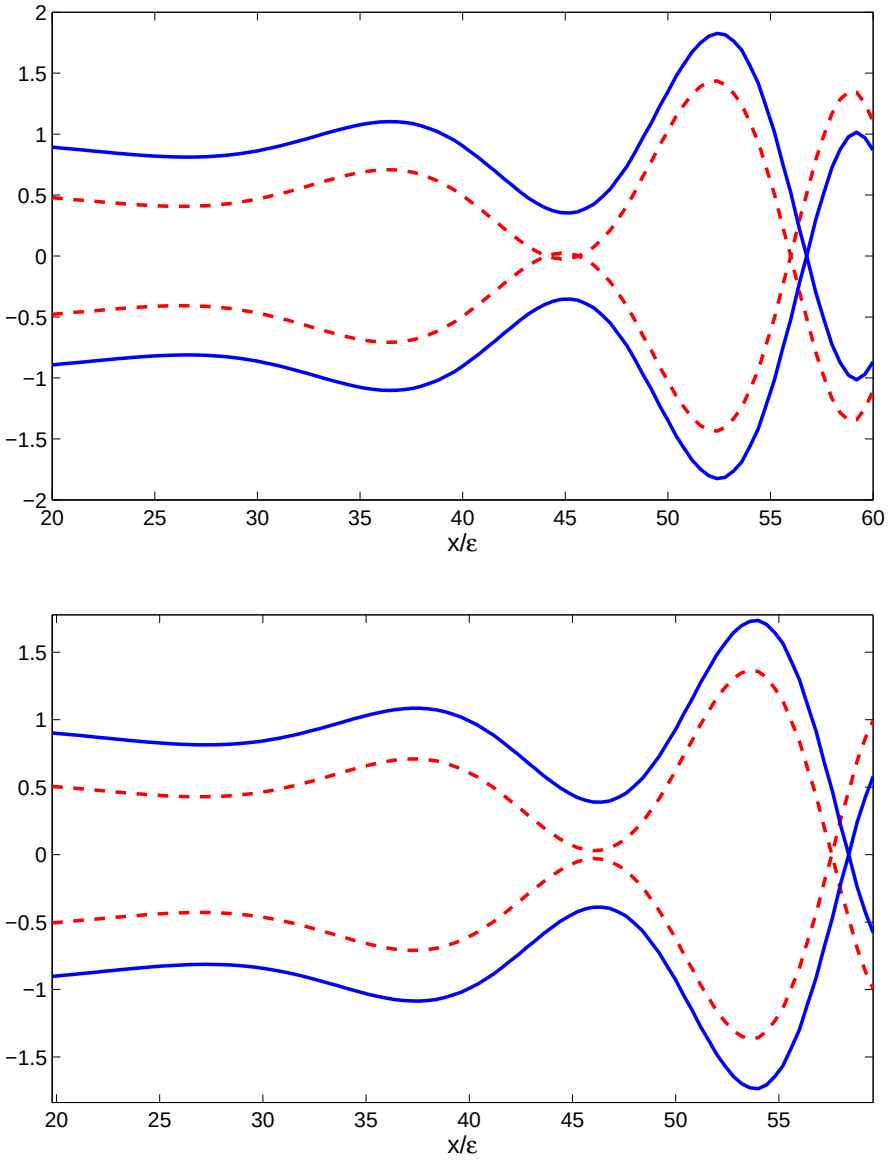

Figure 3.41: Compound jet profiles showing a small increase in χ implies a jump in the breakup length l_b, for the inner jet. Top is $\chi = 0.56$, with $l_b = 44.51$, while bottom is $\chi = 0.57$, with $l_b = 57.57$. Also note the formation of a neck, for $\chi = 0.57$, as the inner jet does not break near $l_b = 44.51$. The other parameters are $We = 100$, $\sigma = 1$, $\rho = 1$, $\epsilon = 0.01$, $\delta = 0.01$.

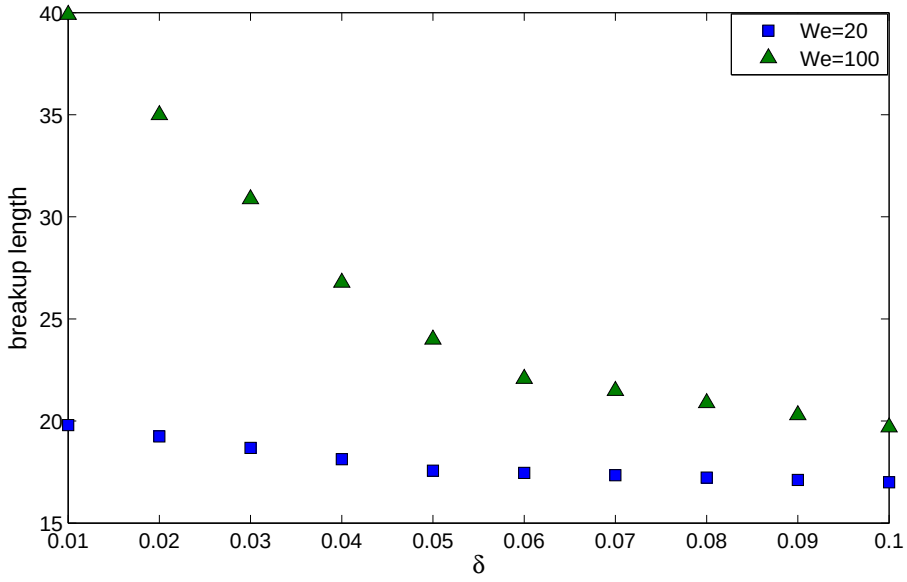

Figure 3.42: A graph of breakup length against disturbance amplitude δ, for different Weber numbers. It is clear from this graph that increasing the disturbance amplitude implies a decrease in the breakup length, for different Weber numbers. The other parameters are $\sigma = 1$, $\rho = 1$, $\chi = 0.5$ and $\epsilon = 0.01$.

3.9 Conclusions

In this chapter, we have investigated the instability of an inviscid compound liquid jet falling under the influence of gravity. We have used a slender jet approximation to determine a one dimensional model, which describes the velocity and radial displacements of the inner and outer free surfaces. We have solved the steady-state equations and investigated its dependence on changes in all the parameters of the model. In particular, we found that a decrease in the Froude number (or an increase in the gravity) causes the jet radii to decrease, while an increase in the Weber number (which could correspond to a decrease in the surface tension of the outer interface) leads to a more rapid decay of the jet radii along the jet. We have then considered the growth of unstable waves on the two interfaces by considering a linear temporal instability analysis. The obtained dispersion relation, which describes the relationship between the growth rate and wavenumber of disturbances, has been solved numerically in order to determine the most unstable wavenumber (which we assume to be the dominant wavenumber which leads to breakup) and the associated maximum growth rate. We have investigated how this most unstable wavenumber varies as we change key critical parameters, like the ratio of surface tension σ and the aspect ratio of inner jet radii χ. Diagrams showing how such changes in the parameters affect the most unstable mode, for different axial distances x along the jet, have been investigated to reveal that the most unstable wavenumber and maximum growth rates are larger as the wave travels down the jet. Furthermore, we found that the most unstable wavenumber decreases with an increase in χ, for different axial distances x, whilst the maximum growth rate decreases with an increase in ρ, and with a decrease in σ, for different axial distances x. Moreover, we found that a decrease in the interfacial surface tension ratio whereas an increase in the density ratio and the Weber

number causes the frequency and the transformed wavespeed of the disturbance to decrease, at $x = 0$. In addition, our results correspond to those given in Sanz & Meseguer (1985), for the case without gravity. We have also used the results from our linear theory to estimate the location of breakup and have shown that the breakup of the jet can occur by the inner jet rupturing first or by the outer interface touching the inner interface, and that the value of χ, at which these two processes occur simultaneously, become smaller as We is decreased. Finally, we have also compared our results favourably with numerical simulations found in Uddin & Decent (2010).

Chapter 4

Breakup, Droplet Formation and Temporal Instability Analysis of Shear Thinning Compound Jets Falling Under Gravity

4.1 Introduction

In this chapter, we perform a theoretical analysis to examine the breakup and droplet formation of an axisymmetric non-Newtonian, shear thinning compound liquid jet which falls vertically under the influence of gravity. We also first investigate the effect of physical parameters on the temporal instability of a non-Newtonian, shear thinning compound liquid jet that falls under the influence of gravity, extending the work of the previous Chapter 3 and also extending the work of Mohsin $et\ al.$ (2012). We use a long-wavelength, slender-jet asymptotic expansion to reduce the governing equations of the problem into a set of one dimensional partial differential equations, which describe the evolution of the

leading-order axial and radial velocity of the jet as well as the radii of both the inner and the outer interfaces. We first determine the steady-state solutions of the one dimensional model equations and then we perform a linear temporal instability analysis to obtain a dispersion relation, which gives us useful information about the maximum growth rate and the maximum wavenumber of the imposed wave-like disturbance. We next use the Lax-Wendroff method to determine the nonlinear temporal solution and we will compare our results with those found in Mohsin $et\ al.$ (2012) for the no-gravity case.

4.2 Model Equations

In order to derive the model equations of this problem, we make the same assumptions as in Section 3.2. The only differences are that now we are considering a non-Newtonian compound liquid jet and are taking $\mathbf{u}^{[i]} = (u^{[i]}, v^{[i]}, 0)$ as the velocity vector describing the jet flow. Here the superscript $i = 1$ is for the inner fluid and $i = 2$ is for the outer fluid.

The continuity equation and the Navier-Stokes equations for this problem are respectively given by

$$u_x^{[i]} + v_r^{[i]} + (v^{[i]}/r) = 0, \tag{4.1}$$

$$\rho_i(u_t^{[i]}+u^{[i]}u_x^{[i]}+v^{[i]}u_r^{[i]}) = -p_x^{[i]}+\eta_i(u_{xx}^{[i]}+\frac{1}{r}(ru_r^{[i]})_r)+2\eta_{ix}u_x^{[i]}+\eta_{ir}\left(v_x^{[i]} + u_r^{[i]}\right)+\rho_i g \tag{4.2}$$

and

$$\rho_i(v_t^{[i]}+u^{[i]}v_x^{[i]}+v^{[i]}v_r^{[i]}) = -p_r^{[i]}+\eta_i(v_{xx}^{[i]}+((rv_r^{[i]})_r/r)_r)+2\eta_{ir}v_r^{[i]}+\eta_{ix}\left(v_x^{[i]} + u_r^{[i]}\right). \tag{4.3}$$

Here η_i is the variable shear rate dependent viscosity and is defined, using the

Carreau model (see Carreau *et al.* (1979)), as

$$\eta_i = \tilde{\eta}_0^{[i]}[(1-\lambda_i)(1+(h\dot{\gamma}_{[i]})^2)^{\frac{n_i-1}{2}} + \lambda_i]. \tag{4.4}$$

Here $\dot{\gamma}_{[i]} = \sqrt{\boldsymbol{E} : \boldsymbol{E}/2}$, where $\mathbf{E}^{[i]} = \nabla \mathbf{u}^{[i]} + (\nabla \mathbf{u}^{[i]})^T$, $\tilde{\eta}_0$ is the zero-shear rate viscosity, h is a time constant, $\lambda\tilde{\eta}_0$ is the viscosity in the limit of infinite shear and n_i is the flow index number within each fluid.

The kinematic, tangential and normal stress boundary conditions, at the inner and the outer interfaces, and all of the rest of the analysis (i.e., non-dimensionalization and asymptotic expansions with notations $U = U_0, a = \mathcal{R}_0$ and $L = \mathcal{L}_0$) remain exactly the same as in Mohsin $et\ al.$ (2012). In addition, similar to Mohsin $et\ al.$ (2012), we also have the same parameters $\rho = \rho_1/\rho_2$ as the density ratio of the inner fluid to the outer fluid, $\sigma = \sigma_1/\sigma_2$ as the interfacial surface tension ratio, $\psi = \tilde{\eta}_0^{[1]}/\tilde{\eta}_0^{[2]}$ as the zero shear rate viscosity ratio, $\mathcal{R}e = \rho_2 LU/\tilde{\eta}_0^{[2]}$ as the Reynolds number and $We = \rho_2 U^2 a/\sigma_2$ as the Weber number (see Mohsin $et\ al.$ (2012), for more details). Moreover, we also have the same first two model equations, as in Mohsin $et\ al.$ (2012), as

$$(R_0^2)_t + (R_0^2\mathcal{U})_x = 0, \tag{4.5}$$

and

$$(S_0^2 - R_0^2)_t + ((S_0^2 - R_0^2)\mathcal{U})_x = 0, \tag{4.6}$$

where, using the slender jet assumption, that at leading-order, the axial velocities are independent of the radial direction r, and also using the no-slip condition, that for viscous fluids, the velocities are continuous at the shared interface $r = R(x,t)$, we wrote $u_0^{[i]} = \mathcal{U}_i(x,t) = \mathcal{U}(x,t)$.

The only difference in this case is that the axial equation of motion, for the

inner and outer fluids, at leading order, gives

$$\frac{\rho\mathcal{R}e}{\psi}\left(\mathcal{U}_t+\mathcal{U}\mathcal{U}_x+\frac{p_{0x}^{[1]}}{\rho}\right)-(\eta_1\mathcal{U}_{xx}+2\mathcal{U}_x\eta_{1x})=\frac{1}{r}\left(ru_{2r}^{[i]}\right)_r+\frac{\rho\mathcal{R}e}{\psi}\left(\frac{1}{F^2}\right) \quad (4.7)$$

and

$$\mathcal{R}e\left(\mathcal{U}_t+\mathcal{U}\mathcal{U}_x+p_{0x}^{[2]}\right)-(\eta_2\mathcal{U}_{xx}+2\mathcal{U}_x\eta_{2x})=\frac{1}{r}\left(ru_{2r}^{[i]}\right)_r+\mathcal{R}e\left(\frac{1}{F^2}\right). \quad (4.8)$$

These equations have general solutions for $u_2^{[1]}$ and $u_2^{[2]}$ in the form of,

$$u_2^{[i]}=Q_i(x,t)\frac{r^2}{4}+M_i(x,t)\log r+N_i(x,t), \quad (4.9)$$

for i=1,2. Here

$$Q_1(x,t)=\frac{\rho\mathcal{R}e}{\psi}\left(\mathcal{U}_t+\mathcal{U}\mathcal{U}_x+\frac{p_{0x}^{[1]}}{\rho}\right)-(\eta_1\mathcal{U}_{xx}+2\mathcal{U}_x\eta_{1x}), \quad (4.10)$$

and

$$Q_2(x,t)=\mathcal{R}e\left(\mathcal{U}_t+\mathcal{U}\mathcal{U}_x+p_{0x}^{[2]}\right)-(\eta_2\mathcal{U}_{xx}+2\mathcal{U}_x\eta_{2x}). \quad (4.11)$$

Here $M_i(x,t)$ and $N_i(x,t)$ are the functions of integration. Further more, we have the conditions in the inner fluid that

$$u_r^{[1]}(x,0,t)=0 \quad \text{and} \quad v^{[1]}(x,0,t)=0, \quad (4.12)$$

and this implies that $M_1=0$, otherwise we have a singular solution for $u_2^{[1]}$, as $r\to 0$ (as in Mohsin $et\ al.$ (2012)).

Similar to Mohsin $et\ al.$ (2012), the tangential stress condition at $r=S(x,t)$, at $O(\epsilon^2)$, gives that

$$2S_{0x}\left(v_{0r}^{[2]}-\mathcal{U}_x\right)+\left(u_{2r}^{[2]}+v_{0x}^{[2]}\right)=0, \quad (4.13)$$

which, after using equation (4.9) and $v_0^{[2]} = -r\mathcal{U}_x/2$ (see Mohsin $et\ al.$ (2012) for the derivation of this equation) gives

$$M_2 = 3S_0S_{0x}\mathcal{U}_x + \frac{S_0^2}{2}\mathcal{U}_{xx} - \frac{1}{2}S_0^2Q_2. \tag{4.14}$$

Similar to Mohsin $et\ al.$ (2012), the tangential stress condition at $r = R(x,t)$, at $O(\epsilon^2)$, gives that

$$\begin{aligned}\frac{\eta_2}{\psi\eta_1}\left(3R_0R_{0x}\mathcal{U}_x + \frac{R_0^2}{2}\mathcal{U}_{xx} - \frac{R_0^2}{2}Q_2 - M_2\right)\\ = 3R_0R_{0x}\mathcal{U}_x + \frac{R_0^2}{2}\mathcal{U}_{xx} - \frac{R_0^2}{2}Q_1.\end{aligned} \tag{4.15}$$

Using the values of Q_1, Q_2 and M_2 in equation (4.15), we get

$$\begin{aligned}\left[S_0^2 + (\rho-1)R_0^2\right](\mathcal{U}_t + \mathcal{U}\mathcal{U}_x) = -\frac{1}{We}\left[\left(S_0^2 - R_0^2 + \frac{R_0^2}{\rho}\right)\kappa_{2x} + \left(\frac{\sigma R_0^2}{\rho}\right)\kappa_{1x}\right]\\ + \frac{\psi}{\mathcal{R}e}\left[3(R_0^2)_x\mathcal{U}_x\eta_1 + \left(2+\frac{1}{\rho}\right)R_0^2(\mathcal{U}_x\eta_1)_x\right] + \frac{3}{\mathcal{R}e}\left[(S_0^2 - R_0^2)\mathcal{U}_x\eta_2\right]_x\\ + \left[S_0^2 + (\rho-1)R_0^2\right]\left(\frac{1}{F^2}\right).\end{aligned} \tag{4.16}$$

Therefore, equations (4.5), (4.6) and (4.16) are the model equations for R_0, S_0 and $\mathcal{U}$. We note that for the no gravity case (i.e., in the limit of $F \to \infty$, as $g = 0$), we get the same equations, as found in Mohsin $et\ al.$ (2012).

In addition, similar to Chapter 3, we have the boundary conditions, at the nozzle $x = 0$, as

$$\mathcal{U}(0,t) = S(0,t) = 1 \quad \text{and} \quad R(0,t) = \chi, \ \text{ where } \ 0 < \chi < 1.$$

We know that $F = U/\sqrt{Lg}$ is the Froude number and L is a characteristic wavelength in the axial (or vertical) direction. Similar to Chapter 3, an appropriate

choice for this length scale L in the vertical direction, is given by $L = U^2/g$ and so F has the value of unity. Since this choice of L is a natural length scale in this problem, we henceforth use $F = 1$ throughout this chapter (apart from the steady-state solutions, where we vary all the parameters of the problem, as we did in Chapter 3).

4.3 Steady-State Solution

We define $\mathcal{U}_0$, R_0 and S_0 as the steady-state solution of model equations (4.5), (4.6) and (4.16) respectively. Similar to Chapter 3, by making use of the boundary conditions at $x = 0$, i.e., $\mathcal{U}_0(0) = S_0(0) = 1 \text{ and } R_0(0) = \chi$, we can write equations (4.5) and (4.6) as

$$R_0 = \frac{\chi}{\sqrt{\mathcal{U}_0}} \quad \text{and} \quad S_0 = \sqrt{\frac{1}{\mathcal{U}_0}}. \tag{4.17}$$

Therefore, after substituting the values for R_0 and S_0, from equation (4.17) into equation (4.16), we end up with one equations in one unknown $\mathcal{U}_0$.

We solve the above nonlinear system of steady-state equations (4.16)-(4.17) using Newton's method and present the solutions in following figures. In Figures 4.1 – 4.6, we plot the steady-state solution for the inner and the outer jet radii and velocity, for various density ratios, Weber numbers and Reynolds number. We observe that an increase in the density ratio (which could correspond to a decrease in the density of the outer fluid), Weber number (which could correspond to a decrease in the surface tension of the outer interface) and Reynolds number leads to a more rapid decay of the jet radii and rapid increase of the jet velocity along the jet. In Figures 4.7 – 4.12, we plot the steady-state solution for the inner and the outer jet radii and velocity, for various Froude numbers, surface tension ratios and zero shear rate viscosity ratios. We observe that an increase in the Froude number (which corresponds to a decrease in the gravity), surface tension ratio and

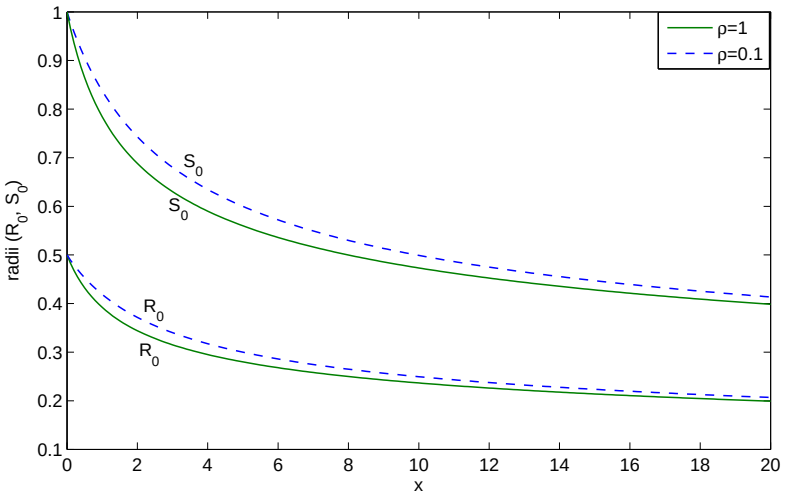

Figure 4.1: The steady-state solution for the inner and the outer jet radii, for various density ratios. It can be seen that an increase in the density ratio causes the jet radii to decrease. The other parameters are $F = 1$, $\mathcal{R}e = 10$, $We = 10$, $\sigma = 1$, $\chi = 0.5$, $\psi = 0.5$, $\lambda_1 = 0.1$, $\lambda_2 = 0.1$, $h = 1$, $n_1 = 0.5$ and $n_2 = 1$.

zero shear rate viscosity ratio leads to a more rapid increase of the jet radii and rapid decrease of the jet velocity along the jet. We note, from these figures, that the velocity of the jet increases while the radii decreases as we increase ρ, We and $\mathcal{R}e$ and decrease F, σ and ψ. In Figure 4.13, we plot the steady-state solution for the inner and the outer jet radii, for various flow index numbers and find that as the compound jet is made more shear thinning, the jet radii decrease.

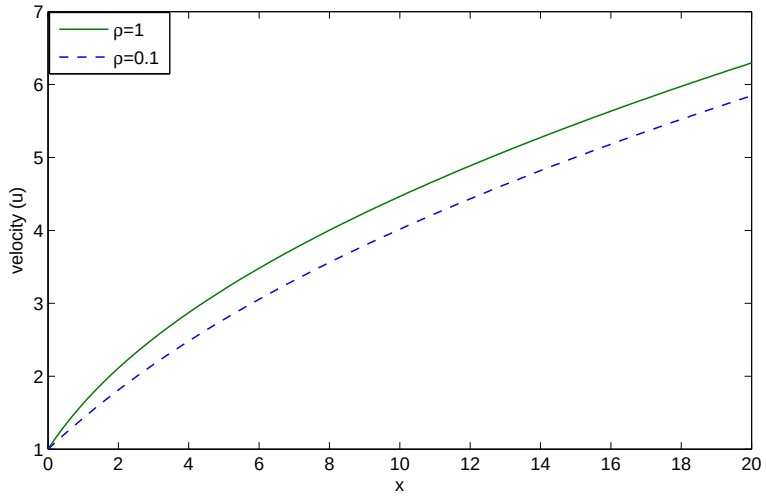

Figure 4.2: The steady-state solution for the inner and the outer jet velocity, for various density ratios. It can be seen that an increase in the density ratio causes the jet velocity to increase. The other parameters are $F = 1$, $\mathcal{R}e = 10$, $We = 10$, $\sigma = 1$, $\chi = 0.5$, $\psi = 0.5$, $\lambda_1 = 0.1$, $\lambda_2 = 0.1$, $h = 1$, $n_1 = 0.5$ and $n_2 = 1$.

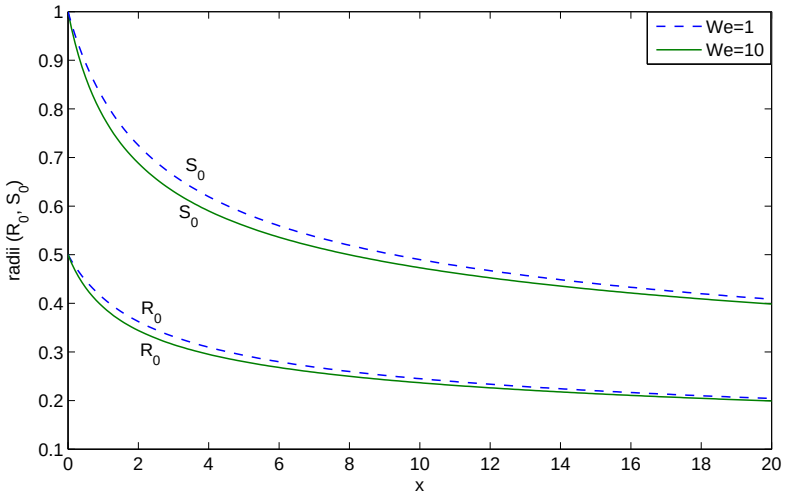

Figure 4.3: The steady-state solution for the inner and the outer jet radii, for various Weber numbers. It can be seen that an increase in the Weber number causes the jet radii to decrease. The other parameters are $F = 1$, $\mathcal{R}e = 10$, $\rho = 1$, $\sigma = 1$, $\chi = 0.5$, $\psi = 0.5$, $\lambda_1 = 0.1$, $\lambda_2 = 0.1$, $h = 1$, $n_1 = 0.5$ and $n_2 = 1$.

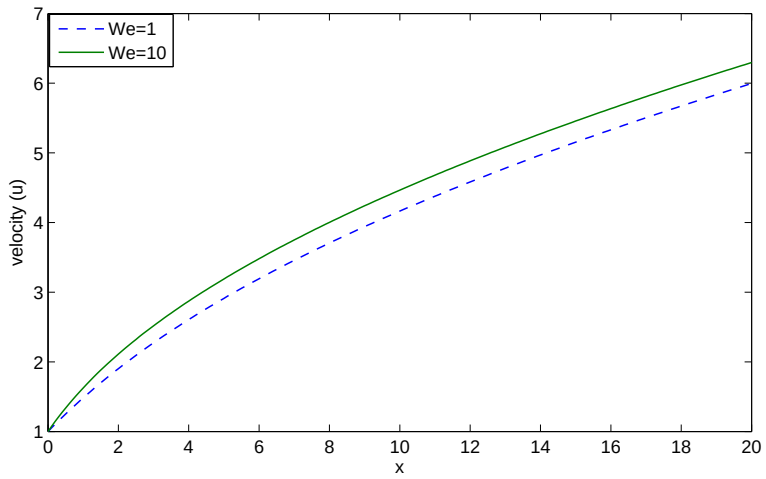

Figure 4.4: The steady-state solution for the inner and the outer jet velocity, for various Weber numbers. It can be seen that an increase in the Weber number causes the jet velocity to increase. The other parameters are $F = 1$, $\mathcal{R}e = 10$, $\rho = 1$, $\sigma = 1$, $\chi = 0.5$, $\psi = 0.5$, $\lambda_1 = 0.1$, $\lambda_2 = 0.1$, $h = 1$, $n_1 = 0.5$ and $n_2 = 1$.

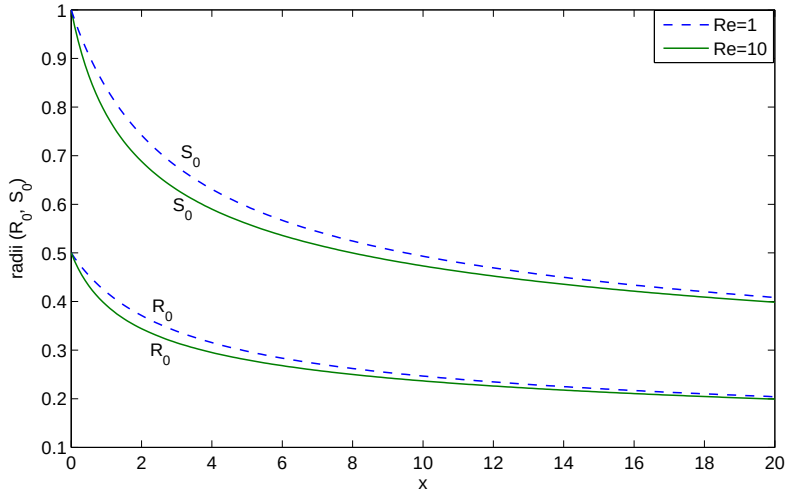

Figure 4.5: The steady-state solution for the inner and the outer jet radii, for various Reynolds numbers. It can be seen that an increase in the Reynolds number causes the jet radii to decrease. The other parameters are $F = 1$, $We = 10$, $\rho = 1$, $\sigma = 1$, $\chi = 0.5$, $\psi = 0.5$, $\lambda_1 = 0.1$, $\lambda_2 = 0.1$, $h = 1$, $n_1 = 0.5$ and $n_2 = 1$.

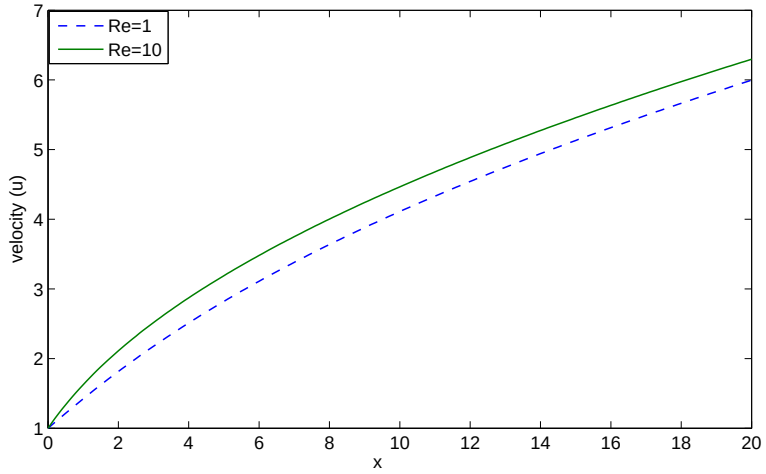

Figure 4.6: The steady-state solution for the inner and the outer jet velocity, for various Reynolds numbers. It can be seen that an increase in the Reynolds number causes the jet velocity to increase. The other parameters are $F = 1$, $We = 10$, $\rho = 1$, $\sigma = 1$, $\chi = 0.5$, $\psi = 0.5$, $\lambda_1 = 0.1$, $\lambda_2 = 0.1$, $h = 1$, $n_1 = 0.5$ and $n_2 = 1$.

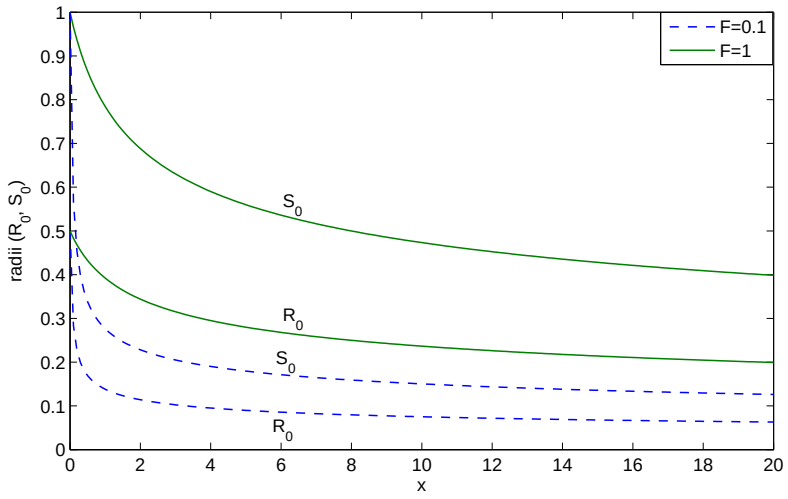

Figure 4.7: The steady-state solution for the inner and the outer jet radii, for various Froude numbers. It can be seen that a decrease in the Froude number (which corresponds to an increase in the gravity) causes the jet radii to decrease. The other parameters are $We = 10$, $\mathcal{R}e = 10$, $\rho = 1$, $\sigma = 1$, $\chi = 0.5$, $\psi = 0.5$, $\lambda_1 = 0.1$, $\lambda_2 = 0.1$, $h = 1$, $n_1 = 0.5$ and $n_2 = 1$.

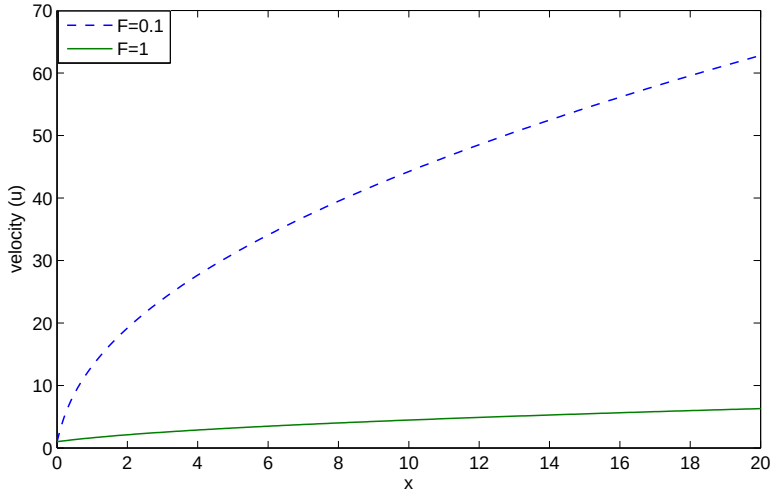

Figure 4.8: The steady-state solution for the inner and the outer jet velocity, for various Froude numbers. It can be seen that a decrease in the Froude number (which corresponds to an increase in the gravity) causes the jet velocity to increase. The other parameters are $We = 10$, $\mathcal{R}e = 10$, $\rho = 1$, $\sigma = 1$, $\chi = 0.5$, $\psi = 0.5$, $\lambda_1 = 0.1$, $\lambda_2 = 0.1$, $h = 1$, $n_1 = 0.5$ and $n_2 = 1$.

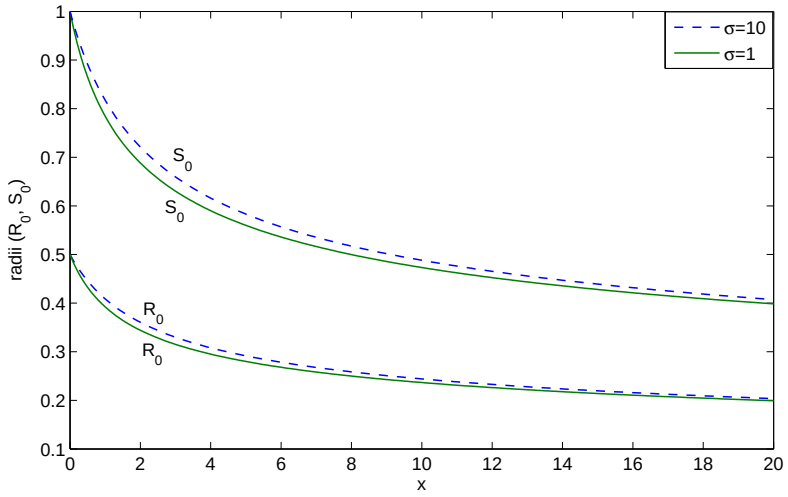

Figure 4.9: The steady-state solution for the inner and the outer jet radii, for various surface tension ratios. It can be seen that an increase in the surface tension ratio causes the jet radii to increase. The other parameters are $F = 1$, $We = 10$, $\mathcal{R}e = 10$, $\rho = 1$, $\chi = 0.5$, $\psi = 0.5$, $\lambda_1 = 0.1$, $\lambda_2 = 0.1$, $h = 1$, $n_1 = 0.5$ and $n_2 = 1$.

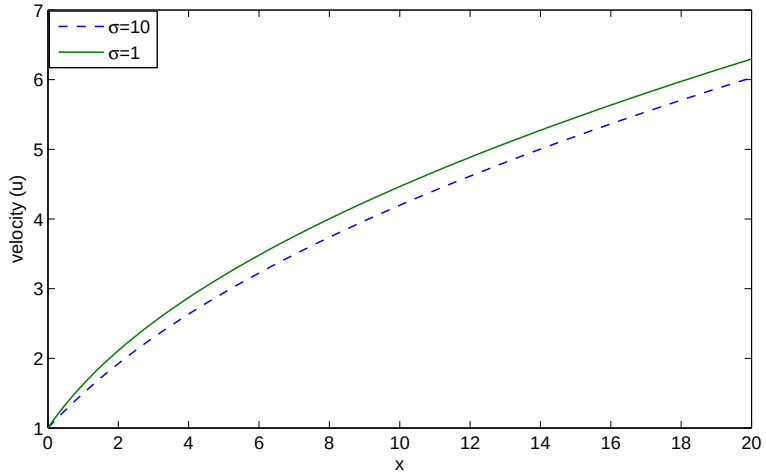

Figure 4.10: The steady-state solution for the inner and the outer jet velocity, for various surface tension ratios. It can be seen that an increase in the surface tension ratio causes the jet velocity to decrease. The other parameters are $F = 1$, $We = 10$, $\mathcal{R}e = 10$, $\rho = 1$, $\chi = 0.5$, $\psi = 0.5$, $\lambda_1 = 0.1$, $\lambda_2 = 0.1$, $h = 1$, $n_1 = 0.5$ and $n_2 = 1$.

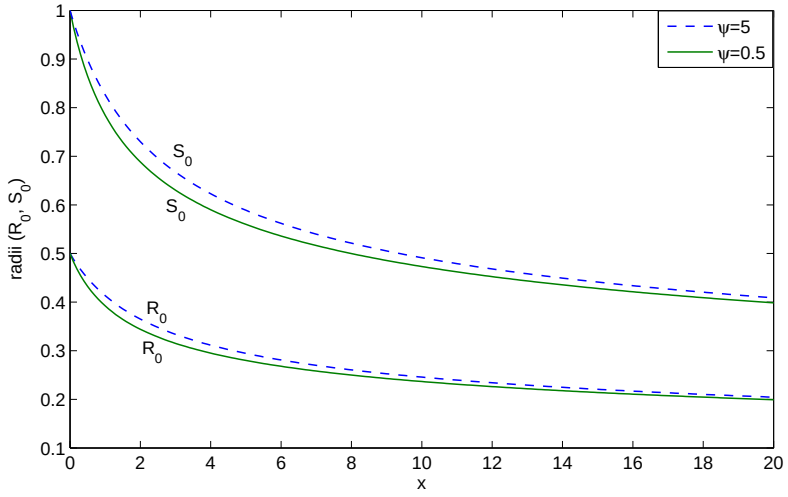

Figure 4.11: The steady-state solution for the inner and the outer jet radii, for various zero shear rate viscosity ratios ψ. It can be seen that an increase in ψ causes the jet radii to increase. The other parameters are $F = 1$, $We = 10$, $\mathcal{R}e = 10$, $\rho = 1$, $\sigma = 1$, $\chi = 0.5$, $\lambda_1 = 0.1$, $\lambda_2 = 0.1$, $h = 1$, $n_1 = 0.5$ and $n_2 = 1$.

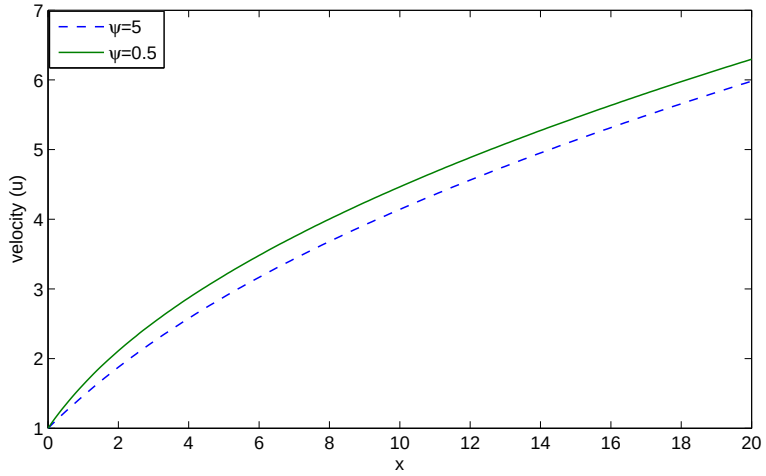

Figure 4.12: The steady-state solution for the inner and the outer jet velocity, for various zero shear rate viscosity ratios ψ. It can be seen that an increase in ψ causes the jet velocity to decrease. The other parameters are $F = 1$, $We = 10$, $\mathcal{R}e = 10$, $\rho = 1$, $\sigma = 1$, $\chi = 0.5$, $\lambda_1 = 0.1$, $\lambda_2 = 0.1$, $h = 1$, $n_1 = 0.5$ and $n_2 = 1$.

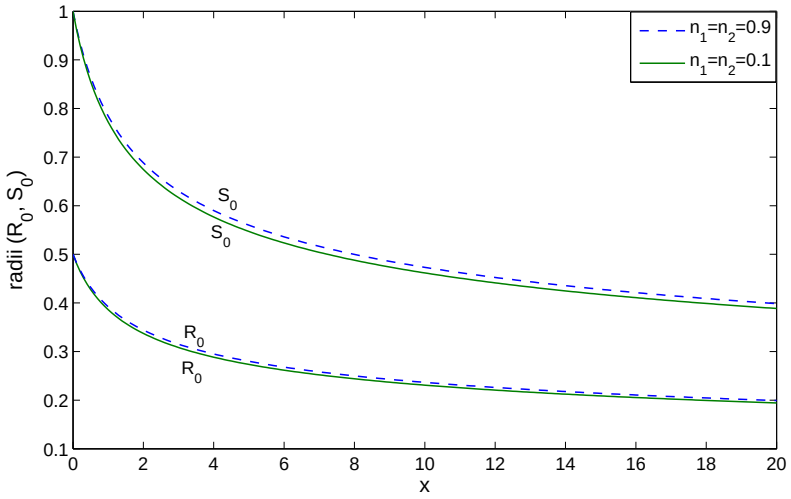

Figure 4.13: The steady-state solution for the inner and the outer jet radii, for various flow index numbers. It can be seen that as the compound jet is made more shear thinning, the jet radii decrease. The other parameters are $F = 1$, $We = 10$, $\mathcal{R}e = 10$, $\rho = 1$, $\sigma = 1$, $\chi = 0.5$, $\psi = 0.5$, $\lambda_1 = 0.1$, $\lambda_2 = 0.1$ and $h = 1$.

4.4 Linear Temporal Instability Analysis

We now investigate the instability of a non-Newtonian shear thinning compound jet by performing a linear temporal instability analysis. Similar to Chapter 3, we consider travelling short-wavelength modes (or short waves) of the form $\exp(\omega\bar{t}+ ik\bar{x})$, where $\bar{t} = t/\epsilon$ and $\bar{x} = x/\epsilon$ are small length and time scales. In addition, $\omega = \omega(x) = O(1)$ and $k = k(x) = O(1)$ are the frequency and the wavenumber of the disturbance. We perturb the steady-state solution by a small time-dependent, short-wave disturbance and assume

$$\mathcal{U} = \mathcal{U}_0(x) + \delta \exp(\omega\bar{t} + ik\bar{x})\hat{\mathcal{U}}_1, \tag{4.18}$$

$$R = R_0(x) + \delta \exp(\omega\bar{t} + ik\bar{x})\hat{R}_1, \tag{4.19}$$

$$S = S_0(x) + \delta \exp(\omega\bar{t} + ik\bar{x})\hat{S}_1, \tag{4.20}$$

where $\delta << \epsilon$. We substitute equations (4.18)-(4.20) into equations (4.26) – (4.28) and we use the full curvature terms in order to prevent instability of waves with zero wavenumber, as we did in the previous chapter (see Brenner $et\ al.$ (1997) for more details). This yields, at leading order, our steady-state equations. At next order $O(\delta/\epsilon)$, we obtain a set of three equations, namely

$$\left(ikR_0^2\right)\hat{\mathcal{U}}_1 + \left(2R_0(\omega + ik\mathcal{U}_0)\right)\hat{R}_1 = 0, \tag{4.21}$$

$$\left(ik(S_0^2 - R_0^2)\right)\hat{\mathcal{U}}_1 - \left(2\omega R_0 + 2ikR_0\mathcal{U}_0\right)\hat{R}_1$$

$$+ \left(2\omega S_0 + 2ikS_0\mathcal{U}_0\right)\hat{S}_1 = 0 \tag{4.22}$$

and

$$(\zeta)\,\hat{\mathcal{U}}_1 + (\alpha)\,\hat{R}_1 + (\beta)\,\hat{S}_1 = 0, \tag{4.23}$$

where

$$\begin{aligned}\zeta = (\omega + ik\mathcal{U}_0)a_1 - (\psi/\mathcal{R}e)[6ikR_0R_{0,x}d_1 + (2+\rho^{-1})ikR_0^2f_1 + 6ikb_1R_0R_{0,x}(\mathcal{U}_{0,x})^2 \\ +(2+\rho^{-1})(ikb_1R_0^2\mathcal{U}_{0,x}\mathcal{U}_{0,xx} + R_0^2\mathcal{U}_{0,x}e_1)] \\ -(3/\mathcal{R}e)[2ika_5(d_2 + b_2(\mathcal{U}_{0,x})^2) + a_6(ikf_2 + ikb_2\mathcal{U}_{0,x}\mathcal{U}_{0,xx} + \mathcal{U}_{0,x}e_2)],\end{aligned}$$

$$\alpha = \frac{\sigma R_0^2 a_4}{\rho We} - \frac{6ik\psi d_1 R_0\mathcal{U}_{0,x}}{\mathcal{R}e} + \frac{6ikd_2R_0\mathcal{U}_{0,x}}{\mathcal{R}e}$$

and

$$\beta = \frac{a_2a_3}{We} - \frac{6ikd_2S_0\mathcal{U}_{0,x}}{\mathcal{R}e}.$$

Here

$$a_1 = (S_0)^2 + (\rho-1)(R_0)^2, \quad a_2 = (S_0)^2 + (\rho^{-1}-1)(R_0)^2,$$

$$a_3 = \left(\frac{-ik}{S_0^2} + ik^3\right), \quad a_4 = \left(\frac{-ik}{R_0^2} + ik^3\right),$$

$$a_5 = S_0S_{0,x} - R_0R_{0,x}, \quad a_6 = S_0^2 - R_0^2,$$

$$b_1 = 3h^2(1-\lambda_1)(n_1-1), \quad b_2 = 3h^2(1-\lambda_2)(n_2-1),$$

$$c_1 = 3h^2(n_1-3), \quad c_2 = 3h^2(n_2-3),$$

$$d_1 = (1-\lambda_1)\left(1 + 3h^2\left(\frac{n_1-1}{2}\right)(\mathcal{U}_{0,x})^2\right) + \lambda_1,$$

$$d_2 = (1-\lambda_2)\left(1 + 3h^2\left(\frac{n_2-1}{2}\right)(\mathcal{U}_{0,x})^2\right) + \lambda_2,$$

$$e_1 = ikb_1\mathcal{U}_{0,xx}(1 + c_1(\mathcal{U}_{0,x})^2),$$

$$e_2 = ikb_2\mathcal{U}_{0,xx}(1 + c_2(\mathcal{U}_{0,x})^2),$$

$$f_1 = \left(1 + \frac{c_1(\mathcal{U}_{0,x})^2}{2}\right) b_1\mathcal{U}_{0,x}\mathcal{U}_{0,xx}$$

and

$$f_2 = \left(1 + \frac{c_2(\mathcal{U}_{0,x})^2}{2}\right) b_2\mathcal{U}_{0,x}\mathcal{U}_{0,xx}.$$

We define

$$\omega' = \omega + ik\mathcal{U}_0, \tag{4.24}$$

which in effect moves us into a frame of reference which moves with the jet velocity $\mathcal{U}_0$.

Equations (4.21)-(4.23), after using (4.24), can be written in matrix form as

$$\begin{pmatrix} ikR_0^2 & 2R_0\omega' & 0 \\ ika_6 & -2R_0\omega' & 2S_0\omega' \\ \zeta & \alpha & \beta \end{pmatrix} \cdot \begin{pmatrix} \hat{\mathcal{U}}_1 \\ \hat{R}_1 \\ \hat{S}_1 \end{pmatrix} = \begin{pmatrix} 0 \\ 0 \\ 0 \end{pmatrix}.$$

For the above system to have a non-trivial solution, we require that the determinant of the matrix to be zero, and, therefore, we obtain

$$\begin{aligned}(4R_0S_0a_1)(\omega')^2 + 2S_0[(-2\psi/\mathcal{R}e)\{6ikR_0^2R_{0,x}d_1 + (2+\rho^{-1})ikR_0^2f_1 \\ +6ikb_1R_0^2R_{0,x}(\mathcal{U}_{0,x})^2 + (2+\rho^{-1})(ikb_1R_0^3\mathcal{U}_{0,x}\mathcal{U}_{0,xx} + R_0^3\mathcal{U}_{0,x}e_1)\} \\ -(6R_0/\mathcal{R}e)\{2ika_5(d_2 + b_2(\mathcal{U}_{0,x})^2) + a_6(ikf_2 + ikb_2\mathcal{U}_{0,x}\mathcal{U}_{0,xx} + \mathcal{U}_{0,x}e_2)\}](\omega') \\ + \left[2S_0\left(\frac{6k^2R_0^3\mathcal{U}_{0,x}}{\mathcal{R}e}(d_2 - \psi d_1) - \frac{ik\sigma R_0^4a_4}{\rho We}\right) + \{2ikR_0(R_0^2 + a_6)\}\left(\frac{6ikd_2S_0\mathcal{U}_{0,x}}{\mathcal{R}e} - \frac{a_2a_3}{We}\right)\right] \\ = 0,\end{aligned} \tag{4.25}$$

which is our required dispersion relation.

At $x = 0$ (i.e., at the nozzle), we have the no-gravity case and we have

$$\mathcal{U}_0 = S_0 = 1 \text{ and } R_0 = \chi$$

as our constant steady-state solutions. Therefore, for the no-gravity case, we will have the same dispersion relation (4.25), with all the derivatives of $\mathcal{U}_0, R_0$ and S_0 being zero.

4.5 Results and discussion

The dispersion relation (4.25) relates ω' to the wavenumber k. For a given value of k, the equation is seen to be a quadratic equation in ω', with coefficients depending on x, the axial distance along the jet. Subsequently, by choosing a value of x and evaluating these coefficients at this particular value, our equation becomes a quadratic equation in ω', with constant coefficients, which may be solved using quadratic formula. An example of solving (4.25), for a value of x and for different k, is shown in Figure 4.14, where the two solutions of (4.25) are shown, of which one is a growing modes (i.e., where $Re(\omega') > 0$ and is unstable) and it is typically assumed that breakup of the jet is caused by this mode with the largest growth rate and, throughout this work, we will focus our attention on this mode and we refer to it as $the\ most\ unstable\ mode$. In such a case, it can be seen that there is a value of the wavenumber k, at which the growth rate is maximal - we refer to this value as $the\ most\ unstable\ wavenumber$ and denote it by k_{max}. The significance of this value of k_{max} is that breakup of the jet is caused by a wave having this wavenumber and so the resulting droplets will scale with this value of k and, in particular, we would expect droplets to become smaller for larger k_{max}. A plot of such most unstable modes for different parameters is investigated in following figures. Since the steady-state values of radii and velocities of the jet vary along x, we see that we have different k_{max} for different axial distances x along the jet.

This change is demonstrated in Figures 4.15 – 4.26, for different parameters of the problem. In Figures 4.15 – 4.26, we plot growth rate versus wavenumber of the disturbance, for a given parameter, at the nozzle, then maximum wavenumber versus the axial distance, for that parameter and next maximum growth rate versus the axial distance, for that parameter.

From Figures 4.15 and 4.16, we find that a decrease in the Weber number causes the maximum wavenumber of the disturbance to decrease while causes the maximum growth rate of the disturbance to increase, for different values of x. Moreover, for a given We, both k_{max} and $[Re(\omega')]_{max}$ decrease, as x decreases. Note that, at $x = 0$, we don't have a constant k_{max} for various We (as in inviscid case). This is due to the fact that for viscous case, $k = f(We)$, as found in Uddin (2007). Due to the shear thinning (or viscosity) factor, we find that k_{max} is directly proportional to We, in particular at $x = 0$, which was also found in Liao $et\ al.$ (2000) and Yang $et\ al.$ (2012). From Figures 4.17 and 4.18, we find that a decrease in the Reynolds number causes both the maximum wavenumber and the maximum growth rate of the disturbance to increase, for different values of x. Moreover, for a given $\mathcal{R}e$, both k_{max} and $[Re(\omega')]_{max}$ decrease as x decreases. We note that for $\mathcal{R}e < 12$, the maximum growth rate at $x = 4$, is slightly less than the corresponding maximum growth rates at $x = 0$ and at $x = 2$. However, this behaviour is reversed for $\mathcal{R}e > 12$. From Figures 4.19 and 4.20, we find that a decrease in the density ratio causes the maximum wavenumber of the disturbance to decrease for $x < 1.8$ while after $x = 1.8$, this behaviour is reversed. We also observe that a decrease in the density ratio causes the maximum growth rate of the disturbance to increase, although for large ρ, the difference in $[Re(\omega')]_{max}$ is slightly small (as shown in Figure 4.20(b)). We further note that as we increase ρ, $x = 0$ curve increases, $x = 4$ curve decreases, while $x = 1.8$ curve remains constant. This shows that the transition of the different behaviour of k_{max} at $x = 0$

and $x = 4$ curves occurs at $x = 1.8$ curve. This transition takes place due to the characteristic behaviour of ρ, for these set of parameters. From Figures 4.21 and 4.22, we find that a decrease in the interfacial surface tension ratio σ causes both the maximum wavenumber and the maximum growth rate of the disturbance to decrease, for different values of x. Moreover, for a given σ, both k_{max} and $[Re(\omega')]_{max}$ decrease as x decreases. In addition, we found that there does not exists any discontinuity (or transition) in k_{max} against σ in this case, as found in inviscid-gravity case. This may be due to the fact that in this case, we have only one velocity, whereas, in the inviscid case, we have two different velocities. From Figures 4.23 and 4.24, we find that a decrease in the zero shear rate viscosity ratio ψ causes both the maximum wavenumber and the maximum growth rate of the disturbance to decrease, although for large ψ, the difference in $[Re(\omega')]_{max}$ is relatively small. Moreover, for a given ψ, both k_{max} and $[Re(\omega')]_{max}$ decrease as x decreases. From Figure 4.25, we find that a decrease in the inner jet radius χ causes both the maximum wavenumber and the maximum growth rate of the disturbance to increase. Moreover, for a given χ, both k_{max} and $[Re(\omega')]_{max}$ decrease as x decreases. From Figure 4.26, we find that as the compound jet is made more shear thinning (i.e., as flow index numbers n_1 and n_2 are decreased), both the maximum wavenumber and the maximum growth rate of the disturbance decrease. That is, as the compound jet is made more shear thinning, we get more stable jets (i.e., we get more smaller disturbance curve). Moreover, for a given n_1 and n_2, both k_{max} and $[Re(\omega')]_{max}$ increase as x increases.

In Figure 4.27, we plot a diagram to show how changing the surface tension ratio σ and the parameter χ affect the wavenumber of the most unstable mode together with the associated maximal growth rate of this mode. Figure 4.27 consists of a set of points which represent the values of inverse maximum wavenumber $(k_{max})^{-1}$ and associated maximum growth rate $[Re(\omega')]_{max}$, obtained when all

parameters are kept fixed, except either σ or χ. Here we consider the parameter space $0.3 < \chi < 0.8$ and $0.5 < \sigma < 5$. Together, this constitutes a map of different maximum wavenumbers and associated maximum growth rates, as σ and χ are varied. We have chosen to plot the inverse wavenumber with growth rate as this is consistent with the work of our previous chapter and with the work of Sanz & Meseguer (1985) but we note that here, unlike in Sanz & Meseguer (1985), we plot only the largest or most unstable wavemode (as we did in our previous chapter) with the reasoning that this mode is responsible for breakup. There are two sets of curves shown in Figure 4.27 which are drawn firstly by fixing χ and varying σ. With reference to all such figures (Figures 4.27 and 4.28) of this nature, these curves represent fixed χ for different σ, with χ increasing as one moves from left to right with the value of χ being represented by the solid lines used in the figure. Curves obtained by fixing σ but varying χ are shown as dashed lines in Figure 4.27 and for all values of σ, such curves are continuous in nature.

Since the jet is accelerating downwards in the vertical direction, the steady-state solution is a function of the vertical distance x from the nozzle. This, in turn, affects the coefficients of our dispersion relation and we, therefore, see differences in the relationship between the most unstable wavenumber and its associated growth rate, as we move down the jet. Figure 4.27 shows three such cases which correspond to $x = 0$, $x = 2$ and $x = 4$. A careful examination of the curves presented in Figure 4.27 (for example one may compare extreme values of the maximal growth rate and most unstable or maximum wavenumber for a fixed value of χ, for three different axial distances) reveals that, for the parameter ranges considered here, $(k_{max})^{-1}$ decreases as x increases, that is, the maximum wavenumber increases for any given χ and for all σ, as x increases. Moreover, the associated growth rates are also larger for a given χ and σ, as x increases. This indicates that breakup lengths and droplet sizes are likely to be smaller for a shear

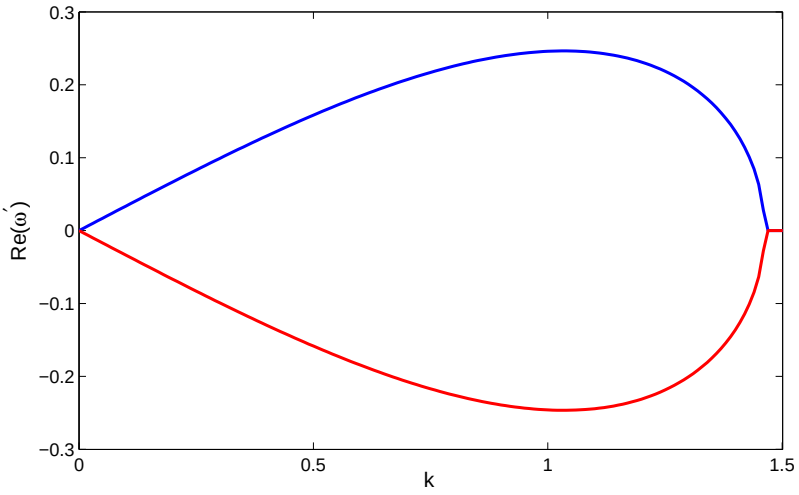

Figure 4.14: The solutions of dispersion relation (4.25), with only the real part plotted, which represents two growth rates of the disturbance versus wavenumber, at $x = 0$. The parameters, used here, are $F = 1$, $We = 10$, $Re = 50$, $\rho = 1$, $\sigma = 0.5$, $\chi = 0.5$, $\psi = 1$, $\lambda_1 = 0.1$, $\lambda_2 = 0.1$, $h = 1$, $n_1 = 0.5$ and $n_2 = 0.9$. These parameters will be our base case parameters for the rest of the figures.

thinning compound liquid jet falling under gravity.

From Figures 4.27 and 4.28, we find that as we increase ρ, $[Re(\omega')]_{max}$ decreases at $x = 0, 2, 4$, while k_{max} increases at $x = 0$ and decreases at $x = 2, 4$. This is the same qualitative behaviour which was observed before in Figures 4.19 and 4.20. We also find, from these two Figures 4.27 and 4.28, that both maximum wavenumber k_{max} and maximum growth rate $[Re(\omega')]_{max}$ increase, as x increases. Furthermore, we find from these two figures that both maximum wavenumber k_{max} and maximum growth rate $[Re(\omega')]_{max}$ increase as we increase σ, for $\chi = 0.5$, a qualitative behaviour which is also found before in Figures 4.21 and 4.22, for $\chi = 0.5$, but this time, for larger values of We and $\mathcal{R}e$, and for smaller values of n_1 and n_2.

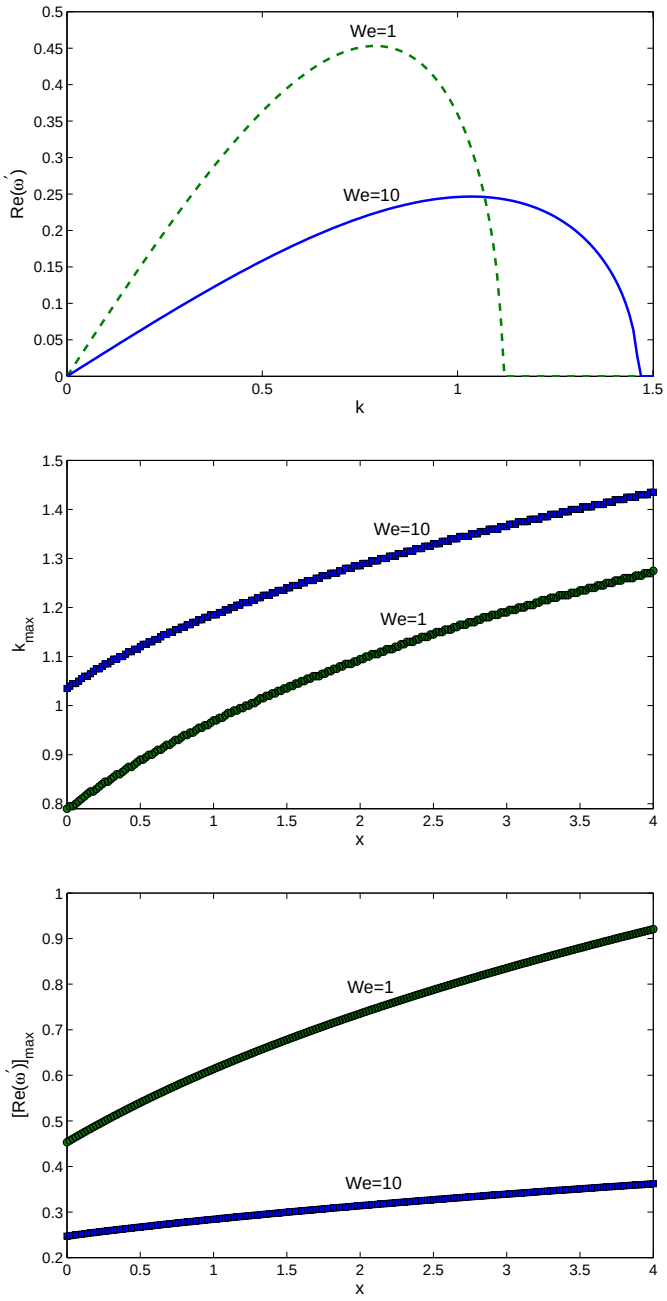

Figure 4.15: Top: Growth rate $Re(\omega')$ versus wavenumber k of the disturbance, for different We, at $x = 0$. Middle: k_{max} versus axial distance x, for different We. Bottom: $[Re(\omega')]_{max}$ versus x, for different We. It can be seen that a decrease in We causes k_{max} to decrease while causes $[Re(\omega')]_{max}$ to increase. The other parameters are the same as in the previous Figure 4.14.

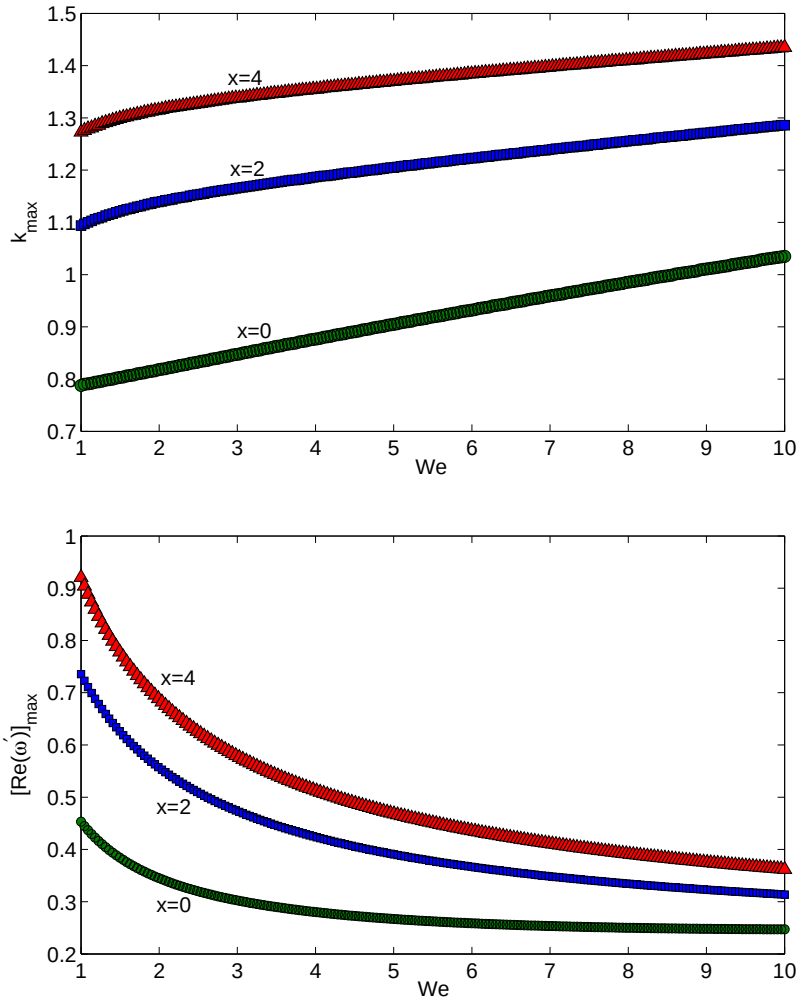

Figure 4.16: Top: Maximum wavenumber k_{max} against the Weber number We, for different values of x. Bottom: Maximum growth rate $[Re(\omega')]_{max}$ versus the Weber number, for different values of x. It can be seen that a decrease in the Weber number causes the maximum wavenumber of the disturbance to decrease while causes the maximum growth rate of the disturbance to increase, for different values of x. Note that, at $x = 0$, we don't have a constant k_{max} for various We (as in inviscid case). This is due to the fact that for viscous case, $k = f(We)$, as found in Uddin (2007). Due to the shear thinning (or viscosity) factor, we find that $k_{max} \propto We$, in particular at $x = 0$, which was also found in Liao $et\ al.$ (2000) and Yang $et\ al.$ (2012). The other parameters are the same as in Figure 4.14.

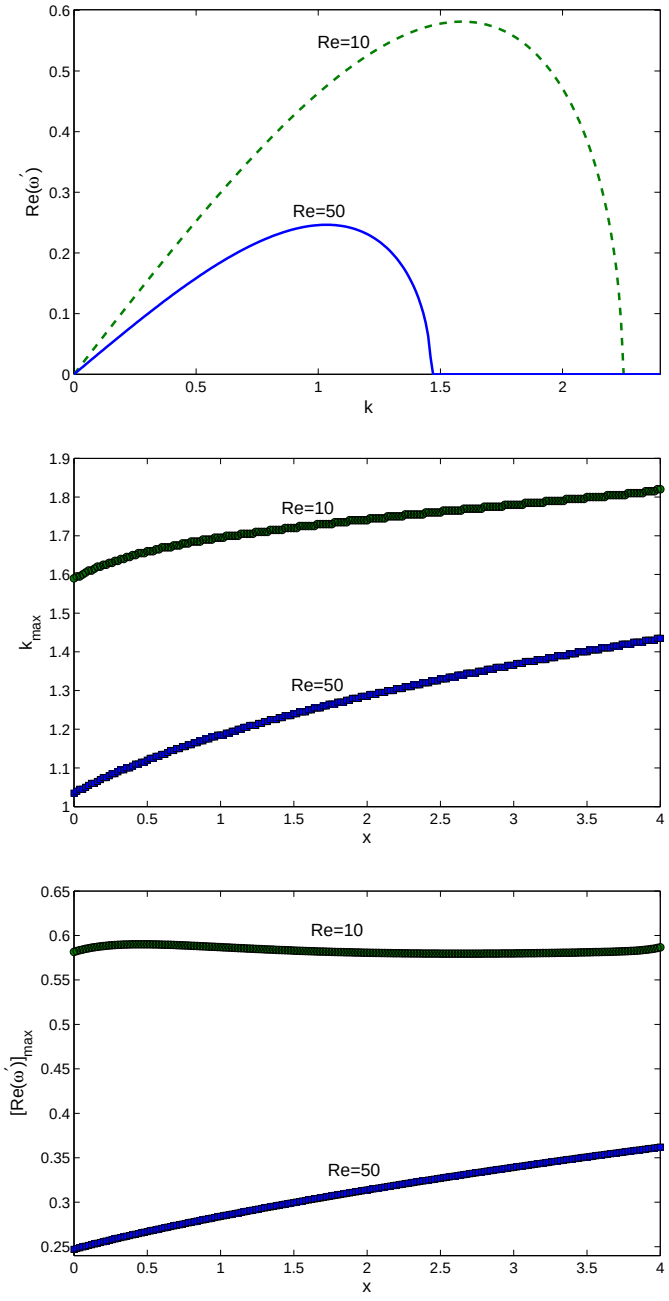

Figure 4.17: Top: Growth rate $Re(\omega')$ versus wavenumber k of the disturbance, for different $\mathcal{R}e$, at $x = 0$. Middle: k_{max} versus x, for different $\mathcal{R}e$. Bottom: $[Re(\omega')]_{max}$ versus x, for different $\mathcal{R}e$. It can be seen that a decrease in the Reynolds number causes both k_{max} and $[Re(\omega')]_{max}$ to increase. The other parameters are the same as in Figure 4.14.

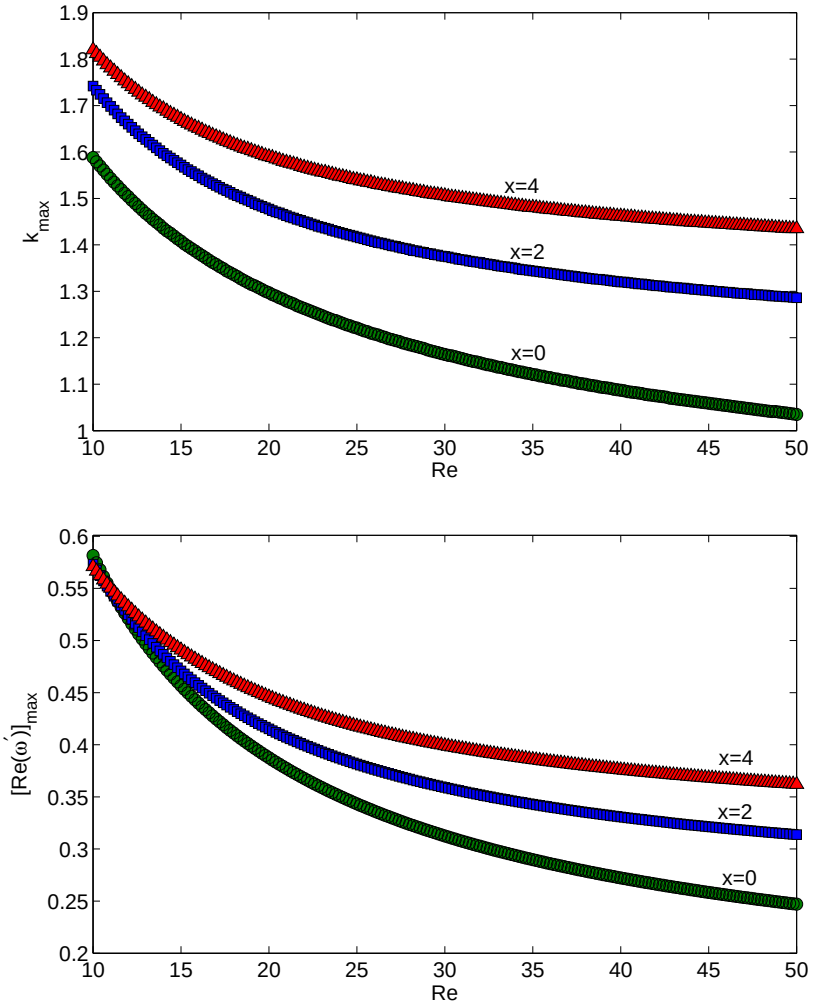

Figure 4.18: Top: Maximum wavenumber k_{max} against the Reynolds number $\mathcal{R}e$, for different values of x. Bottom: Maximum growth rate $[Re(\omega')]_{max}$ versus $\mathcal{R}e$, for different values of x. It can be seen that a decrease in the Reynolds number causes both the maximum wavenumber and the maximum growth rate of the disturbance to increase, for different values of x. We note that for $\mathcal{R}e < 12$, the maximum growth rate at $x = 4$, is slightly less than the corresponding maximum growth rates at $x = 0$ and at $x = 2$. However, this behaviour is reversed for $\mathcal{R}e > 12$. The other parameters are the same as in Figure 4.14.

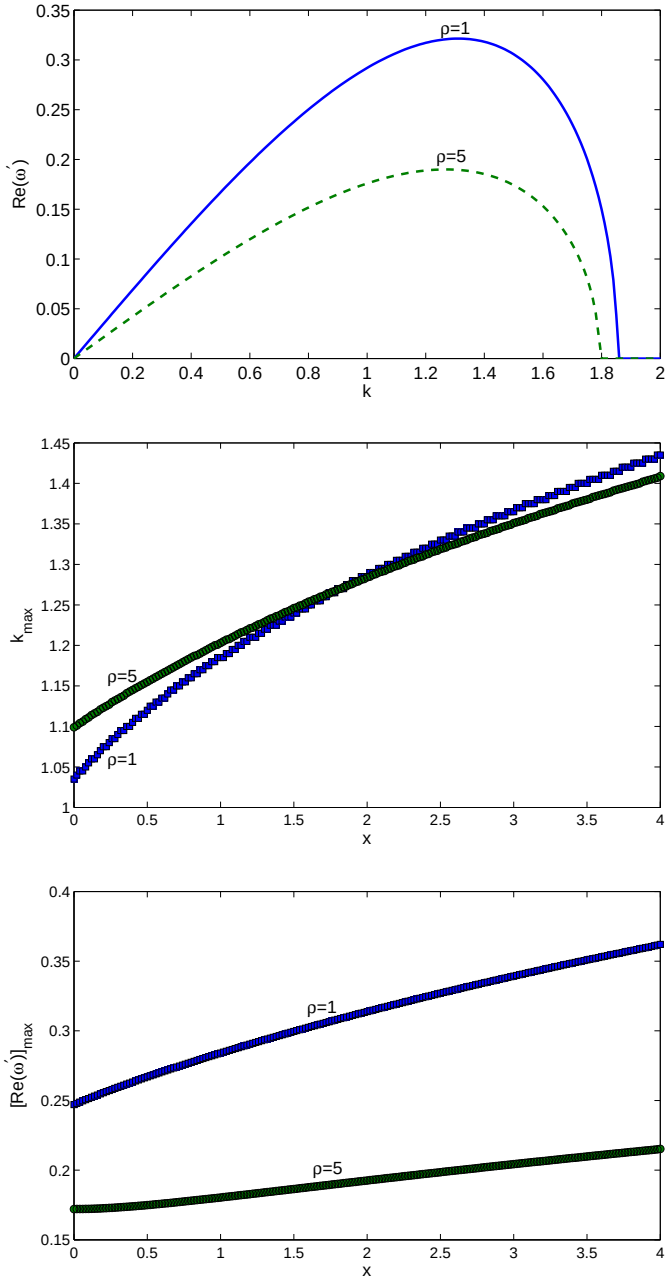

Figure 4.19: Top: $Re(\omega')$ versus k, for different ρ, at $x = 1.8$. At this x, $k_{max} = 1.27$ remains constant, for different ρ. Middle: k_{max} versus x, for different ρ. A decrease in ρ causes k_{max} to decrease for $x < 1.8$. After $x = 1.8$, this behaviour is reversed. Bottom: $[Re(\omega')]_{max}$ versus x, for different ρ. It can be seen that a decrease in ρ causes $[Re(\omega')]_{max}$ to increase. The other parameters are the same as in Figure 4.14.

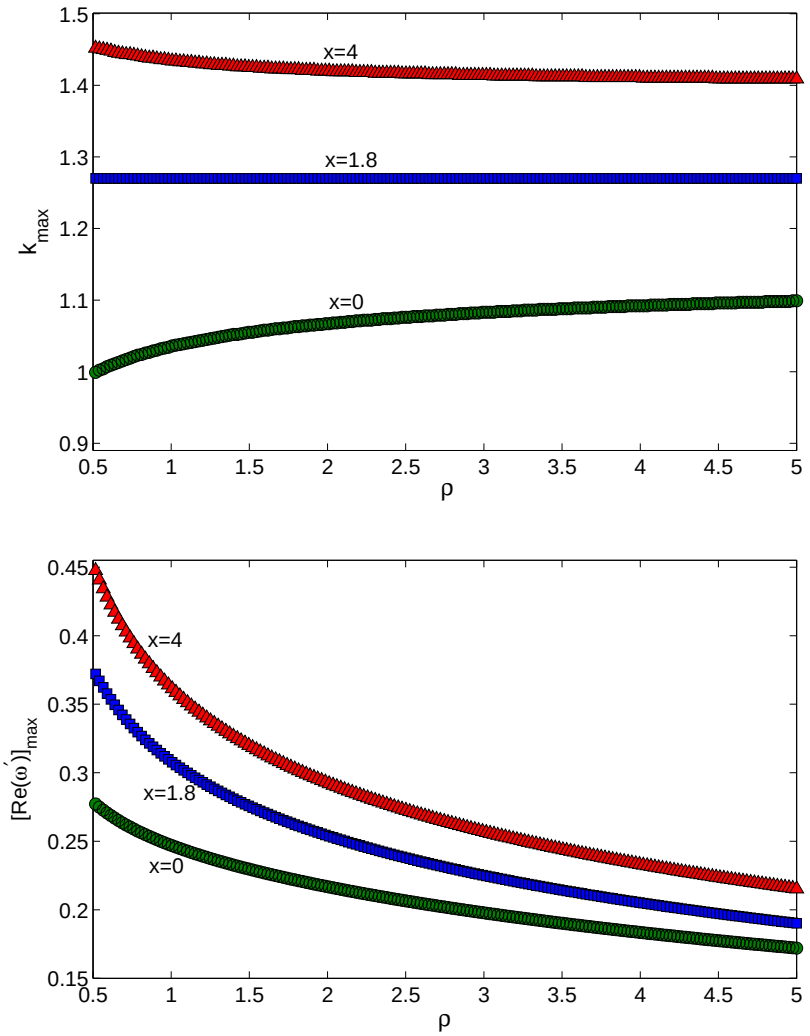

Figure 4.20: Maximum wavenumber k_{max} in the top, while maximum growth rate $[Re(\omega')]_{max}$ in the bottom, against density ratio ρ, for different values of x. It can be seen that a decrease in the density ratio causes the maximum wavenumber to decrease for $x = 0$, and increase for $x = 4$, as found in the previous graph, while causes the maximum growth rate to increase, although for large ρ, this difference is slightly small. We note that as we increase ρ, $x = 0$ curve increases, $x = 4$ curve decreases, while $x = 1.8$ curve remains constant. This shows that the transition of the different behaviour of k_{max} at $x = 0$ and $x = 4$ curves occurs at $x = 1.8$ curve. This transition takes place due to the characteristic behaviour of ρ, for these set of parameters. The other parameters are the same as in Figure 4.14.

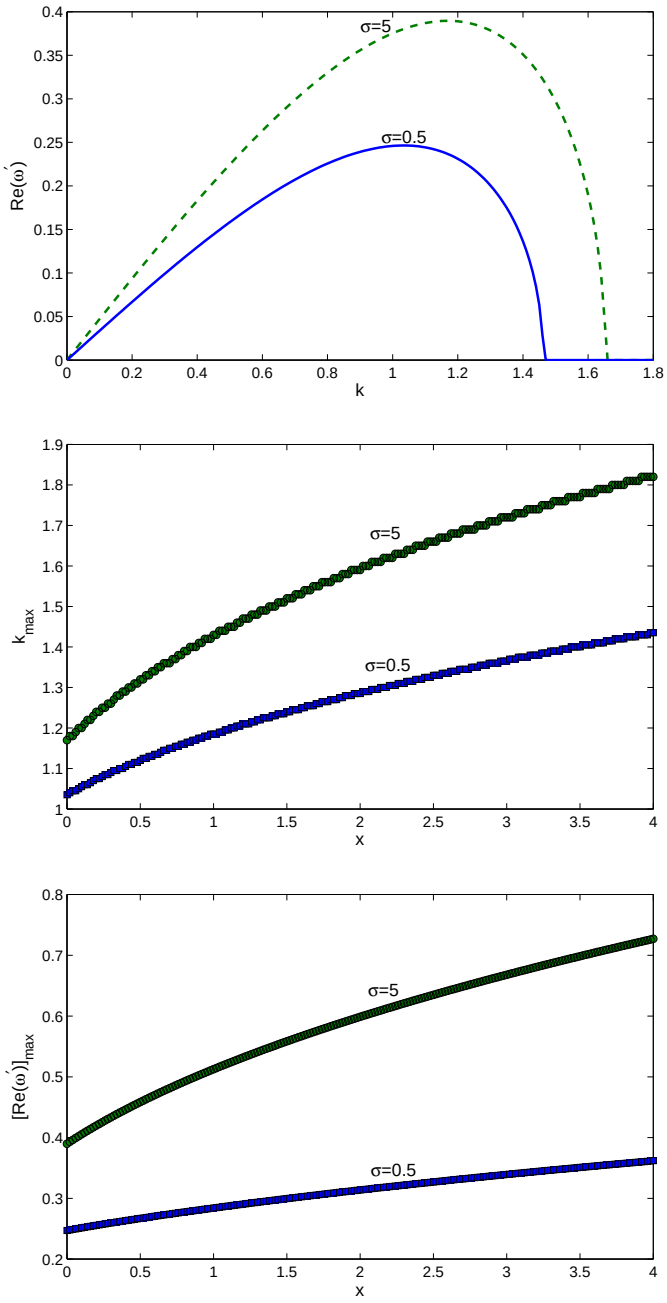

Figure 4.21: Top: Growth rate $Re(\omega')$ versus wavenumber k of the disturbance, for different values of the interfacial surface tension ratio σ, at $x = 0$. Middle: Maximum wavenumber k_{max} versus axial distance x, for different σ. Bottom: Maximum growth rate $[Re(\omega')]_{max}$ versus axial distance x, for different σ. A decrease in σ causes both k_{max} and $[Re(\omega')]_{max}$ to decrease. The other parameters are the same as in Figure 4.14.

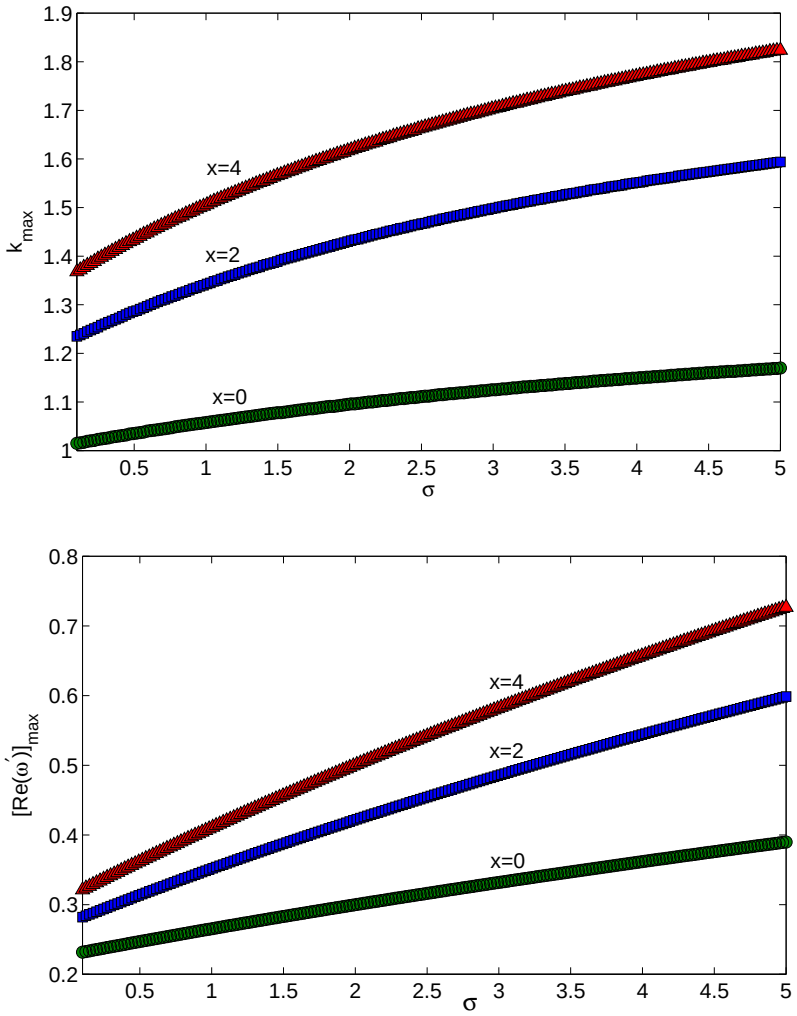

Figure 4.22: Maximum wavenumber k_{max} in the top, while maximum growth rate $[Re(\omega')]_{max}$ in the bottom, against the interfacial surface tension ratio σ, for different values of x. It can be seen that a decrease in σ causes both the maximum wavenumber and the maximum growth rate of the disturbance to decrease, for different values of x. We found that there does not exists any discontinuity (or transition) in k_{max} against σ in this case, as found in inviscid-gravity case. Physical Explanation: This may be due to the fact that in this case, we have only one velocity, whereas, in the inviscid case, we have two different velocities. The other parameters are the same as in Figure 4.14.

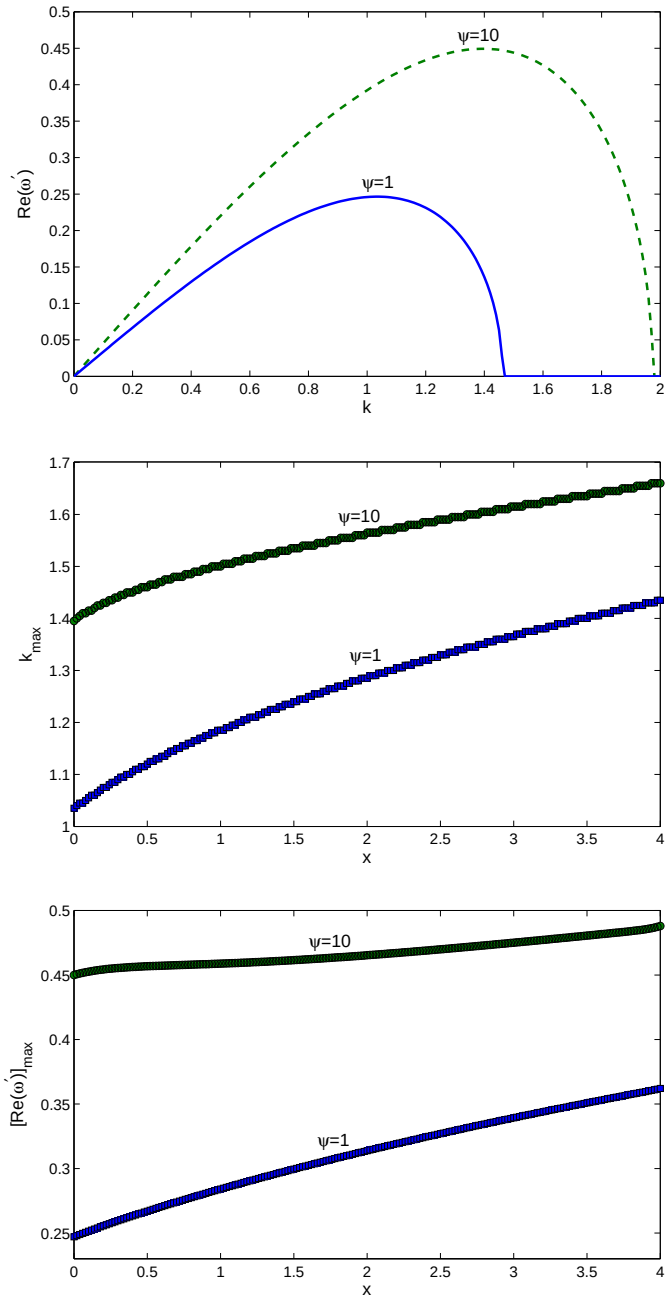

Figure 4.23: Top: Growth rate $Re(\omega')$ versus wavenumber k, for different ψ, at $x = 0$. Middle: k_{max} versus x, for different ψ. Bottom: $[Re(\omega')]_{max}$ versus x, for different ψ. A decrease in ψ causes both k_{max} and $[Re(\omega')]_{max}$ to decrease. The other parameters are the same as in Figure 4.14.

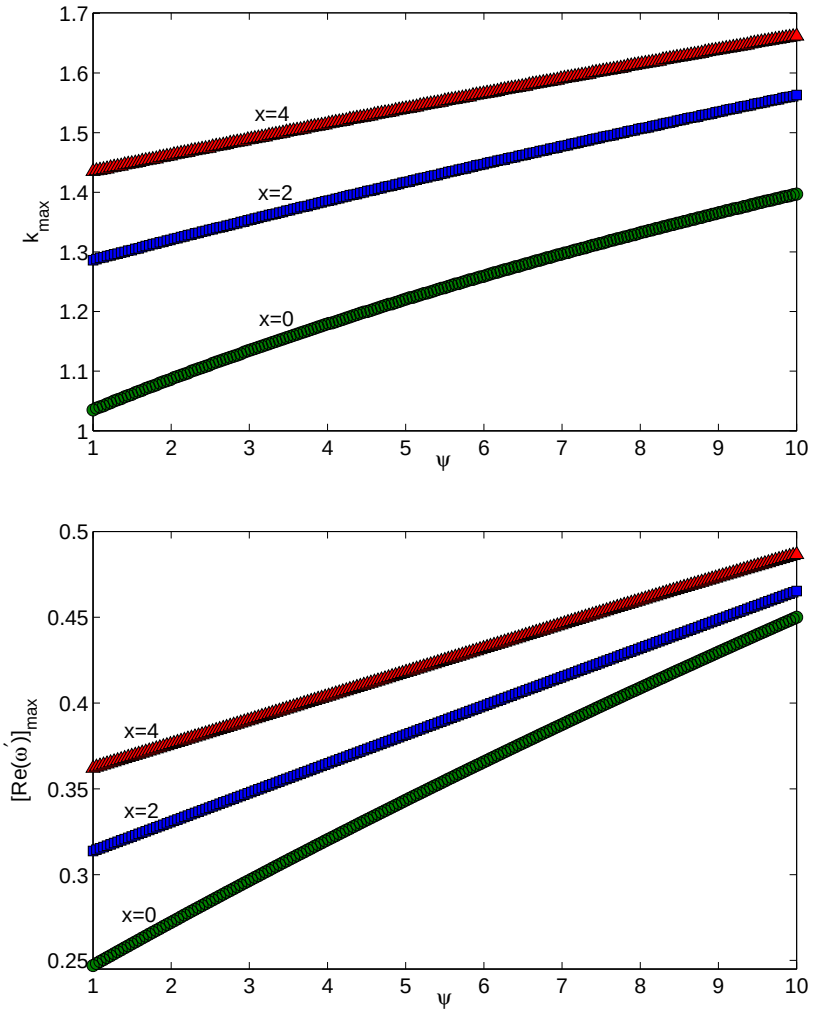

Figure 4.24: Maximum wavenumber k_{max} against density ratio ψ, for different values of x. Clearly, an increase in ψ causes both the maximum wavenumber and the maximum growth rate of the disturbance to increase, although for large ψ, the difference in $[Re(\omega')]_{max}$ is relatively small. The other parameters are the same as in Figure 4.14.

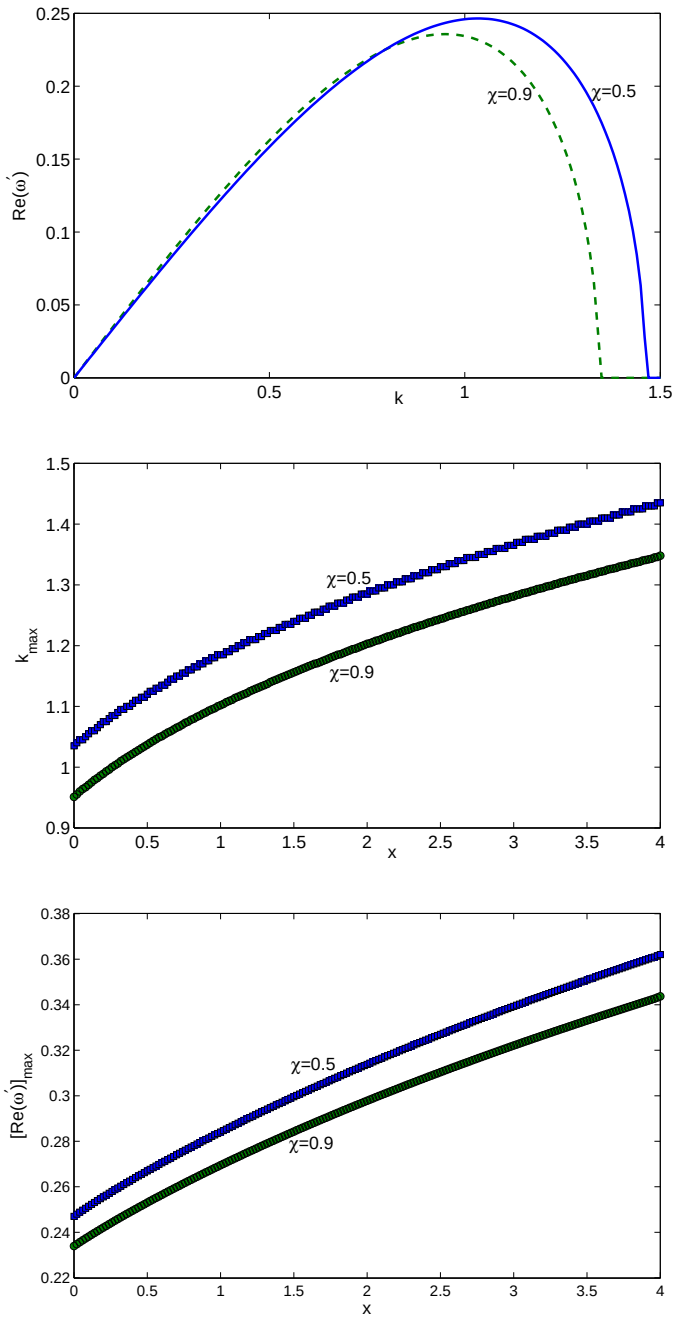

Figure 4.25: Top: Growth rate $Re(\omega')$ versus wavenumber k of the disturbance, for different values of the inner jet radius χ, at $x = 0$. Middle: Maximum wavenumber k_{max} versus axial distance x, for different χ. Bottom: Maximum growth rate $[Re(\omega')]_{max}$ versus axial distance x, for different χ. A decrease in χ causes both k_{max} and $[Re(\omega')]_{max}$ to increase. The other parameters are the same as in Figure 4.14.

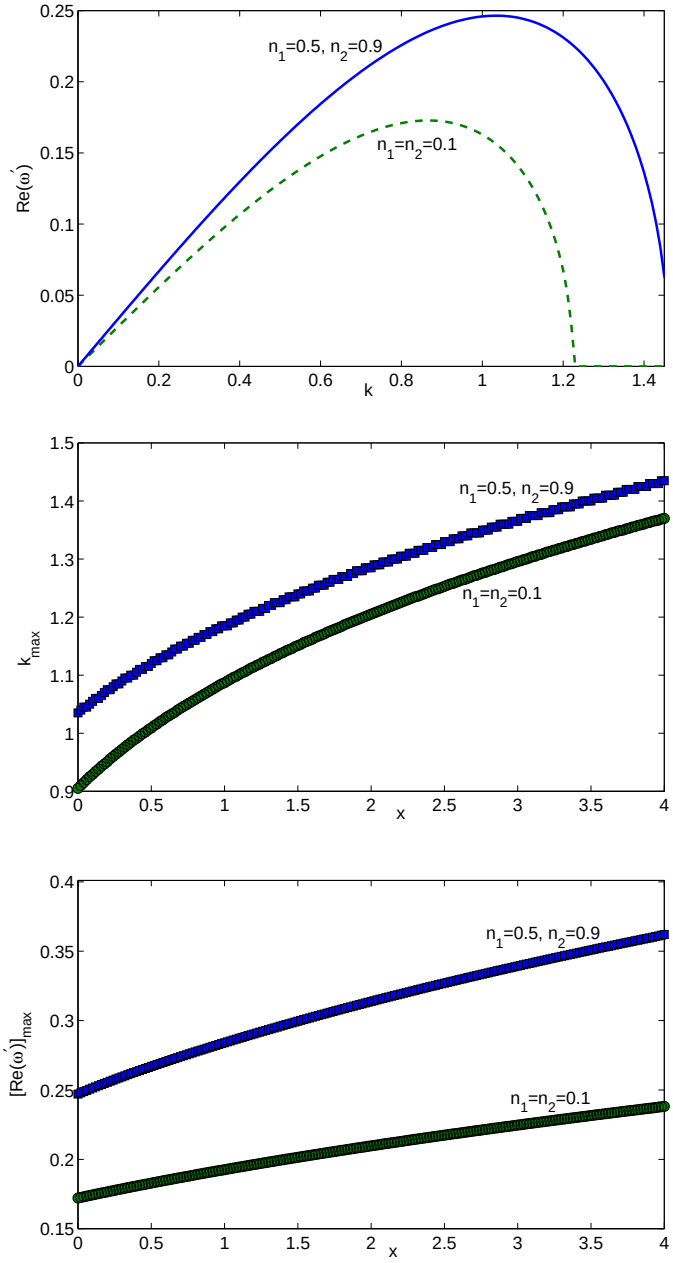

Figure 4.26: Top: Growth rate $Re(\omega')$ versus wavenumber k of the disturbance, for different values of the flow index numbers n_1 and n_2, at $x = 0$. Middle: Maximum wavenumber k_{max} versus axial distance x, for different n_1 and n_2. Bottom: Maximum growth rate $[Re(\omega')]_{max}$ versus axial distance x, for different n_1 and n_2. As the compound jet is made more shear thinning, both k_{max} and $[Re(\omega')]_{max}$ decrease. The other parameters are the same as in Figure 4.14.

4.6 Non-Linear Temporal Solution

We next remove the zero subscripts from our variables so that we have the following nonlinear system as

$$\left[S^2+(\rho-1)R^2\right](\mathcal{U}_t+\mathcal{U}\mathcal{U}_x)=-\frac{1}{We}\left[\left(S^2-R^2+\frac{R^2}{\rho}\right)\kappa_{2x}+\left(\frac{\sigma R^2}{\rho}\right)\kappa_{1x}\right]$$
$$+\frac{\psi}{\mathcal{R}e}\left[3(R^2)_x\mathcal{U}_x\eta_1+\left(2+\frac{1}{\rho}\right)R^2(\mathcal{U}_x\eta_1)_x\right]+\frac{3}{\mathcal{R}e}\left[(S^2-R^2)\mathcal{U}_x\eta_2\right]_x$$
$$+\left[S^2+(\rho-1)R^2\right]\left(\frac{1}{F^2}\right), \tag{4.26}$$

$$(R^2)_t+(R^2\mathcal{U})_x=0 \tag{4.27}$$

and

$$(S^2-R^2)_t+[(S^2-R^2)\mathcal{U}]_x=0, \tag{4.28}$$

where we now have included the full expression for the mean curvature term by retaining the symbols κ_i. This approach of retaining the full expression for the mean curvature term is essential for linear instability analysis (see previous section for the justification of this approach for linear theory) and also for non-linear temporal solutions (see Appendix B for the justification of this approach for non-linear theory). We note that since for viscous compound liquid jets, the inner and the outer fluids have the same velocity $\mathcal{U}$ (due to the no-slip condition), so the inner and the outer interfaces R and S will move with the same phase. Therefore, the inner jet will always break first, for viscous compound liquid jets, with or without gravity (as in Mohsin $et\ al.$ (2012)). On the other hand, since for inviscid compound liquid jets, the inner and the outer fluids have different velocities, so the inner and the outer interfaces R and S will move with the different phase. Therefore, sometimes the inner jet breaks first and sometimes the outer jet breaks first, for inviscid compound liquid jets, with or without gravity (as in Chapter 3).

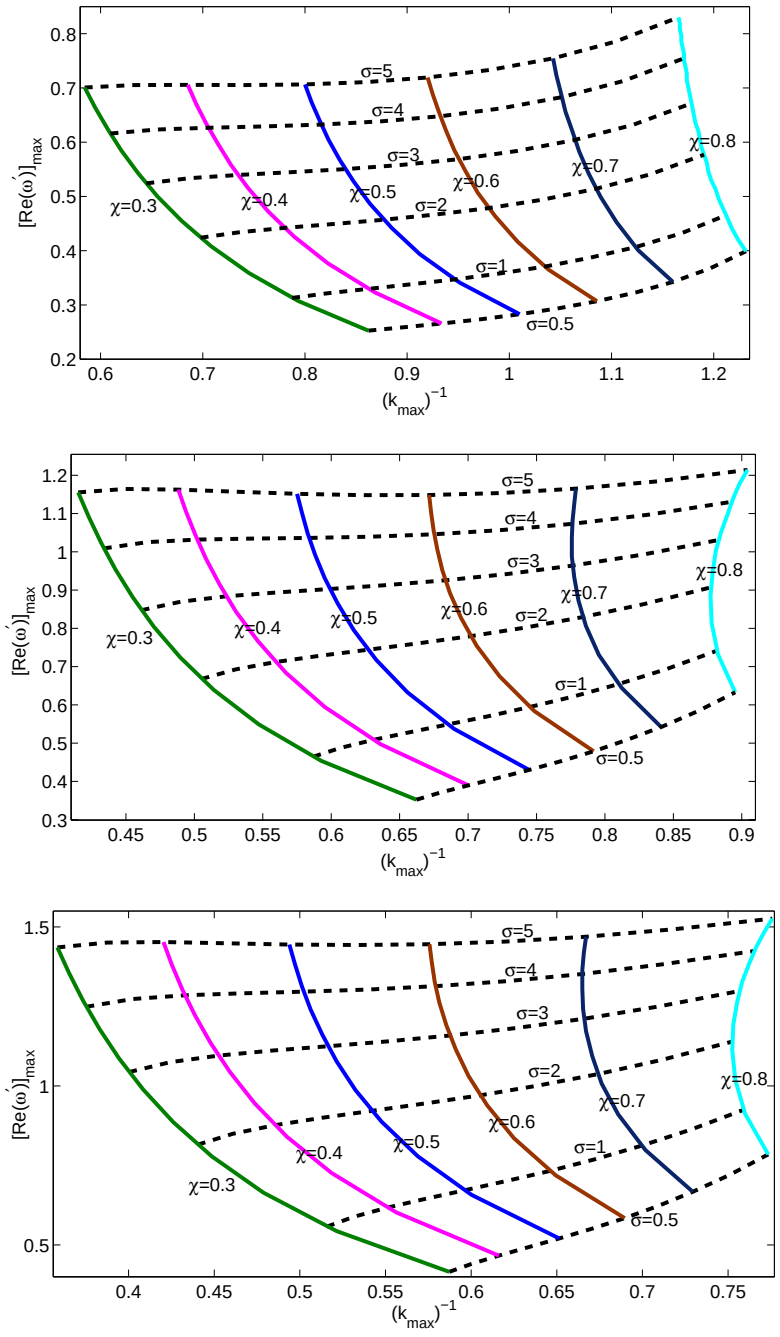

Figure 4.27: Maximum growth rate $[Re(\omega')]_{max}$ against inverse maximum wavenumber $(k_{max})^{-1}$, for various values of σ and χ, for $\rho = 0.5$. The graphs from top to bottom represent $x = 0$, $x = 2$ and $x = 4$ respectively. The other parameters are $F = 1$, $We = 30$, $Re = 70$, $\psi = 1$, $\lambda_1 = 0.1$, $\lambda_2 = 0.1$, $h = 1$, $n_1 = 0.3$ and $n_2 = 0.3$. The solid lines are for $\sigma = 0.5 - 5$, while the dashed lines are for $\chi = 0.3 - 0.8$.

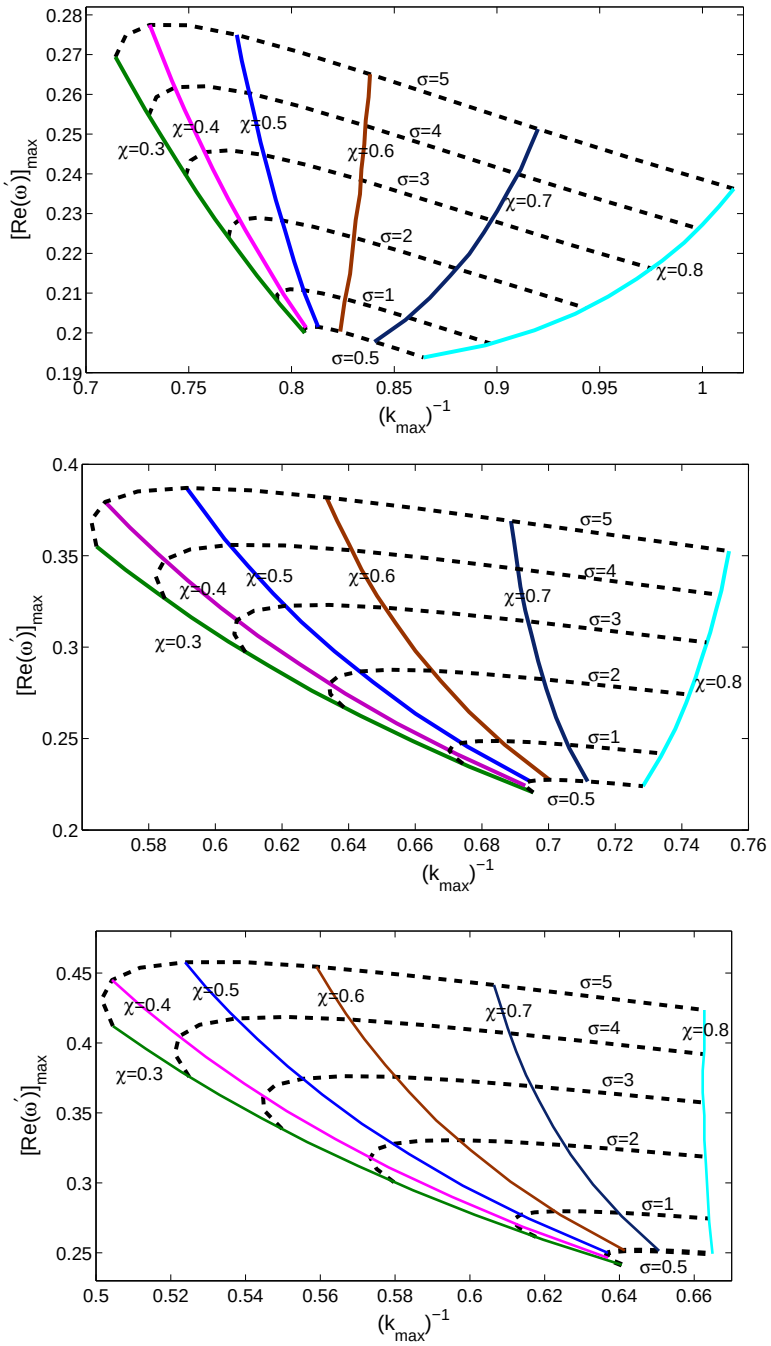

Figure 4.28: Maximum growth rate $[Re(\omega')]_{max}$ against inverse maximum wavenumber $(k_{max})^{-1}$, for various values of σ and χ, for $\rho = 2$. The graphs from top to bottom represent $x = 0$, $x = 2$ and $x = 4$ respectively. The other parameters are the same as in the previous figure. The solid lines are for $\sigma = 0.5 - 5$, while the dashed lines are for $\chi = 0.3 - 0.8$.

We next solve non-linear temporal equations (4.26) – (4.28), using a form of finite difference method, known as the Lax-Wendroff method (see Appendix B for the description of this method). We note that in order to ensure the convergence of this numerical method, we must full fill a necessary condition for convergence, known as the CFL (Courant-Friedrichs-Lewy) condition that the time step has to be much less than half of the square of the spatial step. That is,

$$dt << \frac{(dx)^2}{2}.$$

In Figure 4.29, we perform an accuracy check of the Lax-Wendroff method, by taking different spatial step sizes and next for our all of the following graphs, we choose a spatial step size of 5×10^{-4} (i.e., $n = 2,000$ so that $dx = 5e - 4$), as in Uddin $et\ al.$ (2008).

Similar to Uddin & Decent (2010), the boundary conditions, at the nozzle exit $x = 0$, are

$$\mathcal{U}(0,t) = 1 + \delta \sin\left(\frac{\kappa}{\epsilon}t\right), \tag{4.29}$$

$$R(0,t) = \chi \quad \text{and} \quad S(0,t) = 1, \tag{4.30}$$

where δ is the non-dimensional initial amplitude and is made dimensionless with respect to the radius of the orifice. Moreover, κ is the wavenumber of the imposed sinusoidal disturbance. In addition, the inclusion of ϵ indicates that we are looking for small and fast waves, as in the previous Section 4.5 (see Gurney (2010), for further details). We next take a fixed value of ϵ as $\epsilon = 0.01$. Furthermore, χ is the initial radius of the inner thread of fluid and $0 < \chi < 1$. The downstream boundary conditions are obtained by the quadratic extrapolation of the last internal mesh points.

The initial conditions of the system are chosen so that

$$\mathcal{U}(x,0) = \mathcal{U}_0,\ S(x,0) = S_0 \ \text{ and } \ R(x,0) = R_0.$$

Here $\mathcal{U}_0$, R_0 and S_0 are the solutions of the steady-state equations. We stop our numerical simulations of liquid jet equations when the minimum dimensionless jet radius becomes 0.05. We took the location of this minimum point to be the location of the breakup.

4.7 Results and discussion

In Figure 4.30, we plot the breakup of a viscous compound jet with both shear thinning core and shell fluids, having $n_1 = n_2 = 0.4$ (top), a Newtonian core and a shear thinning shell fluid (middle top) and vice versa (middle bottom), and then both Newtonian core and shell fluids (bottom) for wave number $\kappa = 0.65$. We note that the breakup lengths and satellite droplets are smallest when we have both shear thinning core and shell fluids. In Figure 4.31, we plot the breakup lengths for a viscous compound jet with both shear thinning core and shell fluids, having $n_1 = n_2 = 0.4$, a Newtonian core and a shear thinning shell fluid and vice versa, and then both Newtonian core and shell fluids, for different disturbance wavenumbers. Clearly, the breakup lengths are smallest when we have both shear thinning core and shell fluids and largest when we have both Newtonian core and shell fluids. In Figure 4.32, we plot the main drop sizes for a viscous compound jet with both shear thinning core and shell fluids, a Newtonian core and a shear thinning shell fluid and vice versa, and then both Newtonian core and shell fluids, for different κ. Clearly, the main drop sizes are smallest when we have both shear thinning core and shell fluids, although for $\kappa = 1.2$, there is not much difference in main drop sizes for all of the four cases. In addition, main drop sizes decrease as κ is increased because the wavelength is decreased. In Figure 4.33, we plot the

satellite drop sizes for a viscous compound jet with both shear thinning core and shell fluids, a Newtonian core and a shear thinning shell fluid and vice versa, and then both Newtonian core and shell fluids, for different κ. Clearly, the satellite drop sizes are smallest when we have both shear thinning core and shell fluids. In addition, the satellite drop sizes decrease as we increase κ. Therefore, the larger the wavenumber is (or the smaller the wavelength is), the smaller the main and satellite drops will be.

In Figure 4.34, we plot the breakup lengths for a viscous compound jet with both shear thinning core and shell fluids, having $n_1 = n_2 = 0.4$, a Newtonian core and a shear thinning shell fluid and vice versa, and then both Newtonian core and shell fluids, for different interfacial surface tension ratios. Clearly, the breakup lengths are smallest when we have both shear thinning core and shell fluids and largest when we have both Newtonian core and shell fluids. In addition, breakup lengths decrease as we increase σ. In Figure 4.35, we plot the main drop sizes for a viscous compound jet with both shear thinning core and shell fluids, a Newtonian core and a shear thinning shell fluid and vice versa, and then both Newtonian core and shell fluids, for different interfacial surface tension ratios. Clearly, the main drop sizes are smallest when we have both shear thinning core and shell fluids. In Figure 4.36, we plot the satellite drop sizes for a viscous compound jet with both shear thinning core and shell fluids, a Newtonian core and a shear thinning shell fluid and vice versa, and then both Newtonian core and shell fluids, for different interfacial surface tension ratios. Clearly, the satellite drop sizes are smallest when we have both shear thinning core and shell fluids. In addition, the satellite drop sizes decrease as σ is decreased. From Figures 4.34 – 4.36, we find that as σ is increased, the breakup lengths are smaller and less amount of fluid is consumed in the main drop size, which in turn, has an impact of a more increase in the satellite droplet size. This happens because increasing σ results in high curvature, which in

turn results in quick snap-off at the neck. Consequently, the jet will break quickly and a big satellite drop will also form.

In Figure 4.37, we plot the breakup lengths for a viscous compound jet with different flow index numbers for the inner and outer fluids. We only vary the flow index number of the shell fluid while keeping the flow index number of the inner fluid constant. Clearly, the breakup lengths are smallest when we have both shear thinning core and shell fluids and largest when we have both Newtonian core and shell fluids. This result is anticipated as viscosity is a stabilizing factor (since viscosity dissipates energy). Therefore, shear thinning, which reduces the viscosity, destabilizes the jet, leading to shorter breakup lengths. Figure 4.37 is a comparison with Mohsin $et\ al.$ (2012) and we note that due to gravity, breakup lengths are smaller, which is true physically. We also find that the breakup lengths are smaller when the core fluid is strongly shear thinning, as in Mohsin $et\ al.$ (2012). Here we have chosen the same parameters as in Figure 6 of Mohsin $et\ al.$ (2012). In Figure 4.38, we plot the main drop sizes for a viscous compound jet with different flow index numbers for the inner and outer fluids. We only vary the flow index number of the shell fluid while keeping the flow index number of the inner fluid constant. We find that the main drops are smallest when we have both Newtonian core and shell fluids. In addition, main drop sizes decrease as n_2 is increased. We also find that for small values of n_2 (at $n_2 = 0.4, 0.45$), changing n_1 does not make any difference to the main drop sizes. In Figure 4.39, we plot the satellite droplet sizes for a compound viscous jet with different flow index numbers for the inner and outer fluids, with varying the disturbance amplitude δ. We only vary the flow index number of the shell fluid while keeping the flow index number of the inner fluid constant. We observe that for a Newtonian core, increasing δ implies a decrease in the satellite droplets, which is a similar qualitative behaviour as found in Mohsin $et\ al.$ (2012). We also observe that for a shear thinning core, increas-

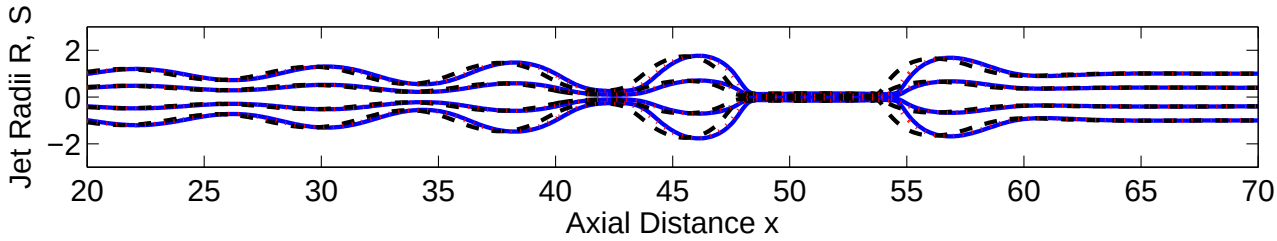

Figure 4.29: The accuracy check of our numerical method. The dashed, dotted and solid lines respectively represent the number of points (with spatial step size) $n = 1,000$ ($dx = 1e-3$), $n = 2,000$ ($dx = 5e-4$) and $n = 4,000$ ($dx = 2.5e-4$). Here $dt = 0.000025$ and the other parameters are $F = 1$, $We = 40$, $Re = 950$, $\sigma = 1$, $\rho = 1$, $\psi = 1$, $\chi = 0.5$, $\delta = 0.05$, $\kappa = 0.85$, $\lambda_1 = 0.1$, $\lambda_2 = 0.1$, $h = 1$, $n_1 = 0.2$ and $n_2 = 0.9$.

ing δ implies an increase in the satellite droplets, which is a similar qualitative behaviour as found in Mohsin $et\ al.$ (2012). We also observe that as n_1 and n_2 are increased (or as the inner and the outer fluids are made less shear thinning), less discharge of fluid takes place into the main drop size, which in turn, has an impact of a more increase in the satellite droplet size.

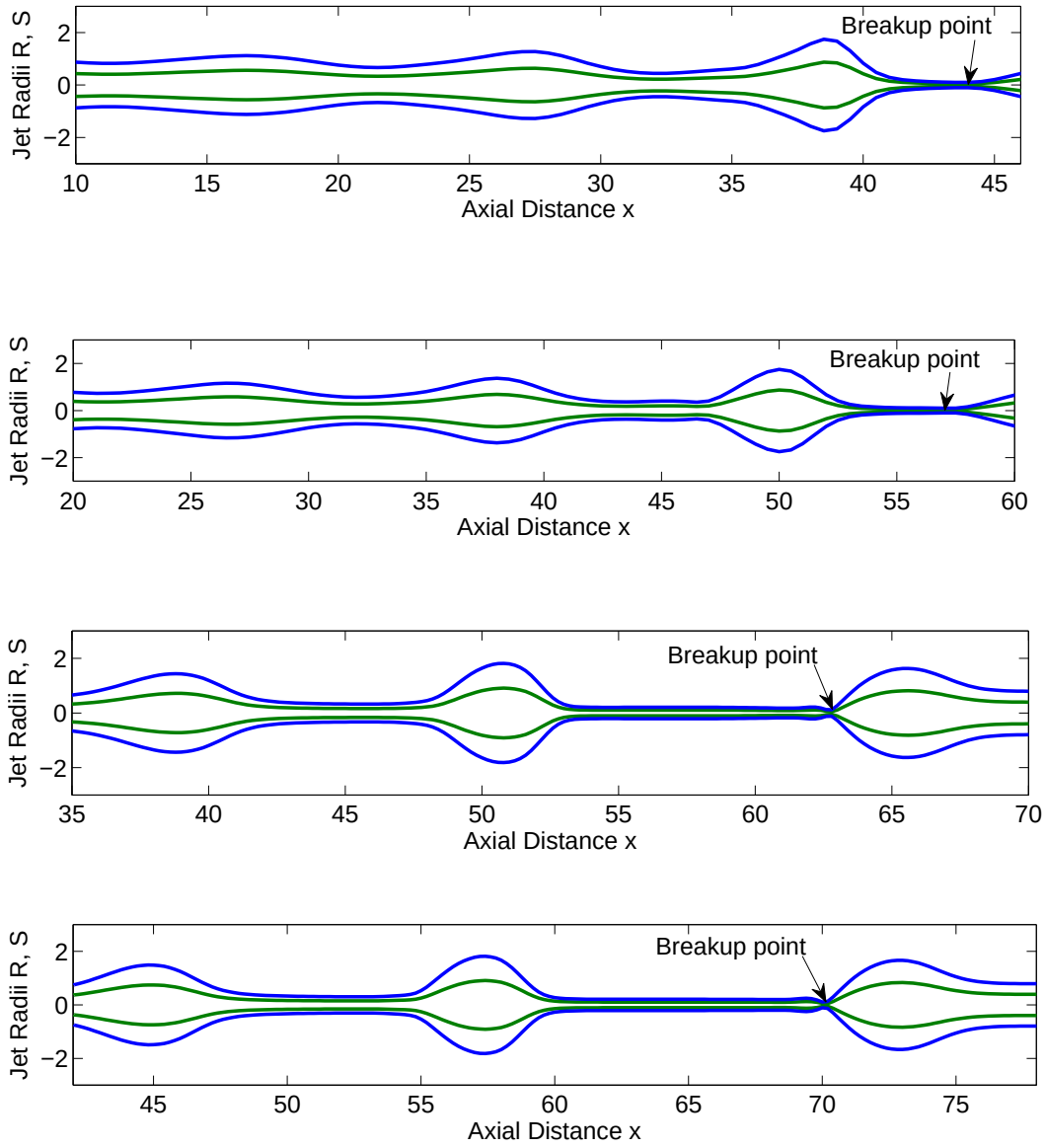

Figure 4.30: The breakup of a viscous compound jet with both shear thinning core and shell fluids, having $n_1 = n_2 = 0.4$ (top), a Newtonian core and a shear thinning shell ($n_2 = 0.4$) fluids (middle top) and vice versa (middle bottom), and then both Newtonian core and shell fluids (bottom) for wave number $\kappa = 0.65$. We note that the breakup lengths and satellite droplets are smallest when we have both shear thinning core and shell fluids. The other parameters are $We = 15$, $Re = 550$, $\sigma = 1$, $\rho = 1$, $\psi = 1$, $\chi = 0.5$, $\delta = 0.05$, $\lambda_1 = 0.1$, $\lambda_2 = 0.1$ and $h = 1$.

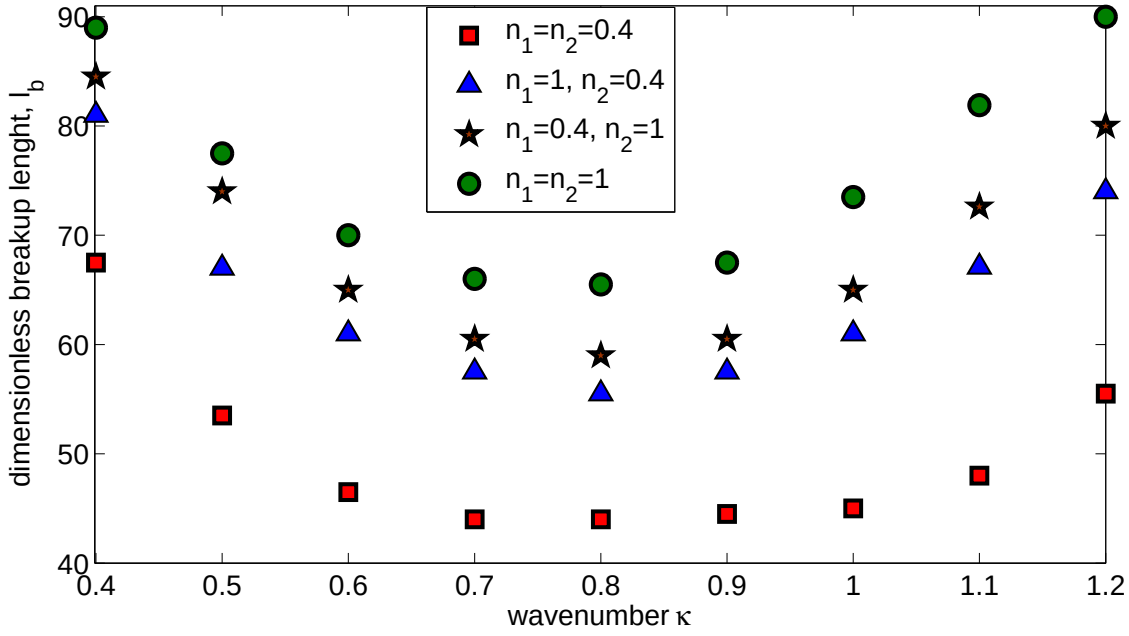

Figure 4.31: Breakup lengths for a viscous compound jet with both shear thinning core and shell fluids, having $n_1 = n_2 = 0.4$ (bottom), a Newtonian core and a shear thinning shell ($n_2 = 0.4$) fluids (middle bottom) and vice versa (middle top), and then both Newtonian core and shell fluids (top), for different disturbance wavenumbers. Clearly, the breakup lengths are smallest when we have both shear thinning core and shell fluids and largest when we have both Newtonian core and shell fluids. The other parameters are the same as in the previous figure.

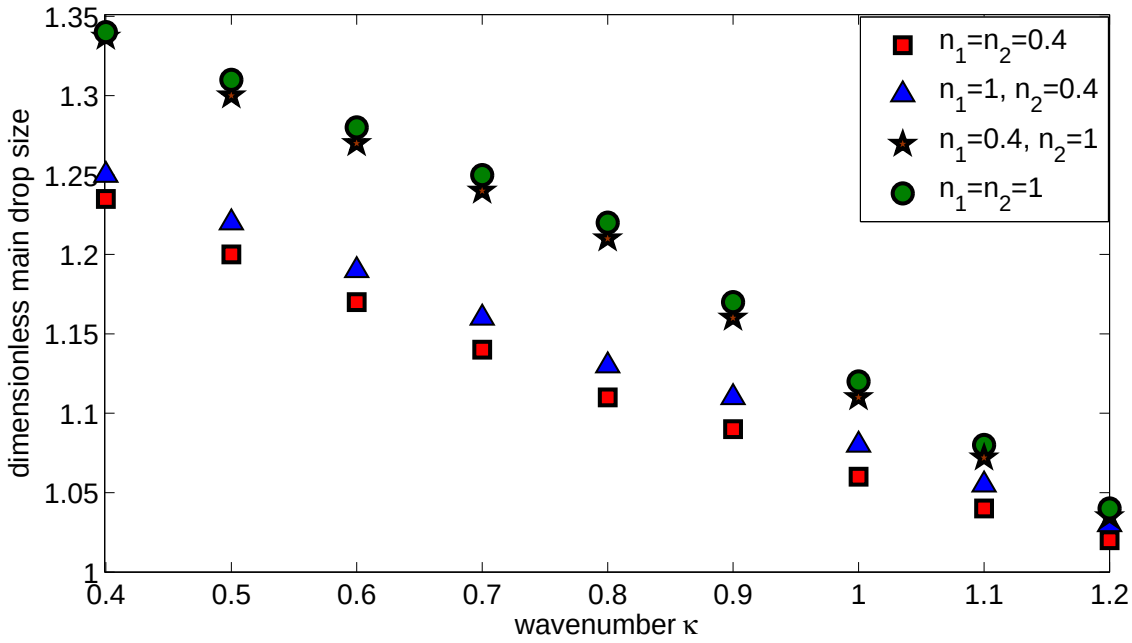

Figure 4.32: Main drop sizes for a viscous compound jet with both shear thinning core and shell fluids, a Newtonian core and a shear thinning shell fluid and vice versa, and then both Newtonian core and shell fluids, for different κ. Clearly, the main drop sizes are smallest when we have both shear thinning core and shell fluids, although for $\kappa = 1.2$, there is not much difference in main drop sizes for all of the four cases. The other parameters are the same as in the previous figure.

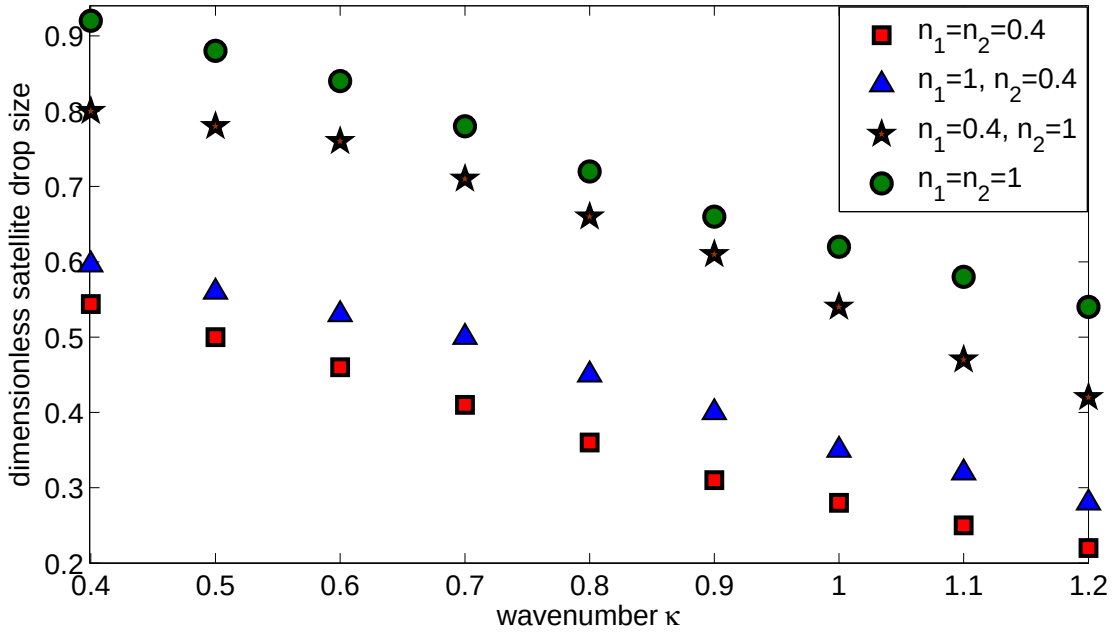

Figure 4.33: Satellite drop sizes for a viscous compound jet with both shear thinning core and shell fluids, a Newtonian core and a shear thinning shell fluid and vice versa, and then both Newtonian core and shell fluids, for different κ. Clearly, the satellite drop sizes are smallest when we have both shear thinning core and shell fluids. In addition, the satellite drop sizes decrease as we increase κ. The other parameters are the same as in the previous figure.

4.8 Conclusions

In this chapter, we have investigated the instability of a shear-thinning compound liquid jet falling under the influence of gravity. We have used a slender jet approximation to determine a one dimensional model, which describes the velocity and radial displacements of the inner and outer free surfaces. We have solved the steady-state equations and investigated its dependence on changes in all the parameters of the model. In particular, we found that an increase in the Weber number (which could correspond to a decrease in the surface tension of the outer interface) and Reynolds number leads to a more rapid decay of the jet radii and rapid increase of the jet velocity along the jet. We have then considered the growth of unstable waves on the two interfaces by considering a linear temporal instability analysis. The obtained dispersion relation, which describes the relationship between the growth rate and wavenumber of disturbances, has been solved numerically in order to determine the most unstable wavenumber (which we assume to be the dominant wavenumber which leads to breakup) and the associated maximum growth rate. We have investigated how this most unstable wavenumber varies as we change key critical parameters, like the ratio of surface tension σ and the aspect ratio of inner jet radii χ. Diagrams showing how such changes in the parameters affect the most unstable mode, for different axial distances x along the jet, have been investigated to reveal that the most unstable wavenumber and maximum growth rates are larger as the wave travels down the jet. We also find that a decrease in the density ratio causes the maximum wavenumber of the disturbance to decrease for $x < 1.8$ while after $x = 1.8$, this behaviour is reversed. We also observe that a decrease in the density ratio causes the maximum growth rate of the disturbance to increase, although for large ρ, the difference in $[Re(\omega')]_{max}$ is slightly small. We further note that as we increase ρ, $x = 0$ curve increases,

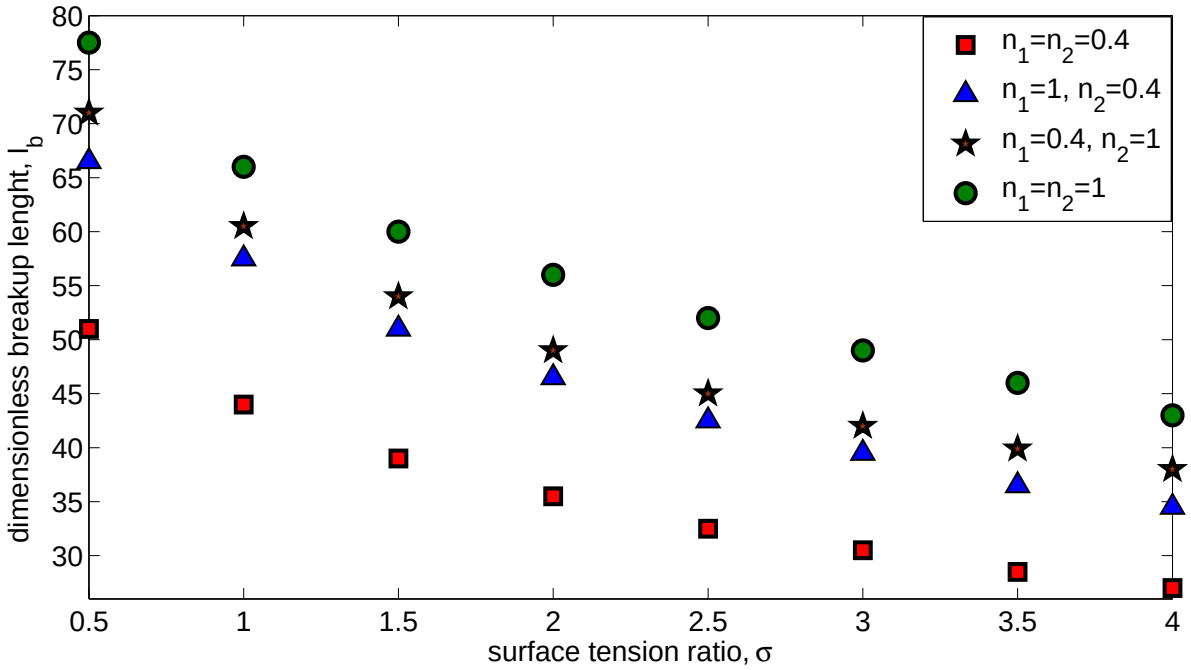

Figure 4.34: Breakup lengths for a viscous compound jet with both shear thinning core and shell fluids, having $n_1 = n_2 = 0.4$, a Newtonian core and a shear thinning shell fluid and vice versa, and then both Newtonian core and shell fluids, for different interfacial surface tension ratios. Clearly, the breakup lengths are smallest when we have both shear thinning core and shell fluids and largest when we have both Newtonian core and shell fluids. In addition, breakup lengths decrease as we increase σ. The other parameters are $We = 20$, $Re = 500$, $\rho = 1$, $\psi = 1$, $\kappa = 0.7$, $\chi = 0.5$, $\delta = 0.05$, $\lambda_1 = 0.1$, $\lambda_2 = 0.1$ and $h = 1$.

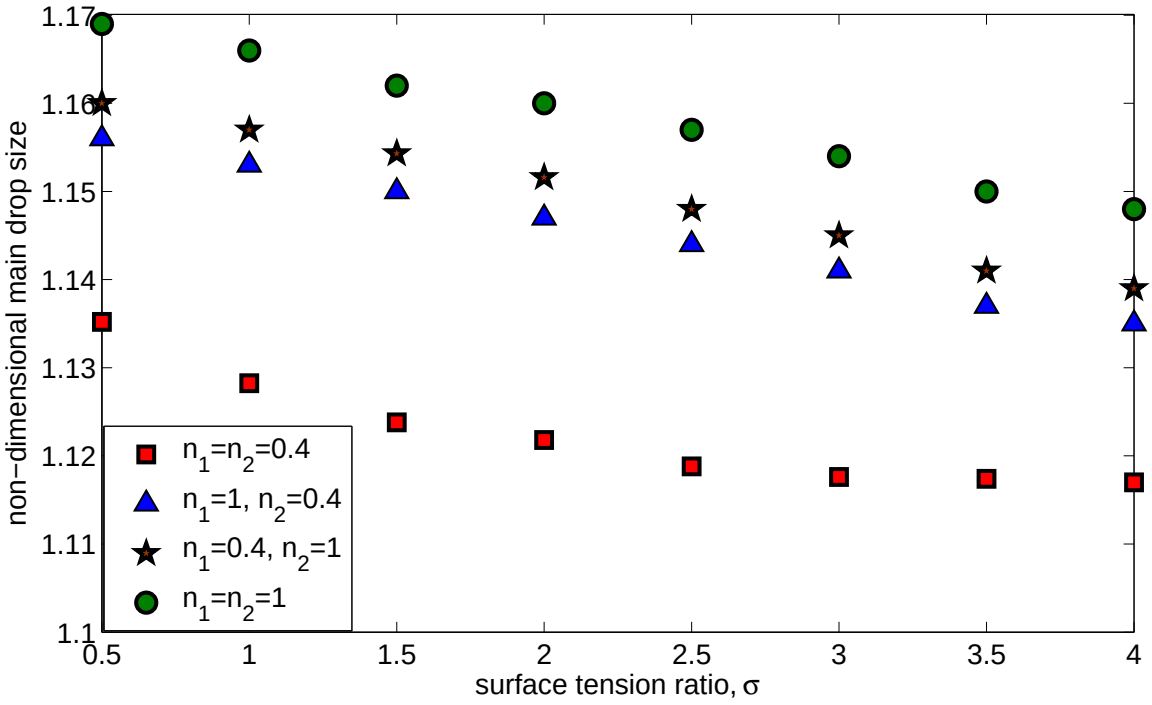

Figure 4.35: Main drop sizes for a viscous compound jet with both shear thinning core and shell fluids, a Newtonian core and a shear thinning shell fluid and vice versa, and then both Newtonian core and shell fluids, for different interfacial surface tension ratios. Clearly, the main drop sizes are smallest when we have both shear thinning core and shell fluids. The other parameters are the same as in the previous figure.

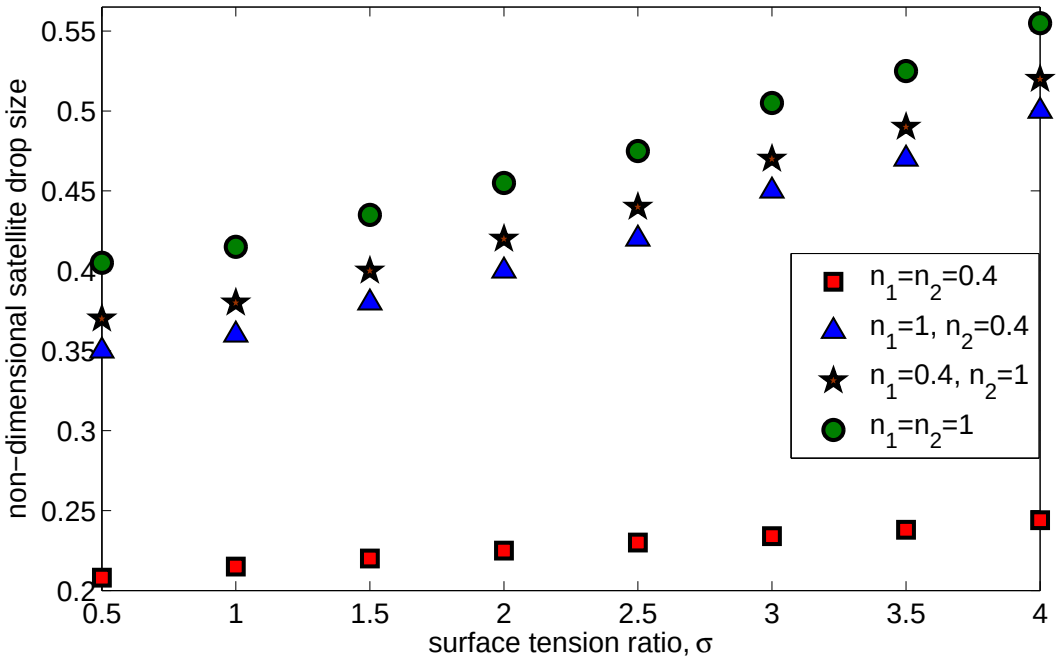

Figure 4.36: Satellite drop sizes for a viscous compound jet with both shear thinning core and shell fluids, a Newtonian core and a shear thinning shell fluid and vice versa, and then both Newtonian core and shell fluids, for different interfacial surface tension ratios. Clearly, the satellite drop sizes are smallest when we have both shear thinning core and shell fluids. In addition, the satellite drop sizes decrease as σ is decreased. The other parameters are the same as in the previous figure.

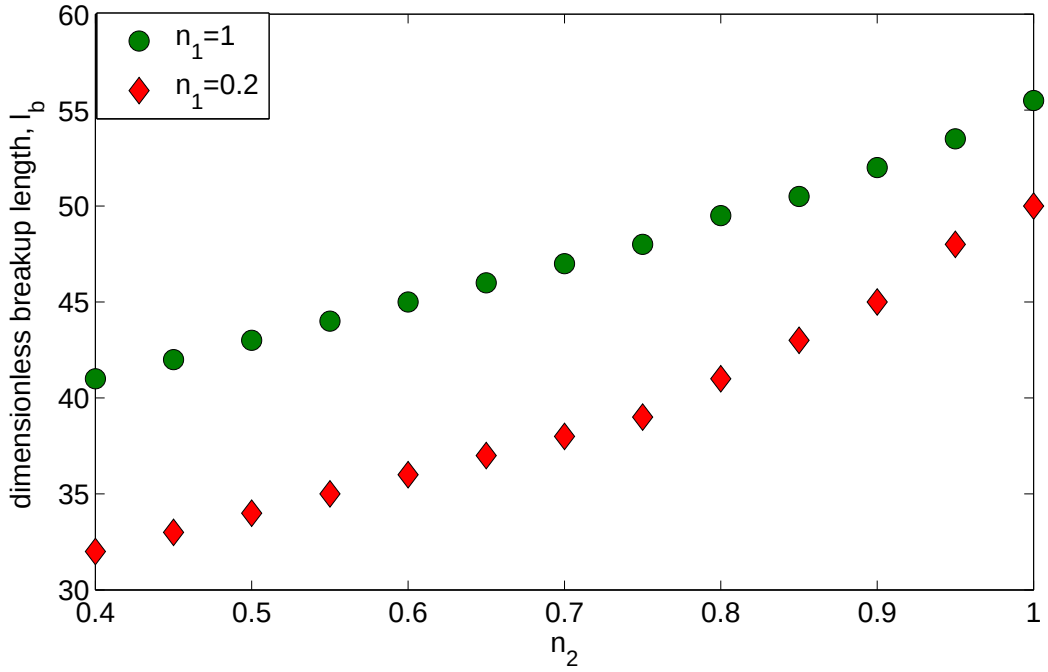

Figure 4.37: Breakup lengths for a viscous compound jet with different flow index numbers for the inner and outer fluids. We only vary the flow index number of the shell fluid while keeping the flow index number of the inner fluid constant. Clearly, the breakup lengths are smallest when we have both shear thinning core and shell fluids and largest when we have both Newtonian core and shell fluids. This figure is a comparison with Mohsin *et al.* (2012) and we note that due to gravity, breakup lengths are smaller. We also find that the breakup lengths are smaller when the core fluid is strongly shear thinning, as in Mohsin *et al.* (2012). Here we have chosen the same parameters as in Figure 6 of Mohsin *et al.* (2012), as $We = 16.4$, $Re = 480$, $\delta = 0.05$, $\kappa = 0.88$, $\sigma = 0.5$, $\rho = 1$, $\psi = 0.5$, $\chi = 0.7$, $\lambda_1 = 0.1$, $\lambda_2 = 0.1$ and $h = 1$.

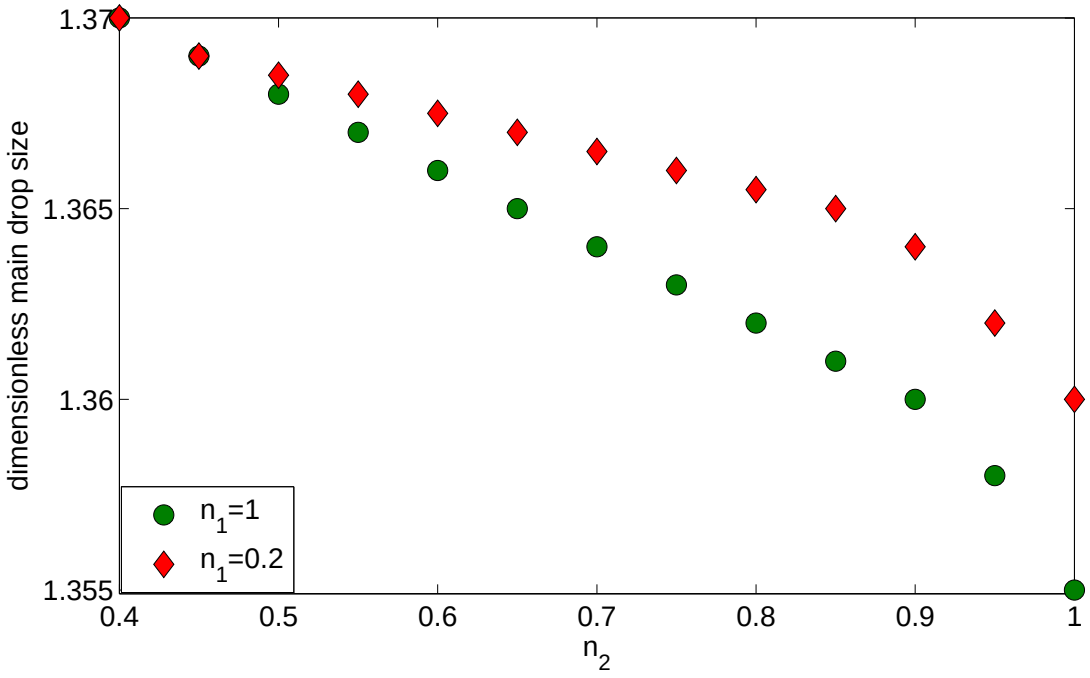

Figure 4.38: Main drop sizes for a viscous compound jet with different flow index numbers for the inner and outer fluids. We only vary the flow index number of the shell fluid while keeping the flow index number of the inner fluid constant. We find that the main drops are smallest when we have both Newtonian core and shell fluids. In addition, main drop sizes decrease as n_2 is increased. We also find that for small values of n_2 (at $n_2 = 0.4, 0.45$), changing n_1 does not make any difference to the main drop sizes. The other parameters are the same as in the previous figure.

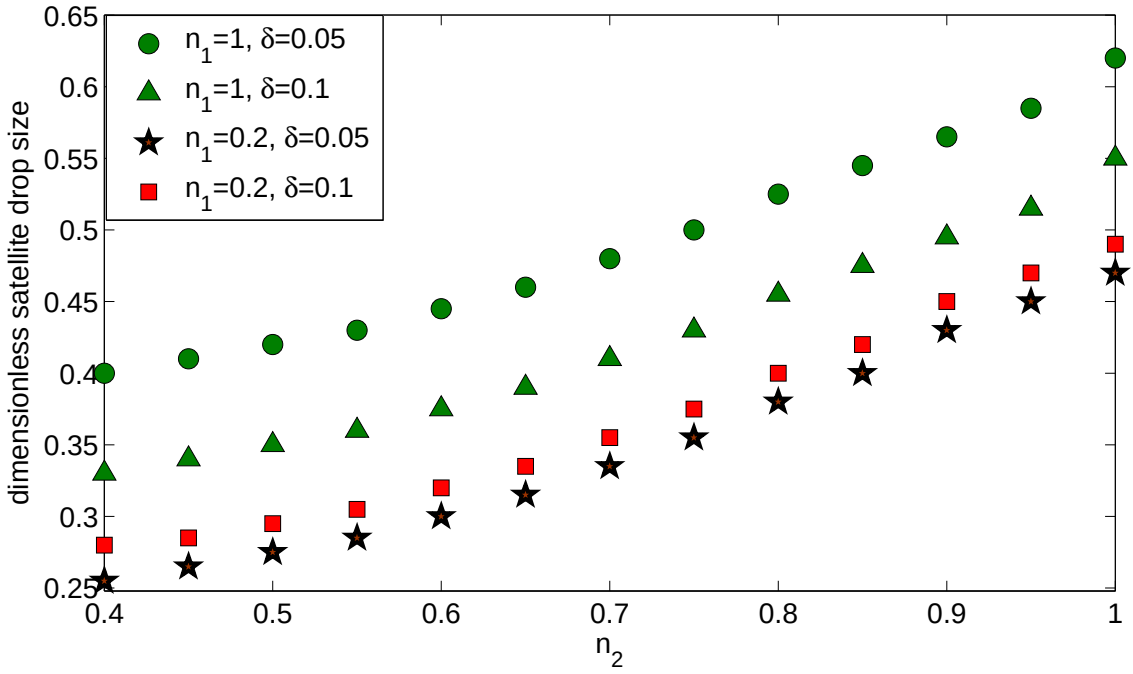

Figure 4.39: Satellite droplet sizes for a compound viscous jet with different flow index numbers for the inner and outer fluids, with varying the disturbance amplitude δ. We only vary the flow index number of the shell fluid while keeping the flow index number of the inner fluid constant. We observe that for a Newtonian core, increasing δ implies a decrease in the satellite droplets, which is a similar qualitative behaviour as found in Mohsin *et al.* (2012). We also observe that for a shear thinning core, increasing δ implies an increase in the satellite droplets, which is a similar qualitative behaviour as found in Mohsin *et al.* (2012). As n_1 and n_2 are increased (or as the inner and the outer fluids are made less shear thinning), less discharge of fluid takes place into the main drop size, which in turn, has an impact of a more increase in the satellite droplet size. The other parameters are the same as in the previous figure.

$x = 4$ curve decreases, while $x = 1.8$ curve remains constant. This shows that the transition of the different behaviour of k_{max} at $x = 0$ and $x = 4$ curves occurs at $x = 1.8$ curve. This transition takes place due to the characteristic behaviour of ρ, for these set of parameters. In addition, we found that there does not exists any discontinuity (or transition) in the maximum wavenumber k_{max} against any parameter of the problem in this case, as found in inviscid-gravity case, for σ. This may be due to the fact that in this case, we have only one velocity, whereas, in the inviscid case, we have two different velocities.

We have also solved the model equations using a numerical method based on finite differences. We have investigated the effects of changing the key parameters on the breakup lengths, main drop sizes and satellite drop sizes. In particular, we have found that breakup lengths, main drops and satellite drops are always smallest when we have both shear thinning core and shell fluids, for different values of the disturbance wavenumber κ. We also find that the satellite drops decrease as we increase κ. Furthermore, as the interfacial surface tension ratio σ is increased, the breakup lengths are smaller and less amount of fluid is consumed in the main drop size, which in turn, has an impact of a more increase in the satellite droplet size. Moreover, the satellite drop sizes are smallest when we have both shear thinning core and shell fluids. We also found that due to gravity, breakup lengths are smaller and are also smaller when the core fluid is strongly shear thinning, as in Mohsin $et\ al.$ (2012).

We observed that for a Newtonian core, increasing δ implies a decrease in the satellite droplets, which is a similar qualitative behaviour as found in Mohsin $et\ al.$ (2012). We also observed that as n_1 and n_2 are increased (or as the inner and the outer fluids are made less shear thinning), less discharge of fluid takes place into the main drop size, which in turn, has an impact of a more increase in the satellite droplet size.

Chapter 5

Description and Application of The Needham-Leach Method

5.1 Description of The Needham-Leach Method

We first describe the Needham-Leach method, which is an asymptotic method, and then we describe an application of this method, which is in Decent (2009). The Needham-Leach method is very useful to find the large spatial and temporal asymptotic solution of many classes of differential equations, such as, the generalized Fisher equation in reaction-diffusion systems, KdV equation and the Navier-Stokes equations (see Leach & Needham 2001 & 2004, Leach $et\ al.$ 2003 and Decent (2009) for more details). In this method, we consider the model equations of a given problem along with initial and boundary conditions and we divide the whole domain in following five different space and time asymptotic regions, as shown in Figure 5.1.

(I) $s \to 0$ and $t \to 0$; (II) $s = O(1)$ and $t \to 0$; (III) $s \to \infty$ and $t = O(1)$; (IV) $s \to \infty$ and $t \to \infty$ and (V) $s = O(1)$ and $t \to \infty$.

We find the solution to the model equations in each region, which consists

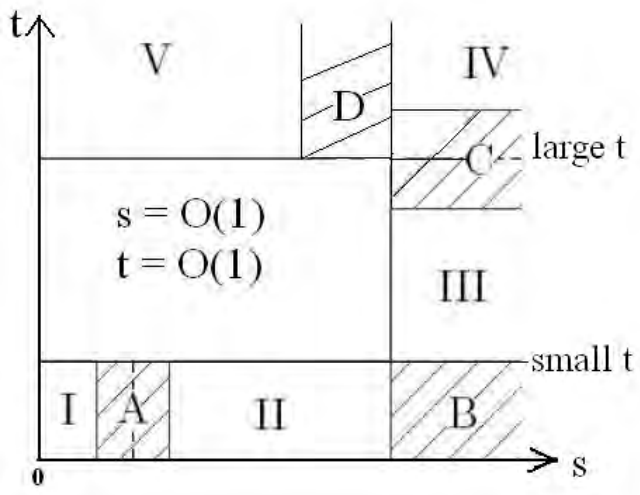

Figure 5.1: A diagram showing the representation of the different regions of the Needham-Leach asymptotic method. Reproduced from Gurney (2010).

of some unknown constants and then we do asymptotic matching between each neighbouring region to find out the values of the unknown constants. In this way, the whole asymptotic domain will be covered. The regions A, B, C and D in Figure 5.1 are the regions where the asymptotic matching, between each neighbouring regions, will take place.

This method starts with considering the initial conditions at $t = 0$ and then posing small time asymptotic, $t \to 0$, and also using the boundary condition at $s = 0$, in the first region, where both $s \to 0$ and $t \to 0$. We then substitute the small time and space asymptotics into the model equations and we find the solution in this region I. This solution is then expanded in order to pose asymptotic expansions in next region II, where $t \to 0$ and $s = O(1)$. We next substitute asymptotic expansions of region II into the model equations and we find the solution in region II. After that, we do asymptotic matching between the two regions to determine the values of unknown constants. This procedure is repeated in next

regions III, IV and V until the whole asymptotic domain is fully covered. This asymptotic method gives deep investigations into the partial differential equations in each region of the liquid jet equations. We now give an application of the Needham-Leach method.

5.2 Application of The Needham-Leach Method

As an application of the Needham-Leach method, we review Decent (2009). Decent (2009) has applied the Needham-Leach method for the very first time to the liquid jets and has obtained very useful information regarding the regions of the liquid jet breakup. This seminal work of Decent (2009) forms the base of our new work in this thesis. Decent (2009) studied the behaviour of a slender viscous jet, as it moves towards breakup, using the Needham-Leach method. Decent (2009) successfully applied the Needham-Leach method to the viscous liquid jet equations and obtained some useful results.

In particular, Decent (2009) found an equation, in region IV, which describes an uncontrollable and unstable nonlinear travelling wave at large times. This equation, which we call as the g_0-equation, is given by

$$Re\left(g_0'\right)^4 - 4zReWeg_0'g_0 + 2z^2ReWe\left(g_0'\right)^2 - 4zReWe\left(g_0'\right)^2 + 4ReWeg_0'g_0$$

$$+2ReWe\left(g_0'\right)^2 + 2ReWe\left(g_0\right)^2 + 6We\left(g_0'\right)^2 g_0 - 6We\left(g_0'\right)^3 z$$

$$+6We\left(g_0'\right)^3 + Re\left(g_0'\right)^2 = 0. \tag{5.1}$$

In the above equation, z is defined as $z = s/t = O(1)$, for large space and time.

In addition, g_0 is obtained in the asymptotic limit $Re \to \infty$ and is given by

$$g_0 = \frac{\sqrt{Q_0}}{4\sqrt{We}} \tag{5.2}$$

where

$$Q_0 = -We^2 - 10z^2We + 20zWe - 10We - 6z^2We^2 - z^4We^2 + 2 + 4z^3We^2$$

$$+4zWe^2 - \sqrt{We\,(z-1)^2\,(We - 2zWe + z^2We - 4)^3}. \tag{5.3}$$

Decent (2009) also solved the g_0-equation computationally for $Re = O(1)$ and that computational solution is given in Figures 5.2 and 5.3.

The g_0-equation (5.1) describe the dynamics of an uncontrollable and unstable nonlinear travelling wave at large times. Note that the real part of g_0 is the temporal growth rate, for negative values and it is the temporal decay rate, for positive values. Figure 5.2 shows the computational solution of the real part of g_0. Decent (2009) noted from this figure that the temporal growth rate lies in a range of values of z, which can be represented by $z_1 < z < z_2$. In addition, from equations (5.2) and (5.3), Decent (2009) found that $z_1 \to max\left(1 - 2/\sqrt{We}, 0\right)$ and $z_2 \to 1 + 2/\sqrt{We}$ as $Re \to \infty$. Further more, the imaginary part of g_0 is the local frequency of the uncontrollable nonlinear travelling wave. Figure 5.3 shows the computational solution of the imaginary part of g_0.

Decent (2009) noted that the small unstable growing linear waves come out of the orifice $z = 0$. These waves grow gradually until they become nonlinear before $z = z_1$. In the region $z_1 < z < z_2$, Decent (2009) found a new nonlinear wave, given by equation (5.1), which starts at $z = z_1$. This new nonlinear wave does not depend on the controllable frequency ω or controllable amplitude δ and

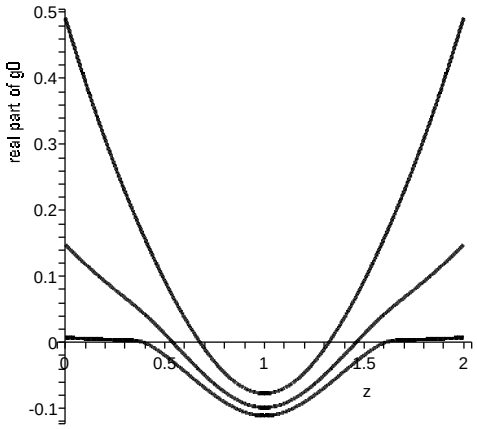

Figure 5.2: The real part of g_0 plotted against z for $We = 10$ for $Re = 15$ (top), 50 (middle) and 1000 (bottom). Figure taken from Decent (2009).

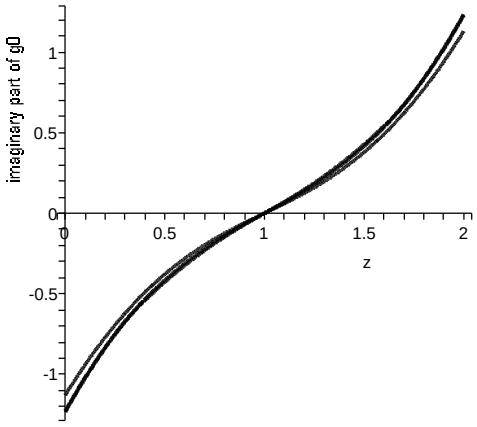

Figure 5.3: The imaginary part of g_0 plotted against z for $We = 10$ for $Re = 15$ (top for $z < 0$ and bottom for $z > 0$), 50 (middle) and 1000 (bottom for $z < 0$ and top for $z > 0$). Figure taken from Decent (2009).

so we cannot control it. Hence $z = z_1$ is the onset (or the beginning point) of the uncontrollable nonlinear travelling wave. Gurney (2010) has next used the Needham-Leach method on straight inviscid liquid jet equations and also considered the impact of rotation on straight inviscid liquid jet equations.

5.3 Derivation of Temporal Growth Rate and Wavenumber

In this section, we derive the temporal growth rate and wavenumber of the fastest growing temporal linear mode in the limit of $Re \to \infty$, using the linear temporal instability analysis. These quantities have not been given nor derived in Decent (2009). We perturb the steady-state solution by a small time-dependent disturbance and assume

$$R = 1 + \delta \exp(\lambda t + iks) R_1 \tag{5.4}$$

and

$$u = 1 + \delta \exp(\lambda t + iks) u_1, \tag{5.5}$$

where δ, λ and k are respectively the amplitude, frequency and wavenumber of the disturbance. Moreover, R_1 and u_1 are constant vectors. Substituting the above equations into the model equations of straight axi-symmetric viscous liquid jets (see Decent (2009)) and taking the limit $Re \to \infty$, we get

$$2\lambda R_1 + iku_1 + 2ikR_1 = 0 \tag{5.6}$$

and

$$(\lambda We + ikWe)u_1 + (ik^3 - ik)R_1 = 0. \tag{5.7}$$

Equations (5.6) and (5.7) can be written in the matrix form as

$$\begin{pmatrix} ik & 2\lambda + 2ik \\ \lambda We + ikWe & ik^3 - ik \end{pmatrix} \cdot \begin{pmatrix} u_1 \\ R_1 \end{pmatrix} = \begin{pmatrix} 0 \\ 0 \end{pmatrix}.$$

For the above system to have a non-trivial solution, we require that

$$\det \begin{pmatrix} ik & 2\lambda + 2ik \\ \lambda We + ikWe & ik^3 - ik \end{pmatrix} = 0.$$

That is,

$$ik(ik^3 - ik) - (2\lambda + 2ik)(\lambda We + ikWe) = 0, \tag{5.8}$$

and so we obtain a dispersion relation of the form

$$2\lambda^2 We + 4i\lambda kWe = -k^4 + k^2 + 2k^2 We. \tag{5.9}$$

Hence from this dispersion relation, we obtain

$$\lambda = \left[\frac{k^2(1-k^2)}{2We}\right]^{1/2} + i(-k) = \lambda_r + i\lambda_i, \tag{5.10}$$

where

$$\lambda_r = \text{Growth rate} = \left[\frac{k^2(1-k^2)}{2We}\right]^{1/2} \tag{5.11}$$

and

$$\lambda_i = \text{Frequency} = -k. \tag{5.12}$$

Now using the fact that

$$\frac{d\lambda_r}{dk} = 0$$

for the fastest (maximum) growth rate, we obtain, from equation (5.11), that

$$k = 1/\sqrt{2}, \tag{5.13}$$

which is the wavenumber of the fastest growing temporal linear wave-mode in the limit of $Re \to \infty$.

Substituting this value of k into equation (5.11), we get

$$\lambda_r = \sqrt{2}/\left(4\sqrt{We}\right), \tag{5.14}$$

which is the temporal growth rate of the fastest growing temporal linear wave-mode in the limit of $Re \to \infty$. This completes our review on Decent (2009).

5.4 Summary

In this chapter, we presented a description about the Needham-Leach method. In addition, we described an application of this method, that is in Decent (2009), which forms the base of some of our next chapters. At the end, we have derived the temporal growth rate and wavenumber of the fastest growing temporal linear mode in the limit of $Re \to \infty$, which are not derived in Decent (2009).

Chapter 6

Asymptotic Solution of Straight Vertically Falling Newtonian Liquid Jet Under the Influence of Gravity

6.1 Introduction

In the previous chapter, we reviewed Decent (2009), which describes the application of the Needham-Leach method to a Newtonian liquid jet, without gravity. In this chapter, we extend the analysis of Decent (2009) by examining the asymptotic solution of straight vertically falling Newtonian liquid jet, falling under the influence of gravity. Note that in the laboratory, we cannot easily perform the problem given in Decent (2009) which do not have gravity in it because under the normal circumstances, we have the force of gravity acting in the laboratory. However, our problem can easily be performed in the laboratory as we have included gravity in our problem. Hence, this problem is a practical generalization of Decent (2009).

6.2 Model Equations

The model equations for a straight downward falling Newtonian jet, falling under the influence of gravity, are given by

$$R_t = -\frac{R}{2}u_s - uR_s \tag{6.1}$$

and

$$u_t + uu_s = -\frac{1}{We}\left(\frac{1}{R(1+\epsilon^2 R_s^2)^{\frac{1}{2}}} - \frac{\epsilon^2 R_{ss}}{(1+\epsilon^2 R_s^2)^{\frac{3}{2}}}\right)_s + \frac{3}{Re}\cdot\frac{1}{R^2}\left[\frac{\partial}{\partial s}\left(R^2\frac{\partial u}{\partial s}\right)\right] + \frac{1}{F^2}. \tag{6.2}$$

Here $\mathbf{u} = (u_s, u_r, u_\theta) = (u, v, 0)$ is the velocity vector, $\mathbf{g} = (g, 0)$ is the gravity, ρ is the density of the liquid, μ is the viscosity, t is time and p is the pressure. In these equations, we have taken $u(s,t)$ as the velocity component parallel to the centreline of the jet, $R(s,t)$ as the distance of the axi-symmetric free-surface away from the jet's centreline and s as the distance along the jet's centreline from the orifice. The non-dimensional constants appearing in these equations are the Froude number, the Reynolds number and the Weber number and these are respectively given by

$$F = \frac{U}{\sqrt{Lg}}, \qquad Re = \frac{\rho UL}{\mu} \quad \text{and} \quad We = \frac{\rho U^2 a}{\sigma}. \tag{6.3}$$

Here a is the radius of the orifice, U is the exit speed of the jet and L is the typical axial length scale (which can be taken as $L = U^2/g$) chosen so that, in keeping

with the slender jet assumption, we define a small parameter ϵ as

$$\epsilon = a/L << 1.$$

These equations have been derived in Partridge (2006) (by taking $Rb \to \infty$ and $Y_s = 1$). We define new length and time scales $\tilde{s}$ and $\tilde{t}$ such that

$$\tilde{s} = \frac{s}{\epsilon}, \qquad \tilde{t} = \frac{t}{\epsilon}.$$

So equation (6.1) can be written as

$$\frac{1}{\epsilon} R_{\tilde{t}} = -\frac{1}{\epsilon}\frac{R}{2} u_{\tilde{s}} - \frac{1}{\epsilon} u R_{\tilde{s}}, \tag{6.4}$$

or

$$R_{\tilde{t}} + \frac{R}{2} u_{\tilde{s}} + u R_{\tilde{s}} = 0. \tag{6.5}$$

Similarly equation (6.2) can be written as

$$\begin{aligned} u_{\tilde{t}} + u u_{\tilde{s}} = -\frac{1}{We} \left(\frac{1}{R(1+R_{\tilde{s}}^2)^{\frac{1}{2}}} - \frac{R_{\tilde{s}\tilde{s}}}{(1+R_{\tilde{s}}^2)^{\frac{3}{2}}} \right)_{\tilde{s}} \\ + \frac{3}{Re\,\epsilon} \cdot \frac{1}{R^2} \left[\frac{\partial}{\partial \tilde{s}} \left(R^2 \frac{\partial u}{\partial \tilde{s}} \right) \right] + \frac{\epsilon}{F^2}. \end{aligned} \tag{6.6}$$

We define

$$\tilde{Re} = Re\,\epsilon = \frac{\rho U L}{\mu} \cdot \frac{a}{L} = \frac{\rho U a}{\mu}$$

and we also define

$$\frac{\epsilon}{F^2} = \frac{1}{\tilde{F}^2},$$

or

$$\tilde{F} = \frac{F}{\sqrt{\epsilon}} = \frac{U}{\sqrt{Lg}} \cdot \sqrt{\frac{L}{a}} = \frac{U}{\sqrt{ag}}.$$

Therefore, equation (6.6) becomes

$$u_{\tilde{t}} + uu_{\tilde{s}} + \frac{1}{We}\left[\frac{1}{R}\left(1+R_{\tilde{s}}^2\right)^{-1/2} - R_{\tilde{s}\tilde{s}}\left(1+R_{\tilde{s}}^2\right)^{-3/2}\right]_{\tilde{s}}$$

$$-\frac{3}{\tilde{Re}}\frac{(R^2u_{\tilde{s}})_{\tilde{s}}}{R^2} - \frac{1}{\tilde{F}^2} = 0. \tag{6.7}$$

Equations (6.5) and (6.7) are now used as the model equations for a straight downward falling Newtonian jet, falling under the influence of gravity.

The non-dimensional initial conditions are

$$R\left(\epsilon\tilde{s}, \epsilon\tilde{t}=0\right) = 1 \quad \text{and} \quad u\left(\epsilon\tilde{s}, \epsilon\tilde{t}=0\right) = 1.$$

The boundary conditions at the orifice are

$$R\left(\epsilon\tilde{s}=0, \epsilon\tilde{t}\right) = 1 \quad \text{and} \quad u\left(\epsilon\tilde{s}=0, \epsilon\tilde{t}\right) = 1 + \delta\sin\left(\omega\epsilon\tilde{t}\right).$$

We define u_0 and R_0 as the steady-state solution of equations (6.5) and (6.7). We also assume that $u \to u_0$ and $R \to R_0$ as $\tilde{s} \to \infty$, which physically means that in the far-field, the jet is considered to be undisturbed.

Note that now our original equations are in $\tilde{s}$ and $\tilde{t}$. As mentioned in section 5.1, we divide the domain in five asymptotic regions and apart from regions IV and V, the solutions in regions I-III are the same as given in Decent (2009). We are only interested in regions IV and V as they will give us useful information about the g_0-equation.

We, therefore, examine this problem in region IV (the nonlinear waves sec-

tion), where $\tilde{s} \to \infty$ and $\tilde{t} \to \infty$ so that $z = \tilde{s}/\tilde{t} = O(1)$. Similar to Gurney (2010), we introduce a new length scale $\bar{s}$, defined by

$$\bar{s} = \epsilon\tilde{s} = O(1), \text{ as } \epsilon \to 0.$$

The reason for introducing this new length scale $\bar{s}$ is that we want to have the $O(1)$ values of the steady-state problem (as $\bar{s} = O(1)$). Similar to the expansions that Gurney (2010) and Decent (2009) used in region IV, we pose the following multiple-scales type expansions

$$u = u_0(\bar{s}) + \left[\exp\left(-tg_0\left(z,\bar{s}\right)\right)\left\{h_0\left(z,\bar{s}\right) + O\left(\frac{1}{\sqrt{t}}\right)\right\} + h.o.t.\right] \tag{6.8}$$

and

$$R = R_0(\bar{s}) + \left[\exp\left(-tg_0\left(z,\bar{s}\right)\right)\left\{\zeta_0\left(z,\bar{s}\right) + O\left(\frac{1}{\sqrt{t}}\right)\right\} + h.o.t.\right] \tag{6.9}$$

as $\tilde{t} \to \infty$ and $h.o.t.$ denotes higher-order terms. The steady-state equations for u_0 and R_0 can be obtained from equations (6.5) and (6.7), using $\bar{s} = \epsilon\tilde{s}$, and are given by

$$\frac{1}{2}u_0'R_0 + u_0R_0' = 0 \tag{6.10}$$

and

$$\epsilon u_0 u_0' + \frac{1}{We}\left(\frac{-\epsilon R_0'}{R_0^2(1+\epsilon^2 R_0'^2)^{\frac{1}{2}}} - \frac{\epsilon^3 R_0' R_0''(R_0^{-1}) + \epsilon^3 R_0'''}{(1+\epsilon^2 R_0'^2)^{\frac{3}{2}}} + \frac{3\epsilon^5 R_0' R_0''^2}{(1+\epsilon^2 R_0'^2)^{\frac{5}{2}}}\right)$$

$$-\frac{3}{\tilde{R}e}(\epsilon^2 u_0'' + 2\epsilon^2 u_0' R_0' R_0^{-1}) - \frac{\epsilon}{F^2} = 0, \tag{6.11}$$

where we have used $1/\tilde{F}^2 = \epsilon/F^2$ and $' = \partial/\partial\bar{s}$. Note that we can take $L = U^2/g$, which will imply that F is fixed as $F = 1$, as $F = U/\sqrt{Lg}$. However, we keep F as a parameter in this chapter.

6.3 Leading-Order Solution

We expand u_0 and R_0 as

$$u_0(\bar{s}) = u_{00}(\bar{s}) + \epsilon u_{01}(\bar{s}) + \epsilon^2 u_{02}(\bar{s}) + O(\epsilon^3) \tag{6.12}$$

and

$$R_0(\bar{s}) = R_{00}(\bar{s}) + \epsilon R_{01}(\bar{s}) + \epsilon^2 R_{02}(\bar{s}) + O(\epsilon^3). \tag{6.13}$$

Hence at leading-order, we have the following inviscid equations

$$\frac{1}{2}u_{00}' R_{00} + u_{00} R_{00}' = 0 \tag{6.14}$$

and

$$u_{00}u_{00}' - \frac{1}{We}\left(\frac{R_{00}'}{R_{00}^2}\right) - \frac{1}{F^2} = 0. \tag{6.15}$$

The steady-state solutions of above two equations (6.14) and (6.15), using a Runga-Kutta 4th-order method, are shown in Figures 6.1-6.4.

Figures 6.1 and 6.2 show respectively that the leading-order radius R_{00} decreases and the leading-order velocity u_{00} increases, as Weber number We decreases (or as the surface tension increases). Figures 6.3 and 6.4 show respectively that the leading-order radius R_{00} decreases and the leading-order velocity u_{00} in-

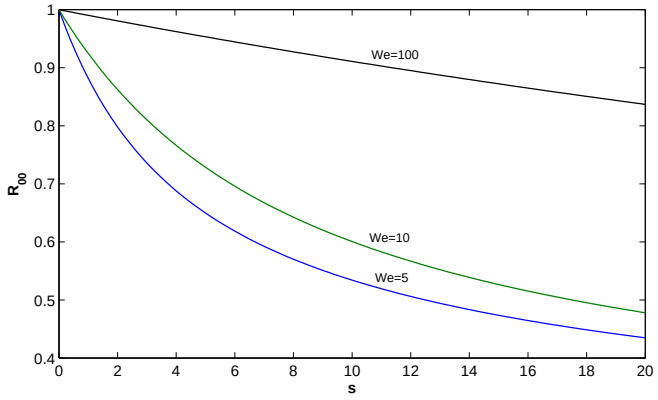

Figure 6.1: A graph showing the behaviour of the leading-order radius R_{00} of the jet plotted against the axial length s, for various Weber numbers. Here $F = 1$.

creases, as Froude number F decreases (or as the gravity increases). From Figures 6.1-6.4, we also note that the jet thins and accelerates, as it leaves the orifice, due to the gravity, which has also been observed in experiments (See Hawkins $et\ al.$ (2010) and Varga $et\ al.$ (2003)).

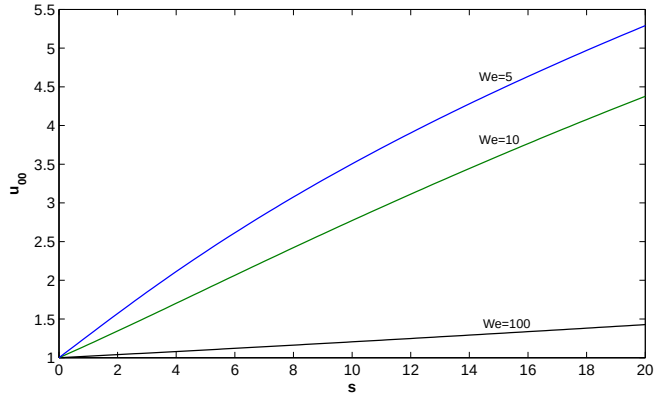

Figure 6.2: A graph showing the behaviour of the leading-order velocity u_{00} of the jet plotted against the axial length s, for various Weber numbers. Here $F = 1$.

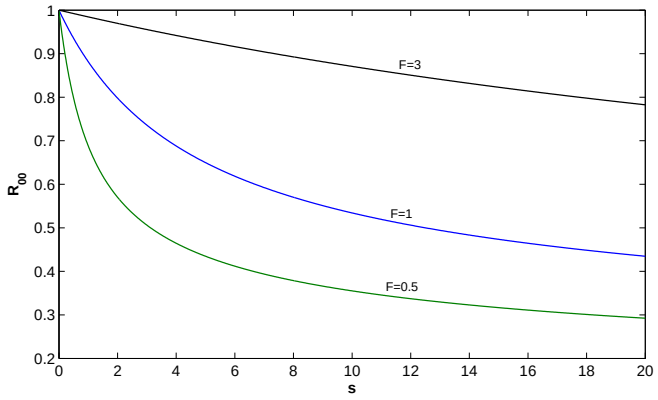

Figure 6.3: A graph showing the behaviour of the leading-order radius R_{00} of the jet plotted against the axial length s, for various Froude numbers. Here $We = 5$.

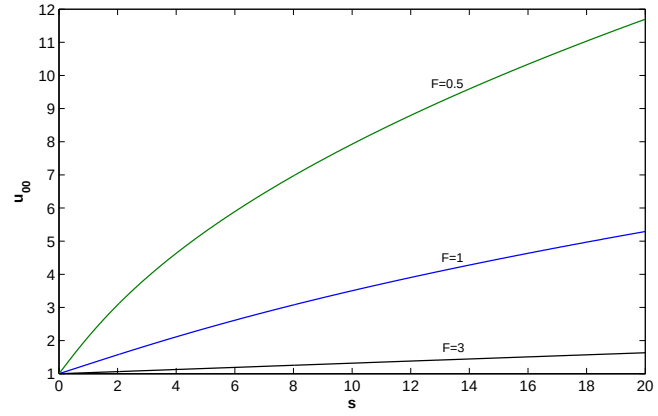

Figure 6.4: A graph showing the behaviour of the leading-order velocity u_{00} of the jet plotted against the axial length s, for various Froude numbers. Here $We = 5$.

6.4 Determination of the nonlinear travelling wave

Substituting equations (6.8) and (6.9) into equation (6.5), we obtain at leading-order in ϵ

$$h_0 = 2\zeta_0 \left(\frac{-g_0 + z g_{0,z} - u_{00} g_{0,z}}{R_{00} g_{0,z}} \right). \tag{6.16}$$

Putting $u_{00} = R_{00} = 1$ in equation (6.16), we get

$$h_0 = \zeta_0 \left(\frac{-2g_0 + 2z g_{0,z} - 2g_{0,z}}{g_{0,z}} \right), \tag{6.17}$$

which is the same equation (95) of Decent (2009). We expected to get this equation as it corresponds to the problem described in Decent (2009) with no gravity in which $u_{00} = R_{00} = 1$.

Substituting equations (6.8), (6.9) and (6.16) into equation (6.7), we obtain a nonlinear ordinary differential equation for g_0 in z, at leading-order in ϵ, of the form

$$ReR_{00} \left(g_{0,z}\right)^4 + \frac{Re}{R_{00}} \left(g_{0,z}\right)^2 - 4zReWeg_0 g_{0,z} + 2z^2 ReWe \left(g_{0,z}\right)^2 - 4zReWeu_{00} \left(g_{0,z}\right)^2$$

$$+4ReWeu_{00} g_0 g_{0,z} + 2ReWeu_{00}^2 \left(g_{0,z}\right)^2 + 2ReWe \left(g_0\right)^2 + 6Weg_0 \left(g_{0,z}\right)^2 - 6Wez \left(g_{0,z}\right)^3$$

$$+6Weu_{00} \left(g_{0,z}\right)^3 = 0. \tag{6.18}$$

Putting $u_{00} = R_{00} = 1$ in equation (6.18), we get

$$Re\left(g_{0,z}\right)^4+Re\left(g_{0,z}\right)^2-4zReWeg_0g_{0,z}+2z^2ReWe\left(g_{0,z}\right)^2-4zReWe\left(g_{0,z}\right)^2+4ReWeg_0g_{0,z}$$

$$+2ReWe\left(g_{0,z}\right)^2+2ReWe\left(g_0\right)^2+6Weg_0\left(g_{0,z}\right)^2-6Wez\left(g_{0,z}\right)^3+6We\left(g_{0,z}\right)^3=0,$$

which is the same equation (92) of Decent (2009).

Solving equation (6.18), for large Reynolds number (i.e., $Re\rightarrow\infty$), gives

$$g_0=\frac{\sqrt{Q_0}}{4\sqrt{We}R_{00}^{3/2}} \tag{6.19}$$

where

$$Q_0=-We^2u_{00}^4R_{00}^2-10z^2WeR_{00}+20zWeu_{00}R_{00}-10Weu_{00}^2R_{00}-6z^2We^2u_{00}^2R_{00}^2$$

$$-z^4We^2R_{00}^2+2+4z^3We^2u_{00}R_{00}^2+4zWe^2u_{00}^3R_{00}^2$$

$$-\sqrt{R_{00}We\left(z-u_{00}\right)^2\left(Weu_{00}^2R_{00}-2zWeu_{00}R_{00}+z^2WeR_{00}-4\right)^3}. \tag{6.20}$$

Putting $u_{00}=R_{00}=1$ in equations (6.19) and (6.20), we get

$$g_0=\frac{\sqrt{Q_0}}{4\sqrt{We}} \tag{6.21}$$

where

$$Q_0=-We^2-10z^2We+20zWe-10We-6z^2We^2-z^4We^2+2+4z^3We^2$$

$$+4zWe^2 - \sqrt{We\,(z-1)^2\,(We-2zWe+z^2We-4)^3}, \tag{6.22}$$

which are the same equations (112) and (113) of Decent (2009).

Recall that, for negative values of g_0, the real part of g_0 is $the\ temporal\ growth\ rate$ and, for positive values, it is $the\ temporal\ decay\ rate$. In addition, the imaginary part of g_0 is $the\ local\ frequency$ of the nonlinear travelling wave. Further more, recall that that Decent (2009) graphically found that there is a range of values of z for which the real part of g_0 is negative and in that range, the asymptotic expansions become non-uniform at large t. This range of values is denoted by $z_1 < z < z_2$. In addition, Decent (2009) found that $z_1 \to max\left(1 - 2/\sqrt{We}, 0\right)$ and $z_2 \to 1 + 2/\sqrt{We}$ as $Re \to \infty$.

In our case, we find from equations (6.19) and (6.20), that

$$z_1 \to max\left(u_{00} - 2/\sqrt{R_{00}We}, 0\right) \text{ and } z_2 \to u_{00} + 2/\sqrt{R_{00}We} \text{ as } Re \to \infty.$$

These values of z_1 and z_2 corresponds to the same values of of z_1 and z_2 of Decent (2009) in the limit $u_{00} = 1$ and $R_{00} = 1$.

6.4.1 Behaviour for small z

We next examine the solutions in this region as $z \to 0$ (as we want to have the initial conditions for $g_0(z)$). We pose

$$g_0 = M_0 + M_1 z + M_2 z^2 + O\left(z^3\right) \tag{6.23}$$

as $z \to 0$. We substitute the above equation into the g_0-equation (6.18), and we find at leading-order

$$ReR_{00}M_1^4 + ReR_{00}^{-1}M_1^2 + 4ReWeu_{00}M_1M_0 + 6Weu_{00}M_1^3$$

$$+6WeM_1^2M_0 + 2ReWeM_0^2 + 2ReWeu_{00}^2M_1^2 = 0, \tag{6.24}$$

which is the same equation (102) of Decent (2009) in the limit $u_{00} = 1$ and $R_{00} = 1$.

At the next-order in this expansion, we find that either $M_2 = 0$ or that

$$2ReR_{00}M_1^3 + ReR_{00}^{-1}M_1 + 2ReWeu_{00}^2M_1$$

$$+2ReWeu_{00}M_0 + 6WeM_1M_0 + 9Weu_{00}M_1^2 = 0, \tag{6.25}$$

which is the same equation (110) of Decent (2009) in the limit $u_{00} = 1$ and $R_{00} = 1$.

Hence we have two simultaneous equations (6.24) and (6.25) for M_0 and M_1. Note that differentiating equation (6.24) with respect to M_1 gives equation (6.25).

We solve equations (6.24) and (6.25) in some asymptotic limits to find M_0 and M_1. For $Re \to \infty$, we find

$$M_0 = -\frac{M_1}{2u_{00}We}\left(R_{00}^{-1} + 2R_{00}M_1^2 + 2u_{00}^2We\right) + O\left(\frac{1}{Re}\right) \tag{6.26}$$

and

$$M_1 = \pm\frac{1}{2R_{00}}\sqrt{-2 - u_{00}^2R_{00}We \pm \sqrt{u_{00}^4R_{00}^2We^2 - 4u_{00}^2R_{00}We}}$$

$$+ O\left(\frac{1}{Re}\right), \tag{6.27}$$

where the $\pm$ alternatives can be taken in any combination to satisfy equations (6.24) and (6.25). Note that the above two equations correspond to equations

(123) and (122) of Decent (2009) in the limit $u_{00} = 1$ and $R_{00} = 1$.

We now solve equations (6.24) and (6.25) for $We \to 0$. This is found to give

$$M_0 = -M_1 \left(\frac{2u_{00}^2 Re + 9u_{00} M_1}{2u_{00} Re + 6M_1} \right) + O\left(We\right) \tag{6.28}$$

and

$$M_1 = \pm \frac{i}{\sqrt{2}\, R_{00}} + O\left(We\right), \tag{6.29}$$

which correspond to equations (125) and (124) of Decent (2009) in the limit $u_{00} = 1$ and $R_{00} = 1$.

6.5 Computational Solution

We next solve equations (6.24) and (6.25) without any asymptotic limits to find M_0 and M_1 computationally and then we use these values of M_0 and M_1 as the initial conditions for $g_0(z)$. Hence we solve g_0-equation (6.18), with the initial conditions

$$g_0(z = 0) = M_0 \text{ and } g_0'(z = 0) = M_1,$$

for both $Re = O\left(1\right)$ and $We = O\left(1\right)$, computationally using a Runga-Kutta fourth-order method. We next present the results in the following figures. Note that when we change s, then $u_0(s)$ and $R_0(s)$ will also change, resulting a change in M_0 and M_1 (as $M_0 = M_0(u_0, R_0)$ and $M_1 = M_1(u_0, R_0)$), which in turn will change g_0.

Figure 6.5 shows that as we increase s, the solution of the g_0-equation is shifted to higher values of z, giving more time to break the jet before $z = z_1$. Figure 6.6 shows that at $z = z_3$, the solution of the g_0-equation changes its sign. Also note that $z = z_3$ remains at the same point in the real and imaginary solutions of g_0.

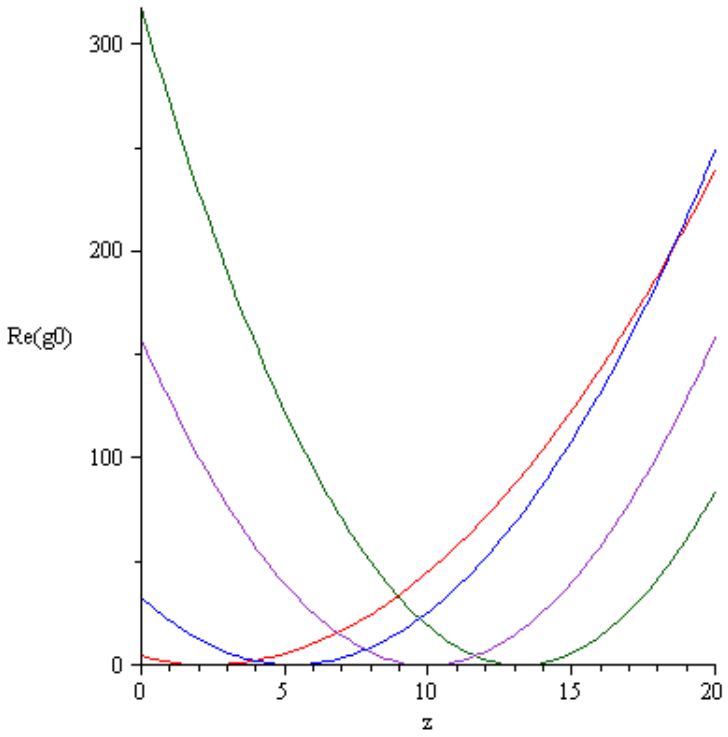

Figure 6.5: A graph showing the real part of the solution $Re(g_0)$ plotted against z, red for $s = 5$, blue for $s = 20$, pink for $s = 60$ and green for $s = 100$. We note that for larger values of s, the curves are translated along the z-axis. Here $We = 10$ and $Re = 15$.

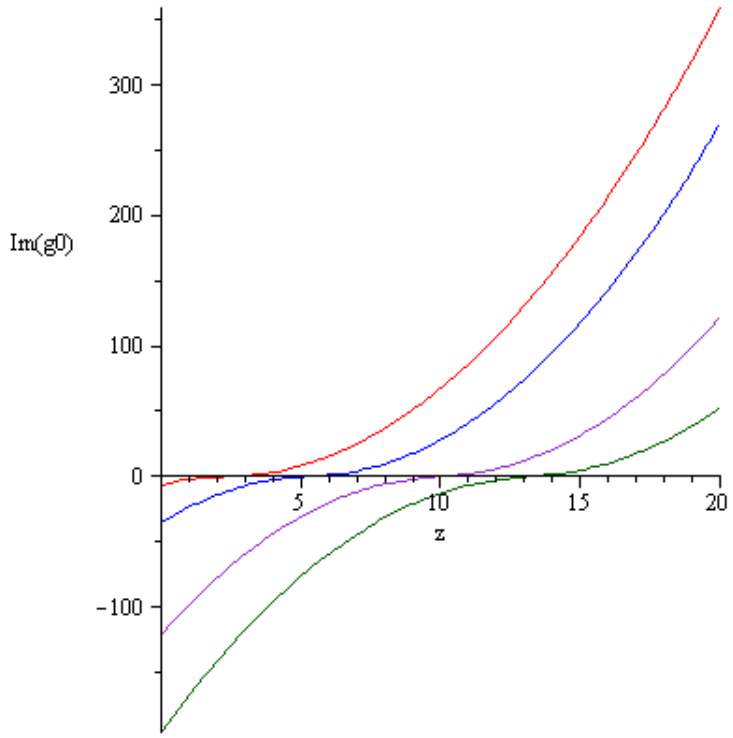

Figure 6.6: A graph showing the imaginary part of the solution $Im(g_0)$ plotted against z, red for $s = 5$, blue for $s = 20$, pink for $s = 60$ and green for $s = 100$. We again note that for larger values of s, the curves are translated along the z-axis. Here $We = 10$ and $Re = 15$.

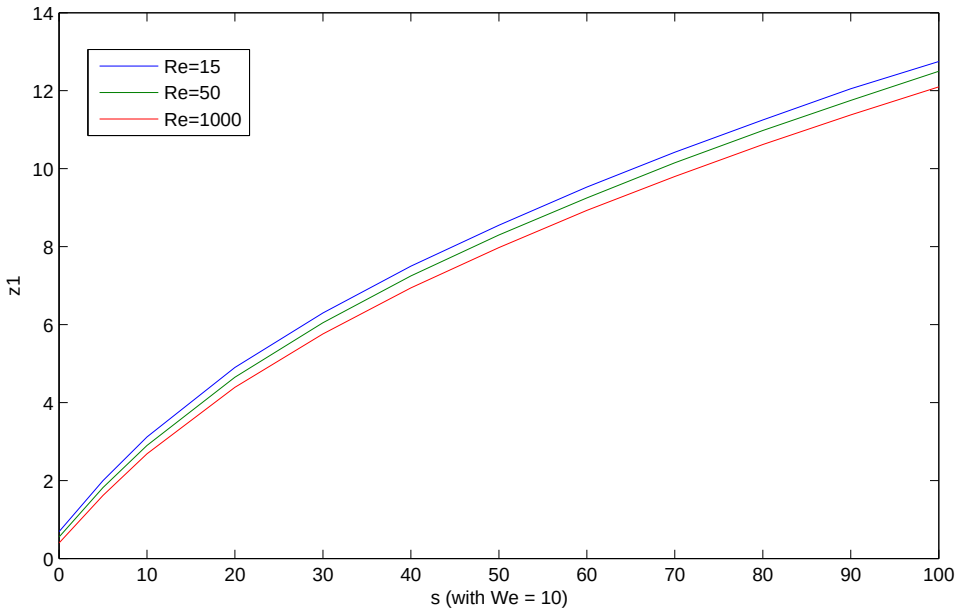

Figure 6.7: A graph between s and z_1 for We = 10.

Recall that z_1 is the place where the nonlinear waves start to dominate, while at z_2 we have a mixture of both linear and nonlinear waves and at z_3, the instability is at its maximum value. We now plot some graphs of s against z_1, z_2, z_3 and Real $(g_0(z_3))$.

Note that since $Im(g_0(z_3)) = 0$, at z-axis, for all values of We and Re, so we do not need to plot graph of s against $Im(g_0(z_3))$ as it will be a straight line on s-axis. Also note that

$$Real(g_0(z_3)) = Im(g_0(z_3)), \text{at } z - \text{axis}.$$

Figure 6.7 shows that z_1 increases as s increases and z_1 decreases with increasing values of Re. Figure 6.8 shows that z_1 increases as s increases and z_1 also increases with increasing values of We. Note that in order to get the uniform droplets with no satellite droplets, linear waves must dominate in the jet's breakup

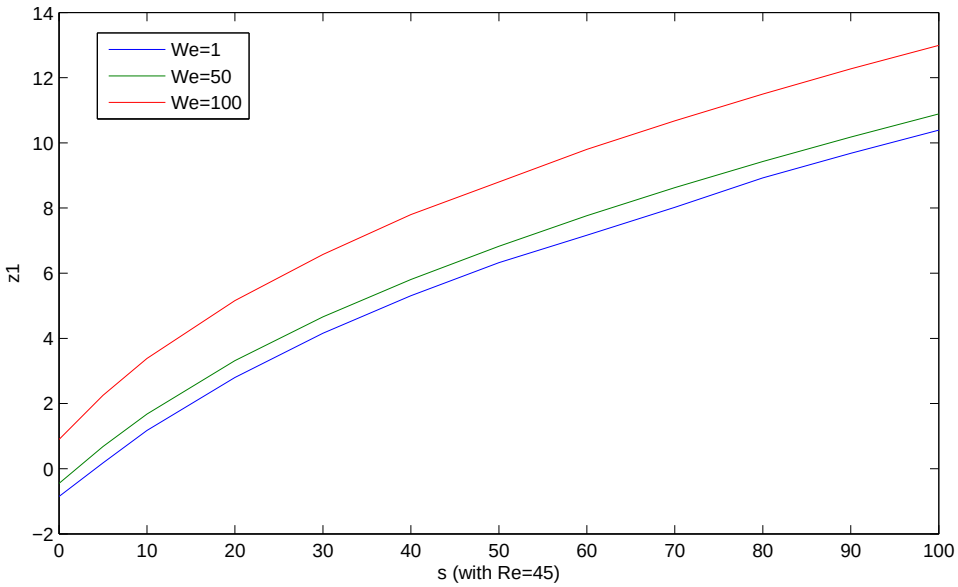

Figure 6.8: A graph between s and z_1 for $Re = 45$.

process. The linear waves remain dominant as the jet come out of the orifice until the point z_1. We, therefore, must have a large value z_1 so that we can easily break our jet before z_1. We have found, from Figures 6.7 and 6.8 respectively, that in order to get a large value of z_1, we must have a small value of Re and a large value of We.

Figure 6.9 shows that z_2 increases as s increases and z_2 also increases with increasing values of Re. Figure 6.10 shows that z_2 increases as s increases and z_2 decreases with increasing values of We. Figures 6.11 and 6.12 show that z_3 increases as s increases and z_3 is not affected by increasing Re and We. Figure 6.13 shows that Real $(g_0(z_3))$ decreases as s increases and Real $(g_0(z_3))$ also decreases with increasing values of Re. Figure 6.14 shows that Real $(g_0(z_3))$ decreases as s increases and Real $(g_0(z_3))$ increases with increasing values of We.

We now compare our results with those given in Decent (2009). The following figures 6.15 and 6.16 show that our results are in perfect agreement with those

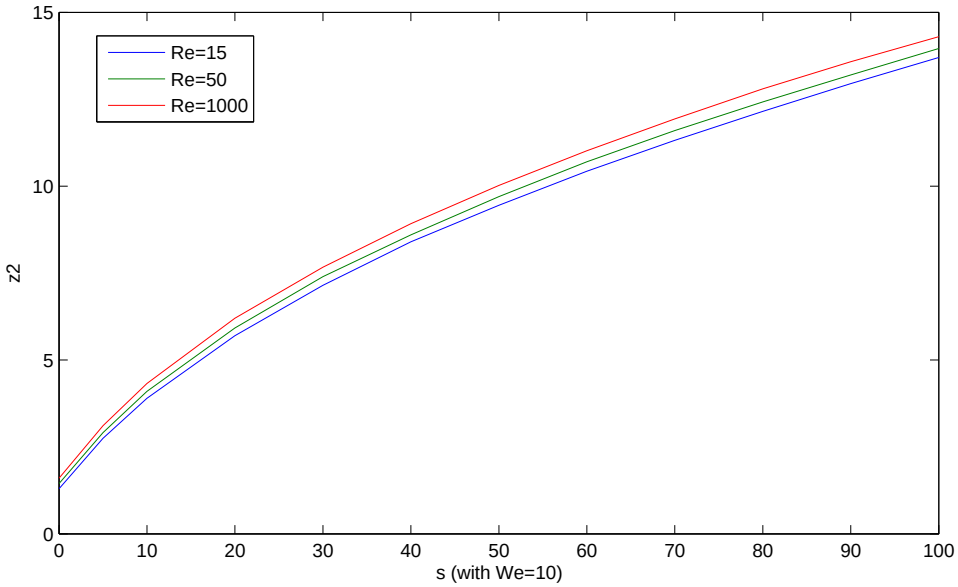

Figure 6.9: A graph between s and z_2 for $We = 10$.

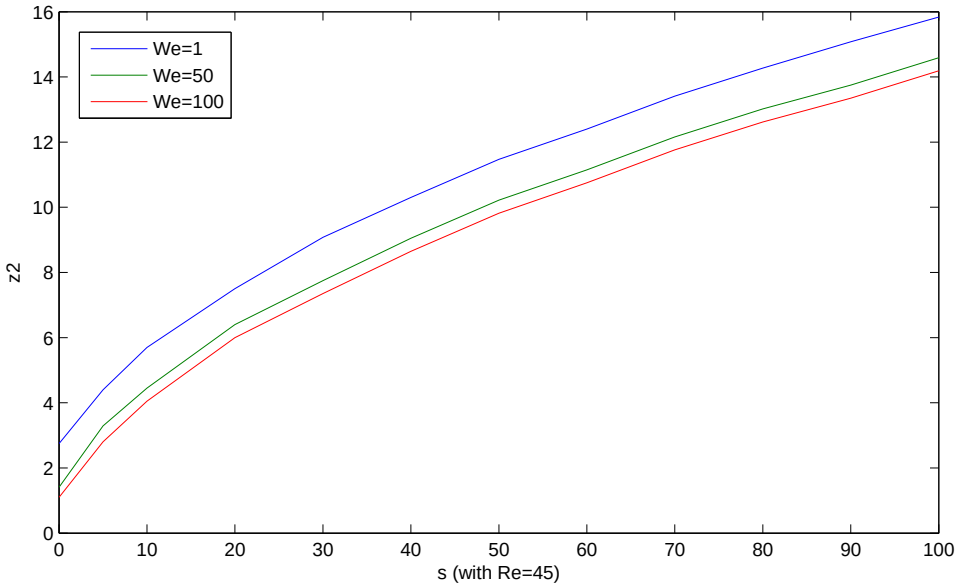

Figure 6.10: A graph between s and z_2 for $Re = 45$.

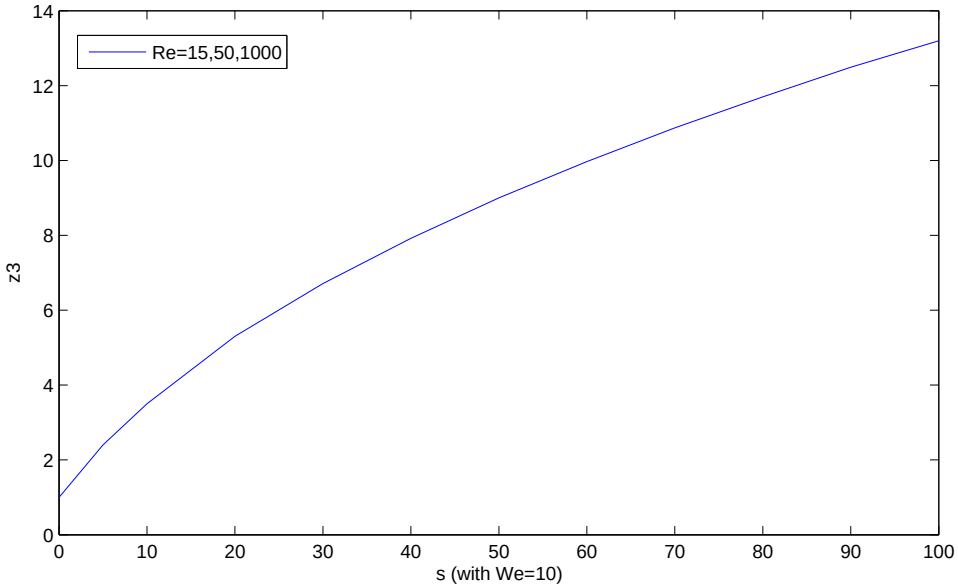

Figure 6.11: A graph between s and z_3 for $We = 10$.

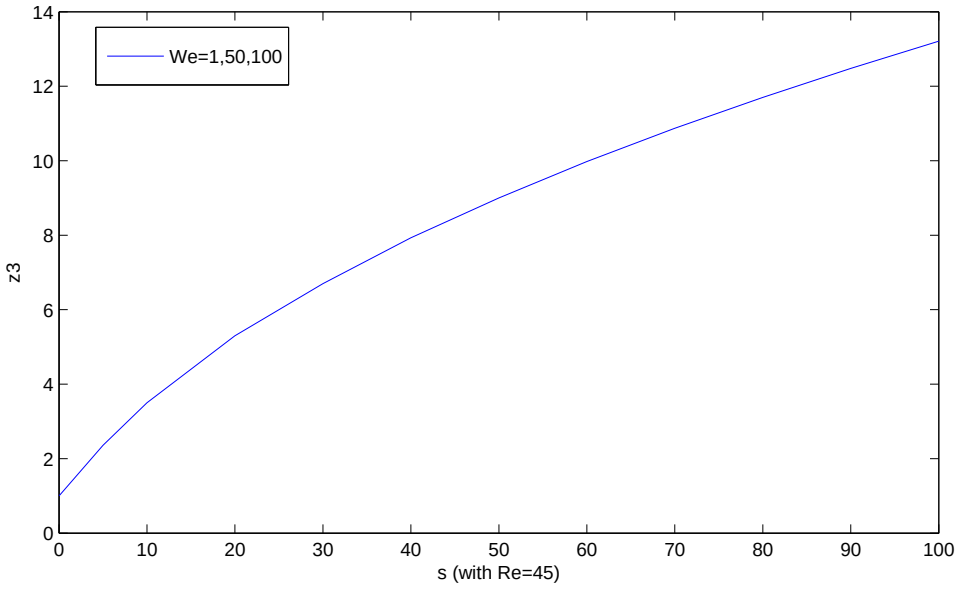

Figure 6.12: A graph between s and z_3 for $Re = 45$.

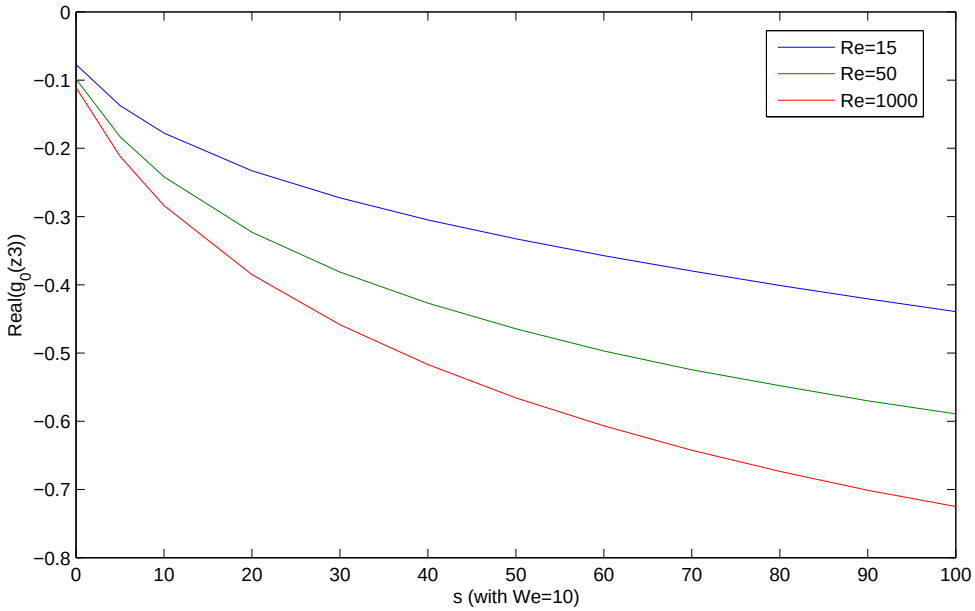

Figure 6.13: A graph between s and Real $(g_0(z_3))$ for We = 10.

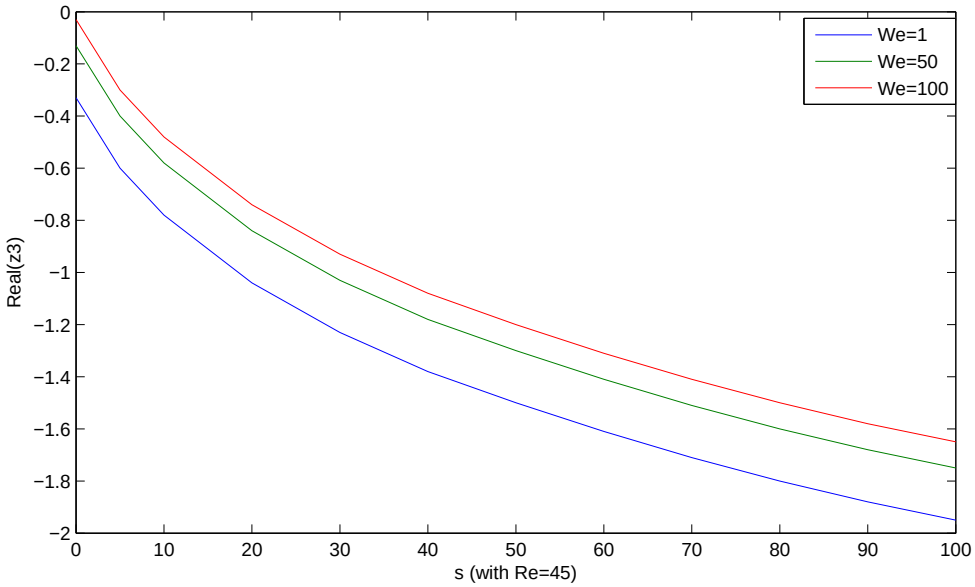

Figure 6.14: A graph between s and Real $(g_0(z_3))$ for Re = 45.

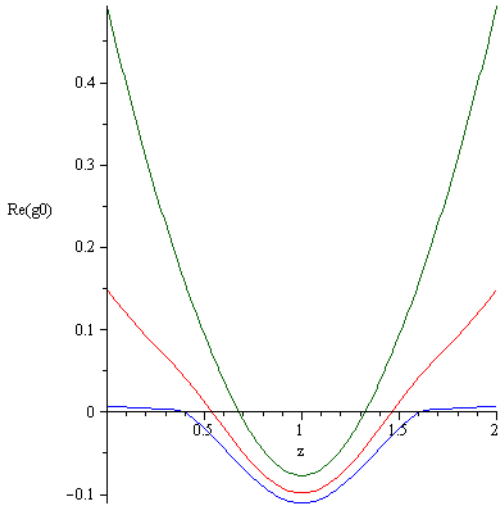

Figure 6.15: The real part of g_0 plotted against z with $s = 0$ for $We = 10$ for $Re = 15$ (green curve on top), 50 (red curve on middle) and 1000 (blue curve on bottom). This figure is exactly the same as figure 9 of Decent (2009).

given in Decent (2009). Also, we can see that for large values of s, the curves are translated along the z-axis, as shown in figures 6.17 and 6.18.

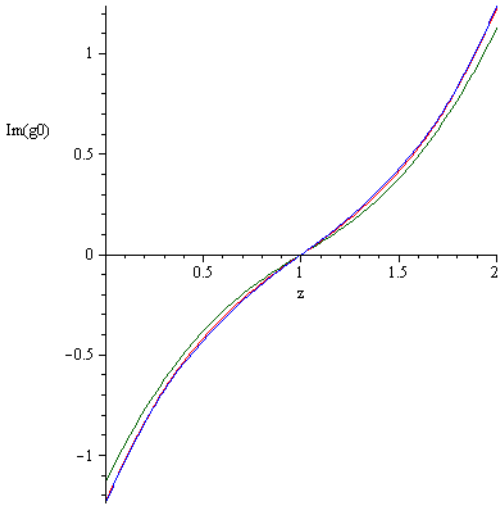

Figure 6.16: The imaginary part of g_0 plotted against z with $s = 0$ for $We = 10$ for $Re = 15$ (green curve on top for $z < 0$; bottom for $z > 0$), 50 (red curve on middle) and 1000 (blue curve on bottom for $z < 0$; top for $z > 0$). This figure is exactly the same as figure 10 of Decent (2009).

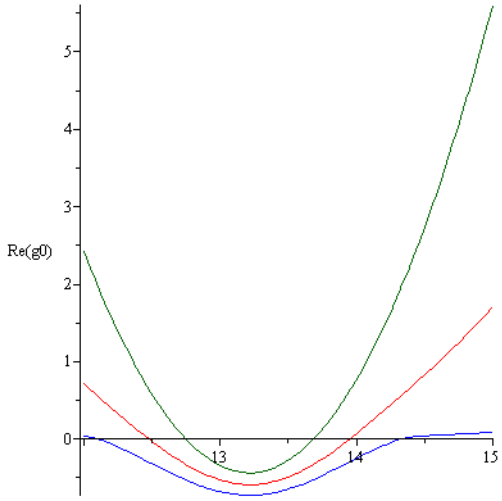

Figure 6.17: The real part of g_0 plotted against z with $s = 100$ for $We = 10$ for $Re = 15$ (green curve on top), 50 (red curve on middle) and 1000 (blue curve on bottom).

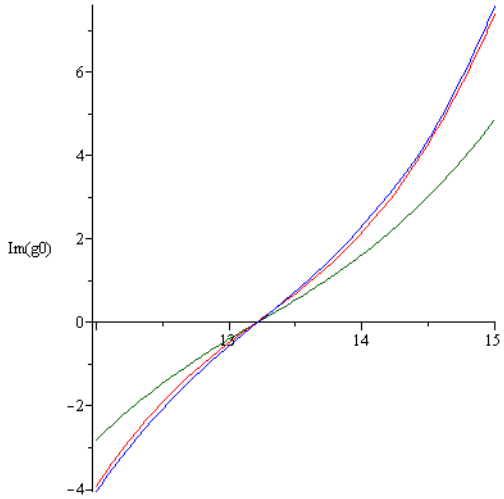

Figure 6.18: The imaginary part of g_0 plotted against z with $s = 100$ for $We = 10$ for $Re = 15$ (green curve on top for $z < 0$; bottom for $z > 0$), 50 (red curve on middle) and 1000 (blue curve on bottom for $z < 0$; top for $z > 0$).

6.6 Linear Waves Regime Analysis

We next examine this problem in region V (the linear waves section), where $\tilde{t} \to \infty$ and $\tilde{s} = O(1)$. We remove tildes and pose the following expansions

$$u = u_0(s, \bar{s}) + \delta \exp(i\omega t) \left(\Gamma_0(s, \bar{s}) + O\left(\frac{1}{\sqrt{t}}\right) \right) + O\left(\delta^2\right) + c.c. \quad (6.30)$$

and

$$R = R_0(s, \bar{s}) + \delta \exp(i\omega t) \left(\Omega_0(s, \bar{s}) + O\left(\frac{1}{\sqrt{t}}\right) \right) + O\left(\delta^2\right) + c.c., \quad (6.31)$$

where $c.c.$ denotes complex conjugate, $\bar{s} = \epsilon s$, $\delta \to 0$ and $\delta << \epsilon$.

Note that we if we have $u = u_0(\bar{s})$ and $R = R_0(\bar{s})$, where $\bar{s} = \epsilon s$, then as $\epsilon \to 0$, we have $\bar{s} \to 0$. This gives $u_0(\bar{s} = 0) = 1$ and $R_0(\bar{s} = 0) = 1$ from the boundary conditions and this corresponds to no-gravity problem. This cannot be true as we have gravity in our problem.

Substituting the above two expansions into equations (6.5) and (6.7) and taking the limits $t \to \infty$, $\delta \to 0$ and $\epsilon \to 0$ gives at leading-order the same equations (6.5) and (6.7) being satisfied while $O(\delta)$ gives

$$2i\omega\Omega_N + R_0\Gamma_{N,s} + 2u_0\Omega_{N,s} = 0, \tag{6.32}$$

and

$$i\omega ReWe\Gamma_N + u_0 ReWe\Gamma_{N,s} - \frac{Re\Omega_{N,s}}{R_0^2} - Re\Omega_{N,sss} - 3We\Gamma_{N,ss} = 0, \tag{6.33}$$

for $N = 0, 1$.

Putting $u_0 = R_0 = 1$ in equations (6.32) and (6.33), we get

$$2i\omega\Omega_N + \Gamma_{N,s} + 2\,\Omega_{N,s} = 0, \tag{6.34}$$

and

$$i\omega ReWe\Gamma_N + ReWe\Gamma_{N,s} - Re\Omega_{N,s} - Re\Omega_{N,sss} - 3We\Gamma_{N,ss} = 0, \tag{6.35}$$

which are the same equations (128) and (129) of Decent (2009).

Equations (6.32) and (6.33) have the general solutions

$$\Gamma_N = \hat{\Gamma}_{1+4N}(\bar{s})\ \exp(k_1 s) + \hat{\Gamma}_{2+4N}(\bar{s})\ \exp(k_2 s) + \hat{\Gamma}_{3+4N}(\bar{s})\ \exp(k_3 s)$$

$$+ \hat{\Gamma}_{4+4N}(\bar{s})\ \exp(k_4 s) \tag{6.36}$$

and

$$\Omega_N = \hat{\Omega}_{1+4N}(\bar{s})\ \exp(k_1 s) + \hat{\Omega}_{2+4N}(\bar{s})\ \exp(k_2 s) + \hat{\Omega}_{3+4N}(\bar{s})\ \exp(k_3 s)$$

$$+ \hat{\Omega}_{4+4N}(\bar{s})\ \exp(k_4 s), \tag{6.37}$$

where k_1, k_2, k_3 and k_4 are the four solutions of the linear dispersion relationship between k and ω which is given by

$$k^4 R_0^2 Re + k^2 Re - 2\omega^2 R_0 ReWe + 4i\omega k u_0 R_0 ReWe - 6i\omega k^2 R_0 We$$

$$+2k^2 u_0^2 R_0 ReWe - 6k^3 u_0 R_0 We = 0. \tag{6.38}$$

That is, the above equation has the solutions $k = k_1, k_2, k_3, k_4$. Putting $u_0 = 1$ and $R_0 = 1$ in equation (6.38), we get

$$k^4 Re + k^2 Re - 2\omega^2 ReWe + 4i\omega k ReWe - 6i\omega k^2 We$$

$$+2k^2 ReWe - 6k^3 We = 0, \tag{6.39}$$

which is the same equation (132) of Decent (2009).

6.6.1 Derivation of Dispersion Relation by Matching

Note that the linear dispersion relation (6.38) can also be derived as follows. We do matching of regions IV and V to get the value of g_0 as

$$g_0 = -(i\omega + kz).$$

We next substitute this value of g_0 into the g_0-equation (6.18) and we then have

$$k^4 R_0^2 Re + k^2 Re - 2\omega^2 R_0 ReWe + 4i\omega k u_0 R_0 ReWe - 6i\omega k^2 R_0 We$$

$$+2k^2 u_0^2 R_0 ReWe - 6k^3 u_0 R_0 We = 0, \tag{6.40}$$

which is the same equation (6.38). We also find the relationship between $\hat{\Gamma}_j$ and $\hat{\Omega}_j$ (for $j = 1, 2, ...8$) which is given by

$$\hat{\Gamma}_j = -\frac{2\hat{\Omega}_j \left(i\omega + u_0 k_{j-4N}\right)}{R_0 k_{j-4N}} \tag{6.41}$$

for $j = 1, 2, ..., 8$ and $N = 0, 1$. This equation (6.41) corresponds to equation (133) of Decent (2009) in the limit of $u_0 = R_0 = 1$.

The boundary conditions at $s = 0$ are $R = 1$ and $u = 1 + \delta \sin(\omega t)$. Using these boundary conditions in expansions (6.30) and (6.31), we obtain

$$\hat{\Omega}_1 + \hat{\Omega}_2 + \hat{\Omega}_3 + \hat{\Omega}_4 = 0, \tag{6.42}$$

$$\hat{\Omega}_5 + \hat{\Omega}_6 + \hat{\Omega}_7 + \hat{\Omega}_8 = 0, \tag{6.43}$$

$$\hat{\Gamma}_1 + \hat{\Gamma}_2 + \hat{\Gamma}_3 + \hat{\Gamma}_4 = -\frac{i}{2} \tag{6.44}$$

and

$$\hat{\Gamma}_5 + \hat{\Gamma}_6 + \hat{\Gamma}_7 + \hat{\Gamma}_8 = 0. \tag{6.45}$$

6.7 Conclusions

In this chapter, we have extended the Needham-Leach method to the viscous-gravity problem. We have noticed that we do not need to examine regions, I, II, and III as they give the same results as in Decent (2009). We have successfully examined this problem in the crucial region IV (the nonlinear waves section) and obtained steady-state solutions for the velocity and the radius, with the information that as the distance s increases (i.e., as the jet flows away from the orifice), the jet's velocity component (parallel to the centreline of the jet) increases while the jet's radius decreases, which shows perfect agreement with the experimental observations.

In addition, we have obtained a fourth-order ODE (6.18) for $g_0(z)$, which describes the behaviour of the nonlinear wave. We first solved that ODE for large Reynolds number (i.e., $Re \to \infty$) and obtained solution for $g_0(z)$. This solution gives us the value of z_1 (where the nonlinear waves start to dominate), the value of z_2 (where we have a mixture of both linear and nonlinear waves) and the value of z_3 (where the instability is at its maximum value). From this, we postulate that in order to obtain the uniform droplets with no or few satellite droplets, we must break the jet before $z = z_1$, so that the linear waves dominate in the breakup process. Note that all of our results correspond perfectly to results in Decent (2009) with no gravity (i.e., in the limit of $u_0 = R_0 = 1$).

We next examined the solution for small z (i.e., $z \to 0$) and obtained the initial conditions for $g_0(z)$ as

$$g_0(z = 0) = M_0 \text{ and } g_0'(z = 0) = M_1,$$

where we found M_0 and M_1 first with asymptotic limits $Re \to \infty$ and $We \to 0$ and next computationally for $Re = O(1)$ and $We = O(1)$. So we have an

initial value problem (i.e., equation (6.18) for $g_0(z)$ with the above known initial conditions) and then we solved this initial value problem computationally, using a Runge-Kutta fourth-order method, which gives us the solutions for $g_0(z)$, both for $Re = O(1)$ and $We = O(1)$.

We also obtained various graphs for z_1 against s, z_2 against s, z_3 against s and $Real(z_3)$ against s, both for $Re = O(1)$ and $We = O(1)$. We also note that the larger z_1 is, the easier it will be to break the jet before z_1, so that the linear waves dominate in the breakup process and hence we can get only uniform droplets. Therefore, our asymptotic theory alone (without any numerics or experiments) tells us how we can obtain only the uniform droplets, which is a big achievement. For that to happen, we discovered (from the graphs of z_1 against s with various Re and We) that we must have a large value of We and a small value of Re.

At the end, we also considered region V (the linear waves section) and we found a linear dispersion relation linking the wavenumber k and the frequency ω, which corresponds to the dispersion relation of Decent (2009) in the limit $u_0 = R_0 = 1$. Moreover, we have also derived the same dispersion relation in another way, by doing the asymptotic matching of regions IV and V. In addition, we also found the solution in this region, which corresponds to the solution of Decent (2009) in the limit $u_0 = R_0 = 1$, showing concrete validation of our work.

Chapter 7

Asymptotic Solution of Rotating Newtonian Liquid Jet

7.1 Introduction

In this chapter, we investigate the rotating Newtonian liquid jets. Our hypothesis is that the jet breakup can be more easily controlled if it breaks up in the regime where $z < z_1$. In order to support our hypothesis, we shall use together the Needham-Leach method, to obtain the g_0-equation, and a numerical model, based on the Lax-Wendroff method to obtain the shape of the mode and the breakup point.

7.2 Problem Statement

The model equations for a rotating downward falling Newtonian jet, falling from a large rotating cylindrical drum and ignoring the effects of gravity, are given by

$$R_t + \frac{1}{2}u_s R + uR_s = 0 \tag{7.1}$$

and

$$u_t + uu_s + \frac{1}{We}\left(\frac{1}{R(1+\epsilon^2 R_s^2)^{\frac{1}{2}}} - \frac{\epsilon^2 R_{ss}}{(1+\epsilon^2 R_s^2)^{\frac{3}{2}}}\right)_s$$
$$-\frac{3\epsilon}{Re}\cdot\frac{1}{R^2}\left[\frac{\partial}{\partial s}\left(R^2\frac{\partial u}{\partial s}\right)\right] - \left[\frac{(X+1)X_s + ZZ_s}{Rb^2}\right] = 0, \tag{7.2}$$

where $u(s,t)$ is the velocity component parallel to the centreline of the jet, $R(s,t)$ is the distance of the axi-symmetric free-surface away from the jet's centreline, s is the distance along the jet's centreline from the orifice (i.e., s is the arc length along the jet) and X and Z are the jet centreline coordinates, so that the centreline of the jet can be described by $x = X(s,t)$ and $z = Z(s,t)$. In these equations, the subscripts denote differentiation with respect to that subscript and t is time. These equations have been derived in Partridge (2006). In these equations, the non-dimensional parameters are the Weber number which is $We = \rho a U^2/\sigma > 0$, the Reynolds number which is $Re = \rho a U/\mu = \rho U s_0 \epsilon/\mu$ and the Rossby number which is $Rb = U/s_0\Omega$, where the liquid's density is ρ, the liquid's viscosity is μ, the surface tension of the liquid-gas interface is σ, the radius of the large cylindrical drum is s_0, the radius of the small orifice is a, the exit speed of the jet is U, Ω is the rotation rate and ϵ is a small parameter defined as

$$\epsilon = a/s_0 << 1.$$

Note that in the previous chapter, we have $\tilde{Re} = \rho a U/\mu = \epsilon\frac{\rho U L}{\mu}$ which is consistent here in this chapter as $Re = \rho a U/\mu = \rho U s_0 \epsilon/\mu$, where $s_0 = L$.

We define $\tilde{s}$ and $\tilde{t}$ as

$$\tilde{s} = \frac{s}{\epsilon}, \qquad \tilde{t} = \frac{t}{\epsilon}.$$

So equation (7.1) can be written as

$$\frac{1}{\epsilon}R_{\tilde{t}} + \frac{1}{\epsilon}\frac{R}{2}u_{\tilde{s}} + \frac{1}{\epsilon}uR_{\tilde{s}} = 0,$$

or

$$R_{\tilde{t}} + \frac{R}{2}u_{\tilde{s}} + uR_{\tilde{s}} = 0. \tag{7.3}$$

Similarly, equation (7.2) can be written as

$$\begin{aligned}\frac{1}{\epsilon}[u_{\tilde{t}} + uu_{\tilde{s}}] = \frac{1}{\epsilon}[-\frac{1}{We}\left(\frac{1}{R(1+R_{\tilde{s}}^2)^{\frac{1}{2}}} - \frac{R_{\tilde{s}\tilde{s}}}{(1+R_{\tilde{s}}^2)^{\frac{3}{2}}}\right)_{\tilde{s}} \\ +\frac{3\epsilon}{Re\,\epsilon}\cdot\frac{1}{R^2}\left[\frac{\partial}{\partial\tilde{s}}\left(R^2\frac{\partial u}{\partial\tilde{s}}\right)\right] + \left[\frac{(X+1)X_{\tilde{s}} + ZZ_{\tilde{s}}}{Rb^2}\right]],\end{aligned}$$

or

$$\begin{aligned}u_{\tilde{t}} + uu_{\tilde{s}} = -\frac{1}{We}\left(\frac{1}{R(1+R_{\tilde{s}}^2)^{\frac{1}{2}}} - \frac{R_{\tilde{s}\tilde{s}}}{(1+R_{\tilde{s}}^2)^{\frac{3}{2}}}\right)_{\tilde{s}} \\ +\frac{3}{Re}\cdot\frac{1}{R^2}\left[\frac{\partial}{\partial\tilde{s}}\left(R^2\frac{\partial u}{\partial\tilde{s}}\right)\right] + \left[\frac{(X+1)X_{\tilde{s}} + ZZ_{\tilde{s}}}{Rb^2}\right].\end{aligned} \tag{7.4}$$

The non-dimensional initial conditions are

$$R\left(\epsilon\tilde{s}, \epsilon\tilde{t} = 0\right) = 1 \quad \text{and} \quad u\left(\epsilon\tilde{s}, \epsilon\tilde{t} = 0\right) = 1.$$

The boundary conditions at the orifice are

$$R\left(\epsilon\tilde{s} = 0, \epsilon\tilde{t}\right) = 1 \quad \text{and} \quad u\left(\epsilon\tilde{s} = 0, \epsilon\tilde{t}\right) = 1 + \delta\sin\left(\omega\epsilon\tilde{t}\right).$$

We define u_0 and R_0 as the steady-state solution of equations (7.3) and (7.4). We also assume that $u \to u_0$ and $R \to R_0$ as $\tilde{s} \to \infty$, which physically means that in

the far-field, the jet is considered to be undisturbed.

7.3 Asymptotic Expansions

Note that now our original equations are in $\tilde{s}$ and $\tilde{t}$. We examine this problem in region IV (the nonlinear waves section), where $\tilde{s} \to \infty$ and $\tilde{t} \to \infty$ so that $z = \tilde{s}/\tilde{t} = O(1)$. We introduce a new length scale $\bar{s}$, defined by

$$\bar{s} = \epsilon\tilde{s} = O(1), \text{ as } \epsilon \to 0.$$

We introduce this notation $\bar{s}$ to remain consistent with the previous chapter's work. We pose the following expansions

$$u = u_0(\bar{s}) + \left[\exp\left(-tg_0\left(z,\bar{s}\right)\right)\left\{h_0\left(z,\bar{s}\right) + O\left(\frac{1}{\sqrt{t}}\right)\right\} + h.o.t.\right] \tag{7.5}$$

and

$$R = R_0(\bar{s}) + \left[\exp\left(-tg_0\left(z,\bar{s}\right)\right)\left\{\zeta_0\left(z,\bar{s}\right) + O\left(\frac{1}{\sqrt{t}}\right)\right\} + h.o.t.\right], \tag{7.6}$$

as $\tilde{t} \to \infty$ and $h.o.t.$ denotes higher-order terms. The steady-state equations for u_0 and R_0 can be obtained from equations (7.3) and (7.4), using $\bar{s} = \epsilon\tilde{s}$, and are given by

$$\epsilon(\frac{1}{2}u_0'R_0 + u_0R_0') = 0, \tag{7.7}$$

$$\epsilon u_0u_0' + \frac{1}{We}\left(\frac{-\epsilon R_0'}{R_0^2(1+\epsilon^2R_0'^2)^{\frac{1}{2}}} - \frac{\epsilon^3R_0'R_0''(R_0^{-1}) + \epsilon^3R_0'''}{(1+\epsilon^2R_0'^2)^{\frac{3}{2}}} + \frac{3\epsilon^5R_0'R_0''^2}{(1+\epsilon^2R_0'^2)^{\frac{5}{2}}}\right)$$

$$-\frac{3}{Re}(\epsilon^2 u_0'' + 2\epsilon^2 u_0' R_0' R_0^{-1}) - \epsilon\left[\frac{(X_0+1)X_0' + Z_0 Z_0'}{Rb^2}\right] = 0, \tag{7.8}$$

$$(X_0')^2 + (Z_0')^2 = 1 \tag{7.9}$$

and

$$\left(u_0^2 - \frac{3\epsilon u_0'}{Re} - \frac{1}{R_0 We}\right)(X_0''^2 + Z_0''^2) = \frac{2u_0}{Rb}(X_0' Z_0'' - Z_0' X_0'')$$

$$+\frac{1}{Rb^2}\left[(X_0+1)X_0'' + Z Z_0''\right], \tag{7.10}$$

where $' = \partial/\partial\bar{s}$. We expand u_0 and R_0 as

$$u_0(\bar{s}) = u_{00}(\bar{s}) + \epsilon u_{01}(\bar{s}) + \epsilon^2 u_{02}(\bar{s}) + O(\epsilon^3) \tag{7.11}$$

and

$$R_0(\bar{s}) = R_{00}(\bar{s}) + \epsilon R_{01}(\bar{s}) + \epsilon^2 R_{02}(\bar{s}) + O(\epsilon^3). \tag{7.12}$$

7.4 Leading-Order Solution

Hence at leading-order in ϵ, we have

$$\frac{1}{2}u_{00}' R_{00} + u_{00} R_{00}' = 0, \tag{7.13}$$

$$u_{00} u_{00}' - \frac{1}{We}\left(\frac{R_{00}'}{R_{00}^2}\right) - \left[\frac{(X_0+1)X_0' + Z_0 Z_0'}{Rb^2}\right] = 0, \tag{7.14}$$

$$(X_0')^2 + (Z_0')^2 = 1 \tag{7.15}$$

and

$$\left(u_{00}^2 - \frac{1}{R_{00}We}\right)(X_0''^2 + Z_0''^2) = \frac{2u_{00}}{Rb}(X_0'Z_0'' - Z_0'X_0'')$$

$$+\frac{1}{Rb^2}\left[(X_0+1)X_0'' + ZZ_0''\right]. \tag{7.16}$$

So we have three equations in three unknowns, namely u_{00}, X_0 and Z_0, as

$$R_{00} = 1/\sqrt{u_{00}},$$

from equation(7.13). The boundary conditions at $s = 0$ are given by

$$u_{00}(0) = X_0'(0) = 1 \text{ and } X_0(0) = Z_0(0) = Z_0'(0) = 0.$$

The steady-state solutions of the above equations are obtained using a Runga-Kutta 4th-order method and are shown in Figures 7.1-7.5 .

Figure 7.1 shows that for very high rotation rate (i.e., for very small value of Rb), the jet curves very largely after leaving the cylindrical orifice, while Figure 7.2 shows that for smaller rotation rates (i.e., for higher values of Rb), the jet curves less after leaving the cylindrical orifice. Figure 7.3 shows that for higher values of surface tension (i.e., for smaller values of We), the jet curves more after leaving the cylindrical orifice. From Figures 7.4 and 7.5, it can be respectively seen that for smaller Rossby numbers, i.e., for larger rotation rates, the velocity of the jet becomes larger along the jet and the radius of the jet becomes smaller along the jet.

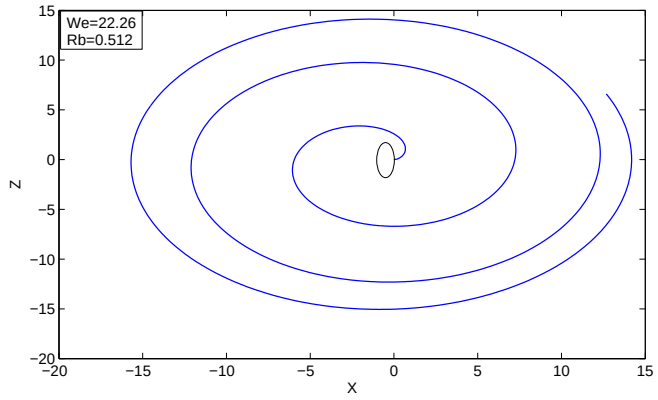

Figure 7.1: A diagram showing the trajectory of an inviscid rotating liquid jet emerging from an cylindrical orifice which is placed at the origin (0,0) for very small Rb. For this very high rotation rate (i.e., for very small value of Rb), the jet curves very largely after leaving the cylindrical orifice.

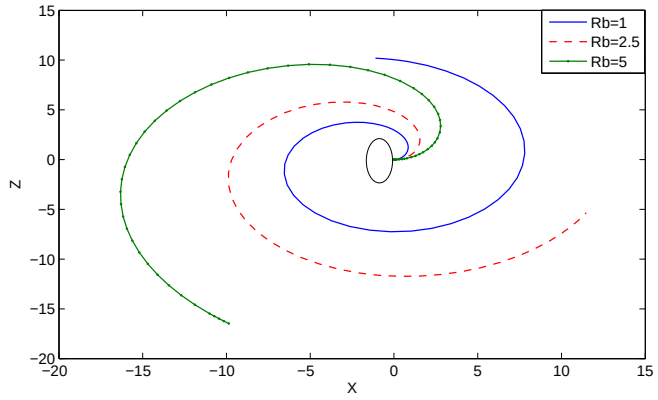

Figure 7.2: A diagram showing the trajectory of an inviscid rotating liquid jet emerging from an cylindrical orifice which is placed at the origin (0,0) for different values of Rb. Note that for higher rotation rates (i.e., for smaller values of Rb), the jet curves more after leaving the cylindrical orifice. Here We = 10.

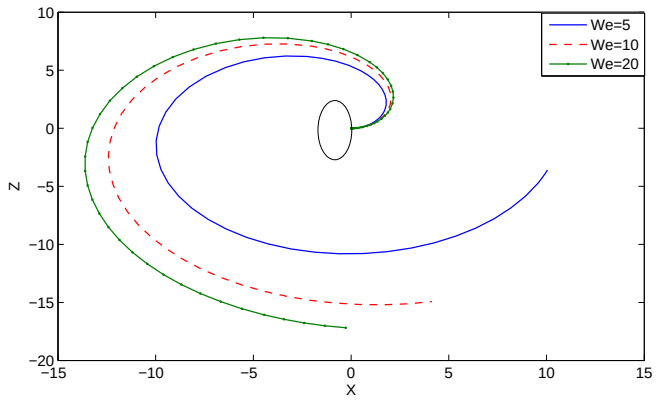

Figure 7.3: A diagram showing the trajectory of an inviscid rotating liquid jet emerging from an cylindrical orifice which is placed at the origin (0,0) for different values of We. Note that for higher values of surface tension (i.e., for smaller values of We), the jet curves more after leaving the cylindrical orifice. Here Rb = 3.5.

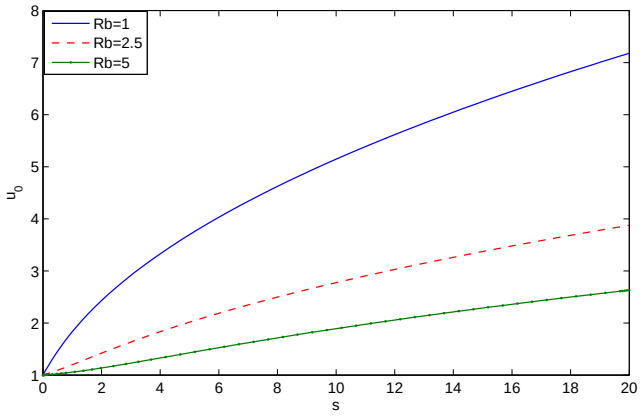

Figure 7.4: A graph showing the leading-order velocity of an inviscid liquid jet for different Rossby numbers. It can be clearly seen that for smaller Rossby numbers, i.e., for larger rotation rates, the velocity of the jet becomes larger along the jet. Here We = 10.

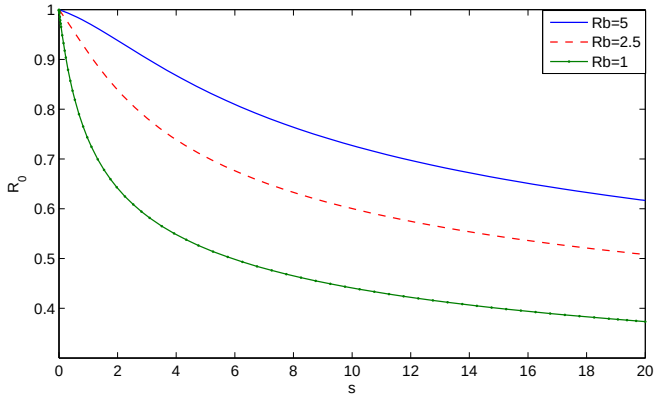

Figure 7.5: A graph showing the leading-order radius of an inviscid liquid jet for different Rossby numbers. It can be clearly seen that for smaller Rossby numbers, i.e., for larger rotation rates, the radius of the jet becomes smaller along the jet. Here We = 10.

7.5 Determination of the nonlinear travelling wave

Next, we find the g_0-equation as follows. Substituting equations (7.5) and (7.6) into equation (7.3), and using $\partial/\partial\tilde{s} = \epsilon\,\partial/\partial\bar{s}$, we obtain, at leading-order in ϵ, an equation of the form

$$h_0 = 2\zeta_0 \left(\frac{-g_0 + z g_{0,z} - u_{00} g_{0,z}}{R_{00} g_{0,z}} \right). \tag{7.17}$$

Putting $u_{00} = R_{00} = 1$ in equation (7.17), we get

$$h_0 = \zeta_0 \left(\frac{-2g_0 + 2z g_{0,z} - 2g_{0,z}}{g_{0,z}} \right), \tag{7.18}$$

which is the same equation (95) of Decent (2009). We expected to get this equation as it corresponds to the no gravity problem in which $u_{00} = R_{00} = 1$.

Substituting equations (7.5), (7.6) and (7.17) into equation (7.4), and using $\frac{\partial}{\partial\tilde{s}} = \epsilon\frac{\partial}{\partial\bar{s}}$, we obtain a nonlinear ordinary differential equation for g_0 in z, at

leading-order in ϵ, of the form

$$ReR_{00}\left(g_{0,z}\right)^4+\frac{Re}{R_{00}}\left(g_{0,z}\right)^2-4zReWeg_0g_{0,z}+2z^2ReWe\left(g_{0,z}\right)^2-4zReWeu_{00}\left(g_{0,z}\right)^2$$

$$+4ReWeu_{00}g_0g_{0,z}+2ReWeu_{00}^2\left(g_{0,z}\right)^2+2ReWe\left(g_0\right)^2+6Weg_0\left(g_{0,z}\right)^2-6Wez\left(g_{0,z}\right)^3$$

$$+6Weu_{00}\left(g_{0,z}\right)^3=0. \tag{7.19}$$

Putting $u_{00}=R_{00}=1$ in equation (7.19), we get

$$Re\left(g_{0,z}\right)^4+Re\left(g_{0,z}\right)^2-4zReWeg_0g_{0,z}+2z^2ReWe\left(g_{0,z}\right)^2-4zReWe\left(g_{0,z}\right)^2+4ReWeg_0g_{0,z}$$

$$+2ReWe\left(g_{0,z}\right)^2+2ReWe\left(g_0\right)^2+6Weg_0\left(g_{0,z}\right)^2-6Wez\left(g_{0,z}\right)^3+6We\left(g_{0,z}\right)^3=0,$$

which is the same equation (92) of Decent (2009).

This result shows that the g_0-equation implicitly depends on the rotation via u_0 and R_0. This is due to the fact that the rotation appears in the steady-state equations, in the form of Rb. So changing Rb in those equations imply a change in u_0 and R_0; the steady-state solutions, which in turn will have a change in the g_0-equation.

However, Rb does not appear explicitly in the g_0-equation. In order to bring Rb explicitly into our g_0-equation, we must have

$$\left[\frac{(X+1)X_{\bar{s}}+ZZ_{\bar{s}}}{Rb^2}\right]=f(u,R).$$

Solving equation (7.19), for large Reynolds number (i.e., $Re \to \infty$), gives

$$g_0 = \frac{\sqrt{Q_0}}{4\sqrt{We}R_{00}^{3/2}} \tag{7.20}$$

where

$$Q_0 = -We^2u_{00}^4R_{00}^2 - 10z^2WeR_{00} + 20zWeu_{00}R_{00} - 10Weu_{00}^2R_{00} - 6z^2We^2u_{00}^2R_{00}^2$$

$$-z^4We^2R_{00}^2 + 2 + 4z^3We^2u_{00}R_{00}^2 + 4zWe^2u_{00}^3R_{00}^2$$

$$-\sqrt{R_{00}We\left(z-u_{00}\right)^2\left(Weu_{00}^2R_{00} - 2zWeu_{00}R_{00} + z^2WeR_{00} - 4\right)^3}. \tag{7.21}$$

Putting $u_{00} = R_{00} = 1$ in equations (7.20) and (7.21), we get

$$g_0 = \frac{\sqrt{Q_0}}{4\sqrt{We}} \tag{7.22}$$

where

$$Q_0 = -We^2 - 10z^2We + 20zWe - 10We - 6z^2We^2 - z^4We^2 + 2 + 4z^3We^2$$

$$+4zWe^2 - \sqrt{We\left(z-1\right)^2\left(We - 2zWe + z^2We - 4\right)^3}, \tag{7.23}$$

which are the same equations (112) and (113) of Decent (2009).

Note that controllable growing linear waves come out of the orifice, they grow gradually and they become nonlinear. From orifice to a point z_1, linear waves are in dominance and their dominance finishes at z_1. After z_1, there is a mixture of both linear and nonlinear waves and this mixture finishes at a point z_2. After

z_2, there are only nonlinear waves. Also, the instability of the waves is at its maximum value at z_3. We assume that the liquid jet do not pass beyond z_3 because the instability is maximum at z_3.

From equations (7.20) and (7.21), we find that

$$z_1 \to max\left(u_{00} - 2/\sqrt{R_{00}We}, 0\right) \text{ and } z_2 \to u_{00} + 2/\sqrt{R_{00}We} \text{ as } Re \to \infty.$$

These values of z_1 and z_2 corresponds to the same values of of z_1 and z_2 of Decent (2009) in the limit $u_{00} = 1$ and $R_{00} = 1$.

7.6 Types of Modes

We have four types of modes, M1, M2, M2/3 and M3. For M1, we have uniform drops along with very few satellite droplets (usually, one satellite droplet in twenty main uniform droplets, as seen in experiments). For M2, we have more number of satellite droplets than M1. For M3, we have long ligaments occurring between the main droplets. The mode M2/3 is the mode which is between M2 and M3 and we can not describe this mode as M2 or M3. So we describe mode M2/3 as the transition period from mode 2 to mode 3. All these various modes are shown in following Figures 7.6 and 7.7.

7.7 Computational Solution

We now find values of z_1 and z_2 numerically, without any asymptotic limit, and then we use these values to plot some figures which show the point of breakup and the mode of breakup M1, M2, M2/3 or M3 along with values of z_1 and z_2.

The idea is that we run the numerical model, with five parameters We, Rb, Re, δ and ω, to find the shape of the mode, the breakup length s_b and the breakup time t_b, and so we find the breakup point $z_b = s_b/t_b$. We use s_b in the steady-state solution of the steady-state equations to find $u_0(s_b)$ and $R_0(s_b)$ (with same param-

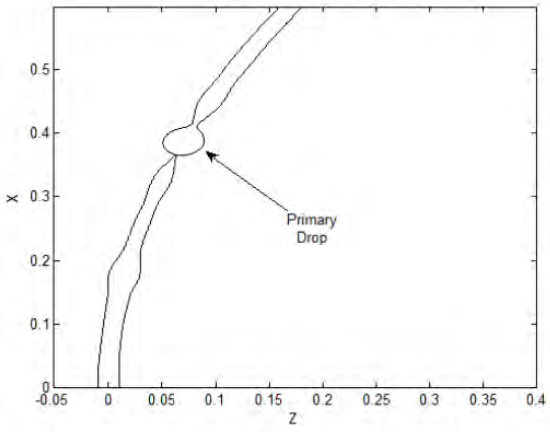

(a) Mode 1

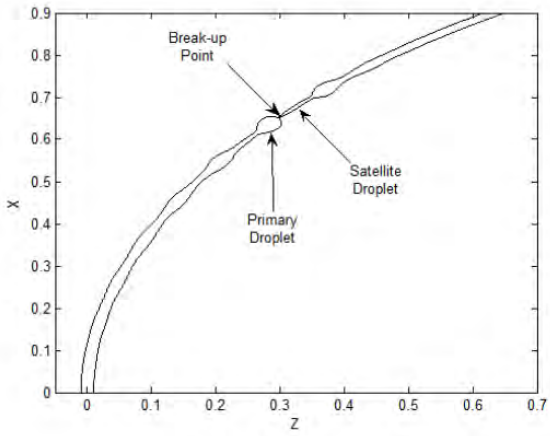

(b) Mode 2

Figure 7.6: Mode classification of M1 and M2. Reproduced from Gurney (2010).

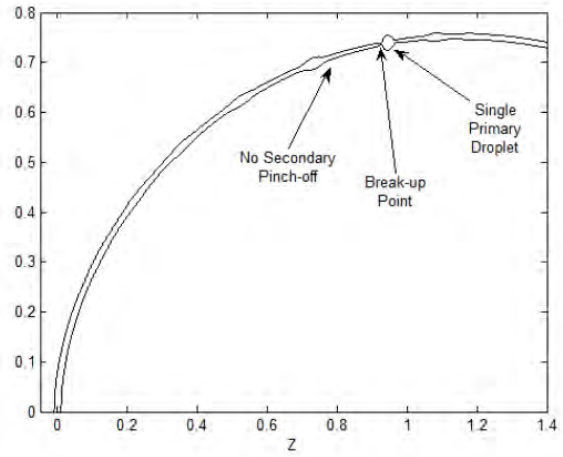

(a) Mode 2/3

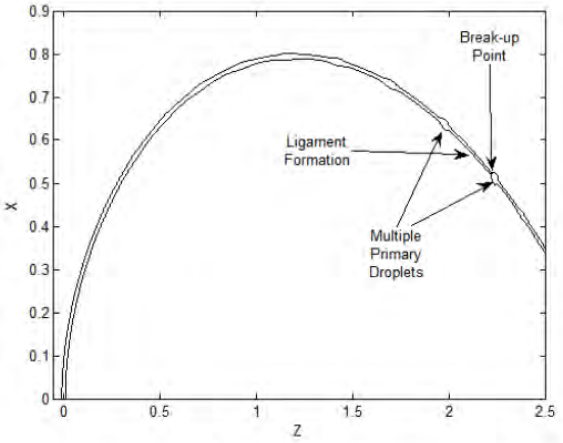

(b) Mode 3

Figure 7.7: Mode classification of M2/3 and M3. Reproduced from Gurney (2010).

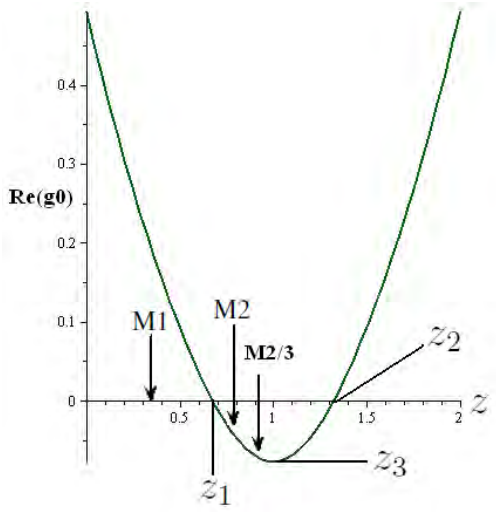

Figure 7.8: Our hypothesis is that we get this kind of mode behaviour.

eters We and Rb used in the numerical code) and then we use $u_0(s_b)$ and $R_0(s_b)$ in the numerics to generate the solution of the g_0-equation (with same parameters We and Re used in the code) to find a solution curve which will show z_1 and z_2. Next, we see that at which place of the curve z_b (calculated earlier from the code) lies and we label that place as M1, M2, M2/3 or M3, depending on the shape of the mode obtained from the numerical model. We mention here that Părău *et al.* (2007) developed these numerical codes to investigate the liquid jet breakup, which we use in this chapter. The basics behind the numerical model is described in Appendix B.

This chapter mainly focuses on z-values, and in particular, it investigates whether the M1 breakup always occurs before z_1 and whether the M2 (or M2/3) breakup always occurs after z_1 or not. That is, we want to find the regions where M1, M2 and M2/3 occur. Our hypothesis is that we get the mode behaviour shown in Figure 7.8.

7.7.1 Impact of Changing the Amplitude on Modes

We start with the set of data

$$We = 22.26, Rb = 0.512, Re = 375, \omega = 1.3$$

and we vary the amplitude δ as $\delta = 0.08, \delta = 0.01$ and $\delta = 0.005$. This set of data is chosen from experiments (see Gurney (2010) and Hawkins (2010) for details). In experiments, this set of data corresponds to a mixture of 40% glycerol and 60% water, used by Hawkins (2010) and there does not exist mode 3 bahaviour, for this set of data in experiments. In addition, in experiments, this set of data with $\delta = 0.08, \delta = 0.01$ and $\delta = 0.005$ gives M1, M2 and M2/3 behaviour respectively (see Gurney (2010)).

We can easily see from Figures 7.9 – 7.14 that the larger the δ is, the smaller the breakup point z_b is. We observe that

$$\delta = 0.08(M1) > 0.01(M2) > 0.005(M2/3),$$

which gives

$$z_b = 1.1(M1) < 2.3(M2) < 3.2(M2/3).$$

Hence for large δ, we have a small breakup point while for small δ, we have a large breakup point. In addition, this set of data shows us that as we decrease δ, z_1 and the breakup point are increased. Further more, decreasing δ implies a change in the modes from M1 to M2 and then to M2/3. Note that the breakup never occurs after z_3, where the instability is maximum (i.e., where the growth rate of the unstable nonlinear wave is maximum). Also note that our numerical model is in agreement with the experimental data for M1 (where $\delta = 0.08$), M2 (where $\delta = 0.01$) and M2/3 (where $\delta = 0.005$).

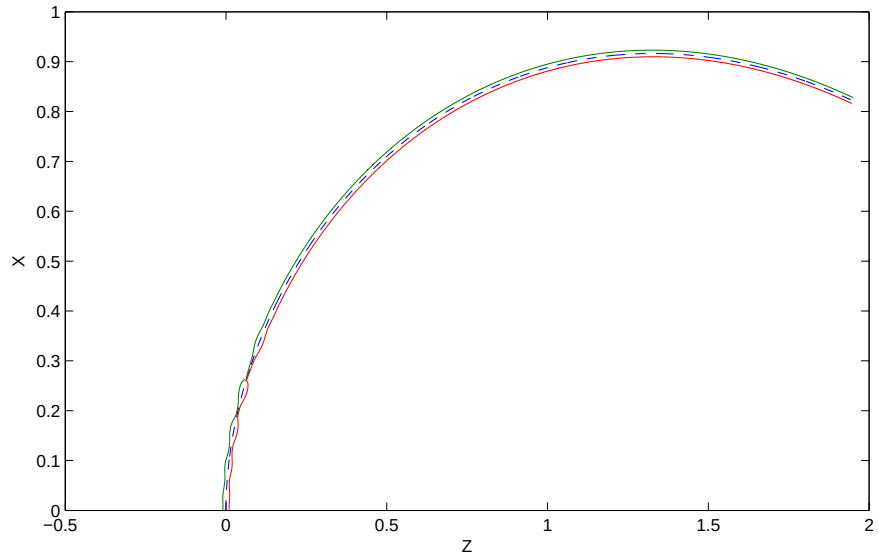

(a) Temporal evolution of the jet.

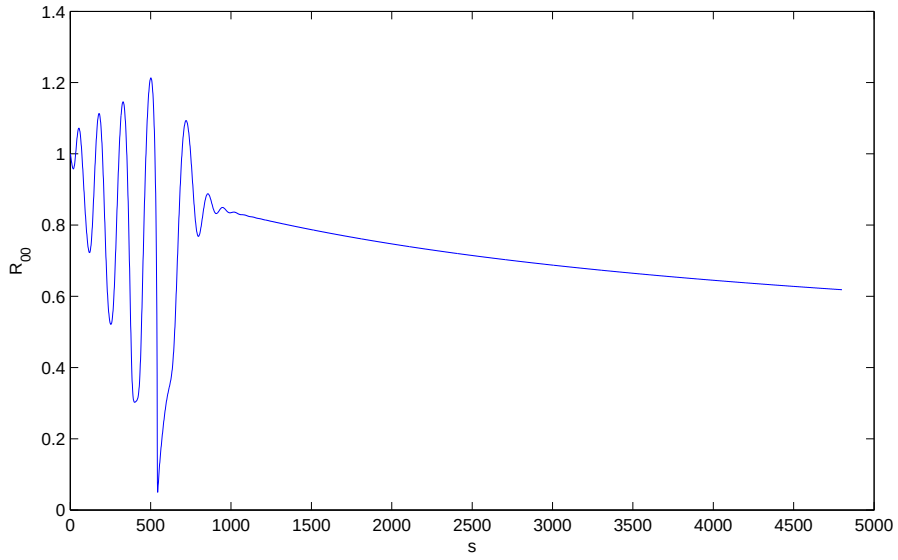

(b) Radius R_{00} against arc length s.

Figure 7.9: Mode 1 breakup in the linear wave regime, corresponding to M1 in following figure. Here $\delta = 0.08$.

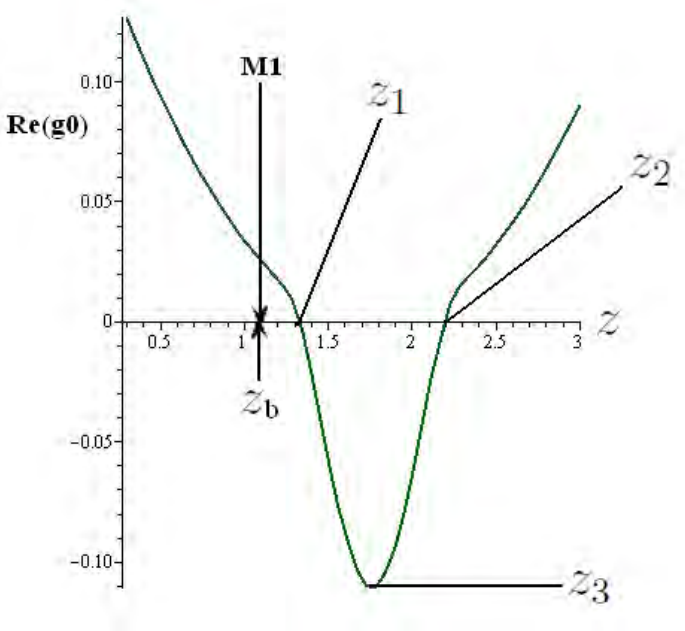

Figure 7.10: M1 with δ = 0.08.

7.7.2 Impact of Changing the Frequency on Modes

We take the set of data

$$We = 22.26, Rb = 0.512, Re = 375, \delta = 0.1$$

and we vary the frequency ω as $\omega = 1.3$, $\omega = 1$ and $\omega = 0.698$. This set of data is chosen from experiments (see Gurney (2010) and Hawkins (2010) for details). This set of data corresponds to a mixture of 40% glycerol and 60% water, used by Hawkins (2010) in experiments. Note that for this set of data, in experiments, there does not exist mode 3 bahaviour. In addition, in experiments, this set of data with $\omega = 1.3$, $\omega = 1$ and $\omega = 0.698$ gives M1, M2 and M2/3 behaviour respectively (see Gurney (2010)).

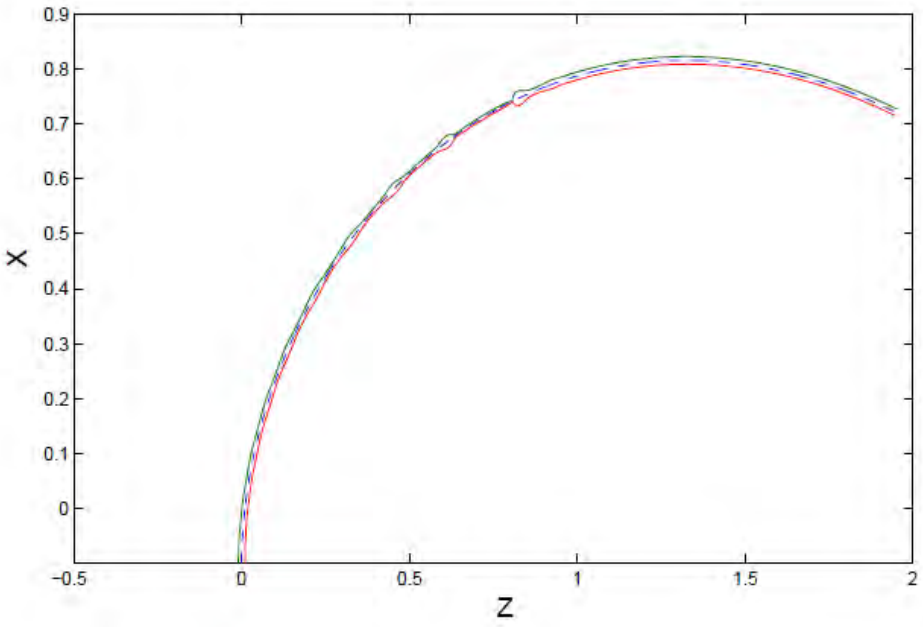

(a) Temporal evolution of the jet.

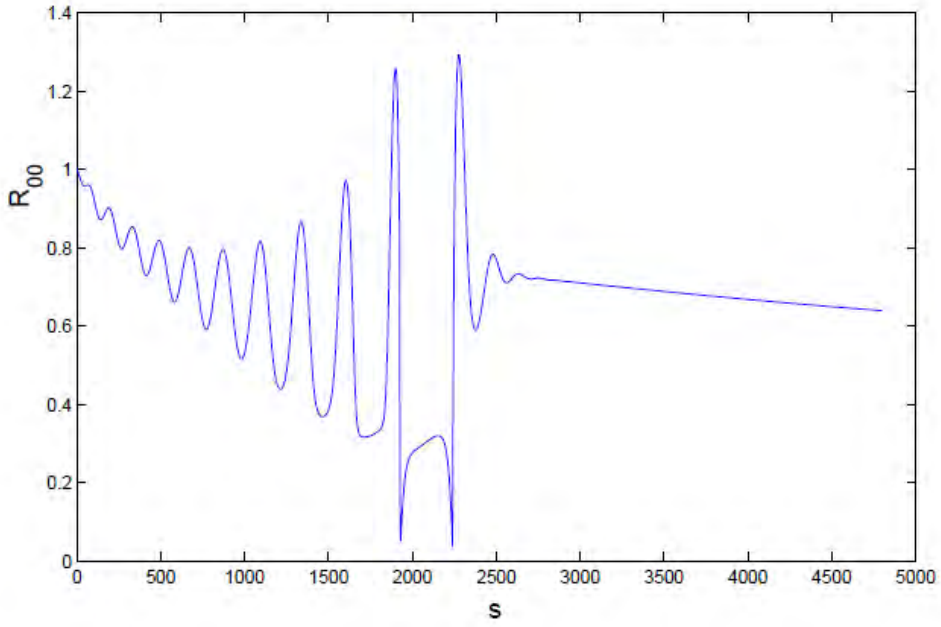

(b) Radius R_{00} against arc length s.

Figure 7.11: Mode 2 breakup with linear and nonlinear mode competition, corresponding to M2 in following figure. Here $\delta = 0.01$.

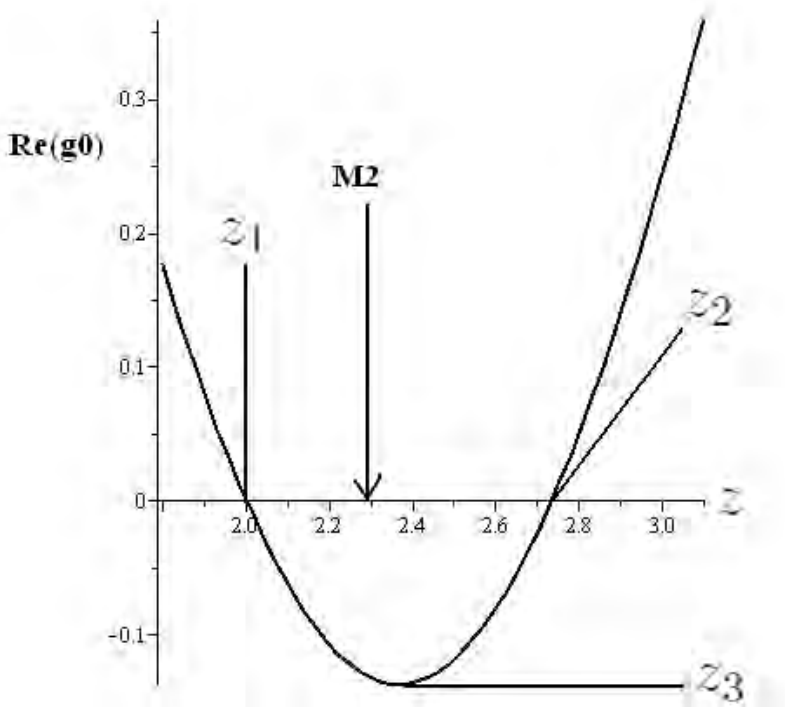

Figure 7.12: M2 with $\delta = 0.01$.

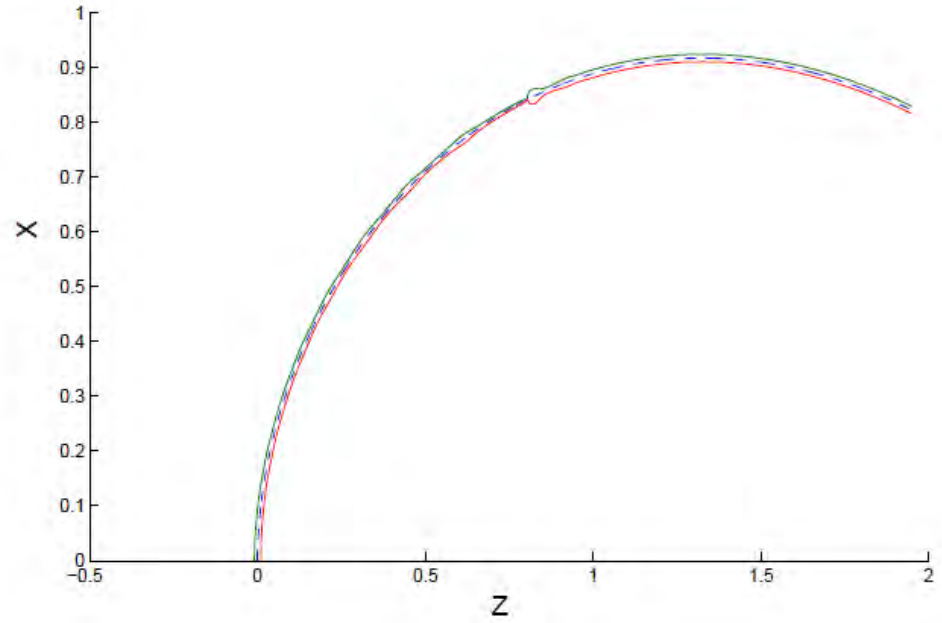

(a) Temporal evolution of the jet.

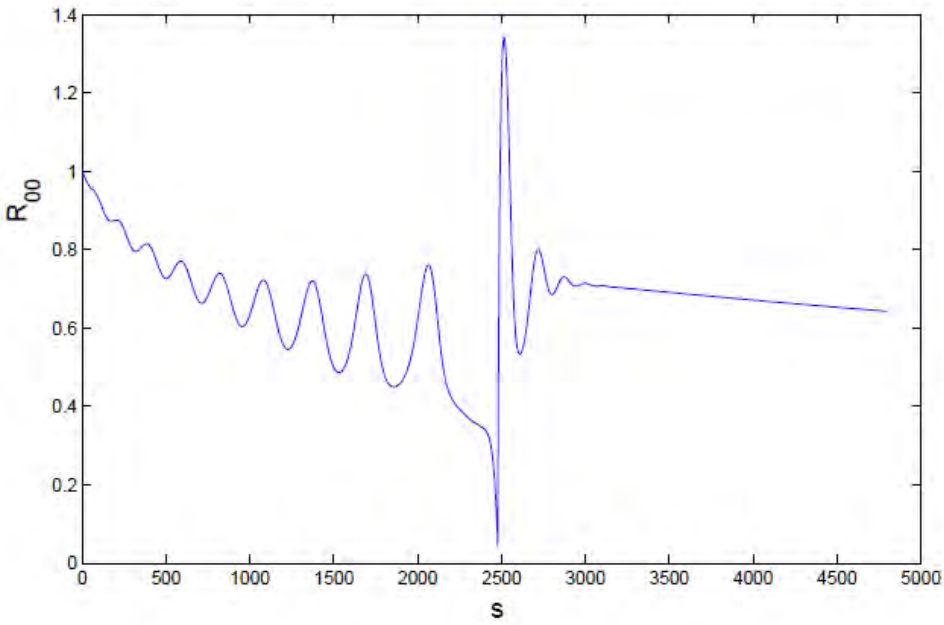

(b) Radius R_{00} against arc length s.

Figure 7.13: Mode 2/3 breakup which corresponds to M2/3 in following figure. Here $\delta = 0.005$.

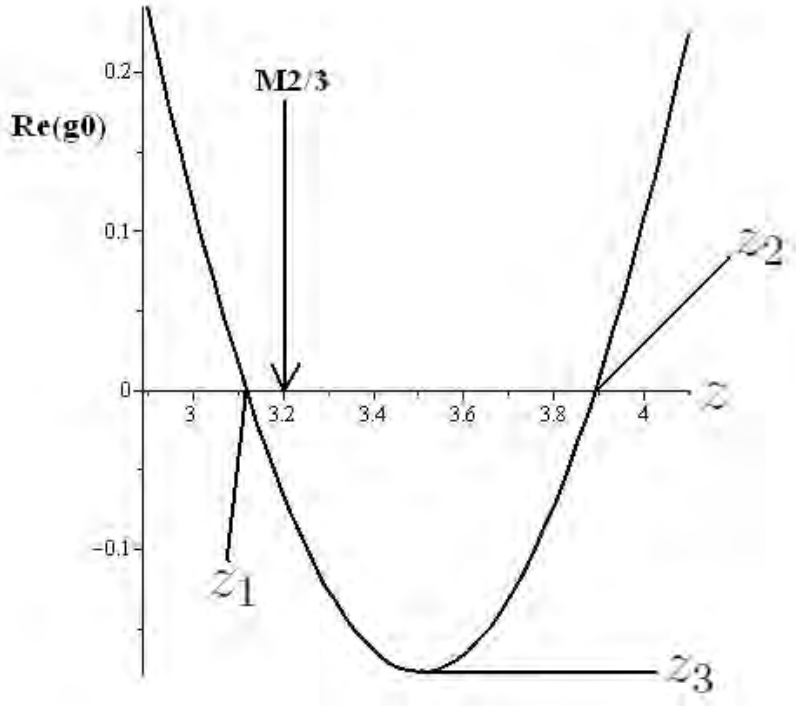

Figure 7.14: M2/3 with $\delta = 0.005$.

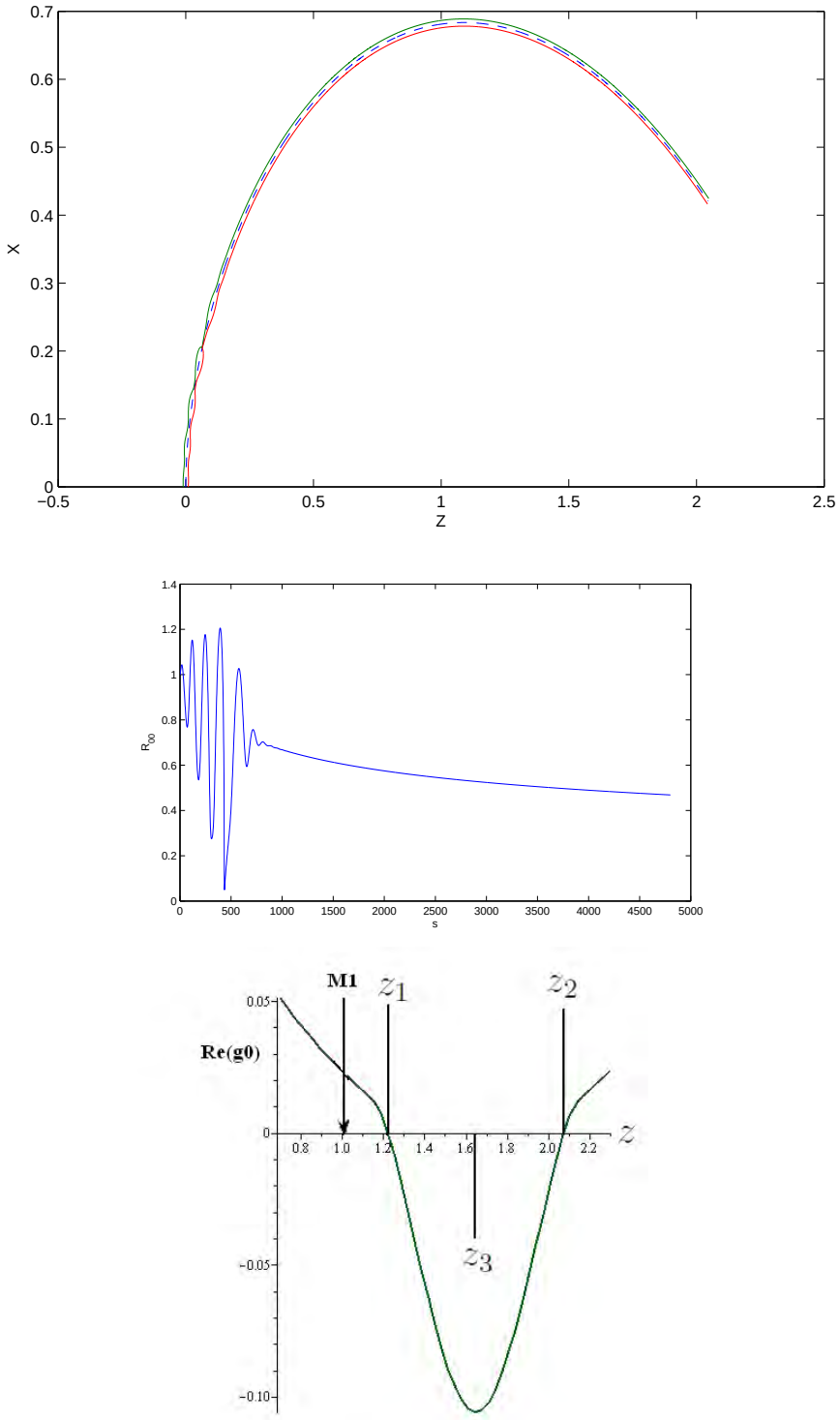

Figure 7.15: Mode 1 breakup in the linear wave regime. Top is the jet temporal evolution, middle is R_{00} against s while bottom is $Real(g_0)$ against z. Here ω = 1.3.

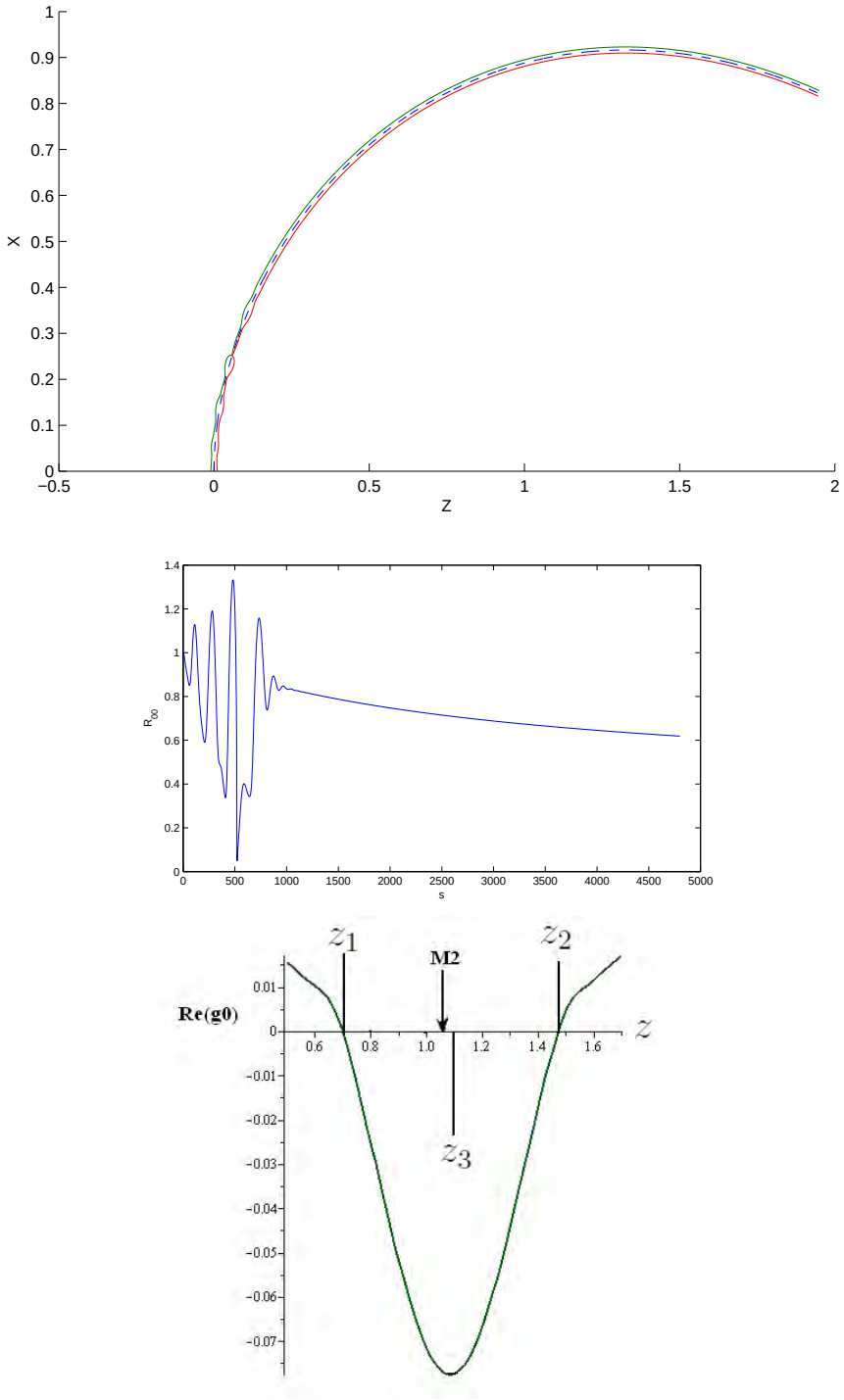

Figure 7.16: Mode 2 breakup with linear and nonlinear mode competition. Top is the jet temporal evolution, middle is R_{00} against s while bottom is $Real(g_0)$ against z. Here $\omega = 1$.

Figures 7.15 – 7.17 show that as we decrease the value of ω (from 1.3 to 1 and then to 0.698), we get a change in the modes from M1 to M2 and then to M2/3. Hence for large ω, we get mode 1 behaviour while for small ω, we get mode 2/3 behaviour. Note that as we decrease ω, z_1 also decreases while the breakup point increases. The above Figures 7.9 – 7.17 suggest that in order to get mode 1 behaviour, we must have large δ (as $\delta = 0.1$ is large) and large ω (as $\omega = 1.3$ is large), for the breakup to occur before z_1. Note that the breakup never occurs after z_3 where the instability is maximum (i.e., where the growth rate of the unstable nonlinear wave is maximum). Also note that our numerical model is in agreement with the experimental data for M1 (where $\omega = 1.3$), M2 (where $\omega = 1$) and M2/3 (where $\omega = 0.698$).

7.7.3 Varying the Reynolds number

We take the set of data

$$We = 22.26, Rb = 0.512, \delta = 0.1, \omega = 1.3$$

and we very Re as $Re = 375$, $Re = 600$ and $Re = 1250$. We know from Gurney (2010) that for small Re (i.e., for highly viscous fluids), we do not get M1. So we consider only large Re, as we are mainly interested in finding the M1 behaviour. From Figures 7.18 – 7.20, we find that that as we increase Re, the breakup point and z_1 are slightly decreased, with the breakup point having less decrease.

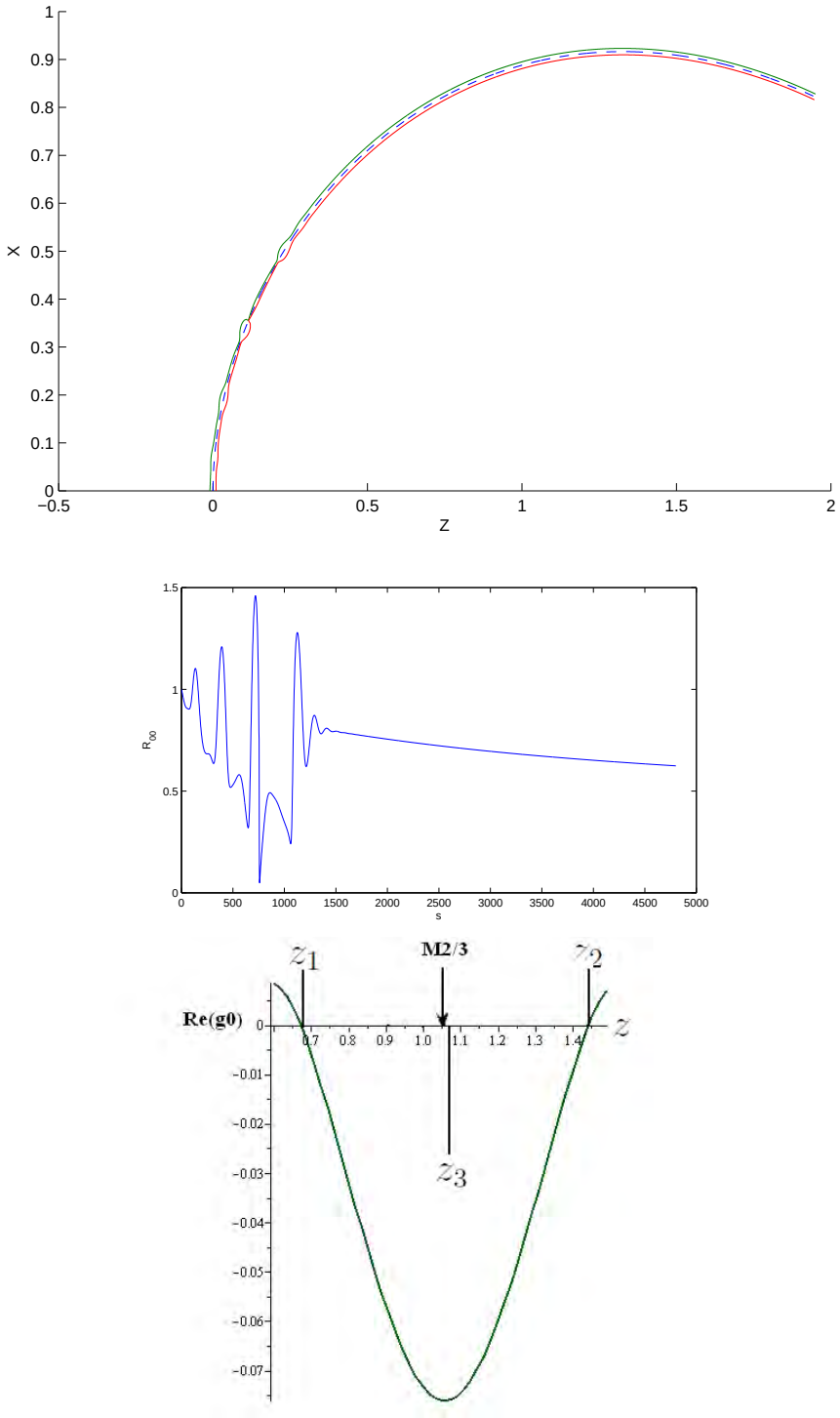

Figure 7.17: Mode 2/3 breakup in the nonlinear wave regime. Top is the jet temporal evolution, middle is R_{00} against s while bottom is $Real(g_0)$ against z. Here ω = 0.698.

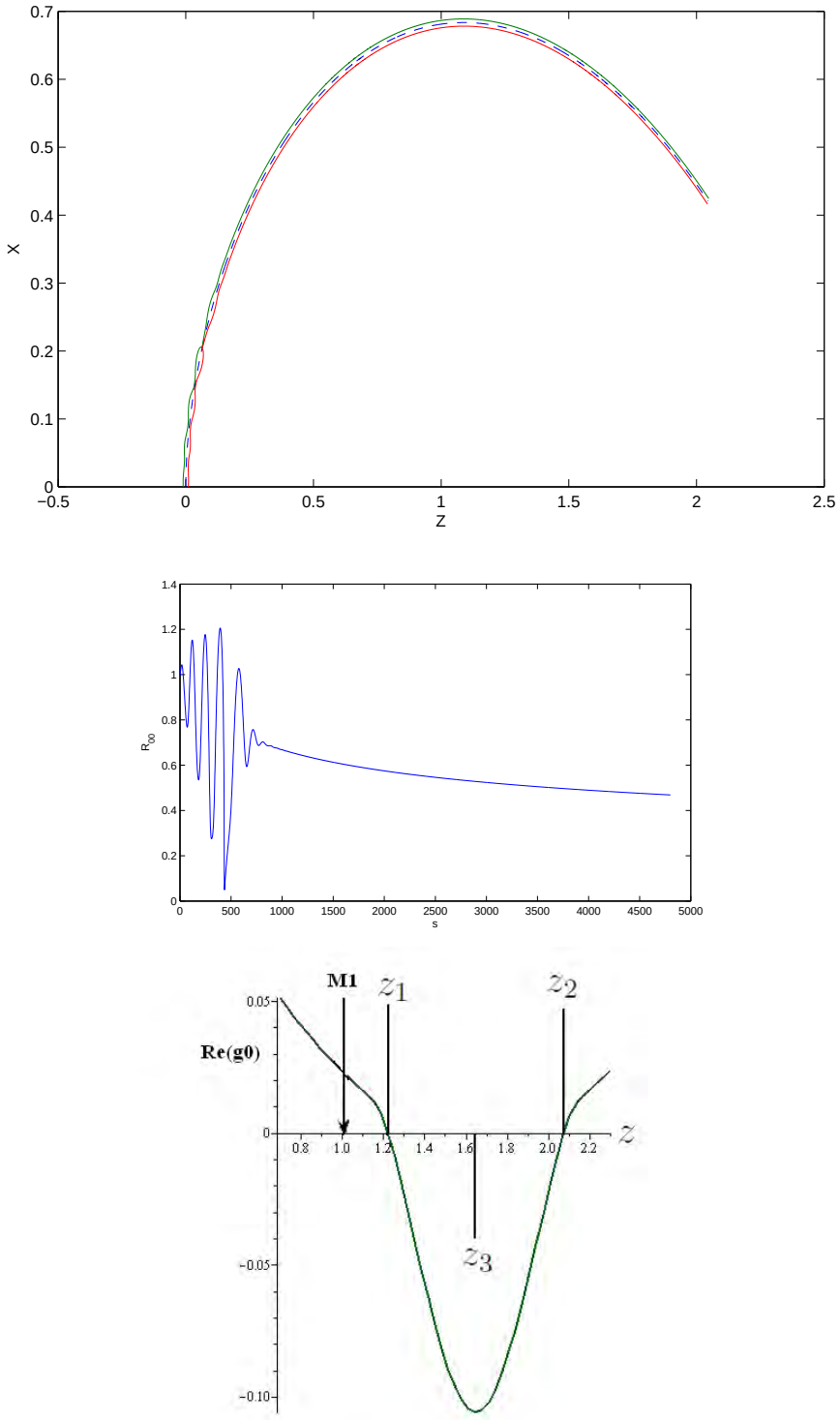

Figure 7.18: Mode 1 breakup in the linear wave regime. Top is the jet temporal evolution, middle is R_{00} against s while bottom is $Real(g_0)$ against z. Here $Re = 375$.

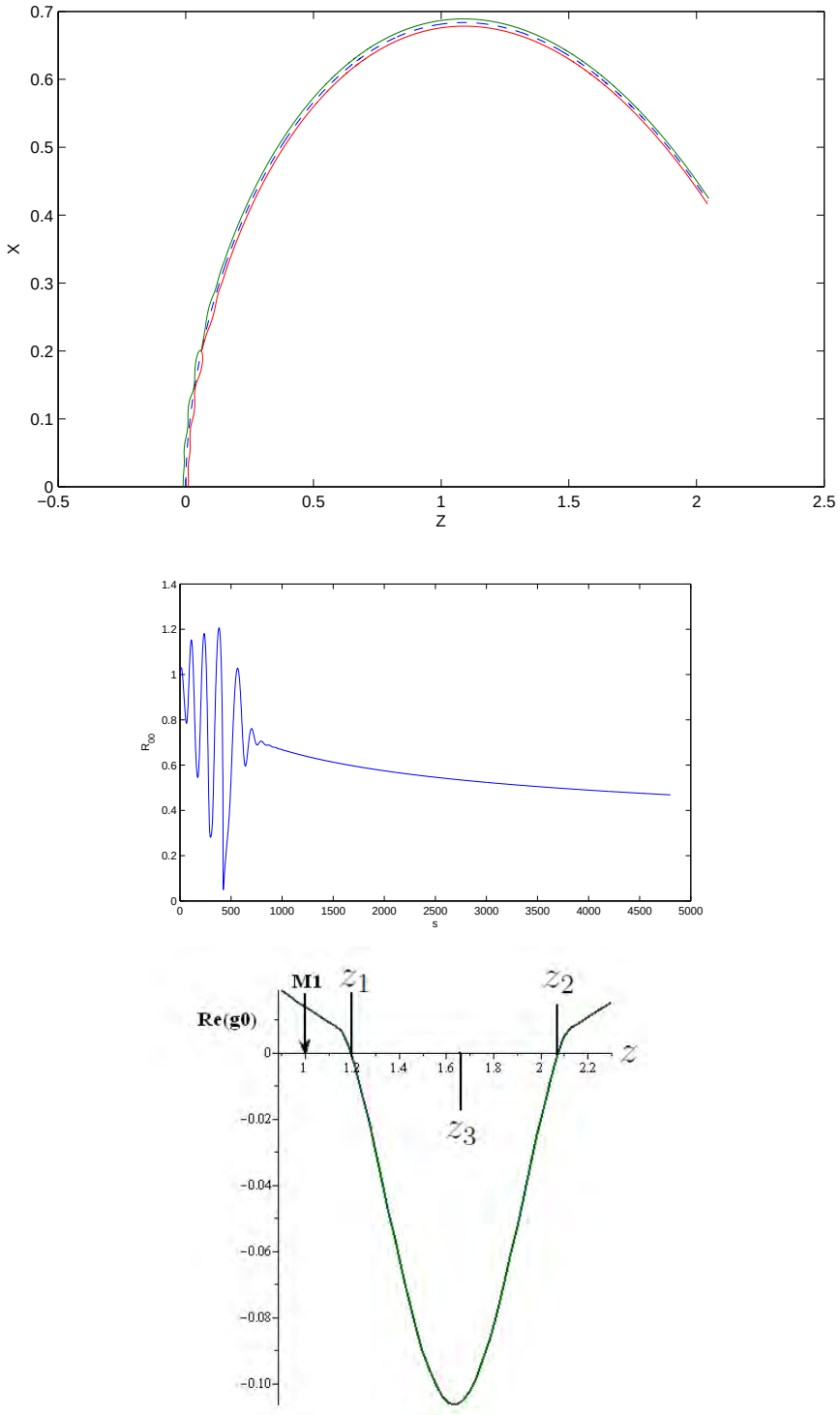

Figure 7.19: Mode 1 breakup in the linear wave regime. Top is the jet temporal evolution, middle is R_{00} against s while bottom is $Real(g_0)$ against z. Here $Re = 600$.

7.7.4 Varying the Weber number

Now we take the data $Rb = 0.512, Re = 375, \delta = 0.1, \omega = 1.3$ and we vary the Weber number We as $We = 20$, $We = 25$, $We = 35$, $We = 50$ and $We = 100$. We take a large number of values of We because we get some interesting results for the larger values of the Weber number.

It can be observed from Figures 7.21 – 7.25 that as we increase We, the values of both the breakup point and z_1 are increased, with z_1 having more increase in its value. From these figures, we find that for higher values of We, we get larger values of z_1 and we do not get M1. We also note that for large values of We, M2 can occur before z_1.

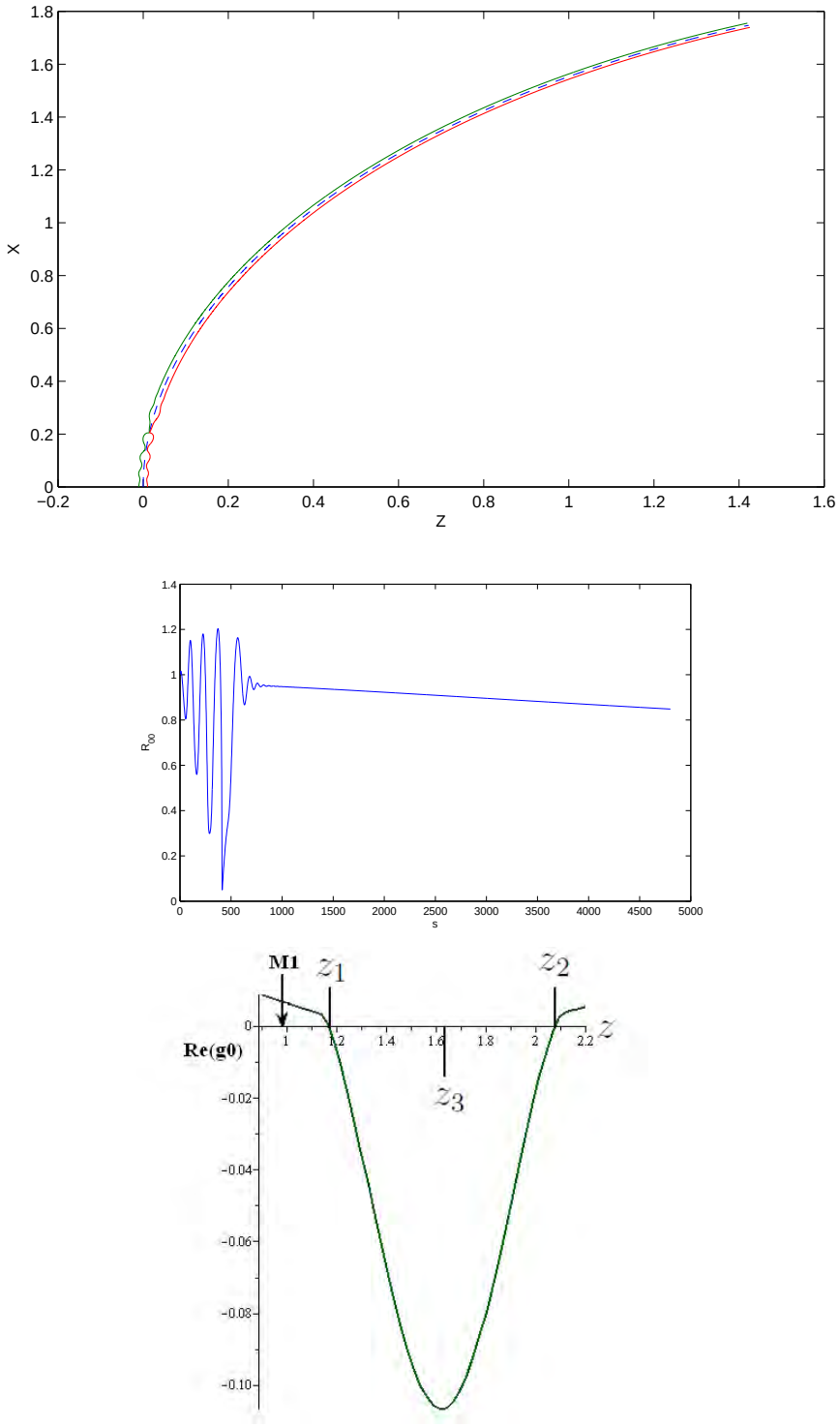

Figure 7.20: Mode 1 breakup in the linear wave regime. Top is the jet temporal evolution, middle is R_{00} against s while bottom is $Real(g_0)$ against z. Here $Re = 1250$.

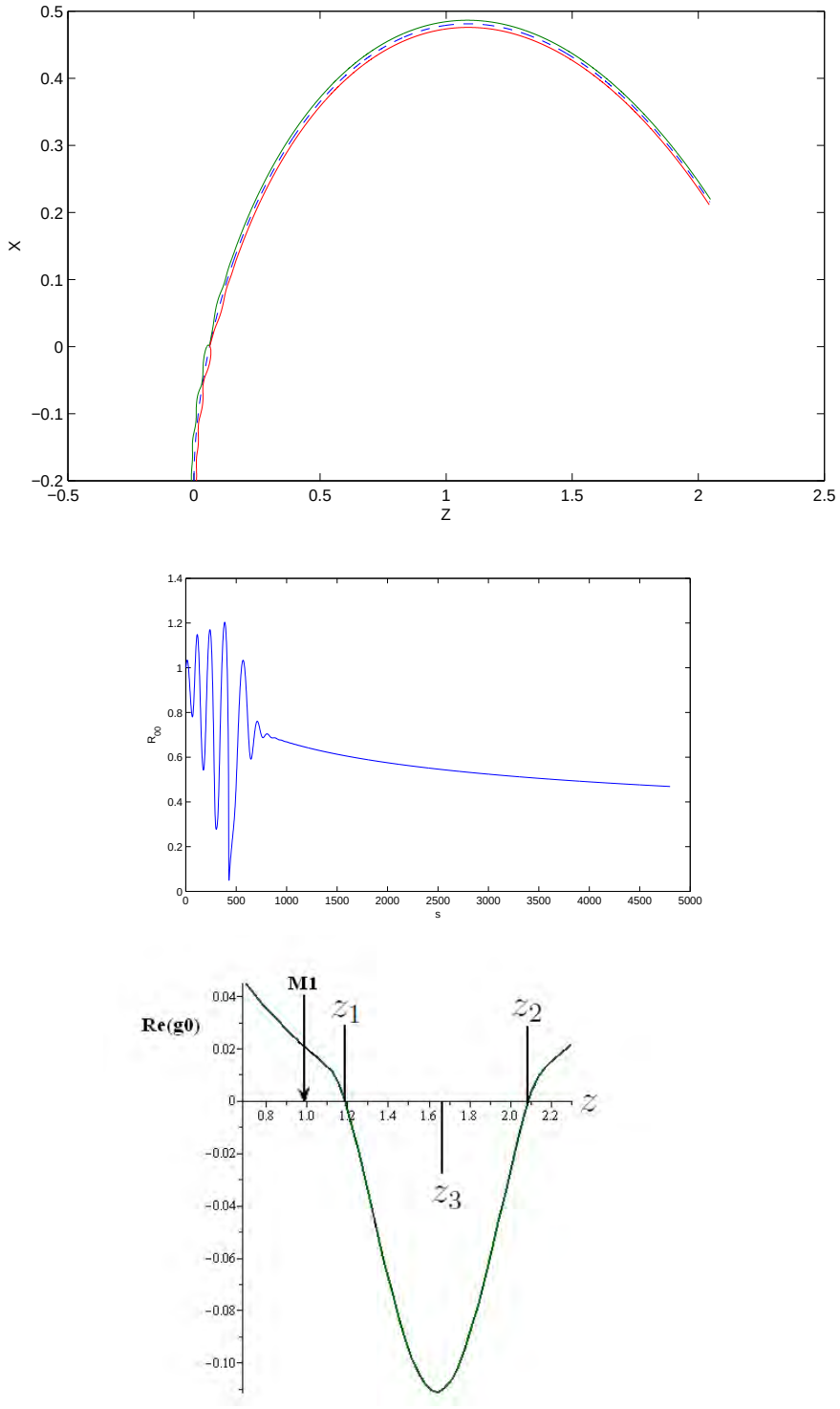

Figure 7.21: Mode 1 breakup in the linear wave regime. Top is the jet temporal evolution, middle is R_{00} against s while bottom is $Real(g_0)$ against z. Here $We = 20$.

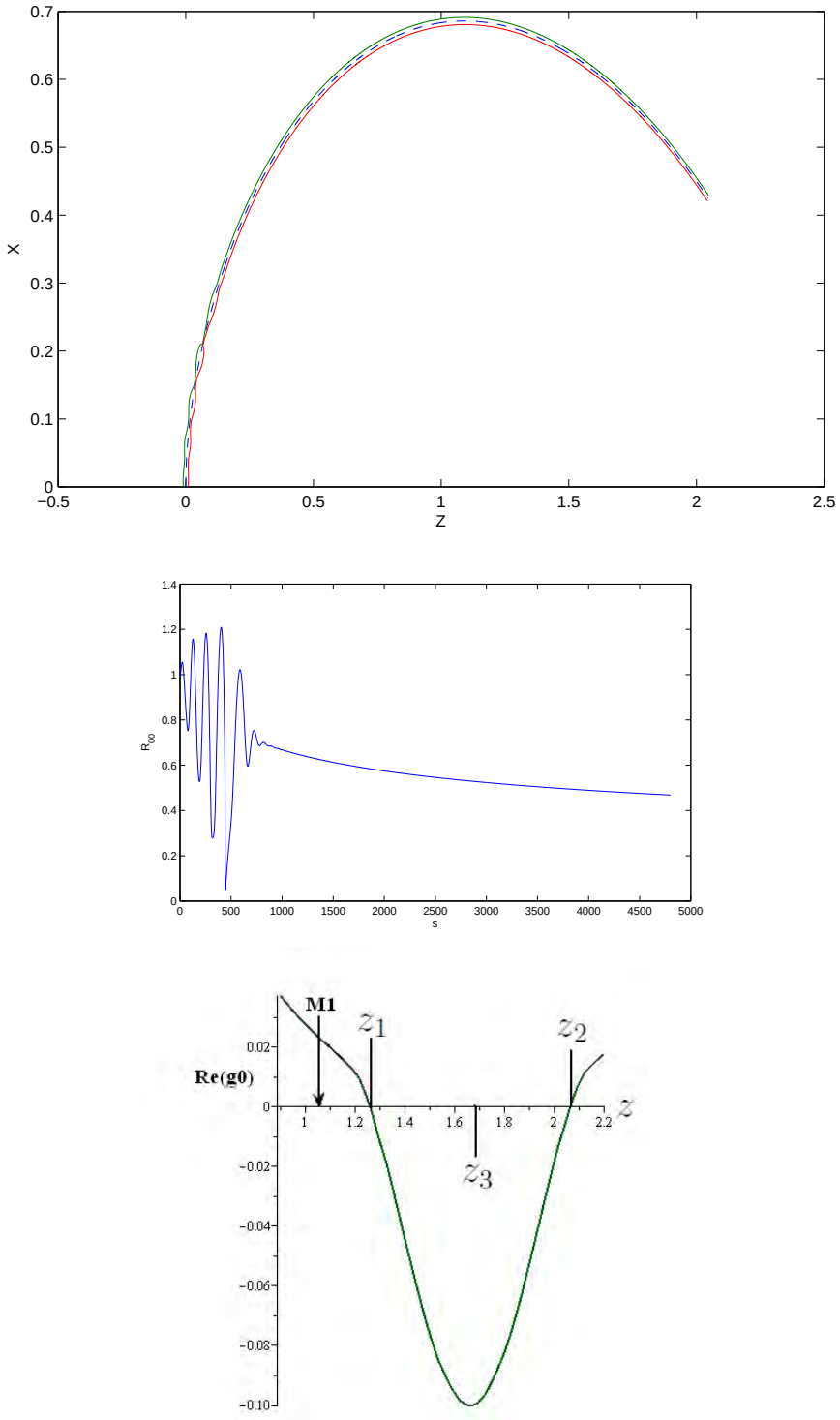

Figure 7.22: Mode 1 breakup in the linear wave regime. Top is the jet temporal evolution, middle is R_{00} against s while bottom is $Real(g_0)$ against z. Here $We = 25$.

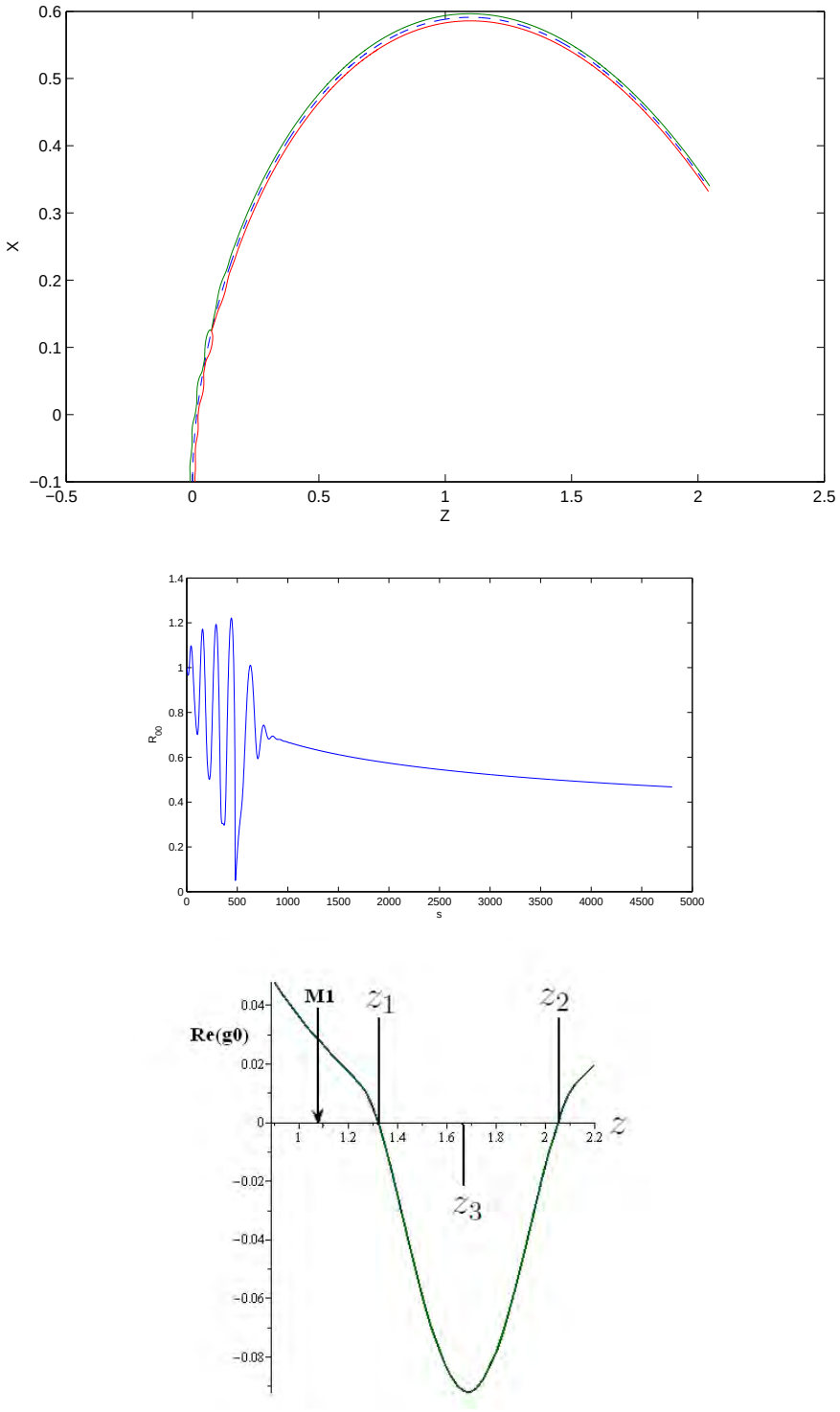

Figure 7.23: Mode 1 breakup in the linear wave regime. Top is the jet temporal evolution, middle is R_{00} against s while bottom is $Real(g_0)$ against z. Here $We = 35$.

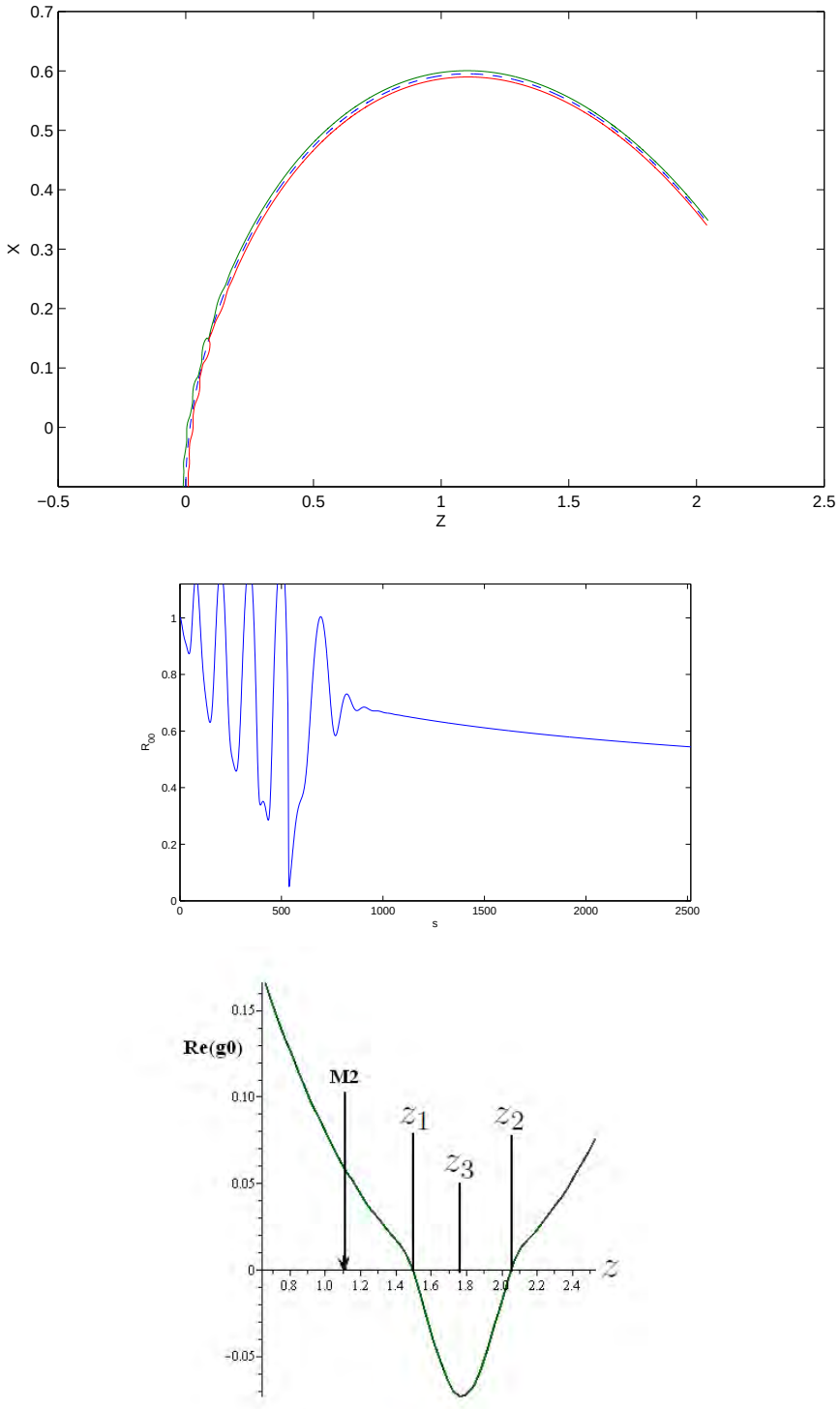

Figure 7.24: Mode 2 breakup with linear and nonlinear mode competition. Top is the jet temporal evolution, middle is R_{00} against s while bottom is $Real(g_0)$ against z. Here $We = 50$.

7.7.5 Varying the Rossby number

Our last parameter to be changed is the Rossby number Rb. For that, we take the set of data

$$We = 22.26, Re = 375, \delta = 0.1, \omega = 1.3$$

and we vary Rb as $Rb = 0.412$, $Rb = 0.512$, $Rb = 0.612$, $Rb = 0.7$, $Rb = 1$ and $Rb = 5$. We take a large number of values of Rb because we get some unexpected results for the larger values of the Rossby number.

It can be observed from Figures 7.26 – 7.31 that as we increase Rb, the values of both the breakup point and z_1 decrease, with z_1 having more large decrease in its value. We also note unexpectedly that M1 can occur after z_1 for higher values of the Rossby number.

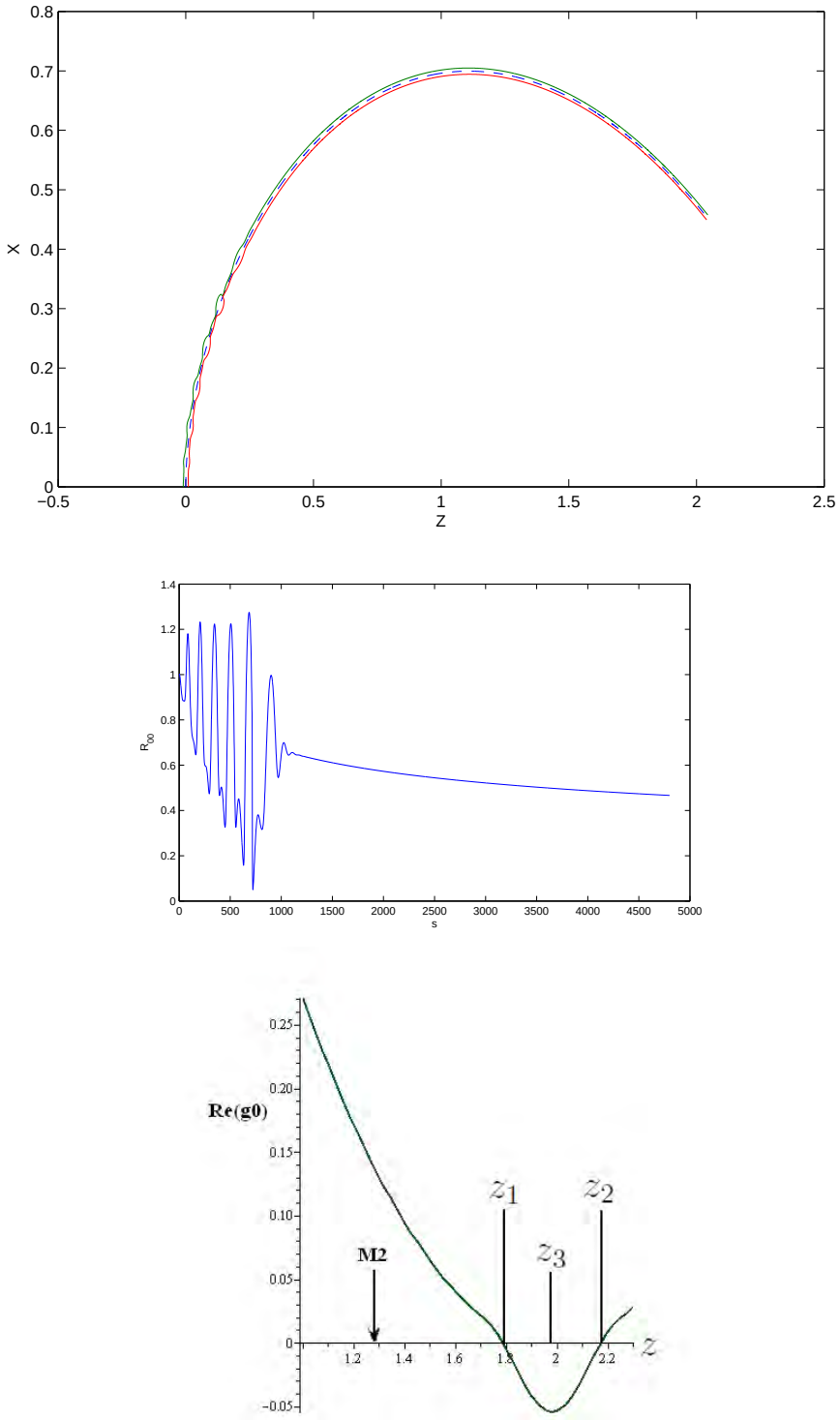

Figure 7.25: Mode 2 breakup with linear and nonlinear mode competition. Top is the jet temporal evolution, middle is R_{00} against s while bottom is $Real(g_0)$ against z. Here $We = 100$.

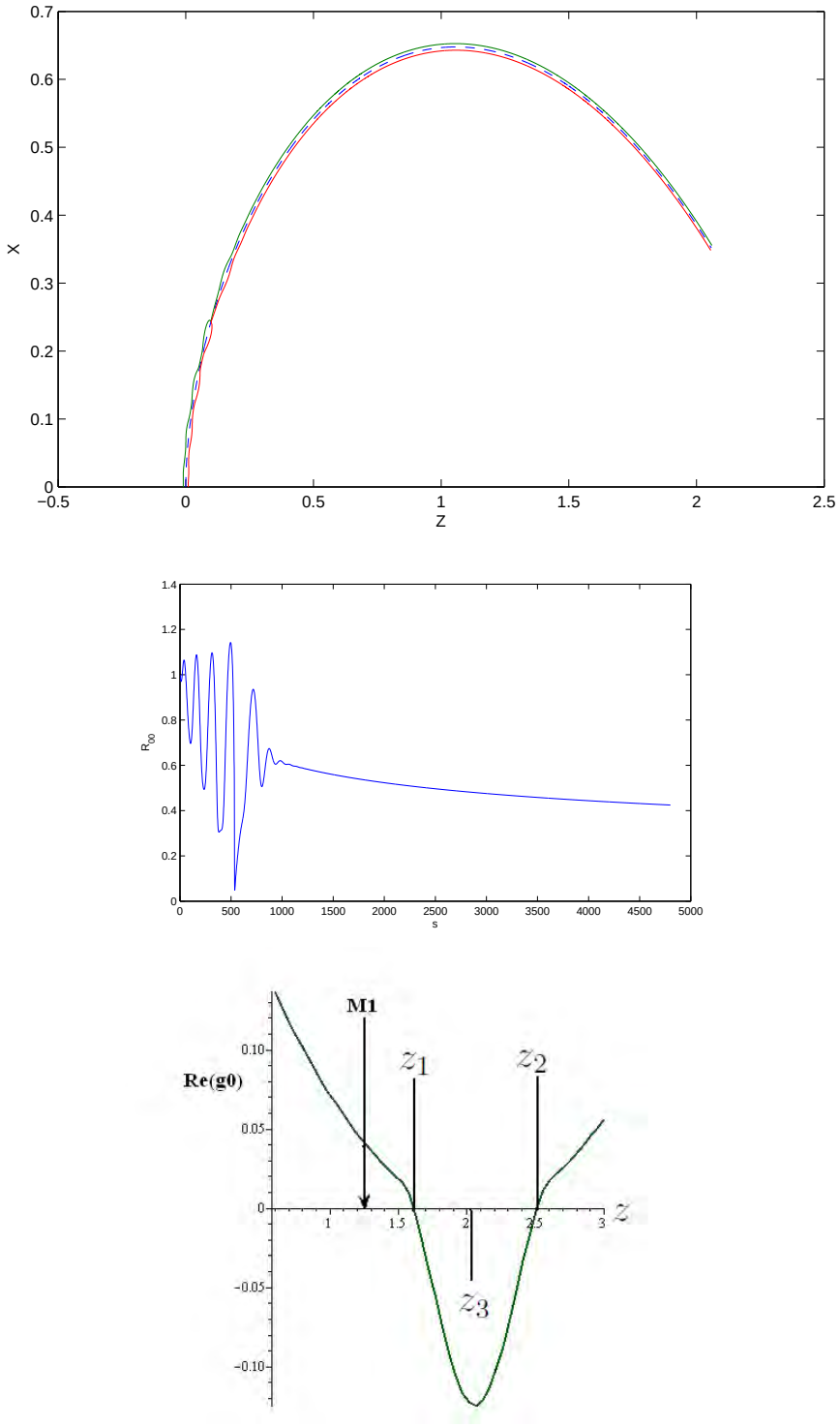

Figure 7.26: Mode 1 breakup in the linear wave regime. Top is the jet temporal evolution, middle is R_{00} against s while bottom is $Real(g_0)$ against z. Here $Rb = 0.412$.

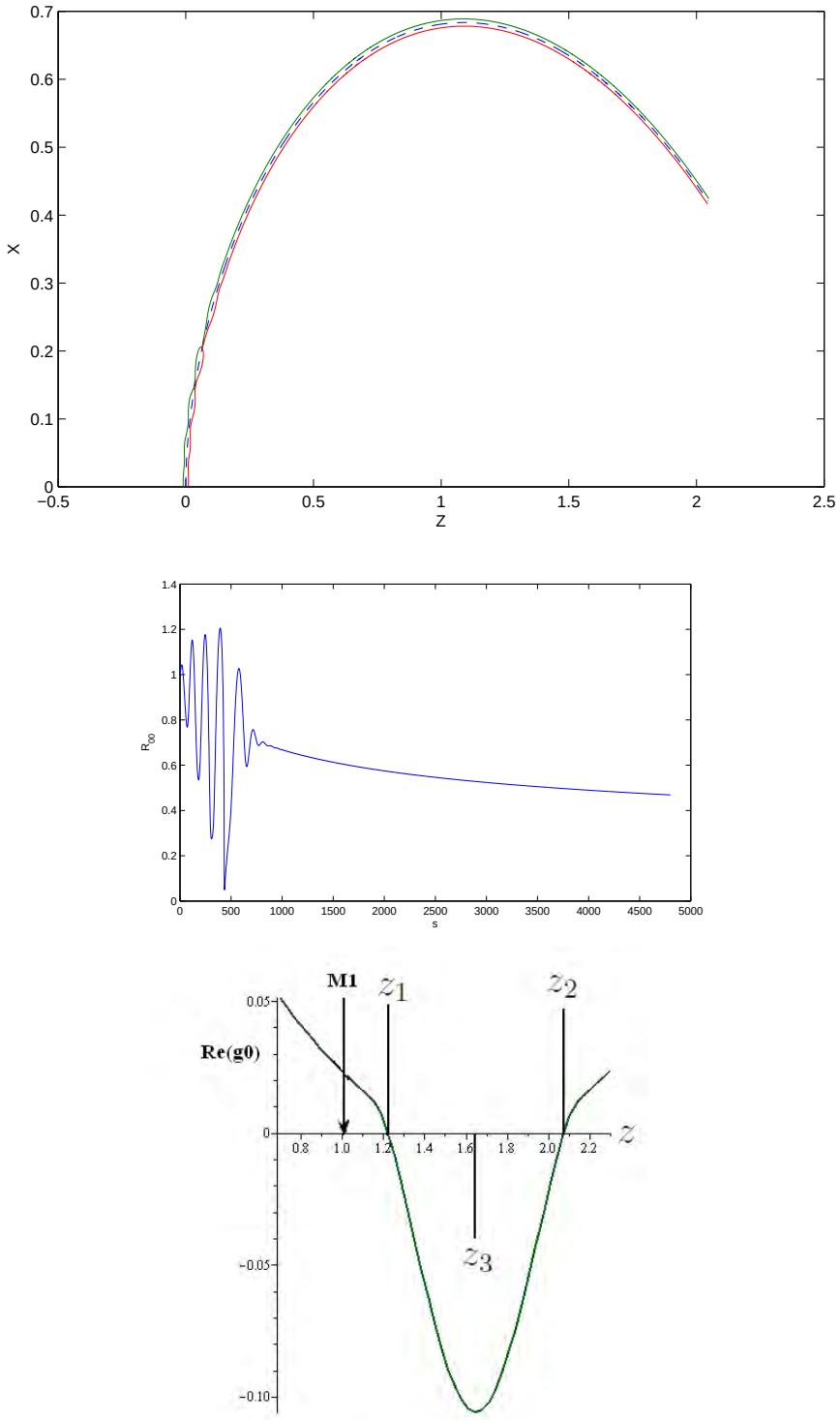

Figure 7.27: Mode 1 breakup in the linear wave regime. Top is the jet temporal evolution, middle is R_{00} against s while bottom is $Real(g_0)$ against z. Here $Rb = 0.512$.

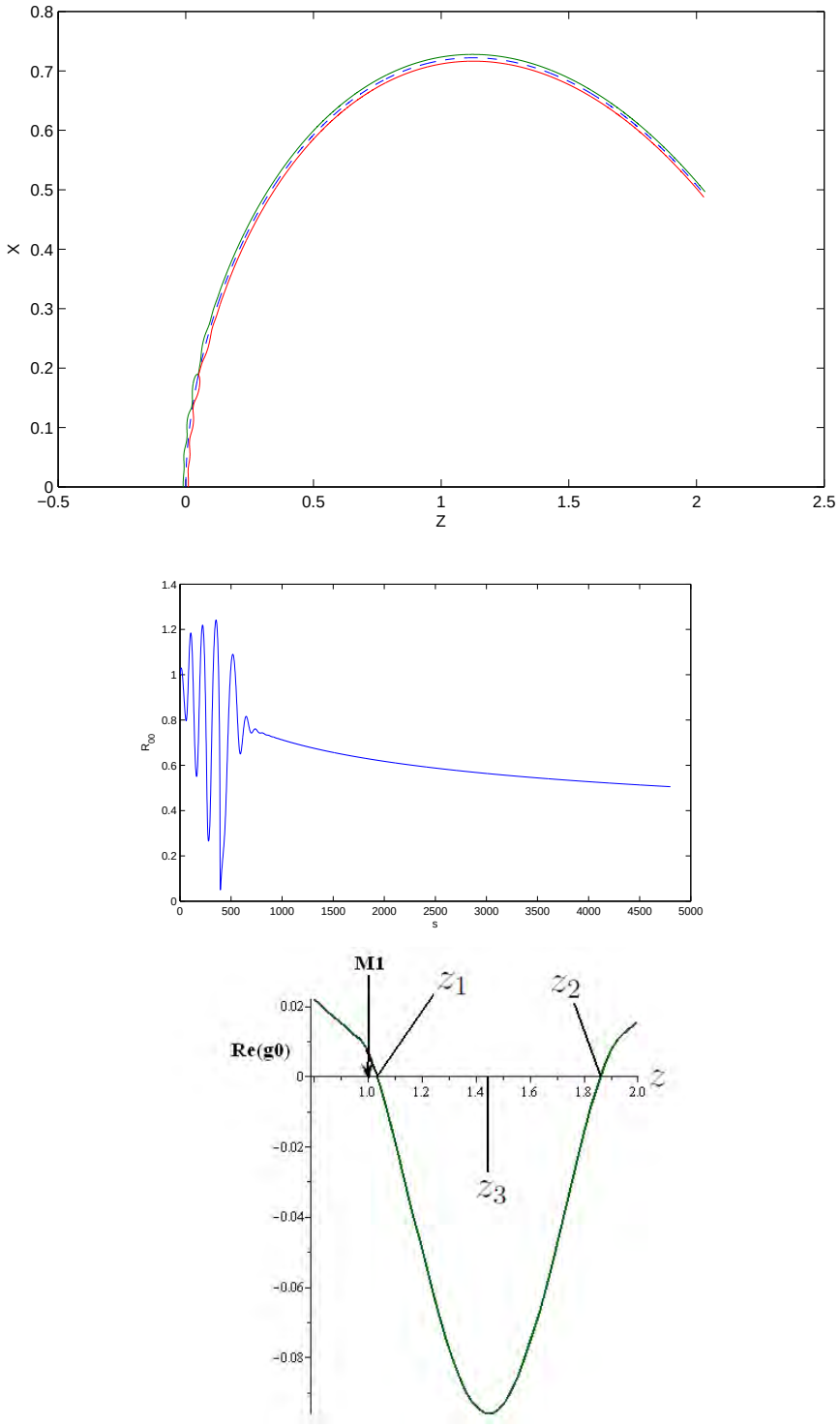

Figure 7.28: Mode 1 breakup in the linear wave regime. Top is the jet temporal evolution, middle is R_{00} against s while bottom is $Real(g_0)$ against z. Here $Rb = 0.612$.

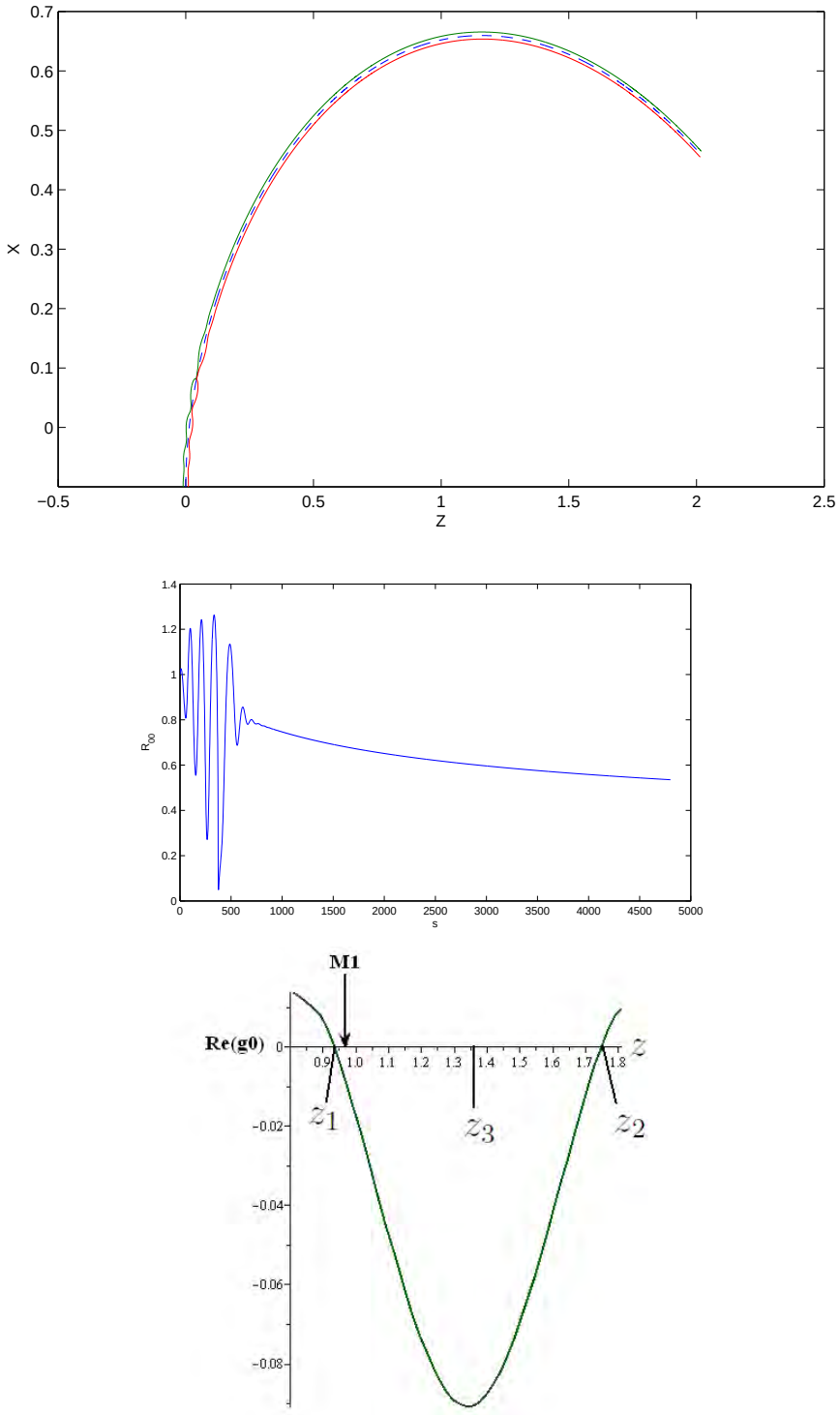

Figure 7.29: Mode 1 breakup in the linear wave regime. Top is the jet temporal evolution, middle is R_{00} against s while bottom is $Real(g_0)$ against z. Here $Rb = 0.7$.

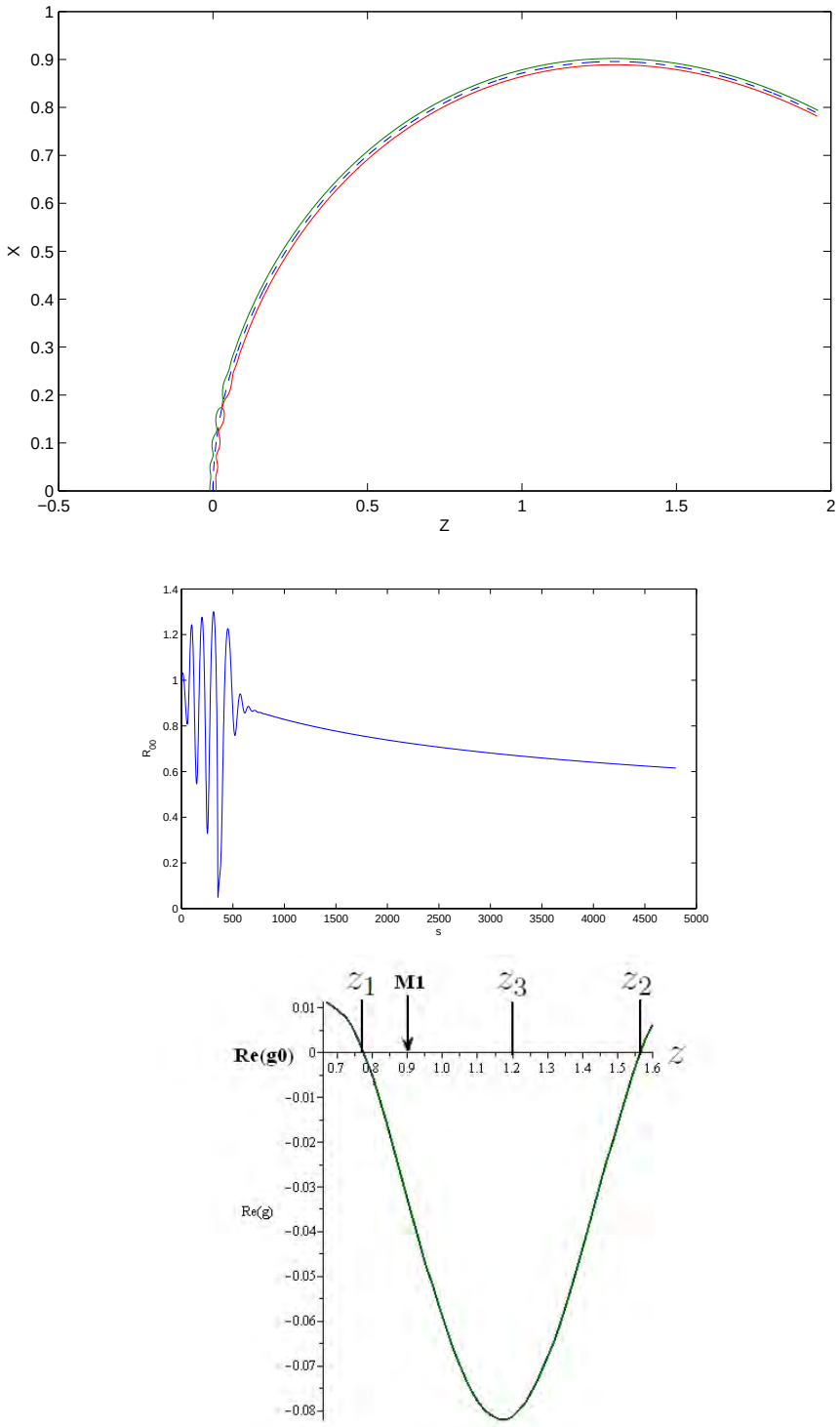

Figure 7.30: Mode 1 breakup in the linear wave regime. Top is the jet temporal evolution, middle is R_{00} against s while bottom is $Real(g_0)$ against z. Here $Rb = 1$.

7.8 Conclusions

In this chapter, we have extended the Needham-Leach method to the rotational-viscous problem. We have noticed that we do not need to examine regions, I, II, and III as they give the same results as in Decent (2009). We have successfully examined this problem in the crucial region IV (the nonlinear waves section) and obtained steady-state solutions for the velocity and the radius. In addition, we have obtained a fourth-order ODE for $g_0(z)$, which describes the behaviour of the unstable and uncontrollable nonlinear wave. We also solved that ODE for large Reynolds number (i.e., $Re \to \infty$) and obtained solution for $g_0(z)$.

In addition, we compared our theory (or hypothesis) with the numerical model. We get some encouraging results by changing the amplitude, the frequency and the Reynolds number in the numerical model which are in agreement with our theory. Our numerical model, however, showed that, for large Rb, M1 can occur after z_1 and, for large We, M2 can occur before z_1.

The numerical model showed a number of results which our hypothesis says that the jet breakup can be more easily controlled if it breaks up in the regime where $z < z_1$. This typically occurs for small s, corresponding to short breakup lengths. We, therefore, conclude that our hypothesis is correct, provided we have some conditions on the parameters, which are that we must have large values of the amplitude, the frequency and the Reynolds number, and small values of the Weber number ($We < 50$) and the Rossby number ($Rb < 0.7$).

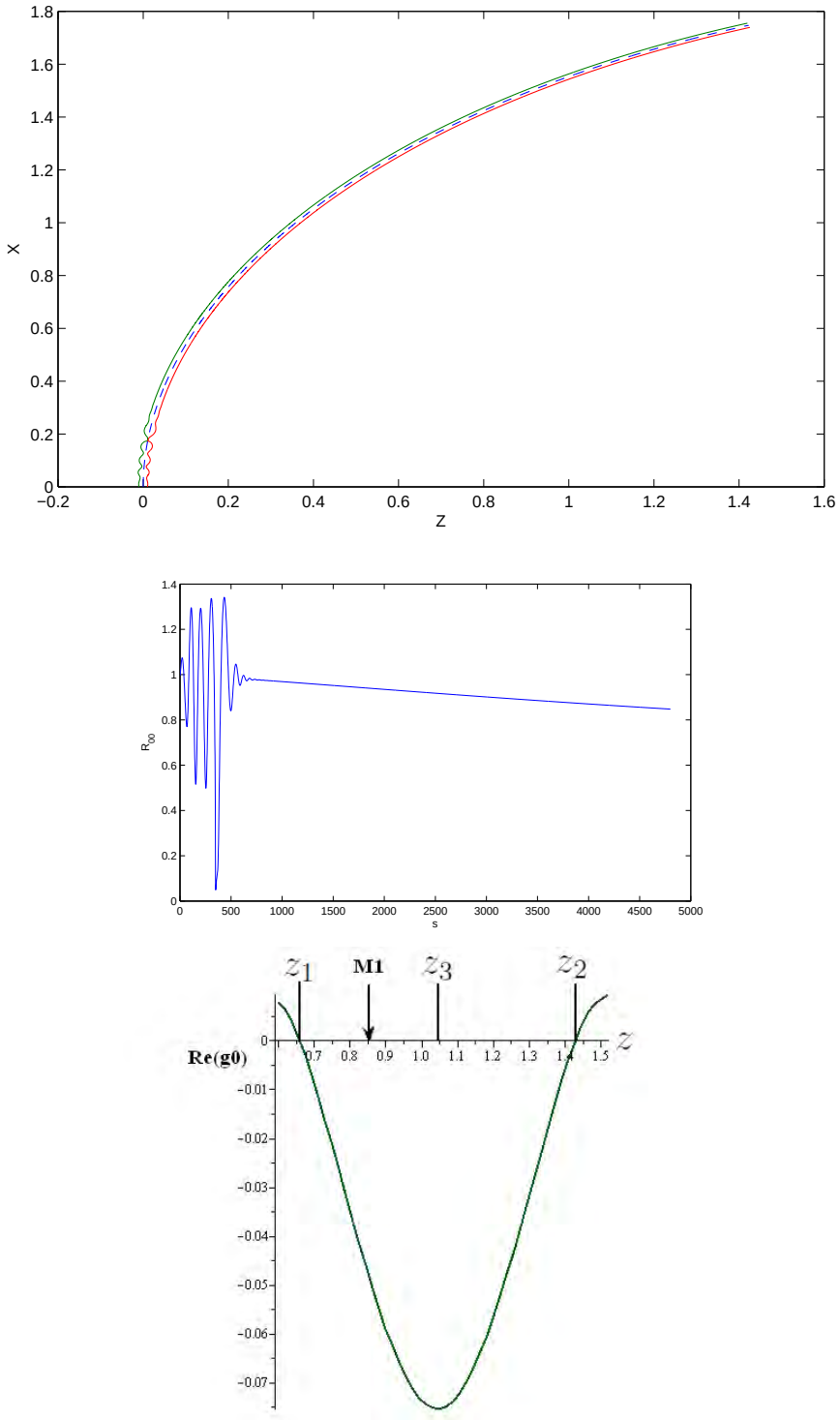

Figure 7.31: Mode 1 breakup in the linear wave regime. Top is the jet temporal evolution, middle is R_{00} against s while bottom is $Real(g_0)$ against z. Here $Rb = 5$.

Chapter 8

Asymptotic Solution of Rotating Newtonian Liquid Jet Under the Influence of Gravity

8.1 Introduction

In the previous chapter, we have solved the rotation and viscous problem without gravity and then we compared our hypothesis with the numerical results. In this chapter, we will do a generalization of the problem described in the previous chapter, by including the effects of gravity.

8.2 Problem Statement

The model equations for a rotating downward falling Newtonian jet, falling from a large rotating cylindrical drum, under the influence of gravity, are given by

$$R_t + \frac{1}{2}u_s R + uR_s = 0 \tag{8.1}$$

and

$$u_t + uu_s + \frac{1}{We}\left(\frac{1}{R(1+\epsilon^2 R_s^2)^{\frac{1}{2}}} - \frac{\epsilon^2 R_{ss}}{(1+\epsilon^2 R_s^2)^{\frac{3}{2}}}\right)_s$$
$$-\frac{3\epsilon}{Re}\cdot\frac{1}{R^2}\left[\frac{\partial}{\partial s}\left(R^2\frac{\partial u}{\partial s}\right)\right] + \frac{Y_s}{F^2} - \left[\frac{(X+1)X_s + ZZ_s}{Rb^2}\right] = 0, \qquad (8.2)$$

where $u\,(s,t)$ is the velocity component parallel to the centreline of the jet, $R\,(s,t)$ is the distance of the axi-symmetric free-surface away from the jet's centreline, s is the distance along the jet's centreline from the orifice (i.e., s is the arc length along the jet) and X,Z and Y are the jet centreline coordinates, so that the centreline of the jet can be described by $x = X(s,t)$, $z = Z(s,t)$ and $y = Y(s,t)$. Note that we have chosen the negative y-axis as the direction of the acceleration due to gravity. In these equations, the subscripts denote differentiation with respect to that subscript and t is time. These equations have been derived in Partridge (2006). In these equations, the non-dimensional parameters are the Weber number which is $We = \rho a U^2/\sigma > 0$, the Reynolds number which is $Re = \rho a U/\mu = \rho U s_0 \epsilon/\mu$, the Froude number which is $F = U/\sqrt{s_0 g}$ and the Rossby number which is $Rb = U/s_0\Omega$, where the liquid's density is ρ, the liquid's viscosity is μ, the surface tension of the liquid-gas interface is σ, the radius of the large cylindrical drum is s_0, the radius of the small orifice is a, the exit speed of the jet is U and g is the acceleration due to gravity. Also, Ω is the rotation rate and ϵ is a small parameter defined as

$$\epsilon = a/s_0 << 1.$$

We define $\tilde{s}$ and $\tilde{t}$ as

$$\tilde{s} = \frac{s}{\epsilon}, \qquad \tilde{t} = \frac{t}{\epsilon}.$$

So equation (8.1) can be written as

$$\frac{1}{\epsilon}R_{\tilde{t}} + \frac{1}{\epsilon}\frac{R}{2}u_{\tilde{s}} + \frac{1}{\epsilon}uR_{\tilde{s}} = 0,$$

or

$$R_{\tilde{t}} + \frac{R}{2}u_{\tilde{s}} + uR_{\tilde{s}} = 0. \tag{8.3}$$

Similarly, equation (8.2) can be written as

$$\frac{1}{\epsilon}[u_{\tilde{t}} + uu_{\tilde{s}}] = \frac{1}{\epsilon}[-\frac{1}{We}\left(\frac{1}{R(1+R_{\tilde{s}}^2)^{\frac{1}{2}}} - \frac{R_{\tilde{s}\tilde{s}}}{(1+R_{\tilde{s}}^2)^{\frac{3}{2}}}\right)_{\tilde{s}}$$
$$+\frac{3\epsilon}{Re\,\epsilon}\cdot\frac{1}{R^2}\left[\frac{\partial}{\partial\tilde{s}}\left(R^2\frac{\partial u}{\partial\tilde{s}}\right)\right] - \frac{Y_{\tilde{s}}}{F^2} + \left[\frac{(X+1)X_{\tilde{s}} + ZZ_{\tilde{s}}}{Rb^2}\right]],$$

or

$$u_{\tilde{t}} + uu_{\tilde{s}} = -\frac{1}{We}\left(\frac{1}{R(1+R_{\tilde{s}}^2)^{\frac{1}{2}}} - \frac{R_{\tilde{s}\tilde{s}}}{(1+R_{\tilde{s}}^2)^{\frac{3}{2}}}\right)_{\tilde{s}}$$
$$+\frac{3}{Re}\cdot\frac{1}{R^2}\left[\frac{\partial}{\partial\tilde{s}}\left(R^2\frac{\partial u}{\partial\tilde{s}}\right)\right] - \frac{Y_{\tilde{s}}}{F^2} + \left[\frac{(X+1)X_{\tilde{s}} + ZZ_{\tilde{s}}}{Rb^2}\right]. \tag{8.4}$$

The non-dimensional initial conditions are

$$R\left(\epsilon\tilde{s}, \epsilon\tilde{t}=0\right) = 1 \quad \text{and} \quad u\left(\epsilon\tilde{s}, \epsilon\tilde{t}=0\right) = 1.$$

The boundary conditions at the orifice are

$$R\left(\epsilon\tilde{s}=0, \epsilon\tilde{t}\right) = 1 \quad \text{and} \quad u\left(\epsilon\tilde{s}=0, \epsilon\tilde{t}\right) = 1 + \delta\sin\left(\omega\epsilon\tilde{t}\right).$$

We define u_0 and R_0 as the steady-state solution of equations (8.3) and (8.4). We also assume that $u \to u_0$ and $R \to R_0$ as $\tilde{s} \to \infty$, which physically means that in

the far-field, the jet is considered to be undisturbed.

8.3 Asymptotic Expansions

Note that now our original equations are in $\tilde{s}$ and $\tilde{t}$. We examine this problem in region IV (the nonlinear waves section), where $\tilde{s} \to \infty$ and $\tilde{t} \to \infty$ so that $z = \tilde{s}/\tilde{t} = O(1)$. We introduce a new length scale $\bar{s}$, defined by

$$\bar{s} = \epsilon\tilde{s} = O(1), \text{ as } \epsilon \to 0.$$

We introduce this notation $\bar{s}$ to remain consistent with the previous chapter's work. We pose the following expansions

$$u = u_0(\bar{s}) + \left[\exp\left(-tg_0\left(z,\bar{s}\right)\right)\left\{h_0\left(z,\bar{s}\right) + O\left(\frac{1}{\sqrt{t}}\right)\right\} + h.o.t.\right] \tag{8.5}$$

and

$$R = R_0(\bar{s}) + \left[\exp\left(-tg_0\left(z,\bar{s}\right)\right)\left\{\zeta_0\left(z,\bar{s}\right) + O\left(\frac{1}{\sqrt{t}}\right)\right\} + h.o.t.\right], \tag{8.6}$$

as $\tilde{t} \to \infty$ and $h.o.t.$ denotes higher-order terms. The steady-state equations for u_0 and R_0 can be obtained from equations (8.3) and (8.4), using $\bar{s} = \epsilon\tilde{s}$, and are given by

$$\epsilon(\frac{1}{2}u_0'R_0 + u_0R_0') = 0, \tag{8.7}$$

$$\epsilon u_0u_0' + \frac{1}{We}\left(\frac{-\epsilon R_0'}{R_0^2(1+\epsilon^2R_0'^2)^{\frac{1}{2}}} - \frac{\epsilon^3R_0'R_0''(R_0^{-1}) + \epsilon^3R_0'''}{(1+\epsilon^2R_0'^2)^{\frac{3}{2}}} + \frac{3\epsilon^5R_0'R_0''^2}{(1+\epsilon^2R_0'^2)^{\frac{5}{2}}}\right)$$

$$-\frac{3}{Re}(\epsilon^2 u_0'' + 2\epsilon^2 u_0' R_0' R_0^{-1}) + \epsilon\frac{Y_0'}{F^2} - \epsilon\left[\frac{(X_0+1)X_0' + Z_0 Z_0'}{Rb^2}\right] = 0, \quad (8.8)$$

$$(X_0')^2 + (Z_0')^2 + (Y_0')^2 = 1, \quad (8.9)$$

$$\frac{X_0'' Z_0' - X_0' Z_0''}{F^2} - \frac{2u_0 Y_0''}{Rb} + \frac{(X_0+1)(Y_0'' Z_0' - Y_0' Z_0'')}{Rb^2}$$

$$+\frac{Z_0(X_0'' Y_0' - X_0' Y_0'')}{Rb^2} = 0 \quad (8.10)$$

and

$$\left(u_0^2 - \frac{3\epsilon u_0'}{Re} - \frac{1}{R_0 We}\right)(X_0''^2 + Y_0''^2 + Z_0''^2) = -\frac{Y_0''}{F^2} + \frac{2u_0}{Rb}(X_0' Z_0'' - Z_0' X_0'')$$

$$+\frac{1}{Rb^2}\left[(X_0+1)X_0'' + Z Z_0''\right], \quad (8.11)$$

where $' = \partial/\partial\bar{s}$.

8.4 Leading-Order Solution

We expand u_0 and R_0 as

$$u_0(\bar{s}) = u_{00}(\bar{s}) + \epsilon u_{01}(\bar{s}) + \epsilon^2 u_{02}(\bar{s}) + O(\epsilon^3) \quad (8.12)$$

and

$$R_0(\bar{s}) = R_{00}(\bar{s}) + \epsilon R_{01}(\bar{s}) + \epsilon^2 R_{02}(\bar{s}) + O(\epsilon^3). \quad (8.13)$$

Hence at leading-order in ϵ, we have

$$\frac{1}{2}u'_{00}R_{00} + u_{00}R'_{00} = 0, \tag{8.14}$$

$$u_{00}u'_{00} - \frac{1}{We}\left(\frac{R'_{00}}{R^2_{00}}\right) + \frac{Y'_0}{F^2} - \left[\frac{(X_0+1)X'_0 + Z_0Z'_0}{Rb^2}\right] = 0, \tag{8.15}$$

$$(X'_0)^2 + (Z'_0)^2 + (Y'_0)^2 = 1, \tag{8.16}$$

$$\frac{X''_0Z'_0 - X'_0Z''_0}{F^2} - \frac{2u_{00}Y''_0}{Rb} + \frac{(X_0+1)(Y''_0Z'_0 - Y'_0Z''_0)}{Rb^2}$$

$$+\frac{Z_0(X''_0Y'_0 - X'_0Y''_0)}{Rb^2} = 0 \tag{8.17}$$

and

$$\left(u^2_{00} - \frac{1}{R_0We}\right)(X''^2_0 + Y''^2_0 + Z''^2_0) = -\frac{Y''_0}{F^2} + \frac{2u_{00}}{Rb}(X'_0Z''_0 - Z'_0X''_0)$$

$$+\frac{1}{Rb^2}\left[(X_0+1)X''_0 + ZZ''_0\right]. \tag{8.18}$$

So we have four equations in four unknowns, namely u_{00}, X_0, Y_0 and Z_0, as

$$R_{00} = 1/\sqrt{u_{00}},$$

from equation(8.14). The boundary conditions at $s = 0$ are given by

$$u_{00}(0) = X_0'(0) = 1 \text{ and } X_0(0) = Y_0(0) = Z_0(0) = Y_0'(0) = Z_0'(0) = 0.$$

The steady-state solution of the above equations is obtained using a Runga-Kutta 4th-order method and is shown in Figures 8.1-8.4.

Since the surface tension causes the jet to break quickly, so reducing surface tension implies long jets. It can be seen from Figure 8.1 that for large We (i.e., for small surface tension), we get a long jet. Figure 8.2 shows that as we decrease We (i.e., increase the surface tension), the jet curves more. Figure 8.3 shows that as we decrease F (i.e., increase the gravity), the jet falls more and rotates less. Figure 8.4 shows that as we increase Rb (i.e., decrease the rotation), the jet rotates less and falls more.

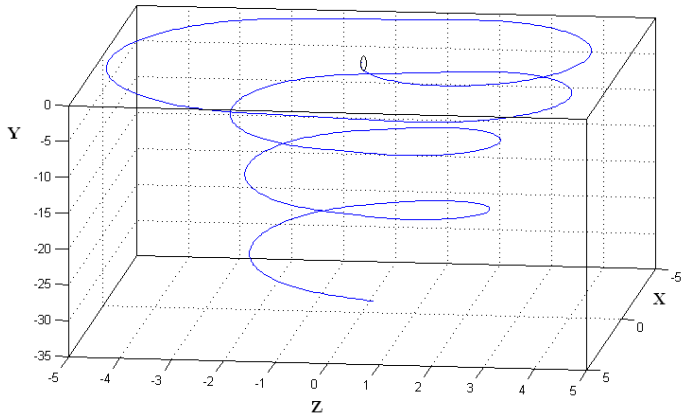

Figure 8.1: A graph showing a long trajectory for We=70, F=10 and Rb=5. Clearly, for large We (i.e., for small surface tension), we get a long jet.

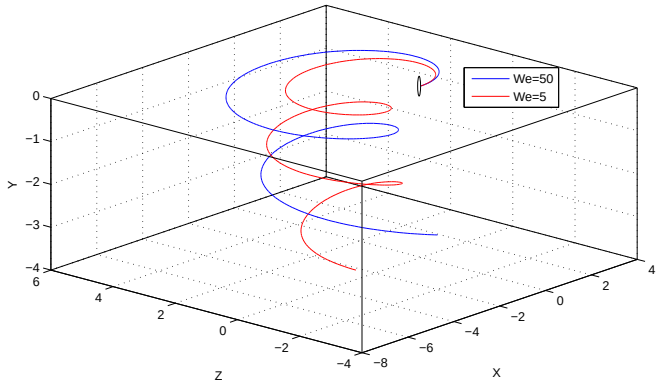

Figure 8.2: A graph showing different trajectories for different Weber numbers. Clearly, as we decrease We (i.e., increase the surface tension), the jet curves more. The other parameters are given by $Rb = 5$ and $F = 15$.

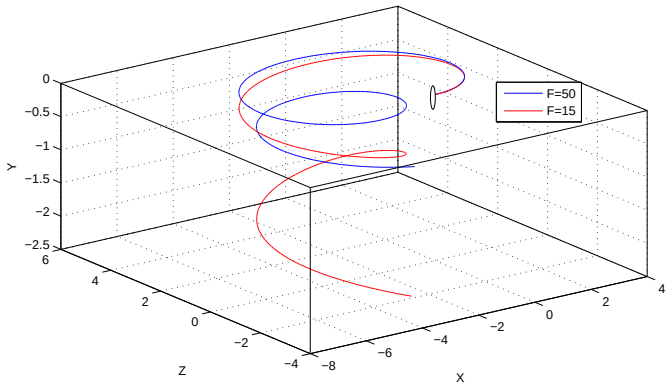

Figure 8.3: A graph showing different trajectories for different Froude numbers. Clearly, as we decrease F (i.e., increase the gravity), the jet falls more and rotates less. The other parameters are given by $We = 70$ and $Rb = 5$.

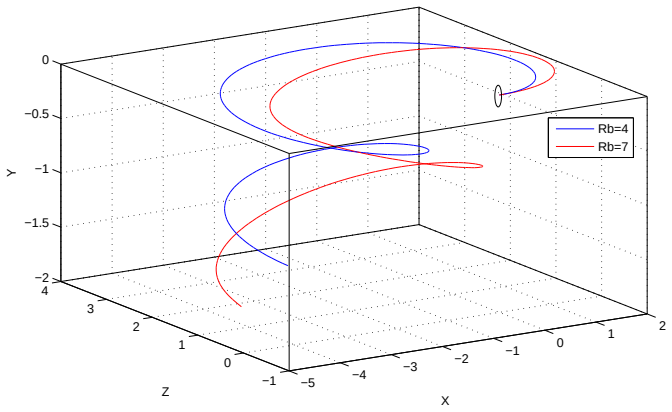

Figure 8.4: A graph showing different trajectories for different Rossby numbers. Clearly, as we increase Rb (i.e., decrease the rotation), the jet rotates less and falls more. The other parameters are given by $We = 5$ and $F = 15$.

8.5 Determination of the nonlinear travelling wave

Next, we find the g_0-equation as follows. Substituting equations (8.5) and (8.6) into equation (8.3), and using $\partial/\partial\tilde{s} = \epsilon\,\partial/\partial\bar{s}$, we obtain, at leading-order in ϵ, an equation of the form

$$h_0 = 2\zeta_0 \left(\frac{-g_0 + z g_{0,z} - u_{00} g_{0,z}}{R_{00} g_{0,z}} \right). \tag{8.19}$$

Putting $u_{00} = R_{00} = 1$ in equation (8.19), we get

$$h_0 = \zeta_0 \left(\frac{-2g_0 + 2z g_{0,z} - 2g_{0,z}}{g_{0,z}} \right), \tag{8.20}$$

which is the same equation (95) of Decent (2009). We expected to get this equation as it corresponds to the no gravity problem in which $u_{00} = R_{00} = 1$.

Substituting equations (8.5), (8.6) and (8.19) into equation (8.4), and using $\frac{\partial}{\partial\tilde{s}} = \epsilon\frac{\partial}{\partial\bar{s}}$, we obtain a nonlinear ordinary differential equation for g_0 in z, at

leading-order in ϵ, of the form

$$ReR_{00}\left(g_{0,z}\right)^4+\frac{Re}{R_{00}}\left(g_{0,z}\right)^2-4zReWeg_0g_{0,z}+2z^2ReWe\left(g_{0,z}\right)^2-4zReWeu_{00}\left(g_{0,z}\right)^2$$

$$+4ReWeu_{00}g_0g_{0,z}+2ReWeu_{00}^2\left(g_{0,z}\right)^2+2ReWe\left(g_0\right)^2+6Weg_0\left(g_{0,z}\right)^2-6Wez\left(g_{0,z}\right)^3$$

$$+6Weu_{00}\left(g_{0,z}\right)^3=0. \tag{8.21}$$

Putting $u_{00}=R_{00}=1$ in equation (8.21), we get

$$Re\left(g_{0,z}\right)^4+Re\left(g_{0,z}\right)^2-4zReWeg_0g_{0,z}+2z^2ReWe\left(g_{0,z}\right)^2-4zReWe\left(g_{0,z}\right)^2+4ReWeg_0g_{0,z}$$

$$+2ReWe\left(g_{0,z}\right)^2+2ReWe\left(g_0\right)^2+6Weg_0\left(g_{0,z}\right)^2-6Wez\left(g_{0,z}\right)^3+6We\left(g_{0,z}\right)^3=0,$$

which is the same equation (92) of Decent (2009).

This result shows that the g_0-equation implicitly depends on the gravity and the rotation via u_0 and R_0. This is due to the fact that the gravity and the rotation appear in the steady-state equations, in the form of F and Rb respectively. So changing F and Rb, in those equations, imply a change in u_0 and R_0; the steady-state solutions, which in turn will have a change in the g_0-equation. In other words, the gravity and the rotation make a difference on the g_0-equation via u_0 and R_0.

However, F and Rb do not appear explicitly in the g_0-equation. In order to bring F and Rb explicitly into our g_0-equation, we must have

$$-\frac{Y_{\bar{s}}}{F^2}+\left[\frac{(X+1)X_{\bar{s}}+ZZ_{\bar{s}}}{Rb^2}\right]=f(u,R).$$

Solving equation (8.21), for large Reynolds number (i.e., $Re \to \infty$), gives

$$g_0 = \frac{\sqrt{Q_0}}{4\sqrt{We}R_{00}^{3/2}} \tag{8.22}$$

where

$$Q_0 = -We^2u_{00}^4R_{00}^2 - 10z^2WeR_{00} + 20zWeu_{00}R_{00} - 10Weu_{00}^2R_{00} - 6z^2We^2u_{00}^2R_{00}^2$$

$$-z^4We^2R_{00}^2 + 2 + 4z^3We^2u_{00}R_{00}^2 + 4zWe^2u_{00}^3R_{00}^2$$

$$-\sqrt{R_{00}We\left(z-u_{00}\right)^2\left(Weu_{00}^2R_{00} - 2zWeu_{00}R_{00} + z^2WeR_{00} - 4\right)^3}. \tag{8.23}$$

Putting $u_{00} = R_{00} = 1$ in equations (8.22) and (8.23), we get

$$g_0 = \frac{\sqrt{Q_0}}{4\sqrt{We}} \tag{8.24}$$

where

$$Q_0 = -We^2 - 10z^2We + 20zWe - 10We - 6z^2We^2 - z^4We^2 + 2 + 4z^3We^2$$

$$+4zWe^2 - \sqrt{We\left(z-1\right)^2\left(We - 2zWe + z^2We - 4\right)^3}, \tag{8.25}$$

which are the same equations (112) and (113) of Decent (2009).

From equations (8.22) and (8.23), we find that

$$z_1 \to max\left(u_{00} - 2/\sqrt{R_{00}We}, 0\right) \text{ and } z_2 \to u_{00} + 2/\sqrt{R_{00}We} \text{ as } Re \to \infty.$$

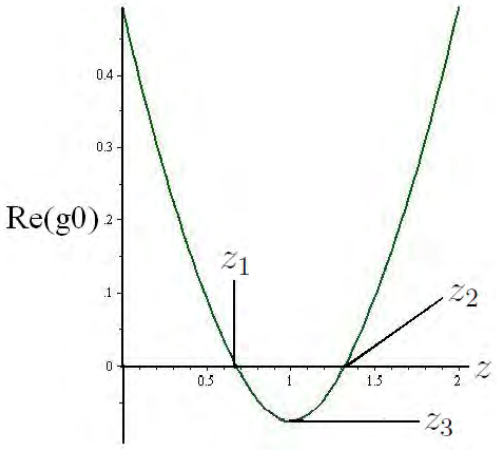

Figure 8.5: A plot illustrating the solution of g_0-equation (8.21). It shows three z-values (z_1, z_2 and z_3) against a temporal growth rate curve. Note that u_0 and R_0, in the g_0-equation (8.21), are obtained from the steady-state solution. The parameters are $We = 22.26$, $Re = 375$, $Rb = 7$ and $F = 15$.

These values of z_1 and z_2 corresponds to the same values of of z_1 and z_2 of Decent (2009) in the limit $u_{00} = 1$ and $R_{00} = 1$. We next find the values of z_1 and z_2 numerically, without any asymptotic limit. These values are shown in Figure 8.5. Note that we do not need to examine regions, I, II, III and V as they give the same results as in Decent (2009).

8.6 Conclusions

In this chapter, we have extended the Needham-Leach method to the rotational-viscous-gravity problem. We have noticed that we do not need to examine regions, I, II, and III as they give the same results as in Decent (2009). We have successfully examined this problem in the crucial region IV (the nonlinear waves section) and obtained steady-state solutions for the velocity and the radius. In addition, we have obtained a fourth-order ODE (8.21) for $g_0(z)$, which describes the behaviour of the unstable and uncontrollable nonlinear wave. We also solved that ODE for large Reynolds number (i.e., $Re \to \infty$) and obtained solution for $g_0(z)$.

This solution gives us the value of z_1 (where the nonlinear waves start to dominate) and the value of z_2 (where we have a mixture of both linear and nonlinear waves). From this, we postulate that in order to obtain the mode 1 behaviour (i.e., uniform droplets with no satellite droplets), we must break the jet before $z = z_1$, so that the linear waves dominate in the breakup process. Note that all of our results correspond perfectly to results in Decent (2009) with no gravity and rotation. At the end, we also solved g_0-equation (8.21) computationally, using a Runge-Kutta fourth-order method, which gives us the numerical solution for $g_0(z)$, for $We = O(1), Re = O(1), Rb = O(1)$ and $F = O(1)$.

Chapter 9

Conclusion

The main objective of this piece of research was to investigate a number of methods which help us to know about the behaviour of liquid jets and especially to control the breakup of liquid jets and, in particular, lead to a reduction in satellite droplets. The first two chapters of this thesis describe introduction and literature review on liquid jets along with the review of some important concepts used in the theory of liquid jets.

In the third chapter, we have investigated the instability of an inviscid compound liquid jet falling under the influence of gravity. We have used a slender jet approximation to determine a one dimensional model, which describes the velocity and radial displacements of the inner and outer free surfaces. We have solved the steady-state equations and investigated its dependence on changes in all the parameters of the model. We have then considered the growth of unstable waves on the two interfaces by considering a linear temporal instability analysis. The obtained dispersion relation, which describes the relationship between the growth rate and wavenumber of disturbances, has been solved numerically in order to determine the most unstable wavenumber (which we assume to be the dominant wavenumber which leads to breakup) and the associated maximum growth rate.

We have investigated how this most unstable wavenumber varies as we change key critical parameters, like the ratio of surface tension σ and the aspect ratio of inner jet radii χ. Diagrams showing how such changes in the parameters affect the most unstable mode, for different axial distances x along the jet, have been investigated to reveal that the most unstable wavenumber and maximum growth rates are larger as the wave travels down the jet. Furthermore, we found that the most unstable wavenumber decreases with an increase in χ, for different axial distances x, whilst the maximum growth rate decreases with an increase in ρ, and with a decrease in σ, for different axial distances x. Moreover, we found that a decrease in the interfacial surface tension ratio whereas an increase in the density ratio and the Weber number causes the frequency and the transformed wavespeed of the disturbance to decrease, at $x = 0$. In addition, our results correspond to those given in Sanz & Meseguer (1985), for the case without gravity.

We also found that for certain parameter values, there exists a non-uniqueness in the value of the maximum wavenumber k_{max}. This behaviour is a result of the two competing wavemodes along the jet and can result in large differences in k_{max}, as certain parameters are changed. We showed that there exists a value of σ, which we refer to as $threshold\ surface\ tension\ ratio\ \sigma^*$, at which we have two competing wavemodes having different wavenumbers. We also showed that σ^* is the same, for all values of x, while k_{max} is larger as x increases. We also found that, for $\sigma < \sigma^*$, an increase in σ causes k_{max} to increase, while for $\sigma > \sigma^*$, an increase in σ causes k_{max} to decrease slightly, for $x = 0$, $x = 2$ and $x = 4$. Furthermore, we found that σ^* increases, as the density ratio ρ is increased. We also found that breakup lengths and droplet sizes are likely to be smaller for a compound liquid jet falling under gravity than those predicted using the analysis of Sanz & Meseguer (1985). We note that due to the presence of a thinning jet in the case with gravity this would be anticipated but our results

here show that the thinning nature of the jet affects the maximal growth rates and most unstable wavenumbers. We have also used the results from our linear theory to estimate the location of breakup and have shown that the breakup of the jet can occur by the inner jet rupturing first or by the outer interface touching the inner interface, and that the value of χ, at which these two processes occur simultaneously, become smaller as We is decreased. At the end, we have also compared our results favourably with numerical simulations found in Uddin & Decent (2010).

In the fourth chapter, we have investigated the breakup, droplet formation and temporal instability analysis of shear thinning compound jets falling under gravity. We have considered the growth of unstable waves on the two interfaces by considering a linear temporal instability analysis. The obtained dispersion relation, which describes the relationship between the growth rate and wavenumber of disturbances, has been solved numerically in order to determine the most unstable wavenumber and the associated maximum growth rate. We have investigated how this most unstable wavenumber varies as we change key critical parameters. We found that the most unstable wavenumber and maximum growth rates are larger as the wave travels down the jet. We also find that a decrease in the density ratio causes the maximum wavenumber of the disturbance to decrease for $x < 1.8$ while after $x = 1.8$, this behaviour is reversed. We also observe that a decrease in the density ratio causes the maximum growth rate of the disturbance to increase, although for large ρ, the difference in the maximum growth rate is slightly small. We further note that as we increase ρ, $x = 0$ curve increases, $x = 4$ curve decreases, while $x = 1.8$ curve remains constant. This shows that the transition of the different behaviour of k_{max} at $x = 0$ and $x = 4$ curves occurs at $x = 1.8$ curve. This transition takes place due to the characteristic behaviour of ρ, for these set of parameters. In addition, we found that there does not exists any discontinuity

(or transition) in the maximum wavenumber k_{max} against any parameter of the problem in this case, as found in inviscid-gravity case, for σ. This may be due to the fact that in this case, we have only one velocity, whereas, in the inviscid case, we have two different velocities.

We have also solved the model equations using a numerical method based on finite differences (the Lax-Wendroff method). We have investigated the effects of changing the key parameters on the breakup lengths, main drop sizes and satellite droplet sizes. In particular, we have found that breakup lengths, main drops and satellite droplets are always smallest when we have both shear thinning core and shell fluids, for different values of the disturbance wavenumber κ. We also find that the satellite droplets decrease as we increase κ. Furthermore, as the interfacial surface tension ratio σ is increased, the breakup lengths are smaller and less amount of fluid is consumed in the main drop size, which in turn, has an impact of a more increase in the satellite droplet size. Moreover, the satellite droplet sizes are smallest when we have both shear thinning core and shell fluids. We also found that due to gravity, breakup lengths are smaller and are also smaller when the core fluid is strongly shear thinning, as in Mohsin $et\ al.$ (2012). We observed that for a Newtonian core, increasing δ implies a decrease in the satellite droplets, which is a similar qualitative behaviour as found in Mohsin $et\ al.$ (2012). We also observed that as n_1 and n_2 are increased (or as the inner and the outer fluids are made less shear thinning), less discharge of fluid takes place into the main drop size, which in turn, has an impact of a more increase in the satellite droplet size.

In the fifth chapter, we gave a description and an application of the Needham-Leach asymptotic method. We derived the temporal growth rate and wavenumber of the fastest growing temporal linear mode in the limit of $Re \to \infty$, using the linear temporal instability analysis. These quantities have not been given nor derived in Decent (2009).

In the sixth chapter, we examined a straight vertically falling Newtonian jet, which is falling under the influence of gravity and applied the Needham-Leach method to it. We obtained the asymptotic solution of that problem and, in addition, we obtained some useful information, like we identified z_1 and z_2, at which the state of the wave changes. In addition, we found the onset of the instability of the nonlinear wave, which we called z_1, both asymptotically and numerically. We also found that z_1 increases with increasing values of Weber number and with decreasing values of Reynolds number. Moreover, we compared our results with those given in Decent (2009) and we found that our results are in perfect agreement with those given in Decent (2009).

In the seventh chapter, we considered a rotating Newtonian jet and we fully analyzed it by using the Needham-Leach method and also the numerical model. We found the solution of that problem as well as the location of the different modes of breakup. We took data from experiments and used this data to compare our theory and numerical model. We ran the numerical code, to find the breakup point z_b and the shape of the mode of breakup. We next used the steady-state solution in the numerics to generate the solution of the g_0-equation to find a solution curve, which showed z_1 and z_2, and then observed that at which place of the curve the breakup point lies. We also observed the impact of changing the five parameters (δ, ω, Re, We and Rb) on modes of breakup. We found that for large δ, we have a small breakup while for small δ, we have a large breakup, and decreasing δ implies a change in modes from M1 to M2 and then to M2/3. We also found that as we increase the value of ω (from $\omega = 0.698$ to $\omega = 1.3$), we get a change in modes from M2/3 to M2 and then to M1. Moreover, we noted that as we increase Re, the breakup point and z_1 are slightly decreased, with the breakup point having less decrease. We also found that for larger values of We, we get larger values of z_1 and we do not get M1. We also noted that for large values of

We, M2 can occur before z_1. In addition, we observed that as we increase Rb, values of both the breakup point z_b and the onset of the instability of the nonlinear wave z_1 decrease, with z_1 having more large decrease in its value. Finally, we unexpectedly observed that M1 can occur after z_1, for large values of the Rossby number, which disproved our hypothesis that M1 can only occur before the onset of the nonlinear wave, which starts at z_1. We, therefore, conclude that our hypothesis (that we always get M1 in $z < z_1$ region) is not valid for large values of the Rossby number.

In the eight chapter, we added the effects of gravity in the previous problem which was analyzed in chapter six and we applied the Needham-Leach method to it, which results in obtaining the asymptotic solution of that problem.

Chapter 10

Future Work

There are many things which we want to do in the future. We can do spatial instability analysis in problems described in chapters three and four of this thesis. We can also add rotation in problems described in chapters three and four of this thesis. We can also apply the Needham-Leach method in problems described in chapters three and four of this thesis. In addition, we can put surfactants in chapters three and four. We can also do an extension of the sixth chapter of this thesis by considering a straight vertically falling non-Newtonian liquid jet, which is falling under the influence of gravity and we can apply the Needham-Leach method to it. We can obtain the asymptotic solution of that problem and, in addition, we can obtain some useful information, like we can identify z_1 and z_2, at which the state of the wave changes. Moreover, we can find the onset of the instability of the nonlinear wave, which we called z_1, both asymptotically. We can also develop a numerical model for this problem to support our asymptotic analysis.

After doing the above problem, we can also add the effects of rotation by considering a rotating non-Newtonian liquid jet, which is falling under the influence of gravity and we can apply the Needham-Leach method to it. We can obtain the asymptotic solution of that problem and, in addition, we can obtain the onset of

the instability of the nonlinear wave. Then we can also develop a numerical model to support our analysis.

Moreover, like we have used a numerical model without gravity in the seventh chapter, in a same way, we can also develop a numerical model with gravity for the sixth chapter to support our analysis in that chapter.

In addition, like we considered non-Newtonian liquid jets asymptotically in Appendix A, we can develop a numerical model for non-Newtonian fluids to support our analysis. Further more, we can add surfactants, which are the special chemicals that decrease the surface tension of fluids, in our work in sixth, seventh and eight chapters. We can get some interesting results in these cases.

Our asymptotic analysis can also be extended to compound liquid jets. We can also split the whole asymptotic domain into five different regions and then apply Needham-Leach method in each region. In addition, we can also make a numerical model to back up our theory for the compound liquid jets. We can use our asymptotic analysis for inviscid, Newtonian and non-Newtonian compound liquid jets, with and without gravity. Further more, we can also examine liquid jets having externally imposed thermal gradients (for example, we can heat the jets). In this case, we will get surface tension gradients as surface tension is temperature dependent.

In addition, we can also compare our future work on compound liquid jets with experiments. In the department of Chemical Engineering, University of Birmingham, we have very recently bought a fast camera to take the pictures of the breakup of compound liquid jets. Hence we can now take pictures of the breakup of compound liquid jets in different situations that were not available before.

Appendix A

Asymptotic Solution of Straight Uniform Non-Newtonian Liquid Jets

A.1 Introduction

The problem presented in this appendix is a generalization of the problem presented in Decent (2009), where a Newtonian fluid, having a constant viscosity, was considered.

A.2 Model Equations

The model equations of this appendix are

$$R_t + \frac{R}{2}u_z + uR_z = 0 \tag{A.1}$$

and

$$u_t + uu_z = -\frac{1}{We}\left(\frac{1}{R(1+\epsilon^2 R_z^2)^{\frac{1}{2}}} - \frac{\epsilon^2 R_{zz}}{(1+\epsilon^2 R_z^2)^{\frac{3}{2}}}\right)_z + \frac{3}{Re}\cdot\frac{1}{R^2}\left[\frac{\partial}{\partial z}\left(\mu_a R^2 \frac{\partial u}{\partial z}\right)\right]. \tag{A.2}$$

These equations are derived in Uddin (2007) and here we have used the same notations as we did in our previous chapters. Here μ_a is given by

$$\mu_a = (1-\lambda)[1+3h^2(u_z)^2]^{\frac{n-1}{2}} + \lambda. \tag{A.3}$$

We define new length and time scales $\tilde{z}$ and $\tilde{t}$ such that

$$\tilde{z} = \frac{z}{\epsilon}, \qquad \tilde{t} = \frac{t}{\epsilon}.$$

So equation (A.1) can be written as

$$R_{\tilde{t}} = -\frac{R}{2}u_{\tilde{z}} - uR_{\tilde{z}}, \tag{A.4}$$

which after dropping tildes becomes

$$R_t + \frac{R}{2}u_z + uR_z = 0. \tag{A.5}$$

In addition, equation (A.2) can be written as

$$u_{\tilde{t}} + uu_{\tilde{z}} = -\frac{1}{We}\left(\frac{1}{R(1+R_{\tilde{z}}^2)^{\frac{1}{2}}} - \frac{R_{\tilde{z}\tilde{z}}}{(1+R_{\tilde{z}}^2)^{\frac{3}{2}}}\right)_{\tilde{z}} + \frac{3}{Re\,\epsilon}\cdot\frac{1}{R^2}\left[\frac{\partial}{\partial\tilde{z}}\left(\mu_a R^2\frac{\partial u}{\partial\tilde{z}}\right)\right]. \tag{A.6}$$

We define

$$\tilde{R}e = Re\,\epsilon = \frac{\rho U L}{\mu_0} \cdot \frac{a}{L} = \frac{\rho U a}{\mu_0}.$$

Therefore, equation (A.6) becomes

$$u_{\tilde{t}} + u u_{\tilde{z}} = -\frac{1}{We}\left(\frac{1}{R(1+R_{\tilde{z}}^2)^{\frac{1}{2}}} - \frac{R_{\tilde{z}\tilde{z}}}{(1+R_{\tilde{z}}^2)^{\frac{3}{2}}}\right)_{\tilde{z}} + \frac{3}{\tilde{R}e} \cdot \frac{1}{R^2}\left[\frac{\partial}{\partial \tilde{z}}\left(\mu_a R^2 \frac{\partial u}{\partial \tilde{z}}\right)\right], \tag{A.7}$$

which after dropping tildes becomes

$$u_t + u u_z + \frac{1}{We}\left(\frac{1}{R(1+R_z^2)^{\frac{1}{2}}} - \frac{R_{zz}}{(1+R_z^2)^{\frac{3}{2}}}\right)_z - \frac{3}{Re} \cdot \frac{1}{R^2}\left(\mu_a R^2 u_z\right)_z = 0, \tag{A.8}$$

where μ_a is given by equation (A.3). Moreover, equation (A.3) can be written as

$$\mu_a = (1-\lambda)[1 + 3\frac{h^2}{\epsilon^2}(u_{\tilde{z}})^2]^{\frac{n-1}{2}} + \lambda. \tag{A.9}$$

Similar to defining $\tilde{z}$ and $\tilde{t}$ earlier, we define

$$\tilde{h} = \frac{h}{\epsilon},$$

so that equation (A.9) becomes as

$$\mu_a = (1-\lambda)[1 + 3\tilde{h}^2(u_{\tilde{z}})^2]^{\frac{n-1}{2}} + \lambda,$$

which after dropping tilde becomes

$$\mu_a = (1-\lambda)[1+3h^2(u_z)^2]^{\frac{n-1}{2}} + \lambda. \tag{A.10}$$

As mentioned earlier (in section 5.1), we divide the domain in five asymptotic regions: (I) $z \to 0$ and $t \to 0$; (II) $z = O(1)$ and $t \to 0$; (III) $z \to \infty$ and $t = O(1)$; (IV) $z \to \infty$ and $t \to \infty$ and (V) $z = O(1)$ and $t \to \infty$. We then find solution in each region and that solution has some unknown constants in it. We next do the asymptotic matching between each neighbouring region to find out the value of unknown constants.

First, we find solution in region I. Since we have initial conditions $u = R = 1$ at time $t = 0$, so in region I, we impose small time asymptotics

$$u = 1 + tF_0(\eta) + O\left(t^{3/2}\right) \tag{A.11}$$

and

$$R = 1 + t^{3/2}G_0(\eta) + O\left(t^2\right) \tag{A.12}$$

where $\eta = z/\sqrt{t} = O(1)$ as $z \to 0$ and $t \to 0$. We substitute above two asymptotic expansions in our model equations (A.5) and (A.8) and we get a system of differential equations

$$3G_0 - \eta G_0' + F_0' = 0, \tag{A.13}$$

$$2F_0 WeRe - 2G_0''' Re - \eta F_0' WeRe - 6F_0'' We = 0, \tag{A.14}$$

where the dash denotes differentiation. Since equations (A.13) and (A.14) are

exactly the same equations as given in Decent (2009), so the solution of these equations is exactly the same as given in Decent (2009).

From equation (A.11), we have at the leading order as $t \to 0$

$$(u_z)^2 = t\,(F_0')^2 + O(t^{3/2}). \tag{A.15}$$

Using the above equation in equation (A.10), we get an expression for the non-Newtonian viscosity as

$$\mu_a = (1-\lambda)[1 + 3h^2 t\,(F_0')^2 + O(t^{3/2})]^{\frac{n-1}{2}} + \lambda, \tag{A.16}$$

where F_0 is given by in Decent (2009).

After doing a careful analysis of all the next regions II-V, we find that asymptotic expansions and solutions in all the next regions will be exactly the same as given in Decent (2009). We, therefore, do not repeat all the expansions and solutions. However, we will calculate an expression for the non-Newtonian viscosity, using equation (A.10), in next regions II-V. In region II, we find

$$\mu_a = (1-\lambda)[1 + 3h^2 \sum_{j=1}^{2} [\{4A^2\beta^2 z^{-4} t^3 + O(t^5)\} \exp(2cz) \exp\left(-2\beta z^2 t^{-1}\right)]_{\beta=\beta_j}]^{\frac{n-1}{2}}$$

$$+\lambda, \text{ as } t \to 0. \tag{A.17}$$

In region III, we find

$$\mu_a = (1-\lambda)[1 + 3h^2 \sum_{j=1}^{2} [\{A_0^2 t^5 \exp\left(2cz - 2\beta z^2 t^{-1} + 2\sigma t\right)$$

$$\{(c-2\beta z t^{-1})^2 z^{-6}+O(z^{-7})\}]_{\beta=\beta_j}]^{\frac{n-1}{2}}+\lambda,\ \text{as}\ z\to\infty. \tag{A.18}$$

In region IV, we find

$$\mu_a=(1-\lambda)[1+3h^2\sum\ [\{(g_0')^2h_0^2t^{-1}+O(t^{-2})\}\exp(-2tg_0)]]^{\frac{n-1}{2}}$$

$$+\lambda,\ \text{as}\ t\to\infty. \tag{A.19}$$

In region V, we find

$$\mu_a=(1-\lambda)[1+3h^2[\delta^2\exp(2i\omega t)\{m_1\gamma_1\exp(m_1z)+m_2\gamma_2\exp(m_2z)$$
$$+m_3\gamma_3\exp(m_3z)+m_4\gamma_4\exp(m_4z)\}^2]]^{\frac{n-1}{2}}+\lambda,\ \text{as}\ t\to\infty \tag{A.20}$$

Note that all the quantities used in equations (B.44)-(B.47) are given in Decent (2009).

A.3 Conclusions

The aim of this appendix was to obtain an asymptotic solution for a non-Newtonian jet. However, we find that the solution of this problem is exactly the same as given in Decent (2009). We, thus, did not find any new solution. But, we did find the non-Newtonian viscosity μ_a in regions I-V, that was not found before.

Appendix B

Computational Methods and Numerics

In this appendix, we describe the computational methods used in Chapters 4 and 7 of this thesis. The model equations for a rotating Newtonian jet, falling from a large rotating cylindrical drum, are given by

$$R_t + \frac{1}{2}u_s R + uR_s = 0 \tag{B.1}$$

and

$$\begin{aligned} &u_t + uu_s + \frac{1}{We}\left(\frac{1}{R(1+\epsilon^2 R_s^2)^{\frac{1}{2}}} - \frac{\epsilon^2 R_{ss}}{(1+\epsilon^2 R_s^2)^{\frac{3}{2}}}\right)_s \\ &-\frac{3}{R^2 Re}\left[\frac{\partial}{\partial s}\left(R^2\frac{\partial u}{\partial s}\right)\right] - \left[\frac{(X+1)X_s + ZZ_s}{Rb^2}\right] = 0. \end{aligned} \tag{B.2}$$

For details of notations used in above equations, see Chapter 7. We define u_0 and R_0 as the steady-state solution of equations (B.1) and (B.2). We also assume that $u \to u_0$ and $R \to R_0$ as $s \to \infty$, which physically means that in the far-field, the jet is considered to be undisturbed. The initial conditions at $t = 0$ are found to

satisfy the following ODEs

$$\frac{1}{2}u_0' R_0 + u_0 R_0' = 0, \tag{B.3}$$

$$u_0 u_0' - \frac{1}{We}\left(\frac{R_0'}{R_0^2}\right) - \left[\frac{(X_0+1)X_0' + Z_0 Z_0'}{Rb^2}\right] - \frac{3}{Re}\left(u_0'' - \frac{u_0'^2}{u_0}\right) = 0, \tag{B.4}$$

$$(X_0')^2 + (Z_0')^2 = 1 \tag{B.5}$$

and

$$\left(u_0^2 - \frac{3u_0'}{Re} - \frac{1}{R_0 We}\right)(X_0''^2 + Z_0''^2) = \frac{2u_0}{Rb}(X_0' Z_0'' - Z_0' X_0'')$$

$$+\frac{1}{Rb^2}\left[(X_0+1)X_0'' + Z Z_0''\right]. \tag{B.6}$$

where $R_0 = 1/\sqrt{u_0}$, from equation (B.3). The boundary conditions at $s = 0$ are given by

$$u_0(0) = X_0'(0) = 1 \text{ and } X_0(0) = Z_0(0) = Z_0'(0) = 0.$$

For inviscid case (i.e., for $Re \to \infty$), this system of equations can be solved using a Runge-Kutta method while for viscous problem (i.e., for $Re = O(1)$), this system of equations can be solved using Newton's method (see P$\breve{a}$r$\breve{a}$u $et\ al.$ (2007) for the solution of viscous equations). Note that the steady-state solution do not have a breakup point as there is no sinusoidal wave in the boundary conditions to break the jet, as shown in Figure B.1.

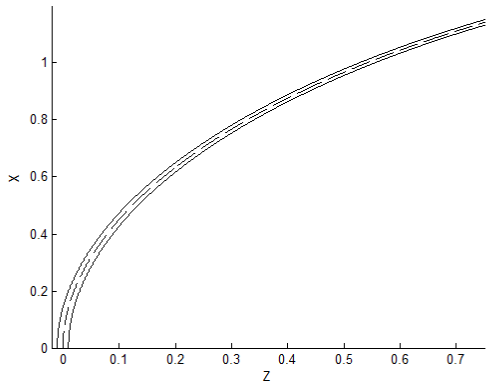

Figure B.1: The solution of the steady trajectory of the jet, with $Re = 5000$, $We = 40$ and $Rb = 3$. Figure taken from Gurney (2010).

B.1 Non-Linear Temporal Solution

By defining $A = R^2$, the system of equations (B.1)-(B.2) can be written as

$$A_t + (Au)_s = 0 \tag{B.7}$$

and

$$u_t + \left(\frac{u^2}{2}\right)_s + \frac{1}{We}\left(\frac{8A + (2\epsilon A_s)^2 - 4\epsilon^2 A A_{ss}}{(4A + (\epsilon A_s)^2)^{3/2}}\right)_s - \frac{3}{ARe}(Au_s)_s$$

$$- \left[\frac{(X+1)X_s + ZZ_s}{Rb^2}\right] = 0. \tag{B.8}$$

The initial conditions at $t = 0$ are obtained from the steady-state ODEs as

$$A(s, t = 0) = R_0^2(s) \text{ and } u(s, t = 0) = u_0(s), \tag{B.9}$$

where $u_0(s)$ and $R_0(s)$ are the steady-state solutions of the ODEs (B.3)- (B.6).

In order to break the jet, we impose a sinusoidal wave disturbance in the form of the boundary conditions at the orifice $s = 0$ as

$$A(s = 0, t) = 1 \text{ and } u(s = 0, t) = 1 + \delta sin\left(\frac{\kappa t}{\epsilon}\right), \tag{B.10}$$

where δ and κ are the amplitude and the frequency of the imposed wave and ϵ is a small parameter. The above system (B.7)-(B.10) is solved numerically using a two-step Lax-Wendroff method, which we describe in the next section.

B.2 Lax-Wendroff Method

A Lax-Wendroff method, is a type of finite difference schemes, which solves a system of equations of the following form

$$\frac{\partial \boldsymbol{u}}{\partial t} = -\frac{\partial}{\partial s}\boldsymbol{F}(\boldsymbol{u}). \tag{B.11}$$

In our case, we have $\boldsymbol{u} = (A, u)^T$ and $\boldsymbol{F}(\boldsymbol{u}) = \left(Au, \frac{u^2}{2}\right)^T$.

We denote $\boldsymbol{u}_i^j$ as the approximate solution of $\boldsymbol{u}$ at the jth time node (or the jth grid point) and the ith space node. We also denote dt as the time step size and ds as the spatial step size. The two-step Lax-Wendroff method is given by

$$\boldsymbol{u}_{i+1/2}^{j+1/2} = \frac{\boldsymbol{u}_{i+1}^j + \boldsymbol{u}_i^j}{2} - (\boldsymbol{F}_{i+1}^j + \boldsymbol{F}_i^j)\frac{dt}{2ds}, \tag{B.12}$$

$$\boldsymbol{u}_i^{j+1} = \boldsymbol{u}_i^j - (\boldsymbol{F}_{i+1/2}^{j+1/2} + \boldsymbol{F}_{i+1/2}^{j-1/2})\frac{dt}{ds}, \tag{B.13}$$

where $\boldsymbol{F}_{i+1/2}^{j+1/2}$ are calculated using the values of $\boldsymbol{u}_{i+1/2}^{j+1/2}$. Using this two-step Lax-Wendroff method, we run the simulations until the jet breakup takes place, which happens when the radius of the jet becomes less than 5% of the initial radius of

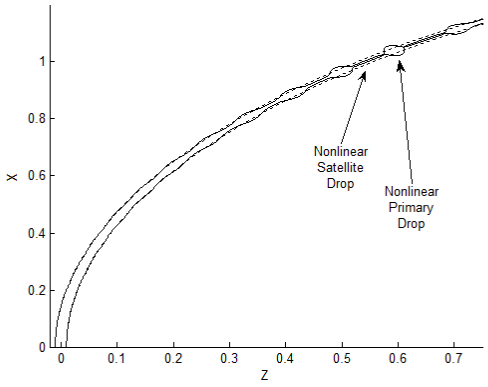

Figure B.2: The solution of the temporal equations of the jet superimposed over the steady-state solution, with $Re = 5000$, $We = 40$, $Rb = 3$ δ = 0.01 and κ = 0.7. Figure taken from Gurney (2010).

the jet. Thus, we get numerical solutions like the one shown in Figure B.2.

B.3 Inclusion of Full-Curvature Terms

Apart from the steady-state solutions, where we only consider the leading-order curvature term, we include the full expression for the mean curvature term for linear instability analysis, to get stable waves (with zero growth rate) for zero wavenumber, and also for non-linear temporal solutions, to avoid instability in numerical solutions, otherwise, we have a numerically unstable solution. Furthermore, experimental diagrams (see Figure B.3) have shown that there is a small spherical drop connected by a slender neck in the region near breakup, which shows the extreme deformation of the surface. Since near breakup, the surface deforms itself, consequently, it becomes necessary to include more terms in curvature. We, therefore, include the higher-order terms in curvature to fully capture the breakup process. Without the expression for the full curvature, the jet is unstable to short wavelength waves, which is not true physically. This approach is used by many authors, see, for example, Yarin (1993), Papageorgiou (1995) and

Brenner $et\ al.$ (1997).

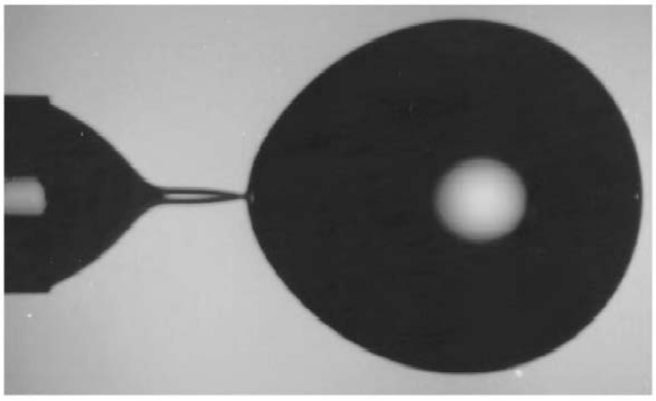

Figure B.3: An experimental photograph showing a small spherical water drop is connected by a slender neck in the region near breakup. Reproduced from Brenner $et\ al.$ (1997).

List of References

[1] Bali, N.P., & Iyengar, N., 2005, A Textbook of Engineering Mathematics. *Laxmi Publications, INDIA.*

[2] Bassi, R., 2011, Absolute Instability in Curved Liquid Jets. *Ph.D. thesis,* The University of Birmingham, UK.

[3] Berkland C., Pollauf E., Varde N., Pack D.W., Kim K.K., 2007, Monodisperse Liquid-filled Biodegradable Microcapsules. *Pharmaceutical Research, **24(5)**:1007–1013.*

[4] Brenner, M. P., Eggers, J., Joseph, K., Sidney, R.N., & Shi, X.D., 1997, Breakdown of scaling in droplet fission at high Reynolds number. *Phys. Fluids., **9**:1573–1590.*

[5] Carreau, P., J., Kee, D., D., and Daroux, M., 1979, An analysis of the viscous behaviour of polymeric solutions, *Can. J. Chem. Eng.,* **57**, 135–140.

[6] Chandrasekhar, S., 1961, Hydrodynamic and Hydromagnetic Stability. *Oxford University Press.*

[7] Chauhan, A., Maldarelli, C., Papageorgiou, D. T. & Rumschitzki, D. S., 2000, Temporal instability of compound threads and jets, *Phys. Fluids,* **420**, 1–25.

[8] Chauhan, A., Maldarelli, C., Rumschitzki D. S. & Papageorgiou, D. T., 2003, An experimental investigation of the convective instability of a jet, *Ch. Eng. Sci.,* **58**, 2421–2432.

[9] Chen, H. Y., Zhao, Y., & Jiang, L., 2009, Compound-fluidic electrospray: An efficient method for the fabrication of microcapsules with multicompartment structure. *Chinese Science Bulletin,* **54**, 3147–3153.

[10] Colinet, P., Legros, J.C. & Velarde, M. G., 2001, Nonlinear dynamics of surface-tension-driven instabilities. *Weinheim ; Wiley-VCH, Cambridge.*

[11] Craster, R. V., Matar, O. K. & Papageorgiou, D. T., 2005, On compound liquid threads with large viscosity contrasts, *J. Fluid Mech.,* **533**, 95–124.

[12] da Vinci, L., 1508, Translated in MacCurdy, ed, The Notebooks of Leonardo da Vinci. *George Brazillier: New York*, page 756.

[13] Decent, S.P., 2009, Asymptotic solution of slender viscous jet breakup. *IMA J. Appl. Math.,* **74**, 741–781.

[14] Eggers, J. & Villermaux, E., 2008, Physics of liquid jets. *Rep. Prog. Phys.*, **71**.

[15] Eggers, J., 1997, Nonlinear dynamics and breakup of free surface flows. *Rev. Mod. Phys.*, **69**, 865-929.

[16] Ellwood, K. R. J., Georgiou, G.C., Papanastasiou, T.C., & J. O. Wilkes, 1990, Laminar jets of Binghamplastic liquids. *J. Rheol.*, **34**, 787–812.

[17] Hardas, N., Danviriyakul, S., Foley, J. L. Nawar, W. W., & Chinachoti,P. 2000, Accelerated stability studies of microencapsulated anhydrous milk fat, *Lebensm.-Wiss. Technol.,* **33**, 506.

[18] Hertz, C. H., 1980, Method and apparatus for forming a compound liquid jet particularly suited for ink-jet printing, *U.S. Patent* **4**, 196, 437.

[19] Hertz, C. H., & Hermanrud, B., 1983, A liquid compound jet, *J. Fluid Mech.,* **131**, 271–287..

[20] Gurney, C. 2010, The Stability and Control of Curved Liquid Jet Breakup. *Ph.D. thesis*, The University of Birmingham, UK.

[21] Hawkins, V. 2010, An Experimental Investigation into the Stability and Control of Curved Liquid Jet Breakup. *Ph.D. thesis*, The University of Birmingham, UK.

[22] Hawkins, L. V., Gurney, C. J., Decent, P. S., Simmons, H. MJ. & Uddin, J., 2010, Unstable Waves on a Curved non-Newtonian Liquid Jet. *J. Phys. A: Math. & Theor.*, **43,** 055501 (18pp).

[23] Holman, J. P. (2002), Heat Transfer, *McGraw-Hill Companies*.

[24] Keller, J.B., Rubinow, S.I. & Tu, Y.O., 1973, Spatial instability of a jet. *Phys. Fluids*, **16,** 2052–2055.

[25] Leach, J.A. & Needham, D.J., 2001, The evolution of travelling waves in generalized Fisher equations via matched asymptotic expansions: Algebraic corrections. *Q. J. Mech. Appl. Math.* **54**, 157–175.

[26] Leach, J.A., Needham, D.J. & Kay, A.L., 2003, The evolution of reaction-diffusion waves in generalized Fisher equations: Exponential decay rates. *Dynamics of Continuous, Discrete and Impulsive Systems, Ser. A* **10**, 417–430.

[27] Leach, J.A. & Needham, D.J., 2004, Matched Asymptotic Expansions in Reaction-Diffusion Theory. *Springer-Verlag, London*.

[28] Lefebvre A., H., 1989, Atomization and Sprays. *New York: Hemisphere*.

[29] Liao, Y., Jeng, S. M., Jog, M. A., & Benjamin, M. A., 2000, The effect of air swirl proffle on the instability of a viscous liquid jet. *J. Fluid Mech.*, **424**, 1–20.

[30] Lin, S.P. & Reitz, R.D., 1998, Drop and spray formation from a liquid jet. *Ann. Rev. Fluid Mech.*, 30:85 (105).

[31] Lin, S.P., 2003, Breakup of Liquid Jets and Sheets. *Cambridge University Press.*

[32] Leib, S.J. & Goldstein, M.E., 1986, The generation of capillary instabilities on a liquid jet. *J. Fluid Mech.,* 168:479 (500).

[33] Mariotte, E., 1686, Traite du Mouvement des Eaux et Des Autres Corps Fluides. *Paris: E Michallet.*

[34] Massoud, M., 2005, Engineering Thermofluids: Thermodynamics, Fluid Mechanics, and Heat Transfer. *Springer.*

[35] Mathiowitz, E., Jacob, J. S., Jong, Y. S., Carino, G. P., Chickering, D. E., Chaturvedi, P., Santos, C. A., Vijayaraghavan, K., Montgomery, S., Bassett, M., & Morrell, C., 1997, Biologically erodable microsphere as potential oral drug delivery system. *Nature, London,* **386**, 410.

[36] Middleman, S., 1995, Modelling axisymmetric flows: Dynamics of films, jets and drops. Burlington, MA: *Academic Press.*

[37] Mitragotri, S., 2006, Current status and future prospects of needle-free liquid jet injectors. *Nature Reviews, Drug Discovery* **5(7)**, 543-548.

[38] Mohsin, M., Uddin, J., Decent, S.P., & Simmons, M.J.H., 2012, Break-up and droplet formation in shear thinning compound liquid jets. *IMA J. Appl. Math.,* **77**, 97–108.

[39] Părău, E.I., Decent, S.P., King, A.C., Simmons, M.J.H. & Wong, D.Y., 2006, Nonlinear travelling waves on a spiralling liquid jet, *Wave Motion,* **43**, 599–618.

[40] Părău, E.I., Decent, S.P., Simmons, M.J.H., Wong, D. & King, A.C., 2007, Nonlinear viscous liquid jets from a rotating orifice. *J. Eng. Math.* **57**, 159–179.

[41] Papageorgiou, D.T., 1995, On the breakup of viscous liquid threads, *Phys. Fluids*, **7**, 1529–1544.

[42] Partridge, L., 2006, An experimental and theoretical investigation into the breakup of curved liquid jets in the prilling process. *Ph.D. Thesis,* The University of Birmignham, UK.

[43] Peregrine, D., H., Shoker, G., & Symon, A., 1990, The bifurcation of liquid bridges. J. Fluid Mech., **212**, 25.

[44] Plateau, J., 1873, Statique Experimentale et Theoretique des Liquides Soumis aux Seules Forces Moleculaires, Gauthier Villars, Paris, ***II***, 319.

[45] Radev, S., & Tchavdarov, B., 1988, Linear capillary instability of compound jets. *Int. J. Multiphase Flow,* **14**, 67–79.

[46] Rayleigh, L., J.W.S., 1878, On the Instability of Jets, *Proc. London Math. Soc.,* **10**, 4–13.

[47] Rayleigh, L., J.W.S., 1879, On the capillary phenomena of jets. Proc. Roy. Soc. London., 29: 4–13.

[48] Reitz, R.D. & Bracco, F.V., 1986, Mechanisms of breakup of round liquid jets. The Encyclopedia of Fluid Mechanics, ed. N Cheremisnoff, 3: 233-49. Houston: Gulf.

[49] Ruyer-Quil, C., Treveleyan, P., Giorgiutti-Dauphine, F., Duprat, C., and Kalliadasis, S., 2008, Modelling film flows down a fibre. J. Fluid Mech., **603**, 431–462.

[50] Sanz, A., and Meseguer, J., 1985, One-dimensional analysis of the compound jet. J. Fluid Mech., **159**, 55–68.

[51] Savart, F., 1833, Annal, Chim. **53**, 337.

[52] Sawhney, G. S., 2011, Fundamentals Of Fluid Mechanics. I. K. International Pvt Ltd.

[53] Schmid, Peter J. & Henningson, Dan S., 2001, Stability and Transition in Shear Flows. *Springer-Verlag, New York, Inc.*

[54] Shikhmurzaev, Y. D., 2008, Capillary flows with forming interfaces. *Chapman & Hall/CRC, London.*

[55] Shkadov, V. Y. & Sisoev, G. M., 1996 Instability of a two layer capillary jet. *Int. J. Multiphase Flow,* **22**, 363–377.

[56] UDDIN, J., (2007) An Investigation into Methods to Control Breakup and Droplet Formation in Single and Compound Liquid Jets. *Ph.D. thesis, University of Birmingham, UK.*

[57] Uddin, J., Decent, S. P. & Simmons, M. H., (2006) The instability of shear thinning and shear thickening liquid jets: linear theory. *J. Fluids Eng.,* **128**, 968–975.

[58] Uddin, J., Decent, S. P. & Simmons, M. H., (2008) Non-linear waves along a rotating non-Newtonian liquid jet. *Int. J. of Eng. Sci.,* **46**, 1253–1265.

[59] Uddin, J., & Decent, S. P., (2009) Curved non-Newtonian liquid jets with surfactants. *J. Fluids Eng.,* **131**, 091203-1–7.

[60] Uddin, J., & Decent, S. P., (2010) Breakup of inviscid compound liquid jets falling under gravity. *J. Phys. A: Math. & Theor.,* **43**, 1–12.

[61] Varga, M. C., Lasheras, J. C., Shoker, G., & Hopfinger, J. E., 2003, Initial breakup of a small-diameter liquid jet by a high-speed gas stream. J. Fluid Mech., **497**, pp. 405434.

[62] Wallwork, I. M., Decent, S. P., King, A. C., & Schulkes, R. M. S., (2002) The Trajectory and Stability of a Spiralling Liquid Jet. Part 1, Inviscid Theory. *J. Fluid Mech.,* **459**, 43–65.

[63] Weber, C., 1931, Zum zerfall eines ussigkeitsstrahles. *Z. Angew. Math. Mech.*, **11**:36-41.

[64] Yang, Li-jun, Qing-fei Fu, Yuan-yuan Qu, Bin Gu, Meng-zheng Zhang, 2012, Breakup of a power-law liquid sheet formed by an impinging jet injector. *Int. J. of Multiphase Flow* **39**:3744.

[65] Yarin, A.L., 1993, Free liquid jets and films : hydrodynamics and rheology. *Harlow : Longman Scientific & Technical ; Wiley, New York.*